

Search for New Phenomena in Dijet Angular Distributions  
Measured with the ATLAS Detector in Proton-Proton Collisions at  $\sqrt{s} = 7$  TeV

---

Thorsten Dietzsch



Dissertation  
submitted to the  
Combined Faculties of the Natural Sciences and Mathematics  
of the Ruperto-Carola-University of Heidelberg, Germany  
for the degree of  
Doctor of Natural Sciences

Put forward by  
Thorsten Dietzsch  
born in Hildesheim, Germany  
Oral examination: July 26th, 2013



**Search for New Phenomena in Dijet Angular  
Distributions Measured with the ATLAS Detector in  
Proton-Proton Collisions at  $\sqrt{s} = 7 \text{ TeV}$**

Referees:

Prof. Dr. Hans-Christian Schultz-Coulon  
PD Dr. Klaus Reygers



# Abstract

The high-energy proton-proton collisions at the LHC allow to probe hard QCD interactions at the highest momentum transfers and to search for physics beyond the Standard Model. Normalised dijet angular distributions are particularly suited for such searches due to their reduced sensitivity to systematic uncertainties. In this thesis,  $4.8 \text{ fb}^{-1}$  of proton-proton collisions at  $\sqrt{s} = 7 \text{ TeV}$ , recorded with the ATLAS detector, are used to measure the dijet angular distributions in five bins of the dijet invariant mass. The data are compared to a QCD prediction which is obtained from Monte Carlo simulations and corrected for NLO effects. In the absence of significant deviations from the background prediction, 95% C.L. Bayesian limits are set on the characteristic parameters of two models for new phenomena. In a quark contact interaction scenario with destructive interference, the compositeness scale  $\Lambda$  is excluded below 7.6 TeV, while the expected limit was 7.7 TeV. A quantum black hole model with six extra dimensions is excluded for values of the reduced Planck scale  $M_D$  below 4.1 TeV, with an expected limit at 4.2 TeV.

# Zusammenfassung

Die hochenergetischen Proton-Proton-Kollisionen am LHC ermöglichen sowohl Tests harter QCD-Wechselwirkungen bei höchsten Impulsüberträgen als auch die Suche nach Physik jenseits des Standardmodells. Normierte Dijet-Winkelverteilungen sind aufgrund ihrer reduzierten Sensitivität auf systematische Unsicherheiten besonders für derartige Suchen geeignet. In der vorliegenden Arbeit werden mit dem ATLAS-Detektor gemessene Proton-Proton-Wechselwirkungen verwendet, um Dijet-Winkelverteilungen in fünf Bereichen der invarianten Dijetmasse zu messen. Die Kollisionen fanden bei einer Schwerpunktsenergie von  $\sqrt{s} = 7 \text{ TeV}$  statt, und die verwendete Datenmenge entspricht einer integrierten Luminosität von  $\mathcal{L} = 4.8 \text{ fb}^{-1}$ . Die Daten werden mit einer QCD-Vorhersage aus Monte-Carlo-Simulationen verglichen, in der störungstheoretische Beiträge nächstführender Ordnung durch geeignete Korrekturen berücksichtigt werden. Da die Messung keine signifikanten Abweichungen von der Untergrundvorhersage zeigt, werden Bayesische 95% C.L.-Ausschlussgrenzen auf die charakteristischen Parameter in zwei Modellen neuer Phänomene gesetzt. In einem Szenario für Quark-Kontaktwechselwirkungen mit destruktiver Interferenz wird die Compositeness-Skala  $\Lambda$  bei einer erwarteten Grenze von 7.7 TeV unterhalb von 7.6 TeV ausgeschlossen. Ein Modell für Quanten-Schwarze-Löcher mit sechs Extradimensionen wird bei einer erwarteten Grenze von 4.2 TeV für Werte der reduzierten Planck-Skala  $M_D$  unterhalb von 4.1 TeV ausgeschlossen.



# Overview

In this thesis, the analysis of dijet angular distributions in  $4.8 \text{ fb}^{-1}$  of proton-proton collision data recorded with the ATLAS detector in 2011 is presented. After the theoretical framework for the production of hadronic jets is laid out in chapter 1, the use of dijet angular distributions as a tool to search for physics beyond the Standard Model is motivated in chapter 2. The ATLAS detector is introduced in chapter 3, followed by the description of the Monte Carlo simulation of the background and the signal processes in chapter 4. The reconstruction and calibration of hadronic jets in ATLAS are important within the framework of this thesis and are explained in detail in chapter 5. The event selection of the analysis is reported in chapter 6, and studies of the selected events are collected in chapter 7. The impact of individual uncertainty components on the analysis and the resulting systematic uncertainties are presented in chapter 8. The experimental results and the comparison of the observed data with the QCD prediction are discussed in chapter 9. The results are used to constrain physics beyond the Standard Model, and the obtained limits on the characteristic scales of two models for such phenomena are reported in chapter 10.

## Author's contributions

The work presented in this thesis has been performed within the ATLAS collaboration. It represents one of three dijet analyses which have been conducted in parallel and in close collaboration by a small group of people: the analysis of the dijet angular distribution as a function of the variable  $\chi$ , the study of the dijet angular distribution with the shape parameter  $F_\chi$  and the spectral analysis of the dijet invariant mass. The first of these three has been the main focus of the author and is presented in this thesis. Many of the systematic studies carried out by the author have however benefited the other two analyses and vice versa.

The author has contributed significantly to every aspect of the presented analysis; from the event selection and the study of the background prediction over the data verification and the determination of the systematic uncertainties up to the evaluation of the agreement of the data with the background prediction and the calculation of limits for new phenomena.

In particular, the author has contributed to the event selection with a study of the influence of a temporary hardware failure in the liquid argon calorimeter. A strategy to

address this problem has been devised and implemented in the analysis of  $\chi$  as well as in the analysis of  $F_\chi$ . Furthermore, the trigger efficiency for the highest dijet invariant mass bin in the analysis has been determined.

The author has improved the K-factor correction of the PYTHIA QCD Monte Carlo simulation and validated the comparison with a different Monte Carlo generator. The recommended weighting scheme for the adjustment of the pile-up conditions in the Monte Carlo simulation to those in data has been tested, and it has been shown that the weighting has to be performed independently for each trigger which contributes to the analysis. These results were also used for the analysis of  $F_\chi$ .

Extensive data verification studies have been performed by the author. The event yields and kinematic distributions after the analysis selection have been studied, and the data have been shown to be in good agreement with the prediction from the Monte Carlo simulation. Beyond the work presented in the scope of this thesis, the author has also contributed with a wide range of similar studies when a statistical fluctuation was observed in the analysis of  $F_\chi$  in the early 2011 data. The author has studied the events with the highest transverse momenta and the highest dijet invariant masses in the analysis of  $\chi$ . The event displays obtained for these events are presented in this thesis. A strategy to study the residual effect of out-of-time pile-up on the analysis with the help of the variable  $F_\chi$  has been developed and used to show that no residual effects are observed.

The systematic uncertainties in the analysis have been studied carefully by the author. The impact of the individual uncertainty components of the jet energy scale has been quantified. The performance of the determination of the total jet energy scale uncertainty with pseudo-experiments has been improved significantly in this work, thus increasing the accuracy of the uncertainty estimate and allowing for the first time to verify the convergence of this method. In addition, two approaches for the estimation of the flavour composition uncertainty have been compared, and the impact of the jet energy and jet angular resolution uncertainties on the analysis has been quantified. The theoretical uncertainties on the analysis from the PDF and the scale uncertainties have been validated within this work.

Finally, the author has also improved the calculation of the  $p$ -values and the limits for phenomena beyond the Standard Model. The inclusion of a larger number of pseudo-experiments allowed to obtain more precise results than before.

The author has represented the analysis in the exotics working group approval and has given the ATLAS open presentation for the approval of the publication in [1]. The analysis has also been published in [2].

# Contents

<b>1. Theoretical framework</b>	<b>1</b>
1.1. The Standard Model of particle physics . . . . .	1
1.2. Jet production in Quantum Chromodynamics . . . . .	2
<b>2. Search for new phenomena in dijet angular distributions</b>	<b>15</b>
2.1. Dijet angular distributions . . . . .	15
2.2. Physics beyond the Standard Model . . . . .	17
2.3. Analysis strategy . . . . .	21
<b>3. The ATLAS detector at the LHC</b>	<b>25</b>
3.1. The LHC . . . . .	25
3.2. The ATLAS detector . . . . .	27
3.3. Data used in this analysis . . . . .	36
<b>4. Simulation of background and signal processes</b>	<b>39</b>
4.1. Simulation of the QCD background . . . . .	39
4.2. Simulation of new phenomena . . . . .	42
4.3. Inclusion of NLO effects . . . . .	43
<b>5. Jet reconstruction and calibration in ATLAS</b>	<b>47</b>
5.1. Jet reconstruction . . . . .	47
5.2. Jet calibration . . . . .	49
5.3. Residual calibration with <i>in situ</i> techniques . . . . .	53
5.4. Jet energy scale uncertainty . . . . .	55
<b>6. Event selection</b>	<b>63</b>
6.1. Overview of the event selection . . . . .	63
6.2. Detailed description of the event selection . . . . .	68
<b>7. Data verification</b>	<b>79</b>
7.1. Event yields . . . . .	79
7.2. Kinematic distributions . . . . .	81
7.3. Pile-up reweighting . . . . .	84
7.4. Residual pile-up effects . . . . .	87
7.5. Events with high- $p_T$ jets . . . . .	92

<b>8. Systematic uncertainties</b>	<b>95</b>
8.1. Experimental uncertainties . . . . .	95
8.2. Theoretical uncertainties . . . . .	112
<b>9. Experimental results</b>	<b>117</b>
9.1. Agreement between the data and the background prediction . . . . .	119
9.2. Comparison with an alternative Monte Carlo prediction . . . . .	121
<b>10. Constraints on physics beyond the Standard Model</b>	<b>125</b>
10.1. Bayesian framework . . . . .	125
10.2. Determination of the posterior pdf . . . . .	126
10.3. Parametrisation of the signal hypotheses . . . . .	127
10.4. Inclusion of systematic uncertainties . . . . .	129
10.5. Limits for quark contact interactions . . . . .	130
10.6. Limits for quantum black holes . . . . .	132
<b>11. Conclusions</b>	<b>135</b>
<b>A. Supplementary material</b>	<b>137</b>
A.1. Kinematic distributions . . . . .	137
A.2. Out-of-time pile-up . . . . .	138
A.3. Events with high- $p_T$ jets and high dijet invariant masses . . . . .	140
A.4. Jet energy scale uncertainty . . . . .	145

# 1. Theoretical framework

This chapter introduces the theoretical framework for the analysis of the dijet angular distributions presented in this thesis. After a short discussion of the Standard Model, the main focus is on jet production in Quantum Chromodynamics.

## 1.1. The Standard Model of particle physics

The theoretical description of the world at microscopic distances and high energies is given by the Standard Model of particle physics (SM). A detailed discussion of the topic may be found e. g. in [3]. The SM is a quantum gauge field theory and describes the interactions of spin-1/2 quarks and leptons through the electromagnetic, the weak and the strong force.

Three generations  
of matter (fermions)

	I	II	III		
mass	2.4 MeV/c <sup>2</sup>	1.27 GeV/c <sup>2</sup>	171.2 GeV/c <sup>2</sup>	0	? GeV/c <sup>2</sup>
charge	$\frac{2}{3}$	$\frac{2}{3}$	$\frac{2}{3}$	0	0
spin	$\frac{1}{2}$	$\frac{1}{2}$	$\frac{1}{2}$	1	0
name	u up	c charm	t top	$\gamma$ photon	H Higgs boson
Quarks					
mass	4.8 MeV/c <sup>2</sup>	104 MeV/c <sup>2</sup>	4.2 GeV/c <sup>2</sup>	0	
charge	$-\frac{1}{3}$	$-\frac{1}{3}$	$-\frac{1}{3}$	0	
spin	$\frac{1}{2}$	$\frac{1}{2}$	$\frac{1}{2}$	1	
name	d down	s strange	b bottom	g gluon	
Leptons					
mass	< 2.2 eV/c <sup>2</sup>	< 0.17 MeV/c <sup>2</sup>	< 15.5 MeV/c <sup>2</sup>	91.2 GeV/c <sup>2</sup>	
charge	0	0	0	0	
spin	$\frac{1}{2}$	$\frac{1}{2}$	$\frac{1}{2}$	1	
name	$\nu_e$ electron neutrino	$\nu_\mu$ muon neutrino	$\nu_\tau$ tau neutrino	Z <sup>0</sup> Z boson	
Leptons					
mass	0.511 MeV/c <sup>2</sup>	105.7 MeV/c <sup>2</sup>	1.777 GeV/c <sup>2</sup>	80.4 GeV/c <sup>2</sup>	
charge	-1	-1	-1	$\pm 1$	
spin	$\frac{1}{2}$	$\frac{1}{2}$	$\frac{1}{2}$	1	
name	e electron	$\mu$ muon	$\tau$ tau	W <sup>±</sup> W boson	

Gauge bosons

Figure 1.1. The fermions and bosons in the Standard Model; from [4].

The leptons do not interact via the strong force and may be grouped into three so-called *families*, each consisting of a left-handed electro-weak  $SU(2)$  doublet as shown in figure 1.1: The electron  $e$ , the muon  $\mu$  and the tau  $\tau$  carry electric charge  $-e$ , while the neutrinos  $\nu_e$ ,  $\nu_\mu$  and  $\nu_\tau$  are neutral. Quarks interact also via the strong force. They exist in six flavours and may also be arranged in three families of electro-weak  $SU(2)$  doublets. The  $u$ ,  $c$  and  $t$  quark carry electric charge  $+2e/3$ , and the electric charge of the  $d$ ,  $s$  and  $b$  quarks is  $-e/3$ .

Since the Standard Model is a gauge theory, the Lagrangian of the theory is invariant under a set of local symmetries if corresponding gauge fields are introduced which lead to the known interactions. The resulting spin-1 gauge bosons are the mediators of the forces, and their number is given by the number of the generators of the gauge group. The photon  $\gamma$ , the  $W^\pm$  and the  $Z^0$  boson are the gauge bosons of the  $SU(2)_L \times U(1)_Y$  electro-weak symmetry group, where  $Y$  refers to the hypercharge generator of  $U(1)_Y$ . Eight gluons are the mediators of the strong force, described by  $SU(3)_C$ . Quantum Chromodynamics, the theory of the strong interaction, is the underlying theory for the SM processes analysed in this thesis. It is discussed in detail below.

In the SM, the gauge bosons and fermions are thought to acquire masses through the Higgs mechanism which denotes the spontaneous breaking of the  $U(1)_Y \times SU(2)_L$  symmetry. The Higgs mechanism also predicts the existence of an associated particle  $H$ , a neutral boson of spin 0. In July 2012, the ATLAS and CMS experiments at CERN announced the discovery of a boson [5, 6] that appears consistent with the SM Higgs particle. In March 2013, the experiments reported updated results which indicate that the particle has spin 0 and positive parity, in agreement with predictions for the SM Higgs boson [7, 8]. Further investigation, in particular of the precise branching fractions, is necessary in order to fully establish the SM-nature of the Higgs-like particle.

Despite its large success, motivations for extensions of the SM exist. In this thesis, the angular distribution of dijet events is utilised to perform a search for quark contact interactions and quantum black holes. These two models will be introduced in chapter 2.

## 1.2. Jet production in Quantum Chromodynamics

Quantum Chromodynamics (QCD) is the gauge theory of the strong interaction. This section introduces the main concepts of QCD that are necessary to describe the physics of dijet processes at the LHC.

QCD is formulated as a non-Abelian gauge theory with the symmetry group  $SU(3)$ , the group of special unitary transformations in three dimensions. Correspondingly, the Lagrangian of the theory is invariant under  $SU(3)$  transformations of the quark fields in colour space if eight gauge fields are introduced, corresponding to the number of generators of  $SU(3)$ . The quanta of these fields and mediators of the strong force are called *gluons*. In contrast to the electromagnetic interaction, gluons carry a colour charge themselves, leading to gluon self-interactions.

Following the notation of [9] and [10], the classical Lagrangian density of QCD may be written as

$$\mathcal{L}_{\text{QCD, classical}} = \sum_q \bar{q}_{q,a} (i\gamma^\mu \partial_\mu \delta_{ab} - g_S \gamma^\mu t_{ab}^C \mathcal{A}_\mu^C - m_q \delta_{ab}) q_{q,b} - \frac{1}{4} F_{\alpha\beta}^A F_A^{\alpha\beta}. \quad (1.1)$$

Here, the quark-field spinors for a quark with flavour  $q$ , mass  $m_q$  and colour-index  $a$  are denoted with  $q_{q,a}$ . The colour-index runs from 1 to 3, the number of colours in QCD. The Dirac  $\gamma$ -matrices are written as  $\gamma^\mu$ . The strong coupling may also be expressed using  $\alpha_s = g_s^2/4\pi$ . The  $t_{ab}^C$  are the eight generators of  $SU(3)$ , and the eight gluon fields are written as  $\mathcal{A}_\mu^C$ , where  $C$  runs from 1 to 8. The gluonic field strength tensor  $F_{\alpha\beta}^A$  is determined from derivatives of the gluon fields and  $f^{ABC}$ , the structure constants of  $SU(3)$ , as

$$F_{\alpha\beta}^A = \partial_\alpha \mathcal{A}_\beta^A - \partial_\beta \mathcal{A}_\alpha^A - g_s f^{ABC} \mathcal{A}_\alpha^B \mathcal{A}_\beta^C. \quad (1.2)$$

The last term in the above equation is quadratic in the gluon field. It arises from the non-Abelian nature of the  $SU(3)$  gauge group and leads to gluon self-interactions and asymptotic freedom as described in the following section. The strong coupling  $g_s$  and the quark masses  $m_q$  are the fundamental parameters of QCD.

The Lagrangian of equation 1.1 may be used to derive Feynman rules and perform perturbative calculations. As a preparatory step, a gauge has to be chosen in order for the gluon propagator to be defined [9]. Among the possible schemes are the *covariant gauges*, defined by

$$\mathcal{L}_{\text{gauge-fixing}} = -\frac{1}{2\lambda} (\partial^\mu \mathcal{A}_\mu^A)^2, \quad (1.3)$$

and specified by a gauge parameter  $\lambda$ . In QCD, an additional *ghost Lagrangian*  $\mathcal{L}_{\text{ghost}}$  has to be added to prevent the propagation of unphysical degrees of freedom.

The full Lagrangian for QCD in the covariant gauge is then given by

$$\mathcal{L}_{\text{QCD}} = \mathcal{L}_{\text{classical}} + \mathcal{L}_{\text{gauge-fixing}} + \mathcal{L}_{\text{ghost}}. \quad (1.4)$$

Figure 1.2 shows the resulting Feynman rules. With these rules, matrix elements and hence cross sections for QCD processes can be calculated in perturbation theory. The perturbative treatment only yields meaningful results if  $\alpha_s$  is small. The next section discusses the dependence of  $\alpha_s$  on the energy scale of the interaction.

### 1.2.1. The running coupling

In the calculation of processes at higher-orders in perturbation theory, ultra-violet (UV) divergences arise from the integration over infinitely high momenta in loops. In QCD, these infinities can be treated in the framework of renormalisation. In the renormalisation procedure, a regularisation is applied as a first step. One example is the so-called dimensional regularisation [11–13] in which the integrals in the calculation converge when evaluated in a space with a number of dimensions  $n$  different to four. In a second step, the divergences are absorbed into the definition of renormalised parameters in the Lagrangian, such as the masses and couplings. The newly-defined parameters depend on the details of the renormalisation scheme. A commonly used renormalisation scheme with dimensional regularisation is the so-called  $\overline{\text{MS}}$  scheme [14].

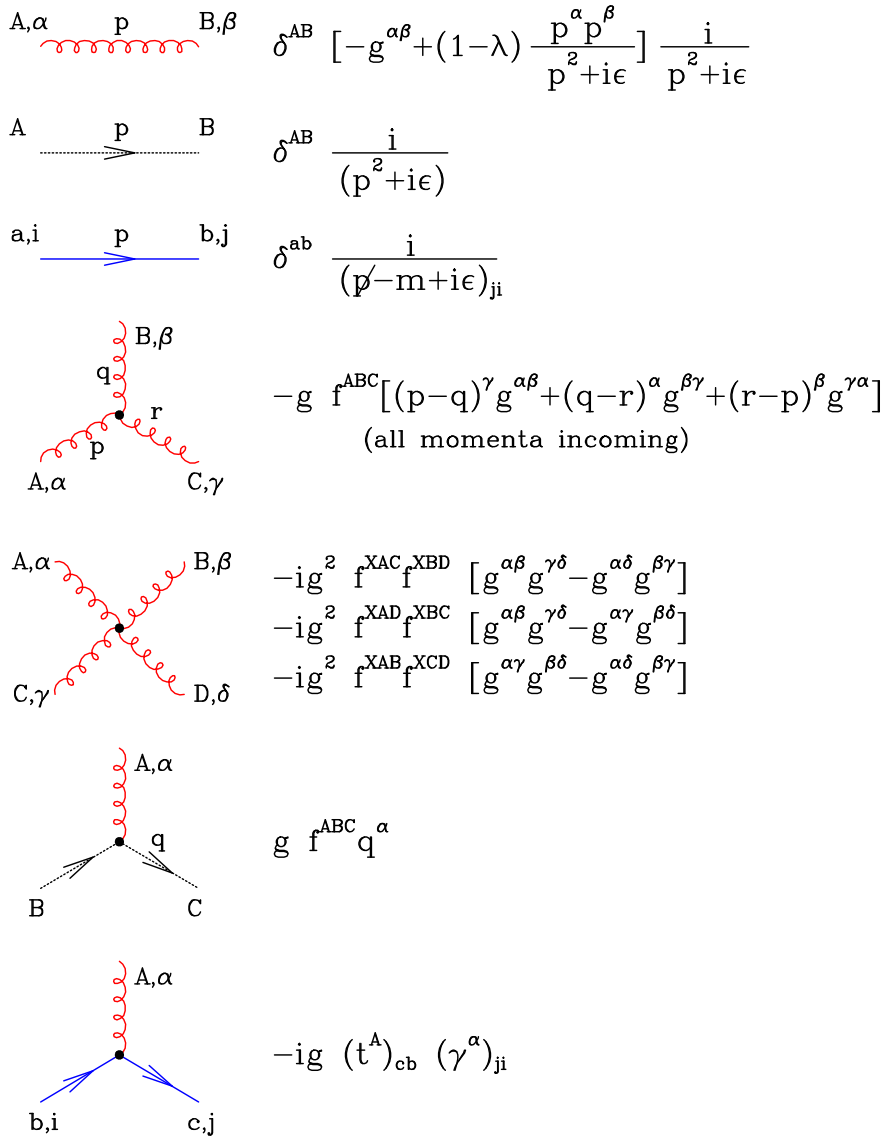


**Figure 1.2.** Feynman rules for QCD in the covariant gauge for gluons (curly lines), fermions (solid lines) and ghosts (dotted lines); from [9].

As a result of the renormalisation procedure, apparent constants in the theory, such as the strong coupling  $\alpha_s$ , become scale-dependent. The exact scale-dependence is described by the *renormalisation group equation*

$$\frac{\partial \alpha_s(Q^2)}{\partial \ln Q^2} = \beta(\alpha_s(Q^2)). \quad (1.5)$$

The so-called *beta function* may be written in a perturbative series in the coupling as

$$\beta(\alpha_s) = -\beta_0 \alpha_s^2 - \beta_1 \alpha_s^3 + \mathcal{O}(\alpha_s^4). \quad (1.6)$$

Solving to leading order, i. e. retaining only the term quadratic in  $\alpha_s$ , the value of  $\alpha_s$  at some large scale  $Q^2$  can be inferred from its value at a reference scale  $\mu$  in the perturbative regime as

$$\alpha_s(Q^2) = \frac{\alpha_s(\mu^2)}{1 + \alpha_s(\mu^2)\beta_0 \ln(\frac{Q^2}{\mu^2})}. \quad (1.7)$$

A common reference scale is the mass of the Z boson,  $M_Z = 91.19 \text{ GeV}$ , with a current world average [10] of

$$\alpha_s(M_Z^2) = 0.1184 \pm 0.0007. \quad (1.8)$$

The exact form of the coefficient  $\beta_0$  is

$$\beta_0 = \frac{11N_C - 2n_f}{12\pi}, \quad (1.9)$$

with  $N_C = 3$ , the number of colours and  $n_f$ , the *active flavours*, the number of flavours with a mass below the scale  $Q$  of the process. Due to gluon self-interactions,  $\beta_0$  is positive in the case of QCD, leading to a decrease of the coupling for increasing momentum scales  $Q^2$ . This phenomenon is known as *asymptotic freedom* and describes the notion that quarks and gluons, when probed at a hard scale inside a hadron, behave as quasi-free particles.

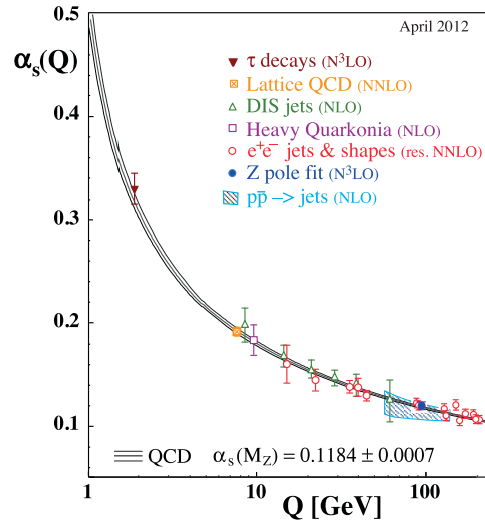


**Figure 1.3.** The dependence of  $\alpha_s$  on the energy scale  $Q$ , obtained with various methods and with the perturbative order of the QCD calculations reported in parentheses; from [10].

The running of the strong coupling is demonstrated in figure 1.3 which shows measurements of  $\alpha_s$  at various energy scales  $Q$ , together with results from perturbative QCD calculations at different orders.

Isolated quarks or gluons are not observed in experiments. Instead, they only appear in colour-neutral bound states. This phenomenon, called *confinement*, is not yet fully understood from a theoretical perspective, as the perturbative treatment breaks down

when the coupling becomes large. However, inverting the above reasoning as an indicative argument, the strong coupling grows as the distance between the quarks increases, such that at some point it becomes energetically favourable to create a new quark-anti-quark pair from the vacuum which can combine with the previous ones into colour-singlet states.

Using the same leading-order approximation as above, the scale dependence of the effective coupling may also be expressed with reference to a scale  $\Lambda$ , defined as the scale where  $\alpha_s$  would become strong if extrapolated to the non-perturbative regime: The general solution to the leading-order approximation of equation 1.5 may be written as  $\alpha_s(Q^2) = (C + \beta_0 \ln Q^2)^{-1}$ , with a constant of integration  $C$ . In equation 1.7,  $C$  has been determined such that  $\alpha_s$  is expressed with respect to the reference scale  $Q^2 = \mu^2$ .  $C$  may also be used to define a scale  $\Lambda$  such that the denominator vanishes,  $C + \beta_0 \ln \Lambda^2 = 0$ , leading to

$$\alpha_s(Q^2) = \left( \beta_0 \ln \frac{Q^2}{\Lambda^2} \right)^{-1}. \quad (1.10)$$

The value of  $\Lambda$  is in the vicinity of 200 MeV, similar to the masses of light hadrons. Hence, indications exist that confinement could follow from the running of the coupling, even if the result is not based on a perturbatively valid treatment [9].

The next section describes how quantitative predictions for the high-energy proton-proton collisions at the LHC may be derived by incorporating both the confinement of quarks and gluons in initial-state hadrons and the short-range partonic interactions which can be treated perturbatively.

### 1.2.2. The QCD improved parton model

Of most interest for this thesis is the QCD production of high transverse momentum jets in proton-proton collisions. In general, cross sections with initial hadrons and high momentum transfer may be described in the language of the *QCD improved parton model*. This model makes use of factorisation theorems [15] to describe the scattering process as consisting of a short, high-momentum subprocess between quasi-free, pointlike partons, preceded and followed by slow, low-momentum processes. These low-momentum processes are described as part of the structure of the incoming hadrons. The QCD improved parton model extends the early parton model described e. g. in [16]. It accounts for the logarithmic scaling violations seen in data [17] and calculated in perturbative QCD with collinear gluon emissions off incoming quarks. To this end, it introduces a factorisation scale  $\mu_F$  with the interpretation that all emissions with momentum above  $\mu_F$  are treated as part of the hard subprocess, whereas all softer emissions are absorbed in the parton distribution functions (PDFs).

The cross section for a process with two incoming hadrons with momenta  $P_1$  and  $P_2$  is written as the convolution of the cross section of the hard subprocess  $\hat{\sigma}$  with the parton

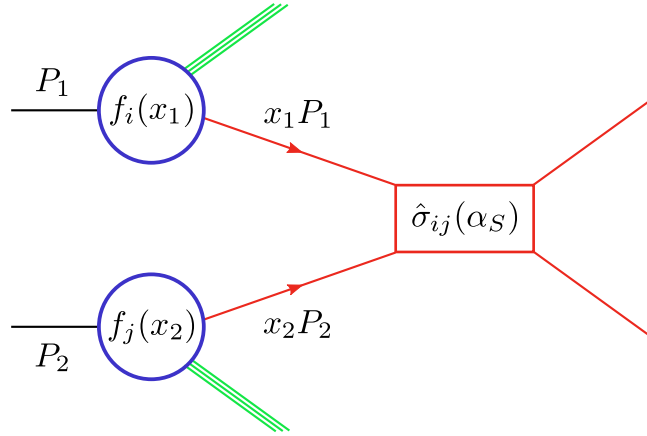


**Figure 1.4.** Illustration of the factorisation of a QCD process in the improved parton model; adapted from [9].

distribution functions  $f_i$  of parton  $i$ :

$$\sigma(P_1, P_2) = \sum_{i,j} \int dx_1 dx_2 f_i(x_1, \mu_F^2) f_j(x_2, \mu_F^2) \times \hat{\sigma}_{i,j} \left( P_1, P_2, \alpha_S(\mu_R^2), \frac{Q^2}{\mu_R^2}, \frac{Q^2}{\mu_F^2} \right) \quad (1.11)$$

The sum runs over the parton types  $i, j$ , and the integral is calculated over the momentum fractions  $x_1$  and  $x_2$  of the partons, such that  $p_{1,2} = x_{1,2}P_{1,2}$ . The *partonic cross section*  $\hat{\sigma}$  depends on the renormalisation scale  $\mu_R$ , while both the parton distribution functions and the subprocess cross section depend on the factorisation scale  $\mu_F$ . When calculated to all orders, the dependence of the results on both arbitrary scales vanishes, but finite-order calculations carry a residual renormalisation and factorisation scale dependence. Systematic variations of these scales have been performed in order to estimate the scale dependence of the result of the analysis and will be described in section 8.2. The  $x$ -dependence of the parton distribution functions has to be measured, e. g. in deep inelastic scattering experiments. A review on this topic may be found in [10]. The  $\mu^2$ -dependence can be calculated in perturbative QCD, using the so-called *DGLAP* equations [18–20].

The QCD improved parton model provides a framework for the description of hard QCD interactions between partons that are confined in initial-state hadrons. The next section discusses the evolution of the final-state partons that result from the hard scattering.

### 1.2.3. Hadronic jets

Due to colour confinement, quarks and gluons in the final state of QCD processes are not directly observable either, but only in the form of colour-neutral particles. The experimental signatures of hard QCD interactions are collimated bunches of hadrons called *jets*. In a basic approximation, a jet is thought to be initiated by an energetic

final-state parton that first creates a shower of quarks and gluons through QCD radiation which subsequently combine to colour-neutral particles, a process called hadronisation [10]. The collimation of the hadrons inside a jet is associated to collinear poles in the gluon emission from final-state partons, leading to gluons being emitted primarily close to the direction of the emitting parton as discussed in [21] and the references therein.

Different approaches have to be combined to obtain a quantitative description of the evolution of the final-state partons from the hard QCD interactions to the jets. *Fragmentation functions* may be used in a similar way to PDFs to factorise the perturbative and the non-perturbative part of the final-state evolution [10]. The radiation process can be described in a perturbative way. For instance, in the PYTHIA Monte Carlo generator [22], final-state radiation is implemented as a Markov process with  $p_T$ -ordered parton showers. Challenges arise e.g. from the need of a consistent connection of higher-order radiation between the matrix element and the parton shower. The hadronisation occurs at low energy scales and is intrinsically non-perturbative. In this energy regime, phenomenological models need to be used, such as the Lund string model [23, 24] implemented in PYTHIA. The Monte Carlo-simulation for this analysis will be discussed in chapter 4.

Formally, jets are not uniquely defined in nature, but they depend on the choice of the *jet algorithm* that is used for the reconstruction, together with the corresponding parameters, and on the procedure that is used for the propagation of the kinematic properties of the input objects to the jet, the so-called *recombination scheme*. From a theoretical perspective, a jet algorithm should have certain properties. For example, the algorithm should be applicable to different types of input objects, such as partons, particles, charged particle tracks and calorimeter energy depositions.

Another very important property is the so-called *infrared (IR)- and collinear safety* [25]. In fixed-order perturbative QCD predictions, real emissions and virtual contributions from loops lead to separate divergences in the calculations. Due to the opposite sign of the two contributions, the divergences cancel in the sum, such that the final result is finite. In the context of jet reconstruction, the cancellation between real and virtual contributions can be spoiled if both types of corrections lead to different numbers of jets in the final state: If a jet is induced by a final-state parton, the virtual correction to the process does not alter the final number of jets. However, if the jet algorithm splits the two partons emerging from a real collinear emission and assigns them to two jets, the real and the virtual contributions do not cancel any longer, and the 1-jet and 2-jet cross sections separately diverge. Similarly, in a situation where two final-state partons are assigned to two jets, a virtual loop between the two partons does not change the number of jets in the final state. In contrast, a soft real emission radiated spatially between the two partons can lead to the assignment of the partonic system to only one final jet. Thus, again, the real and virtual contributions do not cancel and the 1-jet and 2-jet cross sections independently diverge.

The anti- $k_t$  jet algorithm [26] used in this thesis is infrared- and collinear safe to all orders of perturbation theory [25]. The algorithm belongs to the so-called sequential

recombination algorithms that use a distance measure between pairs of input objects and the beam to iteratively cluster the input objects to jets. More detailed information about the anti- $k_t$  algorithm, the corresponding distance parameter and the recombination scheme will be provided in section 5.1.2.

Due to the intrinsic complexity of the final-state evolution of hard QCD interactions, precise theoretical predictions for jet-related measurements can only be made when detailed corrections for the radiation and the hadronisation processes are taken into account. However, a good qualitative understanding of the basic jet processes relevant for this thesis can be gained by interpreting the kinematic properties of the final state partons as those of the jets. This approach is used below for the discussion of the dijet and the single-inclusive jet cross sections.

#### 1.2.4. Kinematic variables

For the subsequent discussion, it is helpful to introduce a number of standard variables. The four-momentum  $p^\mu$  of a parton, particle or jet,

$$p^\mu = (E, p_x, p_y, p_z), \quad (1.12)$$

may be written as

$$p^\mu = (m_T \cosh y, p_T \sin \phi, p_T \cos \phi, m_T \sinh y), \quad (1.13)$$

with the mass  $m$ , the transverse mass  $m_T = \sqrt{m^2 + p_T^2}$ , the transverse momentum  $p_T = \sqrt{p_x^2 + p_y^2}$ , and the azimuthal angle  $\phi$ . The rapidity  $y$  is defined as

$$y = \frac{1}{2} \ln \left( \frac{E + p_z}{E - p_z} \right). \quad (1.14)$$

Rapidity differences are Lorentz invariant, and rapidities add under longitudinal Lorentz boosts. In the high-energy limit, the four-momentum becomes

$$p^\mu = p_T (\cosh y, \sin \phi, \cos \phi, \sinh y). \quad (1.15)$$

The pseudorapidity  $\eta$  is defined as

$$\eta = -\ln \tan(\theta/2), \quad (1.16)$$

with the polar angle  $\theta$ . In the high-energy limit, rapidity and pseudorapidity are the same,  $y = \eta$ . A relative distance between two partons, particles or jets may be defined as

$$\Delta R = \sqrt{(\Delta\phi)^2 + (\Delta\eta)^2}, \quad (1.17)$$

with  $\Delta\phi$  and  $\Delta\eta$  denoting the difference between the objects' azimuthal angles and pseudorapidities, respectively.

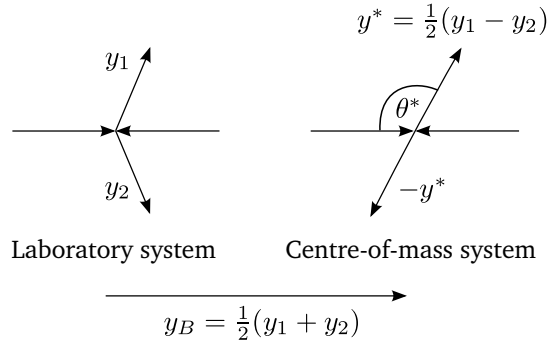


**Figure 1.5.** Kinematics of  $2 \rightarrow 2$  parton processes; adapted from [27].

For the discussion of dijet processes, it is useful to define a number of additional kinematic quantities. In a generic  $2 \rightarrow 2$  partonic subprocess,  $ab \rightarrow cd$ , the Mandelstam variables [28] are defined via the four-momenta of the incoming and outgoing partons  $p_i$  as

$$\hat{s} = (p_a + p_b)^2, \quad \hat{t} = (p_a - p_c)^2, \quad \hat{u} = (p_a - p_d)^2. \quad (1.18)$$

They are related to the scattering angle  $\theta^*$  in the parton centre-of-mass system, illustrated in figure 1.5, via

$$\hat{t} = -\frac{\hat{s}}{2}(1 - \cos \theta^*), \quad \hat{u} = -\frac{\hat{s}}{2}(1 + \cos \theta^*). \quad (1.19)$$

The rapidity  $y_B$  of the two-parton system in the laboratory system is given by the rapidities  $y_1$  and  $y_2$  in the laboratory system as

$$y_B = \frac{1}{2}(y_1 + y_2), \quad (1.20)$$

and the rapidities of the two jets in the partonic centre-of-mass system  $\pm y^*$  are

$$y^* = \frac{1}{2}(y_1 - y_2). \quad (1.21)$$

The centre-of-mass energy of the subprocess  $\sqrt{\hat{s}}$  is equal to the dijet invariant mass  $m_{jj}$ . It can therefore be expressed as

$$\hat{s} = m_{jj}^2 = x_a x_b s, \quad (1.22)$$

with  $s$ , the squared centre-of-mass energy of the proton-proton system, and the proton momentum fractions  $x_a$  and  $x_b$  of the two partons which can be written as

$$x_a = m_T e^{y_B} \cosh y^*, \quad x_b = m_T e^{-y_B} \cosh y^*. \quad (1.23)$$

### 1.2.5. Jet cross sections

Using the QCD improved parton model and the variables defined above, this section describes how cross sections with two final-state partons are obtained. These will be interpreted as an approximation for jet cross sections, as discussed in section 1.2.3. The presentation follows [9] and [27] and assumes massless partons. The differential cross section for the hard  $2 \rightarrow 2$  scattering between two partons, corresponding to the situation introduced in the previous section, may be written as

$$\frac{E_3 E_4 d^6 \hat{\sigma}}{d^3 p_3 d^3 p_4} = \frac{1}{32\pi^2 \hat{s}} \sum |\mathcal{M}|^2 \delta^4(p_1 + p_2 - p_3 - p_4), \quad (1.24)$$

where  $\sum |\mathcal{M}|^2$  denotes the matrix element, averaged and summed over initial and final spins and colours, respectively, and the  $\delta$ -function accounts for momentum conservation.

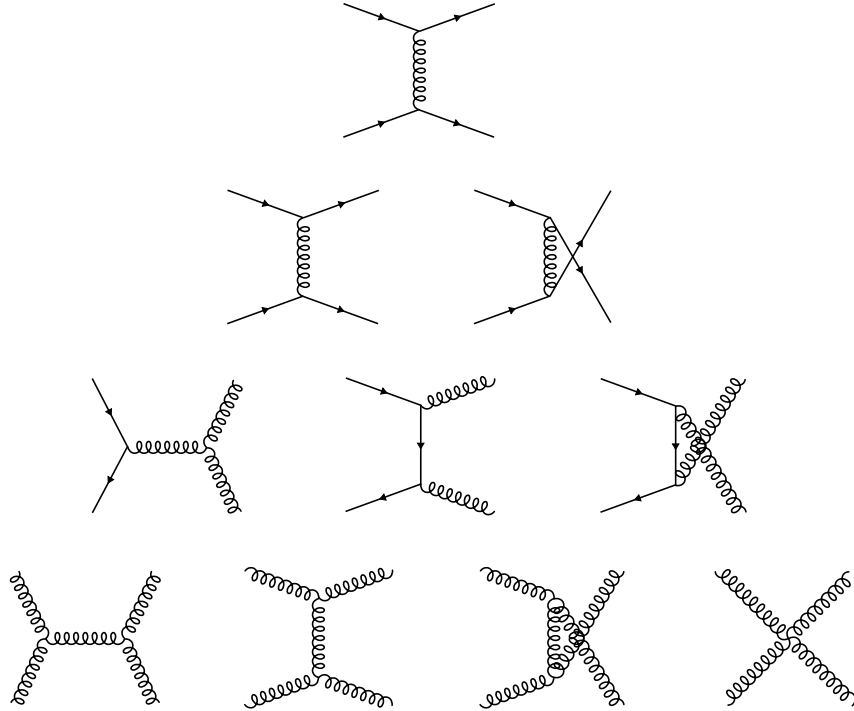


**Figure 1.6.** Feynman diagrams for jet production; adapted from [9].

The Feynman diagrams for this leading-order calculation are presented in figure 1.6, complemented by the diagrams obtained from crossing symmetries. Shown are the  $\hat{s}$ -,  $\hat{t}$ - and  $\hat{u}$ -channel processes with quarks, anti-quarks and gluons in the initial and final state. The matrix elements derived from these Feynman diagrams are presented in table 1.1. Also reported are the values for right-angle scattering in the parton-parton centre-of-mass system, corresponding to  $\hat{t} = \hat{u} = -\hat{s}/2$ . At equal parton luminosities, processes

**Table 1.1.** The squared invariant matrix elements  $\widehat{\sum}|\mathcal{M}|^2/g_S^4$  for  $2 \rightarrow 2$  parton subprocesses with massless partons. The colour and spin indices are averaged (summed) over initial (final) states; from [9, 29].

Process	$\widehat{\sum} \mathcal{M} ^2/g_S^4$	$\widehat{\sum} \mathcal{M} ^2/g_S^4(\theta^* = \pi/2)$
$qq' \rightarrow qq'$	$\frac{4}{9} \frac{s^2 + \hat{u}^2}{\hat{t}^2}$	2.22
$q\bar{q}' \rightarrow q\bar{q}'$	$\frac{4}{9} \frac{s^2 + \hat{u}^2}{\hat{t}^2}$	2.22
$qq \rightarrow qq$	$\frac{4}{9} \left( \frac{s^2 + \hat{u}^2}{\hat{t}^2} + \frac{s^2 + \hat{t}^2}{\hat{u}^2} \right) - \frac{8}{27} \frac{s^2}{\hat{u}\hat{t}}$	3.26
$q\bar{q} \rightarrow q'\bar{q}'$	$\frac{4}{9} \frac{\hat{t}^2 + \hat{u}^2}{\hat{s}^2}$	0.22
$q\bar{q} \rightarrow q\bar{q}$	$\frac{4}{9} \left( \frac{s^2 + \hat{u}^2}{\hat{t}^2} + \frac{\hat{t}^2 + \hat{u}^2}{\hat{s}^2} \right) - \frac{8}{27} \frac{\hat{u}^2}{\hat{s}\hat{t}}$	2.59
$q\bar{q} \rightarrow gg$	$\frac{32}{27} \frac{\hat{t}^2 + \hat{u}^2}{\hat{t}\hat{u}} - \frac{8}{3} \frac{\hat{t}^2 + \hat{u}^2}{\hat{s}^2}$	1.04
$gg \rightarrow q\bar{q}$	$\frac{1}{6} \frac{\hat{t}^2 + \hat{u}^2}{\hat{t}\hat{u}} - \frac{3}{8} \frac{\hat{t}^2 + \hat{u}^2}{\hat{s}^2}$	0.15
$gq \rightarrow gq$	$-\frac{4}{9} \frac{s^2 + \hat{u}^2}{\hat{s}\hat{u}} + \frac{\hat{u}^2 + \hat{s}^2}{\hat{t}^2}$	6.11
$gg \rightarrow gg$	$\frac{9}{2} \left( 3 - \frac{\hat{t}\hat{u}}{\hat{s}^2} - \frac{\hat{s}\hat{u}}{\hat{t}^2} - \frac{\hat{s}\hat{t}}{\hat{u}^2} \right)$	30.4

with two gluons in the initial and final state constitute the largest contribution, due to their colour charge [9].

The single jet inclusive cross section is found by integrating equation 1.24 over the momentum of one final-state parton,

$$\frac{Ed^3\hat{\sigma}}{d^3p} = \frac{1}{16\pi^2\hat{s}} \sum_{\hat{a}} |\mathcal{M}|^2 \delta(\hat{s} + \hat{t} + \hat{u}), \quad (1.25)$$

and, according to the QCD improved parton model discussed in section 1.2.2, convolving the result with the parton distribution functions,

$$\begin{aligned} \frac{Ed^3\sigma}{d^3p} \equiv \frac{d^3\sigma}{d^2p_T dy} &= \frac{1}{16\pi^2s} \sum_{i,j,k,l=q,\bar{q},g} \int_0^1 \frac{dx_1}{x_1} \frac{dx_2}{x_2} f_i(x_1, \mu^2) f_j(x_2, \mu^2) \\ &\times \sum_{\hat{a}} |\mathcal{M}(ij \rightarrow kl)|^2 \frac{1}{1 + \delta_{kl}} \delta(\hat{s} + \hat{t} + \hat{u}). \end{aligned} \quad (1.26)$$

Here,  $E$  denotes the total energy, and  $p$  denotes the total momentum of the jet. The term  $1/(1 + \delta_{kl})$  corrects for processes with identical final-state partons.

Figure 1.7 shows results of an ATLAS measurement [34] of the inclusive jet cross section in proton-proton collisions at  $\sqrt{s} = 7$  TeV as a function of the jet transverse momentum  $p_T$  in bins of the jet rapidity  $|y|$ . The jets were reconstructed with the anti- $k_t$  algorithm with a distance parameter of  $R = 0.6$ . The measurement is compared to theoretical predictions obtained from NLO perturbative QCD calculations, to which non-perturbative corrections were applied. The measurement covers transverse momenta between  $p_T = 20$  GeV and  $p_T = 1.5$  TeV and finds the data to be in agreement with the theoretical predictions over several orders of magnitude.

The dijet cross section can also be obtained with the above formalism, by omitting the integration over one parton momentum that leads to the single jet inclusive cross section. Using  $m_{jj}$ , the dijet invariant mass,  $\theta^*$ , the angle to the beam in the centre-of-mass system of the two-jet system, and the relation

$$dp_T^2 dy_3 dy_4 \equiv s/2 dx_1 dx_2 d \cos \theta^*, \quad (1.27)$$

the dijet cross section may be written as

$$\begin{aligned} \frac{d^2\sigma}{dm_{jj}^2 d \cos \theta^*} &= \frac{1}{32\pi m_{jj}^2} \sum_{i,j=q,\bar{q},g} \int_0^1 dx_1 dx_2 f_i(x_1, \mu^2) f_j(x_2, \mu^2) \\ &\times \delta(x_1 x_2 s - m_{jj}^2) \sum_{\hat{a}} |\mathcal{M}(ij \rightarrow kl)|^2 \frac{1}{1 + \delta_{kl}}. \end{aligned} \quad (1.28)$$

Here, the term  $1/(1 + \delta_{kl})$  again takes processes with identical final-state partons into account. The resulting angular dependence of the dijet cross section will be discussed in section 2.1.

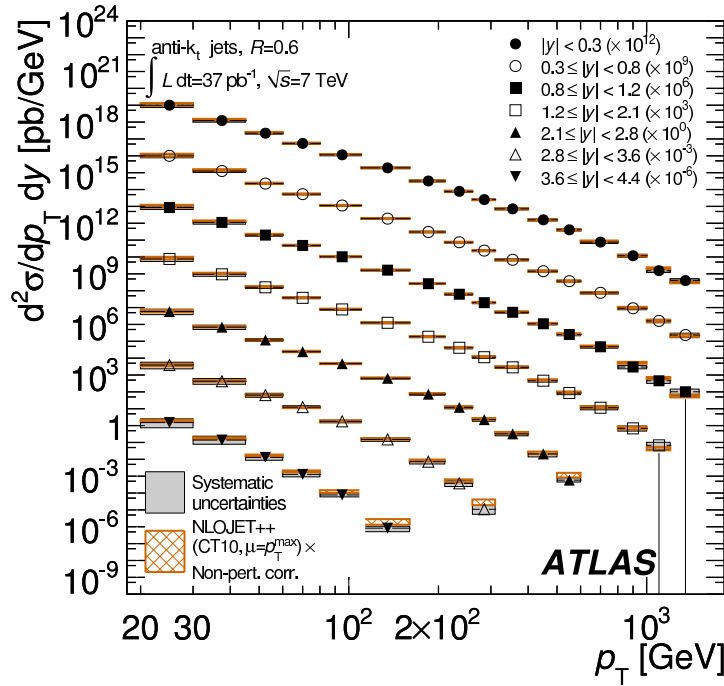


**Figure 1.7.** The inclusive jet cross section as a function of the jet transverse momentum  $p_T$  in bins of the jet rapidity  $|y|$ , for jets reconstructed with the anti- $k_t$  algorithm with a distance parameter of  $R = 0.6$ . The data are compared to predictions from next-to-leading order perturbative QCD calculations performed with NLOJET++ [30–33], modified with non-perturbative corrections. The error bars indicate statistical uncertainties. The quadratic sum of the experimental systematic uncertainties is shown as a dark-shaded band, and the quadratic sum of the theoretical systematic uncertainties is indicated as a light, hatched band. The additional uncertainty of 3.4% from the luminosity determination is not displayed; from [34].

ATLAS has also measured the dijet cross section, as a function of the dijet invariant mass and half the rapidity difference between the leading jets in  $p_T$ ,  $y^* = \frac{1}{2}(y_1 - y_2)$ , for dijet invariant masses between 70 GeV and 5 TeV [34]. The measured cross sections are found to be in good agreement with theoretical predictions from NLO perturbative QCD over several orders of magnitude, although they tend to be lower than the predicted ones for high dijet invariant masses.

## 2. Search for new phenomena in dijet angular distributions

In this chapter, the variable  $\chi$  is introduced, and it is argued that dijet angular distributions are very well suited to search for new phenomena such as quark substructure or strong gravity at small distance scales.

### 2.1. Dijet angular distributions

In this section, the angular dependence of the dijet cross section is discussed, and a variable that can be used to search for physics beyond the Standard Model in the dijet angular distributions is introduced. The presentation follows [9] and [27]. The dijet cross section for massless partons, expressed as a function of the dijet invariant mass  $m_{jj}$  and the angle to the beam in the centre-of-mass system of the two partons  $\theta^*$ , was introduced in the last chapter. It may be written as

$$\frac{d^2\sigma}{dm_{jj}^2 d\cos\theta^*} = \sum_{i,j=q,\bar{q},g} \int_0^1 dx_1 dx_2 f_i(x_1, \mu^2) f_j(x_2, \mu^2) \times \delta(x_1 x_2 s - m_{jj}^2) \frac{d\hat{\sigma}^{ij}}{d\cos\theta^*}, \quad (2.1)$$

with

$$\frac{d\hat{\sigma}^{ij}}{d\cos\theta^*} = \sum_{k,l} \frac{1}{32\pi m_{jj}^2} \sum_{\hat{c}} |\mathcal{M}(ij \rightarrow kl)|^2 \frac{1}{1 + \delta_{kl}}. \quad (2.2)$$

The squared matrix elements  $\mathcal{M}$ , averaged and summed over initial and final colours and spins, respectively, were given in table 1.1. In the case of the proton-proton collisions at the LHC, the dominant subprocesses are  $gg \rightarrow gg$ ,  $gq \rightarrow gq$ ,  $qq' \rightarrow qq'$  and  $qq \rightarrow qq$ . For small scattering angles,  $\theta^* \rightarrow 0$ , all four processes are dominated by the contribution from  $\hat{t}$ -channel gluon exchange. The corresponding terms are quadratic in  $1/\hat{t}$ , with  $\hat{t} = -\hat{s}/2(1 - \cos\theta^*)$ , such that the angular dependence of the differential cross section is

$$\frac{d\hat{\sigma}}{d\cos\theta^*} \sim \frac{1}{\sin^4(\theta^*/2)}, \quad (2.3)$$

as in the case of Rutherford scattering. A transformation of variables can be used to remove the strong angular dependence from the differential partonic cross section.

A convenient variable for this purpose is  $\chi$ , which is defined as

$$\chi = \frac{\hat{u}}{\hat{t}} = \frac{1 + \cos \theta^*}{1 - \cos \theta^*}. \quad (2.4)$$

With this change of variables from  $\theta^*$  to  $\chi$ , the differential partonic cross section becomes

$$\frac{d\hat{\sigma}}{d\chi} = \frac{\partial \cos \theta^*}{\partial \chi} \frac{d\hat{\sigma}}{d \cos \theta^*} = \frac{2}{(1 + \chi)^2} \frac{d\hat{\sigma}}{d \cos \theta^*}. \quad (2.5)$$

For example, the angular dependence of  $gg \rightarrow gg$  processes, written as a function of  $\chi$ , is given by the squared matrix element,

$$\sum |\mathcal{M}|^2 / g_s^4 = \frac{9}{2} \left( 3 - \frac{\chi}{(1 + \chi)^2} + \chi + \chi^2 + \frac{1}{\chi^2} + \frac{1}{\chi} \right), \quad (2.6)$$

multiplied with the Jacobian for the change of variables,  $(\partial \cos \theta^* / \partial \chi) = 2 / (1 + \chi)^2$ . In the small angle, large  $\chi$  limit, the contribution from the matrix element is dominated by the term quadratic in  $\chi$  while the Jacobian is dominated by a term quadratic in  $1/\chi$ , such that the cross section approaches

$$\frac{d\hat{\sigma}}{d\chi} \sim \text{constant}. \quad (2.7)$$

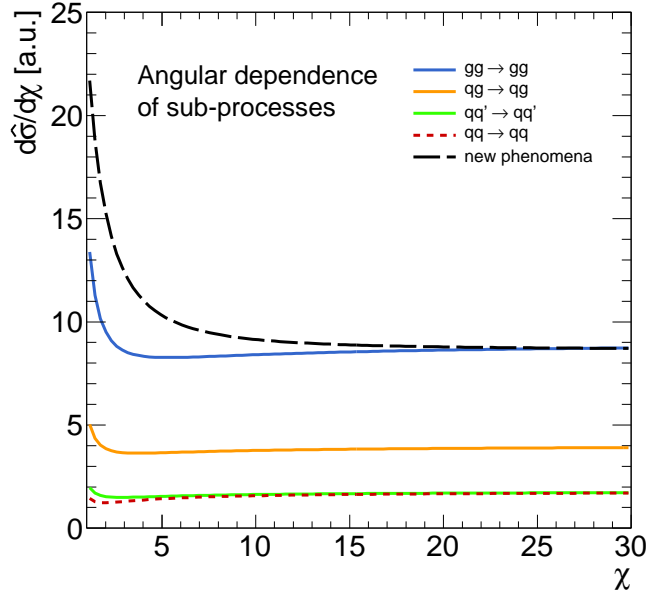


**Figure 2.1.** The angular dependence of the dominant QCD sub-processes at LO and a generic, isotropic scenario of physics beyond the Standard Model.

Figure 2.1 shows the angular dependence of the differential partonic cross sections for the dominant QCD subprocesses as a function of  $\chi$ . Apart from a rise towards low values

of  $\chi$ , the distributions are almost constant. The angular dependence is very similar between the different processes. Many scenarios of physics beyond the Standard Model predict angular distributions that are more isotropic than those of QCD. For example, a scalar gluon exchange [9] would lead to

$$\frac{d\hat{\sigma}}{d\cos\theta^*} \sim \text{constant}, \quad (2.8)$$

which is equivalent to a rise of the differential cross section towards low  $\chi$ -values,

$$\frac{d\hat{\sigma}}{d\chi} \sim \frac{1}{(1+\chi)^2}. \quad (2.9)$$

Such an isotropic extension of the Standard Model is also shown in figure 2.1. Since  $\cos\theta^* = \tanh y^*$ ,  $\chi$  may also be expressed as a function of  $y^*$  as

$$\chi = \frac{1 + \cos\theta^*}{1 - \cos\theta^*} = \frac{\cosh y^* + \sinh y^*}{\cosh y^* - \sinh y^*} = \exp 2y^*. \quad (2.10)$$

The scattering angle in the parton-parton centre-of-mass system and therefore also  $\chi$  can be determined directly from the measured jet rapidities in the ATLAS laboratory system since rapidity differences are boost invariant. In addition, as quark jets and gluon jets cannot be distinguished experimentally on an event-by-event basis, the partonic cross sections are symmetrised in  $\hat{u}$  and  $\hat{t}$ , modifying  $\chi$  to [27]

$$\chi = \frac{1 + |\cos\theta^*|}{1 - |\cos\theta^*|}. \quad (2.11)$$

In the analysis,  $\chi$  is therefore calculated as

$$\chi = \exp 2|y^*| \quad (2.12)$$

from the rapidities of the two jets with the largest transverse momenta in an event.

Finally, using the QCD improved parton model to take the confinement of the partons in the initial protons into account, the dijet angular distribution may be written as

$$\frac{d\sigma}{d\chi} = \int_0^1 dx_1 dx_2 f_1(x_1, \mu^2) f_2(x_2, \mu^2) \frac{d\hat{\sigma}}{d\chi}. \quad (2.13)$$

Since the contributions from new phenomena are expected to modify the partonic cross section, dedicated selections have been used in the analysis to reduce the effect of the PDF convolution on the measurement. The event selection will be discussed in chapter 6.

## 2.2. Physics beyond the Standard Model

The two theories for physics beyond the Standard Model which will be analysed in this thesis are introduced in this section. The first describes a possible substructure of

quarks. The second is concerned with the possible effects of hypothetical strong gravity. Both scenarios lead to more isotropic dijet angular distributions and can thus be studied with dijet events.

### 2.2.1. Quark compositeness

The first model that is investigated in this thesis concerns a possible substructure of quarks. The idea is based on the history of scattering experiments which have probed the structure of matter at ever smaller distance scales. The famous Rutherford experiments [35] established the existence of the atomic nucleus via the scattering of  $\alpha$ -particles on a gold foil. Later, the deep inelastic scattering experiments at SLAC [36, 37] discovered point-like constituents inside the proton and the neutron, which could subsequently be identified with the quarks. The collision energy and the high momentum transfer reached in the proton-proton collisions at the LHC allow the continuation of these studies and to probe the structure of matter down to unprecedented distance scales. In addition to the historical motivation, it has been argued [38] that the apparent *proliferation of quarks* might be explained by hypothetical particles, called *preons*, that combine under a new *hypercolour* force to make up the known quarks.

No complete theory of *quark compositeness* has been established so far. Instead, the phenomenological consequences of a quark substructure are analysed in two kinematic regimes, characterised by  $\Lambda$ , the compositeness scale of the theory [38]. In the first regime,  $\sqrt{s} \gtrsim \Lambda$ , the effective centre-of-mass energy in the partonic subprocess  $\sqrt{s}$  is larger than the compositeness scale, and excited quarks  $q^*$  could emerge as part of the phenomenological consequences. In the second regime,  $\sqrt{s} \ll \Lambda$ , the centre-of-mass energy in the partonic subsystem is much lower than the compositeness scale. The quarks appear point-like and exhibit an effective contact interaction.

In general, the concept of a contact interaction describes the situation in which an extension of the theory is introduced that becomes strong at a characteristic, high-energy scale. In the case where the probed energy scale is far below this scale, signs of the new interaction can nevertheless become evident in an effective low-energy phenomenology. A well-known example of a contact interaction description is the Fermi model of low-energy weak interactions in which  $\beta$ -decay was described by a four-fermion contact interaction. Later, with the availability of higher collision energies, it became clear that the interaction is mediated by heavy  $W$ -bosons.

In the case of quark compositeness, the low-energy approximation takes the form of an apparent four-fermion interaction. It has become customary to model the Lagrangian for the contact interaction with the colour- and isospin singlet operator [38–40]

$$\mathcal{L}_{qqqq}(\Lambda) = \frac{\eta g^2}{2\Lambda^2} \bar{q}_{iL} \gamma^\mu q_{iL} \bar{q}_{jL} \gamma_\mu q_{jL}, \quad (2.14)$$

where the left-handed quark fields  $q_{iL}$  have flavour  $i$  and are arranged in the standard  $SU(2)$  doublets.  $g$  denotes the strong coupling constant of the interaction, with

$g^2/4\pi = 1$ .  $\Lambda$  is the compositeness scale.  $\eta = \pm 1$  governs the sign of the interference between QCD and the contact interaction. As can be seen e.g. from equations 2.16 and 2.17 and the fact that both  $\hat{t}$  and  $\hat{u}$  are negative,  $\eta = +1$  corresponds to destructive interference, while  $\eta = -1$  corresponds to constructive interference. While in early analyses only  $u$  and  $d$  quarks were modelled as composite, today it has become a standard to include all five quark flavours which yield two final-state jets. The full Lagrangian of the theory is given by the sum of  $\mathcal{L}_{qqq}(\Lambda)$  and the QCD Lagrangian  $\mathcal{L}_{\text{QCD}}$  discussed in section 1.2.

By construction, the contact interaction modifies the QCD subprocesses with two quarks in the initial and final state, whereas the processes  $qq \rightarrow gg$ ,  $gq \rightarrow gq$ ,  $q\bar{q} \rightarrow gg$  and  $gg \rightarrow q\bar{q}$  are not altered and contribute to the QCD background in the analysis. The differential partonic cross sections for the modified subprocesses are given e.g. in [40], differentially in  $\hat{t}$ . The angular dependence can be shown more explicitly by writing the cross section differentially in  $\cos \theta^*$ , with

$$\frac{d\hat{\sigma}}{d \cos \theta^*} = \frac{\hat{s}}{2} \frac{d\hat{\sigma}}{d\hat{t}}. \quad (2.15)$$

For example,

$$\frac{d\hat{\sigma}(q_i q_i \rightarrow q_i q_i)}{d \cos \theta^*} = \frac{d\hat{\sigma}(\bar{q}_i \bar{q}_i \rightarrow \bar{q}_i \bar{q}_i)}{d \cos \theta^*} = A, \quad (2.16)$$

with

$$A := \frac{\pi}{2\hat{s}} \left\{ \frac{4}{9} \alpha_s^2 \left[ \frac{\hat{u}^2 + \hat{s}^2}{\hat{t}^2} + \frac{\hat{t}^2 + \hat{s}^2}{\hat{u}^2} - \frac{2\hat{s}^2}{3\hat{t}\hat{u}} \right] + \frac{8}{9} \alpha_s \frac{\eta}{\Lambda^2} \hat{s}^2 \left[ \frac{1}{\hat{t}} + \frac{1}{\hat{u}} \right] + \frac{8}{3} \frac{\hat{s}^2}{\Lambda^4} \right\}. \quad (2.17)$$

Terms proportional to  $\alpha_s^2$  are due to QCD contributions, terms proportional to  $1/\Lambda^4$  arise from the contact interaction, and terms proportional to  $\alpha_s/\Lambda^2$  characterise the interference between the contact interaction and QCD. As described in section 2.1, the QCD part contains a term proportional to  $1/\hat{t}^2$ , corresponding to forward, Rutherford-like scattering from  $\hat{t}$ -channel gluon exchange. In contrast, the plain contact interaction term is proportional to  $\hat{s}^2$  and does not depend on the scattering angle  $\theta^*$ . The other subprocesses are characterised by similar angular dependencies, with the contact interaction term either being proportional to  $\hat{u}^2$ , corresponding to a mild dependence on  $\cos \theta^*$ , or being proportional to  $\hat{s}^2$ , yielding a completely isotropic behaviour with respect to  $\cos \theta^*$ . As discussed in the previous section, a cross section constant in  $\cos \theta^*$  corresponds to a rise in the cross section towards low values of  $\chi$ , different from the almost constant  $\chi$ -dependence of pure QCD.

### 2.2.2. Quantum black holes

The second phenomenon discussed in this thesis are so-called *quantum black holes* which arise as consequences in certain models of large extra dimensions in the context of the hierarchy problem. In high-energy physics, the hierarchy problem denotes the

large difference between the Planck scale,  $M_{pl} \sim 10^{19}$  GeV, and the electroweak scale,  $\Lambda_{EW} \sim 100$  GeV. One solution of the hierarchy problem has been proposed within the ADD model [41, 42] which introduces  $n$  additional, large, flat spatial dimensions of size  $R$ . An alternative solution of the hierarchy problem is proposed in the Randall-Sundrum model [43, 44] which explains the apparent weakness of gravity by a five-dimensional Anti-de Sitter spacetime with a warped metric. The ADD model assumes that the Standard Model fields are confined to the 4-dimensional *brane*, while gravity can propagate into the entire  $(4+n)$ -dimensional *bulk*, thereby leading to a modified gravitational law at distances below  $R$ . Along with the extra dimensions, a new fundamental, *reduced Planck scale*  $M_D$  is thus introduced. Using the PDG convention [10] for the relation of the  $(4+n)$ -dimensional Planck scale to the higher-dimensional gravitational constant  $G_D$ ,  $M_D^{n+2} = (2\pi)^n / (8\pi G_D)$ , the fundamental Planck scale is related to the observed four-dimensional one as  $M_D^{n+2} \propto M_{pl}^2 R^{-n}$ .

The increased strength of gravity at small distances in the models of large extra dimensions led to speculations about the possible formation of microscopic black holes at the LHC as described e. g. in [45, 46]. According to the *hoop conjecture* [47], a black hole may be formed in a parton collision if the impact parameter is smaller than twice the Schwarzschild radius corresponding to a black hole with mass equal to the centre-of-mass energy of the parton system. The size of the higher-dimensional Schwarzschild radius is assumed to be inversely correlated with the fundamental Planck scale  $M_D$  [45, 46], allowing the production of black holes at lower energies in models with large extra dimensions. The production rate of these postulated, so-called *semi-classical black holes* has been estimated assuming a geometrical partonic cross section proportional to the squared Schwarzschild radius, resulting in large rates predicted for the LHC. For example, for a value of the reduced Planck scale of  $M_D \sim 1$  TeV and a centre-of-mass energy of  $\sqrt{s} = 14$  TeV, the production of  $\sim 10^7$  black holes was estimated for an integrated luminosity of  $\mathcal{L} = 30 \text{ fb}^{-1}$  [45, 46]. Assuming the validity of a classical description, semi-classical black holes have been thought to be well described by black hole thermodynamics and to decay thermally via Hawking radiation, leading to spherical decays into all Standard Model fields. No such observation has been made since the start of the LHC.

It has been argued [48] that the condition defined by the hoop conjecture is not sufficient to describe the formation of microscopic black holes and that the actual production threshold  $M_{th}$  could instead be at a much larger scale than  $M_D$ .  $M_{th}$  may thus be outside the accessible energy reach of the LHC even if  $M_D$  is within. According to [48], the difference between the two scales arises from two main reasons: firstly, from the large entropy of the black hole that is necessary for the validity of the thermodynamical description and secondly, from the possible energy loss due to gravitational radiation before the formation of the black hole. Together, these effects may introduce a difference between  $M_D$  and  $M_{th}$  of the order of a few TeV, rendering the observation of semi-classical black holes at the LHC much more improbable than predicted earlier.

The authors of [48] also present the idea that other effects of strong gravity may already emerge close to  $M_D$ , in a regime where the threshold for the production of semi-classical black holes is not yet reached and where quantum effects are not negligible. These possible quantum gravity effects close to the fundamental Planck scale are summarised under the term *quantum black holes* in [48] and correspond to the second theory for physics beyond the Standard Model considered in this thesis. Quantum black holes are thought to decay instantaneously to low-multiplicity final states. Since they decay predominantly into quarks and gluons, quantum black holes produce experimental signatures containing jets. Similar to the quark contact interactions described above, their decays are expected to be more isotropic than QCD interactions. Therefore, it is argued in [48] that compositeness-type searches can be used to search for this phenomenon.

The quantum black hole model considered here [48, 49] describes the cross-section with an on-set behaviour at  $M_D$ . Since the PDFs are steeply falling with the proton momentum fraction, this leads to the expectation that most quantum black holes are produced close to the fundamental Planck scale. The cross section for the quantum gravitational processes is assumed to decrease with the unknown size of  $M_D$  and for any given assumption on  $M_D$ , to increase with the number of extra dimensions [49]. In the absence of a full quantum gravitational theory, no interference between quantum black holes and QCD is considered.

### 2.3. Analysis strategy

Various searches for quark substructure and physics beyond the Standard Model with similar experimental signatures have been performed by particle physics experiments in the past, including the  $D\bar{0}$  and CDF experiments at the Tevatron [50–55] as well as the ATLAS and CMS experiments at the LHC [56–63]. The observables that have been used in these studies comprise the jet transverse energy and momentum distributions, the dijet invariant mass spectrum and several dijet angular variables, such as the fraction of events at low values of  $\chi$  as a function of the dijet invariant mass and the normalised, differential  $\chi$ -distributions as presented in this thesis.

Searches that are based on the transverse jet momentum or the dijet invariant mass make use of an increase of the cross section at large values of these variables due to the contribution from the new phenomena. These studies are, however, subject to large experimental and theoretical uncertainties. For example, the jet energy scale uncertainty translates into event migrations in the steeply falling spectra that can resemble a contact interaction signal. In addition, uncertainties on the parton distribution functions (PDFs) can have a similar effect. In the past, a Tevatron measurement reported an excess of events at large jet transverse momentum and dijet invariant mass [64, 65] that could later be attributed to an underestimation of the gluon PDF at large  $x$  [66].

Dijet angular distributions are less sensitive to systematic uncertainties, such as to the uncertainty due to the jet energy scale: Since the rapidity of a jet is defined as

$y = \frac{1}{2} \ln[(E + p_z)/(E - p_z)]$ , it is independent of any uncertainty that scales all components of the jet four vector  $p^\mu = (E, p_x, p_y, p_z)$  by the same number. The value of  $\chi$  is thus not affected by the jet energy scale uncertainty. Uncertainties from the luminosity measurement and the Monte Carlo prediction for the total cross section are mitigated by normalising the  $\chi$ -spectra to the total cross section.

For the analysis presented in this thesis, the full set of *proton-proton* collision data collected with the ATLAS detector in 2011, corresponding to an integrated luminosity of  $4.8 \text{ fb}^{-1}$ , is used to measure normalised, differential  $\chi$ -spectra in five bins of the dijet invariant mass. The agreement of the observed data with the Standard Model QCD prediction is quantified with two statistical tests. In case no statistically significant deviation from the predicted shape of the  $\chi$ -distributions is found, the results are used to constrain the two models for new phenomena introduced in this chapter, a contact interaction scenario and a theory for quantum black holes.

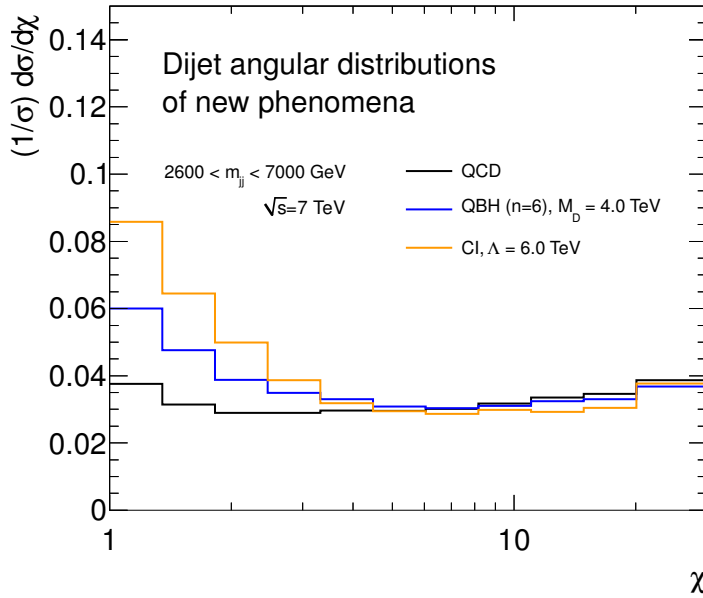


**Figure 2.2.** The normalised, differential  $\chi$ -distributions for events with dijet invariant masses  $m_{jj}$  between 2600 and 7000 GeV. Shown are the distributions after the event selection obtained from Monte Carlo simulations of the QCD background (black) and two signal hypotheses (blue and orange).

Figure 2.2 shows the normalised, differential  $\chi$ -distributions in the highest of the five mass bins. This bin comprises dijet invariant masses  $m_{jj}$  between 2600 and 7000 GeV. Reported are the distributions for the QCD background prediction and the the two models for new phenomena considered in this thesis. The event selection of the analysis has been applied to all three simulations. The quark contact interaction scenario is shown for destructive interference and a compositeness scale of  $\Lambda = 6 \text{ TeV}$ , and the quantum black hole scenario is shown for  $n = 6$  extra dimensions and a reduced Planck scale of  $M_D = 4.0 \text{ TeV}$ . The QCD background prediction and the QCD part of the signal

predictions are corrected with the K-factor distribution which will be described in section 4.3. Details about the Monte Carlo generation of the signal scenarios may also be found in chapter 4. Both theories for physics beyond the Standard Model predict a dijet angular distribution that is more isotropic than the one from QCD, leading to a peak of the  $\chi$ -distributions at low  $\chi$ -values. Due to this sensitivity to isotropic new phenomena and the reduced susceptibility to systematic uncertainties, dijet angular distributions are a valuable tool to perform compositeness-type searches for physics beyond the Standard Model.



## 3. The ATLAS detector at the LHC

The proton-proton collisions analysed in this work were recorded with ATLAS [67], one of the four main detectors at the Large Hadron Collider (LHC) [68] at CERN. The detector and the data set that was analysed in this thesis are described in this chapter.

### 3.1. The LHC

The LHC is located in a circular tunnel with a circumference of 27 km, at a depth of about 100 m below the Franco-Swiss border close to Geneva. It accelerates and collides protons and heavy ions at unprecedented energies. Most of the operation time is allocated for proton-proton collisions. While initial collisions took place at a centre-of-mass energy of  $\sqrt{s} = 900$  GeV, the main physics programme started with the first proton-proton collisions at  $\sqrt{s} = 7$  TeV in March 2010. The analysis presented in this thesis was performed on the full  $\sqrt{s} = 7$  TeV dataset collected in 2011, corresponding to an integrated luminosity of  $\mathcal{L} = 4.8 \text{ fb}^{-1}$ . In 2012, the centre-of-mass energy for proton-proton collisions was increased to  $\sqrt{s} = 8$  TeV which remained the working point until the temporary upgrade and maintenance shutdown in 2013.

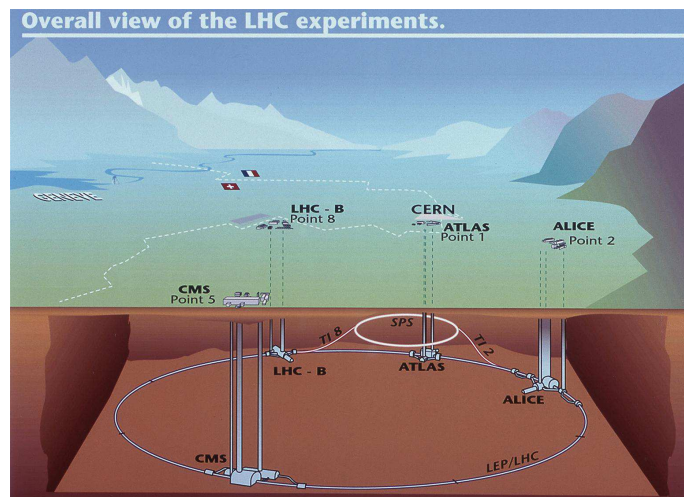


Figure 3.1. The locations of the four main detectors at the LHC; from [69].

The location of the four main detectors at the LHC, situated at the interaction points, is shown in figure 3.1. ATLAS and CMS [70] are general-purpose detectors while ALICE [71] and LHCb [72] have more specific goals: ALICE is mainly used to study the quark-gluon plasma, and LHCb is designed for the investigation of B physics.

The protons that collide in the LHC are extracted from hydrogen gas. They are accelerated to the final collision energy in several stages [68]. The initial acceleration is performed by the linear LINAC 2 accelerator which increases the proton energies to 50 MeV. This step is followed by the successive incrementation of the energy in three different pre-accelerator rings. The Booster ramps the proton energies up to 1.4 GeV before they are injected into the Proton Synchrotron where they are further accelerated to an energy of 25 GeV.

The last pre-accelerator before the LHC is the Super Proton Synchrotron (SPS), illustrated in figure 3.1. Here, the proton energy is raised to 450 GeV. The SPS was also used in test beam measurements [73] in which the response of charged pions was evaluated in modules of the ATLAS detector. The results of these studies are used to complement the determination of the jet energy scale uncertainty at very high jet transverse momenta as discussed in [74] and investigated for this analysis in chapters 5 and 8.

In the LHC, the protons are accelerated to their final energy, corresponding to 3.5 TeV per beam in 2011. The acceleration is performed in two separate beam pipes, with the protons moving in clockwise direction in one beam and in counter-clockwise direction in the other. The two beam pipes cross at the interaction points, and proton-proton collisions are induced. Within the beams, the protons are bundled in packets called *bunches*. In 2011, a typical bunch consisted of about  $1.2 \times 10^{11}$  protons [75]. The proton bunches are further grouped in so-called *bunch trains*. For example, run 191635 from 25th October 2011 comprised 1331 colliding bunches organised in 12 bunch trains [76]. A tight spacing of the bunches within the LHC bunch trains can lead to so-called *out-of-time pile-up* effects in which the energy deposited in the calorimeter during one bunch crossing influences the energy measurement in another. The instantaneous LHC luminosity  $\mathcal{L}$  depends on the ratio of the inelastic collision rate  $R_{\text{inel}}$  and the inelastic proton-proton cross section  $\sigma_{\text{inel}}$ . It may be expressed as [75]

$$\mathcal{L} = \frac{R_{\text{inel}}}{\sigma_{\text{inel}}}. \quad (3.1)$$

In ATLAS, the luminosity can be determined using both the nominal detector sub-components, such as the tile calorimeter discussed in section 3.2.2, and dedicated complementary detector systems like LUCID, which is described in section 3.2.4. The absolute luminosity normalisation is evaluated with so-called *van-der-Meer scans* as described in [75] and the references therein.

In 2011, the highest instantaneous luminosity, reached at the start of a fill, was about  $\mathcal{L}_{\text{peak}} = 3.6 \times 10^{33} \text{ cm}^{-2}\text{s}^{-1}$  [75]. The high instantaneous luminosity was accompanied with a large number of inelastic proton-proton interactions that overlay the primary hard scatter. Both this so-called *in-time pile-up* and the out-of-time pile-up effect men-

tioned above are considered in the jet calibration discussed in chapter 5 and investigated in the context of this analysis in chapter 7.

The time integral of the instantaneous luminosity is the *integrated luminosity*. A typical value of the integrated luminosity per run for the dataset analysed in this thesis is  $\mathcal{L}_{\text{run}} \approx \mathcal{O}(50 \text{ pb}^{-1})$ , with  $1 \text{ b} \equiv 10^{-28} \text{ m}^2$ . The total integrated luminosity delivered by the LHC in 2011 amounts to  $\mathcal{L} = 5.6 \text{ fb}^{-1}$  with an uncertainty of  $\delta\mathcal{L}/\mathcal{L} = \pm 1.8\%$  [75]. After the consideration of the ATLAS data taking efficiency and the application of the data quality criteria discussed in section 6, an integrated luminosity of  $4.8 \text{ fb}^{-1}$  is used in this analysis.

### 3.2. The ATLAS detector

The ATLAS detector [67] is depicted in figure 3.2. It is located at the interaction *point 1* of the LHC and is one of the two multi-purpose physics devices. Among others, its physics goals reach from the precision measurement of Standard Model processes over the search for the Higgs boson, the search for Supersymmetry and new heavy gauge bosons to signatures of quark compositeness and extra spatial dimensions.

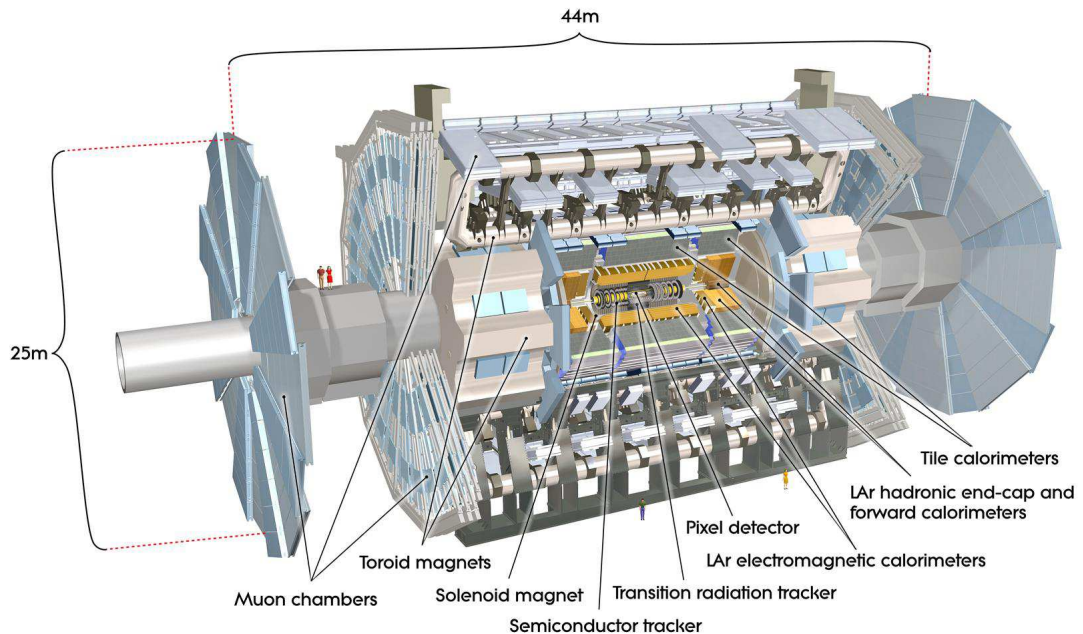


**Figure 3.2.** The ATLAS detector; from [67].

ATLAS consists of cylinder-shaped layers of sub-detectors from the interaction point outwards: the inner detector to measure charged particle tracks and to identify interaction

vertices, a calorimeter system with the goal to measure particle energies and the muon system that identifies and measures high-momentum muons.

Two magnet systems allow the measurement of charged particle momenta in the inner detector and in the muon system. A solenoid provides a 2 T axial field for the inner detector, and a system of one barrel toroid and two end-cap toroids produces 0.5 T and 1 T toroidal magnetic fields for the muon system.

The coordinate system used in ATLAS is defined as follows. The nominal interaction point at the geometrical centre of the detector defines the origin of the coordinate system. The  $z$ -axis is defined by the beam-axis, with the positive direction towards Geneva and the negative direction towards the Jura mountains. The vector from the origin of the coordinate system towards the center of the LHC defines the  $x$ -axis. The orthogonal coordinate system is completed by the upwards-pointing  $y$ -axis. The polar angle from the beam axis is denoted by  $\theta$ , and the azimuthal angle is measured in the transverse plane as  $\phi = \arctan(y/x)$ .  $p_T$ ,  $E_T$  and  $E_T^{\text{miss}}$  are the projections into the transverse plane of the momentum, the energy and the missing energy, respectively. The rapidity is defined as  $y = \frac{1}{2} \ln [(E + p_z)/(E - p_z)]$ , which may be approximated by the pseudorapidity  $\eta = -\ln \tan(\theta/2)$  in the high-energy limit as discussed in section 1.2.4.

#### 3.2.1. The inner detector

The inner detector (ID) sub-system [67, 77, 78] of ATLAS has been constructed for the measurement of charged particle tracks with transverse momenta above  $p_T = 500$  MeV in the central detector region,  $|\eta| < 2.5$ , while pursuing a momentum resolution of  $\sigma_{p_T}/p_T = 0.05\% p_T \oplus 1\%$ . The inner detector measures primary and secondary vertices. In addition, it complements the information from the calorimeter system for the identification of electrons with energies between 500 MeV and 150 GeV within  $|\eta| < 2.0$ . The inner detector is immersed in the 2 T field of the central solenoid magnet. It consists of the three independent sub-systems shown in figure 3.3: the pixel detector, the semiconductor tracker (SCT) and the transition radiation tracker (TRT). While the pixel detector and the SCT extend up to  $|\eta| = 2.5$ , the TRT covers the pseudorapidity region up to  $|\eta| = 2.0$ .

Following the cylindrical symmetry, the inner detector consists of a barrel part which is complemented with end-cap components on both sides. The pixel and the SCT detectors are based on semiconductor sensors and enclose the beam pipe as concentric cylinders in the barrel region, while they are arranged on disks normal to the beam in the end-cap components. The pixel detector is placed closest to the interaction point and provides the finest spatial granularity of the three sub-systems. The TRT measures transition radiation in straw tubes that are filled with a gas mixture. Xenon is used as the base for this gas mixture since it has good absorption properties for the transition radiation photons. The straw tubes are aligned parallel to the beam axis while they point radially

outwards in the end-cap wheels. The pixel and the SCT detectors provide tracking information in  $R$ ,  $\phi$  and  $z$  which is complemented with the measurement of  $R$  and  $\phi$  in the straw tubes of the TRT.

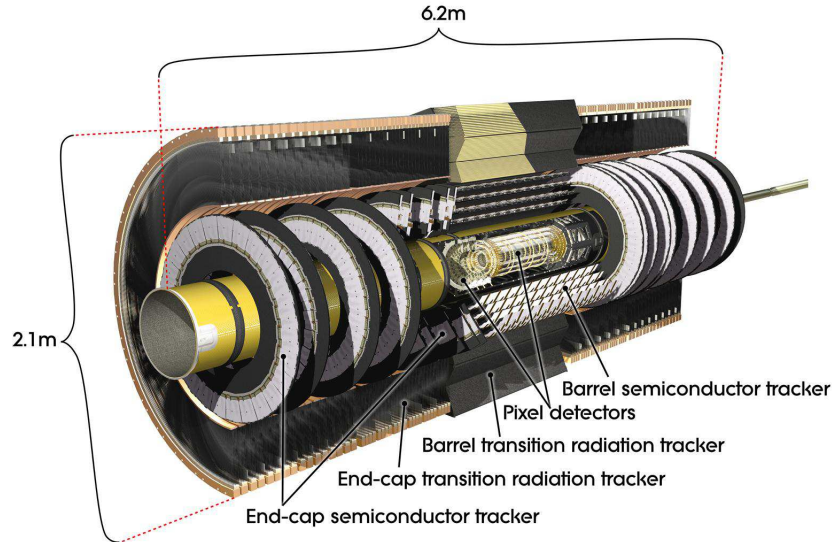


**Figure 3.3.** The ATLAS inner detector; from [67].

While the information from the inner detector is not directly used in the measurement of hadronic jets in this thesis, tracking information is used for the vertex reconstruction, the jet calibration and the evaluation of systematic uncertainties outlined in chapter 5.

### 3.2.2. The calorimeter

The ATLAS calorimeter system is the main detector component used in this analysis. It is used for the reconstruction of the hadronic jets from which the dijet angular distributions are obtained. Besides for the reconstruction of jets, the calorimeter is also used for the identification and measurement of photons, electrons,  $\tau$ -leptons and missing transverse energy, as produced by neutrinos and physics processes beyond the Standard Model. An overview of the calorimeter system is shown in figure 3.4. It covers the pseudorapidity region within  $|\eta| < 4.9$  and consists of electromagnetic and hadronic sub-systems which are discussed in more detail below.

#### The electromagnetic calorimeter

The electromagnetic (EM) calorimeter consists of a barrel part (EMB) that is complemented with two end-caps (EMECs). The barrel covers the region  $|\eta| < 1.475$  while the end-cap components lie within  $1.375 < |\eta| < 3.2$ . Further electromagnetic information

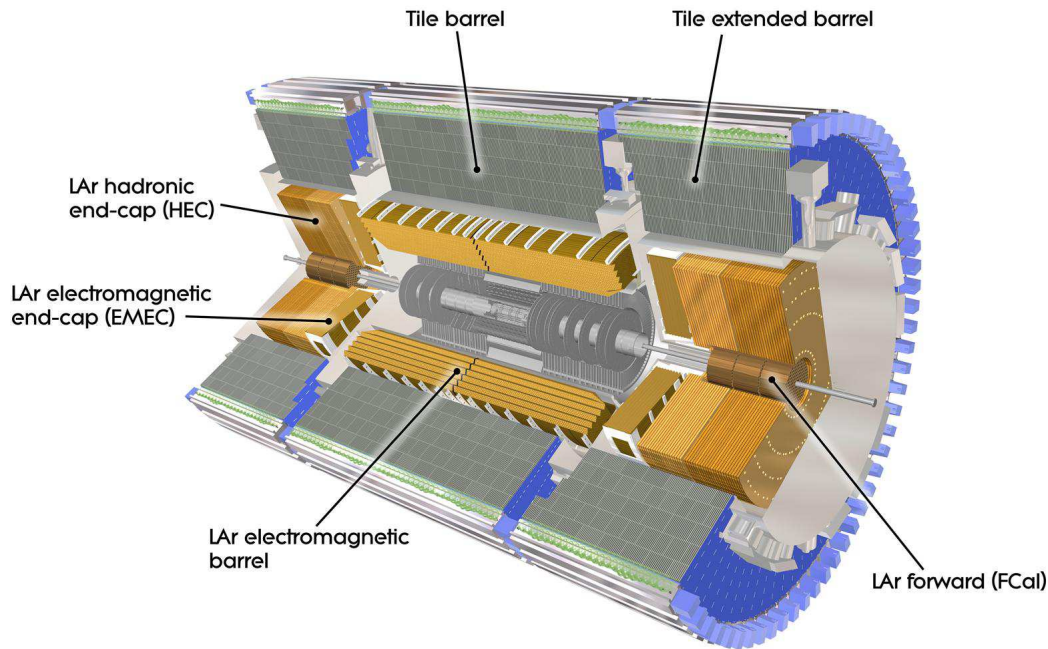


Figure 3.4. The ATLAS calorimeter system; from [67].

is available from a sub-module of the forward calorimeter (FCal) as outlined below. The EM calorimeter uses a sampling technology with lead as absorber material and liquid argon (LAr) as the active medium.

The accordion shape of the electrodes, illustrated in figure 3.5, ensures maximal azimuthal coverage. Within  $|\eta| < 2.5$ , the precision region matched to the coverage of the inner detector, the electromagnetic calorimeter is segmented into three radial layers, and it has two segmentations over the remaining coverage. Complementary layers of liquid argon are instrumented and installed within  $|\eta| < 1.8$  between the inner detector and the EM calorimeter to provide an estimate of the energy loss of particles before their entrance to the EM calorimeter.

A hardware failure prevented the readout of a part of the EM barrel calorimeter in a subset of the 2011 dataset as described in further detail in section 6.2.2. In ATLAS, the calorimeter readout electronics are divided into on-detector front-end and off-detector back-end systems. The front-end electronics amplify, process and digitise the analogue input signals, followed by the digital processing provided by the back-end electronics. Figure 3.6 shows the readout architecture of the LAr calorimeter. The lower box illustrates the electrical circuit in the cryostat. The central box shows the front-end electronics, and the upper row depicts the back-end, off-detector components. The front-end boards are part of the front-end electronics. They are used for the analogue processing

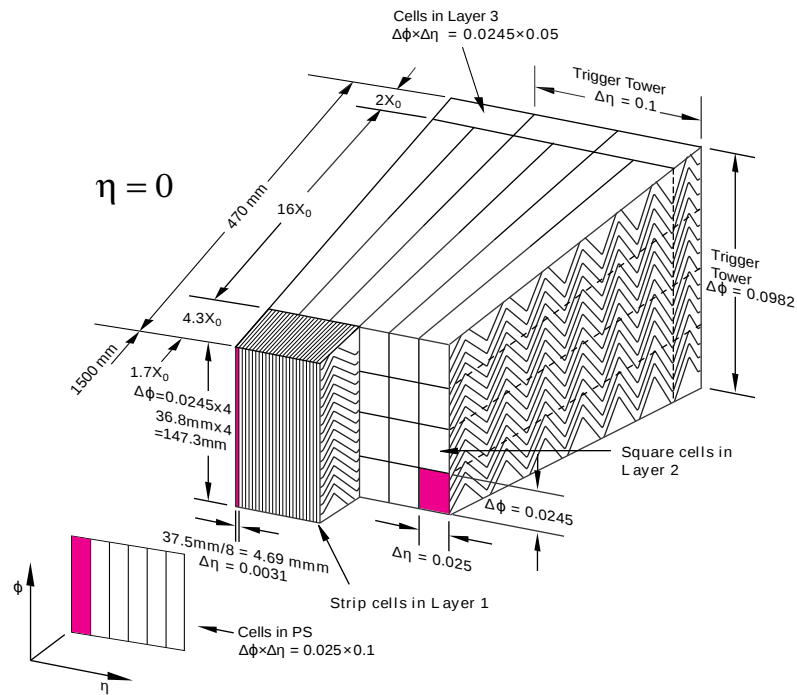


Figure 3.5. Layout of a barrel module in the electromagnetic calorimeter; from [67].

and the digitisation of the raw calorimeter signals. As such, they are crucial for the processing of the calorimeter data. The hardware failure affected several front-end boards, resulting in the reduction of the jet response in the corresponding calorimeter region. A dedicated selection, discussed in section 6.2.2, has been applied to the events in this analysis to cope with the effect.

### The hadronic calorimeter

The hadronic calorimeter consist of three sub-systems: the tile calorimeter, the hadronic end-caps and the forward calorimeter.

The tile calorimeter uses absorbing steel plates interspersed with scintillating tiles as active material. It consists of a barrel component within  $|\eta| < 1.0$  and two so-called *extended barrels* within  $0.8 < |\eta| < 1.7$  as shown in figure 3.4. Each of the barrels comprises 64 modules. Figure 3.7 shows the layout of one module. Wavelength-shifting fibres are used to read out the scintillator tiles and to create a three-dimensional cell structure by mapping several tiles onto one photomultiplier tube. The material of the fibres is selected to convert the wavelength of the scintillation light to visible light, matching the sensitivity of the photomultiplier.

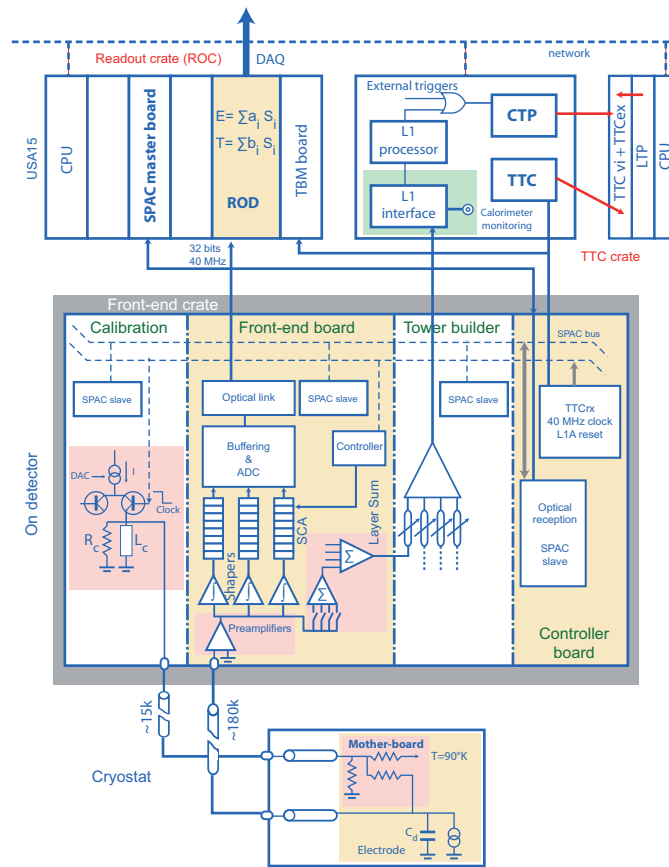
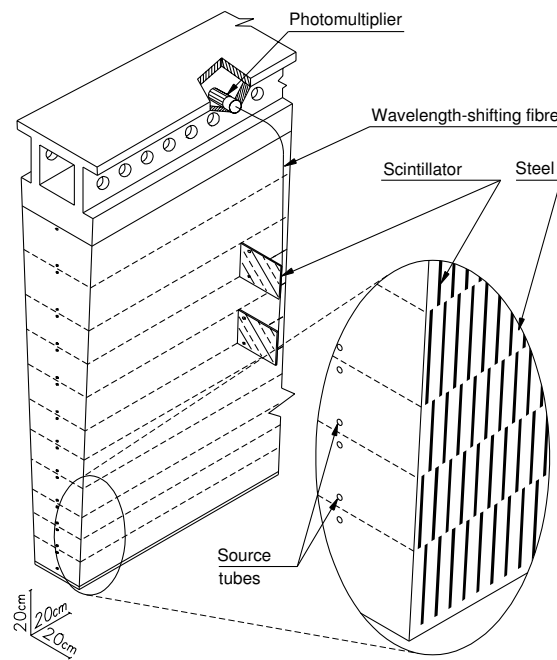


Figure 3.6. The readout architecture of the LAr calorimeter; from [67].

The hadronic end-cap calorimeter (HEC) is located behind the electromagnetic end-cap components and covers the region  $1.5 < |\eta| < 3.2$ . It uses copper as absorber material and liquid argon as the active medium.

The forward calorimeter (FCal) covers the pseudorapidity region  $3.1 < |\eta| < 4.9$ . It consists of three modules among which the first is made of copper and is optimised for electromagnetic measurements, and the second and third are made of tungsten and measure hadronic interactions. Liquid argon is used as the active medium in all three components. The jets used in this analysis are required to be within  $|y| \approx |\eta| < 4.4$  and may thus also be measured with the FCal. The two jets with the highest  $p_T$ , used to reconstruct the dijet system, are, however, required to be within  $|y| < 2.8$  as discussed in section 6.1.



**Figure 3.7.** The layout of one module of the tile calorimeter; from [67].

### 3.2.3. The muon system

The ATLAS muon system is shown in figure 3.8. Its goal is to measure muon tracks and to provide a fast trigger signal. The muon momenta are determined from the track bending achieved with the help of magnetic fields. These are generated by a combination of one large barrel and two end-cap air-core toroid magnets. The muon system covers the pseudorapidity region up to  $|\eta| = 2.7$ .

The muon system consists of a combination of precision tracking and triggering sub-systems. Precision tracking is performed by monitored drift tubes (MDTs), complemented by cathode strip chambers (CSCs) in the forward region. The trigger system has a coverage up to  $|\eta| = 2.4$ . It consists of resistive plate chambers (RPCs) in the barrel and thin gap chambers (TGC) in the end-cap regions.

### 3.2.4. The forward detectors

ATLAS is complemented with three additional detectors in the region of high pseudorapidity. LUCID (LUMinosity measurement using Cerenkov Integrating Detector) and ALFA (Absolute Luminosity For ATLAS) are used for luminosity measurements. LUCID is located at  $\pm 17$  m and ALFA at  $\pm 240$  m from the interaction point. The ZDC (zero-degree calorimeter) provides information on the centrality of heavy-ion collisions, and it is installed at  $\pm 140$  m from the interaction point.

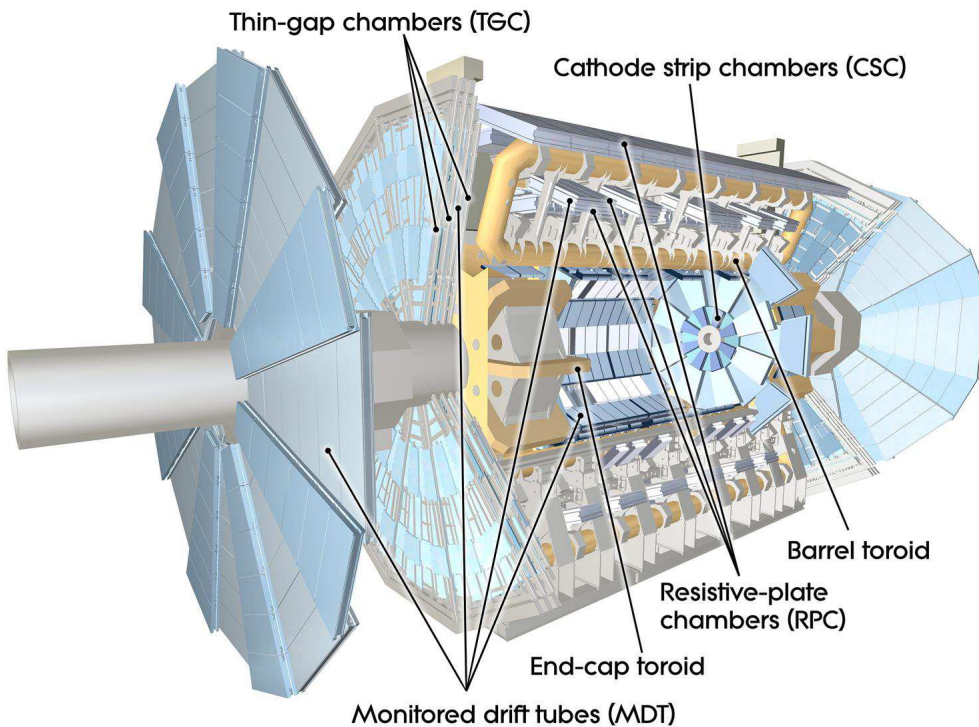


Figure 3.8. The ATLAS muon system; from [67].

### 3.2.5. The trigger system

Compared with the available storage space and the current limitations on the processing speed for events from the LHC, the 40 MHz bunch crossing rate requires a reduction by a factor of approximately  $10^5$ . This reduction needs to be performed with a high efficiency for interesting physics signatures such as the high- $p_T$  jets used in this thesis. To this end, a three-stage trigger system is implemented in ATLAS, comprised of the level-1 trigger (L1), the level-2 (L2) trigger and the event filter (EF). Each of these levels is used to refine the decision of the previous one. Together, L2 and EF are also denoted as high-level trigger (HLT). The HLT part of the trigger system is implemented in software on commercial computers while the L1 trigger uses custom-built hardware to allow the computation of the trigger decision within the available latency of  $2.5 \mu\text{s}$ .

The L1 trigger is designed to provide a first selection of events with interesting signatures while reducing the data rate to about 75 kHz. The signatures can be high- $p_T$  objects, such as muons, electrons, photons,  $\tau$ -leptons and jets, as well as large missing transverse energy or large total transverse energy. Since the L1 trigger decision has to be made within  $2.5 \mu\text{s}$  after the corresponding bunch crossing, it does not use the full information collected by the ATLAS detector but is restricted to reduced-granularity information from the muon system and the calorimeter.

On the first trigger level, the high- $p_T$  jets used in this thesis are identified by the calorimeter trigger (L1Calo). The processor unit responsible for the jet identification is the jet/energy-sum processor (JEP). It operates on *jet trigger elements*, which are energy sums over  $0.2 \times 0.2$ -wide regions in the electromagnetic and the hadronic calorimeter measured in  $\Delta\eta \times \Delta\phi$ . The trigger uses a sliding-window algorithm with different window sizes to identify regions with local maxima of  $E_T$ -sums above pre-defined thresholds as illustrated in figure 3.9. In the case of jets, the output of the L1 trigger are regions-of-interest (RoIs) specified by the jet elements introduced above. The RoIs contain the spatial coordinates, given in pseudorapidity  $\eta$  and azimuthal angle  $\phi$ , and the properties of the observed feature, as e. g. the transverse energy threshold that was passed. In addition to the first reduction in data size and the definition of the RoIs, the L1 trigger is also responsible for the bunch crossing identification.

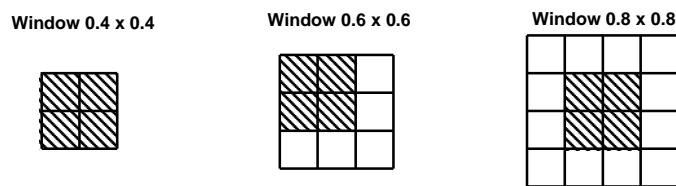


**Figure 3.9.** Illustration of the jet trigger algorithms at the first trigger level. Shown are different window sizes, using jet elements of size  $0.2 \times 0.2$  in  $\Delta\eta \times \Delta\phi$ . The regions-of-interest (RoIs) are depicted as shaded areas; from [67].

In contrast to the L1 trigger, the L2 trigger calculates more refined quantities such as cluster shape variables and compares their values to pre-defined thresholds to determine the trigger decision. The L2 trigger processes events asynchronously and is implemented on a computer farm. It reduces the event rate to 3.5 kHz, and its decision takes on average 40 ms per event. In the case of jets, the L2 trigger applies a simplified cone algorithm to the detector information with full granularity within the RoIs obtained from L1. The properties of the jets found by this cone algorithm, e. g. the transverse energy of the jet, are tested against pre-defined selection criteria.

The event filter reduces the event rate further to about 200 Hz by applying offline analysis algorithms to the events selected by the L2 trigger, using the full detector granularity. With a latency of about four seconds, the event filter applies complex jet reconstruction algorithms which reflect the offline procedures more closely. The jet reconstruction is done using the entire spatial calorimeter information. This is in contrast to the L2 trigger, where only the detector regions around the L1 RoIs are used. The default jet reconstruction at the event filter level in 2011 has been performed using the infrared and collinear safe anti- $k_t$  clustering algorithm [26] with topological clusters of calorimeter cells [79] as input. More information about the anti- $k_t$  algorithm and topological cell clusters will be given in chapter 5. Together, the fullscan approach and the use of topological clusters results in an improved performance with respect to pile-up stability and energy resolution when compared to alternative approaches which use only part of the detector information or a different input to the jet reconstruction [80].

In this analysis, dijet angular distributions are measured from events that contain high- $p_T$  jets. The events are required to have passed single inclusive jet triggers of the type EF-jX-a4tc-EFFS. In this notation, *EF* denotes a trigger on the event filter level, and *a4* stands for the anti- $k_t$  algorithm with a distance parameter of 0.4 that is used to identify jets with a transverse energy threshold of  $X$  GeV. Topological clusters (*tc*) are used as input for the jet reconstruction, and a full scan of the detector is performed (*EFFS*, event filter full scan). The trigger selection in the analysis will be further discussed in section 6.2.4.

To reduce the output rate of a trigger without increasing its threshold, *prescales* may be applied on all three trigger levels to process only a certain fraction of the events that pass the trigger. The actual prescale values of the different triggers are in general adjusted automatically and follow the current luminosity situation. Among the triggers used in this analysis, all but the one with the highest threshold were prescaled during 2011, with varying prescale values over time. For example, in run 191635 from 25th October 2011, the EF-j180-a4tc-EFFS trigger was prescaled with prescale factors between roughly 35 and 50 [81], such that only every 35th to 50th event that had passed this trigger was recorded. The effect of the prescales may be seen in various places in the analysis, such as e. g. in the event yields discussed in section 7.1 and in the weighting of the Monte Carlo simulation that is applied to reflect the pile-up conditions in data and which is described in section 7.3.

### 3.3. Data used in this analysis

The data analysed in this thesis have been recorded with the ATLAS detector between March 21st, 2011, and October 30th, 2011. Table 3.1 shows the arrangement into data taking periods and reports the corresponding dates, run ranges and integrated luminosities. The temporary hardware failure in the liquid argon calorimeter discussed in sections 3.2.2 and 6.2.2 affected the data in periods E to H, corresponding to an integrated luminosity of about  $\mathcal{L} = 1 \text{ fb}^{-1}$ .

**Table 3.1.** Overview of the data range used in this analysis. The luminosity is reported as integrated over all luminosity blocks during stable beams when the ATLAS *ready* flag was set. Period A was used for commissioning, with the magnet fields turned off for most of the runs. It is therefore not included in this analysis. Similarly, period C is not included, since it corresponds to an intermediate period with collisions at a centre-of-mass energy of  $\sqrt{s} = 2.76$  TeV; from [82].

Period	Date range	Run range	Luminosity [ $\text{pb}^{-1}$ ]
B	March 21st – March 24th	177986 – 178109	18
D	April 14th – April 29th	179710 – 180481	182
E	April 30th – May 3rd	180614 – 180776	52
F	May 15th – May 25th	182013 – 182519	156
G	May 27th – June 14th	182726 – 183462	566
H	June 16th – June 28th	183544 – 184169	283
I	July 13th – July 29th	185353 – 186493	406
J	July 30th – August 4th	186516 – 186755	237
K	August 4th – August 22nd	186873 – 187815	676
L	September 7th – October 5th	188902 – 190343	1599
M	October 6th – October 30th	190503 – 191933	1160



## 4. Simulation of background and signal processes

In this chapter, an overview of the Monte Carlo simulation for this analysis is given, and a method for the inclusion of NLO effects is discussed.

### 4.1. Simulation of the QCD background

The analysis of the dijet angular distributions presented in this thesis relies on a solid estimate of the Standard Model QCD background. Both data- and Monte Carlo-driven background estimations are common in high-energy physics. Data-driven approaches are particularly suited for resonance searches with a clearly-defined signal-free region, as in the search for new phenomena in the dijet invariant mass spectrum presented in [2]. Monte Carlo-driven approaches on the other hand are more adequate when the signal is expected to have a non-resonant or on-set behaviour as in the case of the two models discussed in this thesis. A Monte Carlo-based background estimation is therefore used in the analysis presented here.

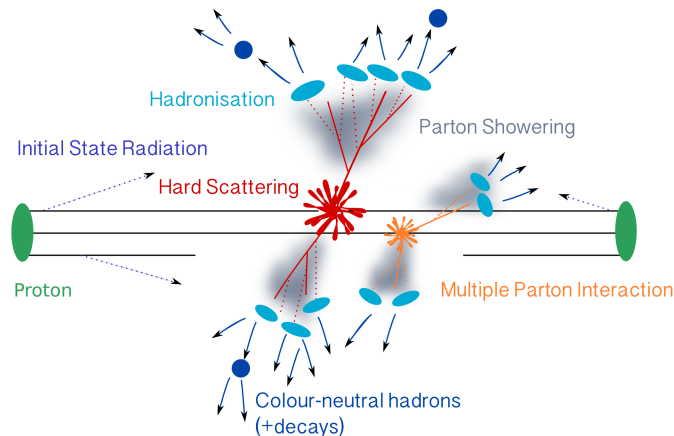


**Figure 4.1.** The structure of a hard QCD interaction.

The high-energy QCD interactions studied in this analysis and depicted in figure 4.1 may be described in the framework of the QCD improved parton model discussed in

section 1.2.2: The differential cross section for QCD processes with incoming hadrons are obtained by the convolution of the partonic cross sections with the proton PDFs. The final-state partons undergo a subsequent radiation process at the end of which they combine to colour-singlet hadrons. In addition to the processes connected to the primary hard scattering, additional interactions from the *underlying event* have to be taken into account to fully describe the QCD interactions at the LHC. The underlying event consists of the soft interactions of the colour-charged *beam-beam-remnants* with the developing hadron shower and of *multiple parton interactions*, i. e. additional parton scatters in the same proton-proton interaction. For the simulation to be compared with the observed data, it also needs to include the interaction of the outgoing particles with the detector. An important effect of the experimental set-up that has to be taken into account in the detector simulation are the so-called *pile-up* effects. Multiple proton interactions in the same bunch crossing (*in-time pile-up*) lead to additional energy deposits in the calorimeter. Moreover, the calorimeter is also sensitive to the energy depositions from interactions in other bunch crossings (*out-of-time pile-up*).

The PYTHIA Monte Carlo generator [22, 83] was used for the simulation of the QCD processes analysed in this thesis. PYTHIA is widely used for the simulation of particle interactions at high energies. It is a so-called *complete generator* in the sense that it simulates the hard QCD interaction, the initial and final state radiation, the underlying event and the hadronisation. PYTHIA 6 [22] was used for most purposes in this analysis, and version 8 [83] was applied for the generation of pile-up interactions.

PYTHIA first generates the  $2 \rightarrow 2$  QCD processes discussed in section 1.2.5 with leading-order accuracy. In the simulation used in this thesis, the structure of the incoming protons was defined by the MRSTMCal [84] modified leading-order parton distribution functions (PDFs). The systematic uncertainties on the  $\chi$ -distributions arising from the uncertainties on the PDFs will be discussed in chapter 8.

PYTHIA uses a parton shower algorithm [22] to simulate the evolution of the outgoing partons. The final-state evolution is described as a series of branchings of each *mother parton* into two *daughter partons*,  $a \rightarrow bc$ . The corresponding processes allowed in QCD and considered in PYTHIA are  $g \rightarrow gg$ , denoting a gluon splitting into two gluons,  $q \rightarrow qg$ , describing a quark splitting into a quark and a gluon and  $g \rightarrow q\bar{q}$ , which defines a gluon that splits into a quark and an anti-quark. Energy and momentum are conserved at each branching such that one daughter parton carries a fraction  $z$  of the energy of the mother parton, and the remaining energy fraction  $(1 - z)$  is carried by the other. The probability for each branching to occur is determined by the DGLAP equations [18–20]. The evolution of the parton shower is governed by a variable  $Q^2$ . In PYTHIA 6,  $Q^2$  can be the squared mass of the mother parton or the squared transverse momentum of the branching which better describes the so-called *coherence effects* as discussed in [22] and the references therein.  $Q^2$  decreases with each branching in the final-state until the parton shower algorithm is stopped at a lower cutoff value around 1 GeV. From there on, the event simulation is continued with the hadronisation, the transition from partons to colour-neutral hadrons.

**Table 4.1.** Division of the PYTHIA [22] Monte Carlo production for inclusive QCD jet samples according to  $\hat{p}_T$ , the transverse momentum of the hard subprocess.

Sample	Sample ID	$\hat{p}_T^{\min}$ [GeV]	$\hat{p}_T^{\max}$ [GeV]
J0	105009	8	17
J1	105010	17	35
J2	105011	35	70
J3	105012	70	140
J4	105013	140	280
J5	105014	280	560
J6	105015	560	1120
J7	105016	1120	2240
J7a	145830	1120	1680
J7b	145831	1680	2240
J8	105017	2240	-

The hadronisation occurs at low-momentum scales and is therefore intrinsically non-perturbative. Hence, no exact calculations exist, and models have to be used to describe the process. The hadronisation model used in PYTHIA is the Lund string model [23, 24]. Other hadronisation models such as the cluster model used in the HERWIG++ Monte Carlo generator [85] exist. The underlying principle of hadronisation may be illustrated by the example of a quark  $q$  and an anti-quark  $\bar{q}$  moving apart in a back-to-back configuration as discussed e. g. in [86]. As their distance increases, a QCD colour flux tube is formed between them. The flux tube is pictured to be uniform over its length, creating a linearly rising potential. When the energy stored in the flux tube becomes large enough, a new  $q'\bar{q}'$  pair is created from the vacuum, leading to the recombination of two colour-singlet pairs  $q\bar{q}'$  and  $q'\bar{q}$ . This process continues until the invariant mass of the newly created colour-singlet pairs is too small to create new  $q\bar{q}$  pairs from the vacuum and only colour-singlet hadrons remain.

To complete the event generation, PYTHIA simulates the underlying event activity discussed above. The AUET2B-LO\*\* configuration [87] which makes use of underlying event data for the simulation of multiple parton interactions was applied here. A comparison of QCD background predictions obtained with different Monte Carlo generators and configurations will be shown in chapter 8.

The simulation of the hard QCD processes studied in this analysis has been performed in bins of  $\hat{p}_T$ , the transverse momentum of the hard subprocess [22], to sample the kinematically less probable events with high- $p_T$  jets with higher statistics. Table 4.1 shows the  $\hat{p}_T$ -range of these samples. Dedicated samples have been generated to increase the

statistics in the high-momentum range. The individual samples are combined, weighted according to the generated number of events in each sample and the corresponding cross section.

The interactions of the final-state hadrons with the ATLAS detector were subsequently simulated with the fast ATLAS detector simulation ATLFast 2.0 [88]. In ATLFast 2.0, the electromagnetic and hadronic showers in the calorimeter are simulated with the FastCaloSim [88] package. Validation studies [89] have shown that the results obtained with the fast detector simulation are consistent with those obtained with the full detector simulation [90] which uses the GEANT4 [91] package. The fast simulation has been chosen for the higher amount of available statistics. The events obtained from the Monte Carlo simulation were subjected to the same event selection as those from data. The event selection will be discussed in chapter 6.

Pile-up contributions were taken into account in the simulation by the procedure described in [92]. In-time pile-up was simulated by adding minimum bias events to the nominal events. These events have been generated with the PYTHIA 8 Monte Carlo generator [83] using the 4C configuration [93] and the MRSTMCAL PDFs [84]. Out-of-time pile-up effects were simulated by grouping the collisions into four bunch trains, with 36 bunches in each train. The bunch spacing was set to 50 ns, corresponding to the situation in data in 2011. The interaction of the pile-up events with the ATLAS detector has been simulated with the full ATLAS detector simulation [90], using the GEANT4 package [91]. The pile-up effects were considered in the jet calibration described in chapter 5 and studied for this analysis in chapter 7.

## 4.2. Simulation of new phenomena

Monte Carlo simulations have also been performed for the two models for physics beyond the Standard Model discussed in chapter 2, a contact interaction (CI) scenario for quark compositeness and a quantum black hole (QBH) scenario. The simulation of the CI scenario has been obtained with the same generator (PYTHIA 6), configuration (AUET2B-LO\*\*) and PDFs (MRSTMCAL) as the QCD background simulation. The scenario of destructive interference has been simulated, leading to more conservative limits on the compositeness scale than the scenario of constructive interference. Signal samples have been generated for the values 4, 6, 8 and 10 TeV of the compositeness scale  $\Lambda$ .

The BLACKMAX [49] generator with the CT10 PDF [94] was used for the simulation of a QBH model with  $n = 6$  extra-dimensions as studied in [48]. BLACKMAX has been configured to simulate gravitational effects resulting in two-body final states. After the hard process, the remaining steps of the event generation have been performed with PYTHIA. A range of Monte Carlo samples with different values of the reduced Planck Scale  $M_D$  have been produced with  $M_D$  set to 0.75, 1.00, 1.50, 2.00, 2.25, 2.50, 2.75, 3.00, 3.50, 4.00, 4.50, 5.00, 5.50 and 6.00 TeV. As in the case of the QCD background

prediction, the Monte Carlo samples for the models of new phenomena have been further processed with the fast detector simulation ATLEFAST 2.0. The predictions for the two signal models were used for the calculation of limits presented in chapter 10.

### 4.3. Inclusion of NLO effects

The background in the analysis of the dijet angular distributions is assumed to be dominated by QCD processes, and the predicted distributions are obtained with the PYTHIA Monte Carlo generator, as discussed above. In PYTHIA, the matrix element calculations are performed at the leading order (LO) in the strong coupling constant. In general, the normalisation of distributions obtained at LO is subject to large uncertainties from higher-order corrections while the shape is usually better described [86]. Since the analysis presented in this thesis studies normalised distributions, LO predictions are expected to already provide a reasonable description of the  $\chi$ -spectra. Nevertheless, a correction as introduced in this section is applied to improve the accuracy and to provide insight into the dependence of the prediction on higher orders.

#### 4.3.1. K-factor approach

The precision of the nominal Monte Carlo prediction obtained with PYTHIA is improved by a K-factor correction, consistent with the approach in previous analyses [57]: The LO matrix elements calculated with PYTHIA are re-weighted with a prediction obtained at NLO accuracy. The NLO matrix elements are determined with the NLOJET++ [30–33] Monte Carlo generator, using the CT10 NLO PDFs [94]. In the correction, the intrinsic higher-order effects in the parton shower process in PYTHIA [22] have to be taken into account. The K-factor  $K(\chi)$  is therefore defined as a function of  $\chi$  by

$$K(\chi) = \frac{\left(\frac{d\sigma}{d\chi}(\chi)\right)_{\text{NLO}} / \left(\frac{d\sigma}{d\chi}(\chi)\right)_{\text{LO,NLOJET++}}}{\left(\frac{d\sigma}{d\chi}(\chi)\right)_{\text{SHOWER}} / \left(\frac{d\sigma}{d\chi}(\chi)\right)_{\text{LO,PYTHIA}}} \propto \frac{\left(\frac{d\sigma}{d\chi}(\chi)\right)_{\text{NLO}}}{\left(\frac{d\sigma}{d\chi}(\chi)\right)_{\text{SHOWER}}}. \quad (4.1)$$

Here,  $((d\sigma/d\chi)(\chi))_{\text{NLO}}$  denotes the NLO matrix element prediction for the differential  $\chi$ -distributions obtained from NLOJET++, and  $((d\sigma/d\chi)(\chi))_{\text{LO,NLOJET++}}$  is the corresponding LO prediction from the same generator.  $((d\sigma/d\chi)(\chi))_{\text{SHOWER}}$  denotes the prediction for the differential  $\chi$ -distributions calculated with PYTHIA, including the hard scattering and the parton showers, but without non-perturbative contributions, i.e. without the hadronisation, the underlying event and the primordial  $k_T$ , which describes the transverse motion of the partons in the initial hadrons [22].  $((d\sigma/d\chi)(\chi))_{\text{LO,PYTHIA}}$  is the LO matrix element prediction from PYTHIA. The proportionality holds since any difference between the LO predictions from the two generators arising from different conventions of  $\alpha_s$  results in a global difference in the normalisation [95]. Since the analysis studies the shape of normalised  $\chi$ -distributions and is as such not sensitive to

normalisation effects,  $((d\sigma/d\chi)(\chi))_{\text{NLO}} / ((d\sigma/d\chi)(\chi))_{\text{SHOWER}}$  is used as the K-factor correction for the predicted  $\chi$ -spectra. The correction is applied as a bin-wise multiplication of the Monte Carlo prediction from PYTHIA with the K-factors before the spectra are normalised to the total cross-section.

### 4.3.2. Cross section predictions at NLO

Following the presentation in [86] and [32], a jet cross section at NLO may be written as

$$\sigma = \sigma^{LO} + \sigma^{NLO}, \quad (4.2)$$

with the LO cross section  $\sigma^{LO}$  determined by integrating  $d\sigma^{LO}$  over the corresponding phase space, here assumed to comprise  $n$  partons in the final state:

$$\sigma^{LO} = \int_n d\sigma^{LO}. \quad (4.3)$$

The NLO contribution to the cross section consists of two parts,

$$\sigma^{NLO} = \int_{n+1} d\sigma^R + \int_n d\sigma^V, \quad (4.4)$$

one for the real corrections, corresponding to the exclusive cross section  $d\sigma^R$  with  $n+1$  partons in the final state, and one for the virtual loop or  $d\sigma^V$  with  $n$  partons in the final state.

In the calculation of the cross section, several kinds of divergences occur. Ultraviolet (UV) divergences appear in the virtual contributions, while infrared (IR) divergences arise both in real and virtual contributions. The UV divergences may be treated by regularisation and renormalisation. The IR divergences occur in form of soft and collinear divergences. The soft divergences cancel in the sum of real and virtual contributions, according to the Bloch-Nordsieck [96] and Kinoshita-Lee-Nauenberg theorems [97, 98]. The remaining collinear divergences may be factorised into structure and fragmentation functions. Numerically, the cancellation of the soft IR divergences is challenging to achieve, since real and virtual contributions lead to different parton multiplicities in the final state ( $n$  versus  $n+1$  in the example above). The numerical integration has thus to be performed individually over the two cases, each of which diverges separately. The NLOJET++ Monte Carlo generator [30, 31] uses the *dipole subtraction method* [32] to solve this problem. Other approaches such as the so-called *phase-space slicing* methods [99, 100] exist.

### 4.3.3. Resulting K-factors

Figure 4.2 shows the  $\chi$ -distributions for the numerator  $((d\sigma/d\chi)(\chi))_{\text{NLO}}$  and the denominator  $((d\sigma/d\chi)(\chi))_{\text{SHOWER}}$  of the K-factor for the highest dijet invariant mass bin

with statistical uncertainties. For low  $\chi$ -values, NLOJET++ predicts a higher cross section than PYTHIA without non-perturbative contributions, while the situation is opposite for  $\chi$ -values larger than 10.

This is reflected in figure 4.3 which shows the K-factors for all five dijet invariant mass bins with statistical uncertainties. For  $\chi$ -values below 10, the K-factor distribution in the highest dijet mass bin is above 1, while it is below 1 for higher values of  $\chi$ . Small discontinuities are observed, e. g. in third-last  $\chi$ -bin of the K-factor distribution for the second-highest dijet mass bin. These discontinuities arise from statistical fluctuations in the PYTHIA simulation without non-perturbative contributions. In general, all K-factors are of the order of unity and relatively flat over the entire  $\chi$ -range, indicating that the shape of the  $\chi$ -spectra is reasonably well described already at LO.

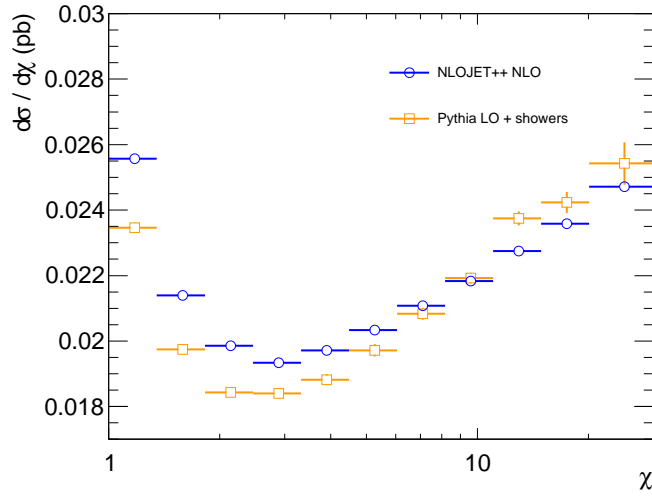


**Figure 4.2.** Differential  $\chi$ -distributions obtained from NLOJET++ and the PYTHIA configuration without non-perturbative corrections described in the text. Shown are the distributions in the highest dijet invariant mass bin, for events with  $2600 < m_{jj} < 7000$  GeV and with statistical uncertainties.

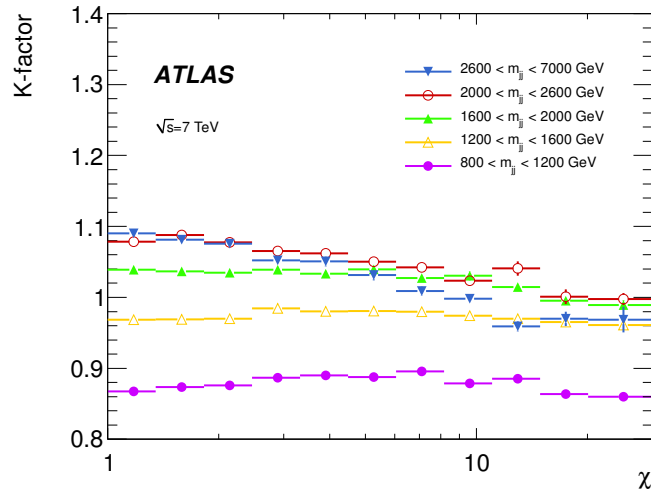


**Figure 4.3.** The K-factors for the  $\chi$ -distributions in the five dijet invariant mass bins; also appeared in [2].

# 5. Jet reconstruction and calibration in ATLAS

The observable  $\chi$ , analysed in this thesis, is calculated from kinematic jet variables. The following chapter describes the definition and calibration of jets in ATLAS. First, the input objects for the jet reconstruction are introduced, and the jet algorithm is discussed. Then, the jet calibration is presented in detail. Special emphasis is given to the residual jet energy calibration, derived from *in situ* techniques, and to the jet energy scale uncertainties, as these play a major role in the analysis.

## 5.1. Jet reconstruction

Jets are reconstructed with a jet algorithm. They are defined by the choice of the algorithm, the values of its parameters and the so-called *recombination scheme* which describes how the kinematic properties of the input objects are propagated to the jet [25]. Jet algorithms can be applied to topological groups of calorimeter cells as described below, but also to charged particle tracks or final state hadrons from Monte Carlo simulations.

### 5.1.1. Topological clusters

The input objects for the reconstruction of calorimeter jets as used in this thesis are so-called topological clusters, or *topo-clusters* [79]. Topo-clusters are three-dimensional assemblies of calorimeter cells, formed from cells with a signal-to-noise ratio above a pre-defined threshold as described below. The signal-to-noise ratio is expressed as the absolute value of the cell energy divided by the cell noise. The cell noise is calculated from the quadratic sum of the electronic noise and an additional noise component to account for pile-up [92],

$$\sigma_{\text{noise}} = \sqrt{(\sigma_{\text{noise}}^{\text{electronic}})^2 + (\sigma_{\text{noise}}^{\text{pile-up}})^2}. \quad (5.1)$$

Here,  $\sigma_{\text{noise}}^{\text{electronic}}$  is the RMS of the cell energy distribution in events without collisions [101], and  $\sigma_{\text{noise}}^{\text{pile-up}}$  is estimated in Monte Carlo simulations and corresponds to an average of eight interactions per bunch crossing. Calorimeter cells with a signal-to-noise ratio above four are used as seeds in the cluster formation. Neighbouring cells

are added if they have a signal-to-noise ratio above two. Then, all neighbouring cells of the already selected cells are included in the topo-cluster regardless of their signal-to-noise ratio. A further step sub-divides the cluster according to local energy maxima to follow the showering of separate close-by particles: The constituent cells in a topo-cluster are scrutinized for local energy maxima above 500 MeV which are subsequently used as seeds for a new iteration of the cluster formation, thereby splitting the original cluster [101]. A four-momentum vector is determined for each final topo-cluster. The energy of the cluster is set to the sum of the energies of its constituent cells calibrated at the electromagnetic scale which will be introduced later in this chapter. Since topo-clusters can have negative energies, the topo-clusters used for the jet reconstruction are required to have positive energy [74, 101]. The clusters are considered to be massless, and their direction is defined as the vector from the origin of the ATLAS coordinate system to the energy-weighted barycentre of the constituent calorimeter cells.

### 5.1.2. Jet algorithm

The jets used in this analysis have been reconstructed with the anti- $k_t$  algorithm [26], with a distance parameter of  $R = 0.6$  and the four-momentum *recombination scheme*. Other recombination schemes exist, such as the  $E_T$ -weighted recombination described in [25]. Due to its favourable properties like infrared and collinear safety [26], the anti- $k_t$  algorithm has become a quasi-standard for the jet reconstruction at the LHC.

Based on a transverse momentum-weighted relative distance measure, the anti- $k_t$  algorithm uses the FASTJET software [102] to iteratively cluster input objects to jets. The jets used in this work have been reconstructed from topo-clusters. Two distance measures,  $d_{ij}$  and  $d_{iB}$ , are defined as

$$d_{ij} = \min(k_{ti}^{-2}, k_{tj}^{-2}) \frac{\Delta_{ij}^2}{R^2} \quad \text{and} \quad d_{iB} = k_{ti}^{-2}. \quad (5.2)$$

Here,  $k_{ti}$  denotes the transverse momentum of object  $i$ , and  $\Delta_{ij}^2 = (y_i - y_j)^2 + (\phi_i - \phi_j)^2$  is the squared spatial distance between the objects  $i$  and  $j$ , calculated from their rapidity  $y$  and azimuth angle  $\phi$ .  $R$  is the distance parameter of the algorithm. Typical values for the distance parameter used in ATLAS are  $R = 0.4$  and  $R = 0.6$ .

The iterative jet reconstruction starts with the calculation of the  $d_{ij}$  and  $d_{iB}$  over all combinations of  $i$  and  $j$ . If the smallest relative distance is one of the  $d_{ij}$ , the objects  $i$  and  $j$  are combined by adding their Lorentz four vectors. Through the weighting factor  $\Delta_{ij}^2/R^2$ , objects are combined with close-by, high-transverse momentum objects early in the clustering process, following the idea that they likely originate from the same hard final-state parton. If the smallest relative distance is one of the  $d_{iB}$ , the input object  $i$  is defined as a jet and no longer used in the algorithm. In both cases, the procedure is repeated until all input objects have been assigned to a jet. The output of the algorithm is a set of jets, defined by their four-momentum vectors.

## 5.2. Jet calibration

Figure 5.1 provides an overview of the calibration chain applied to the jets in this analysis. This section discusses the first three elements of the calibration chain. The corrections incorporated in these steps are mostly based on results from Monte Carlo simulations. The subsequent refinement of the calibration with *in situ* techniques is presented in a dedicated section of this chapter.

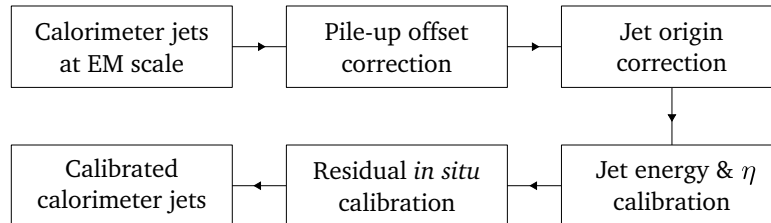


**Figure 5.1.** The jet calibration chain; adapted from [74].

### 5.2.1. Pile-up offset correction

A correction [74, 92] is applied to the jets in order to reduce the effect of pile-up on the reconstructed jet energy and transverse momentum. In-time pile-up, i.e. multiple proton interactions in the same bunch crossing, leads to additional energy deposits in the calorimeter and thereby increases the reconstructed energy and momentum of jets originating from the hard scatter. Moreover, due to the small bunch spacing within the LHC bunch trains in 2011, the measured jet transverse momenta are sensitive to out-of-time pile-up, since the energy deposits from interactions in other bunch crossings lead to modifications of the recorded calorimeter signals.

To assess the effect, simulated jets reconstructed from the energy deposits in the calorimeter have been matched to jets reconstructed from stable particles (*truth jets*) in a Monte Carlo simulation which includes pile-up. In-time pile-up is simulated as Poisson-distributed minimum bias interactions which are added to the hard scatter. Four LHC bunch trains are modelled to take out-of-time pile-up effects into account [92]. The  $p_T$  of jets reconstructed from calorimeter energy deposits has been studied as a function of the number of reconstructed primary vertices  $N_{PV}$  and the expected number of average interactions per bunch crossing  $\mu$  in several bins of the truth jet  $p_T$ .  $N_{PV}$  has been used as a measure of the amount of in-time pile-up, while the out-of-time pile-up is characterised by  $\mu$ .

Figure 5.2 shows the reconstructed transverse jet momentum as a function of the number of primary vertices for  $7.5 \leq \mu < 8.5$  and the expected number of average interactions per bunch crossing for  $N_{PV} = 6$ . The reconstructed  $p_T$  of central anti- $k_t$  jets with

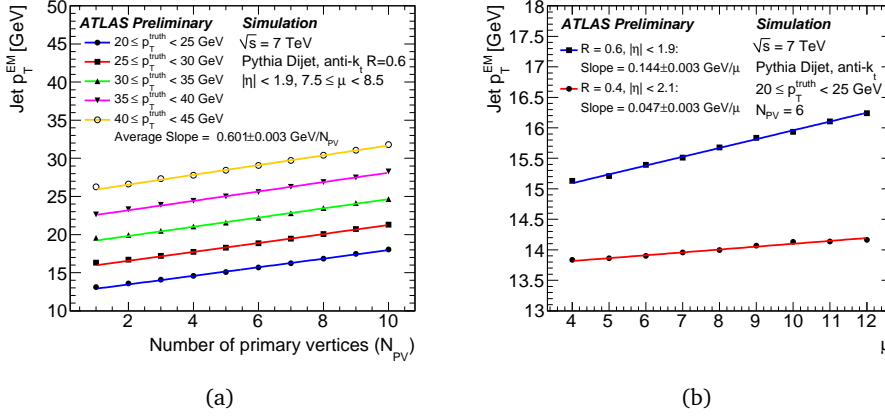


**Figure 5.2.** (a) The average reconstructed transverse momentum  $p_{T,EM}^{jet}$  for jets from Monte Carlo simulations, reconstructed with the anti- $k_t$  algorithm with  $R = 0.6$  and calibrated at the EM scale, is shown as a function of the number of reconstructed primary vertices  $N_{PV}$  in several bins of the truth jet transverse momentum  $p_T^{truth}$ . The average number of interactions per bunch crossing  $\mu$  is held between 7.5 and 8.5. (b) Fixing the number of primary vertices  $N_{PV}$  to 6, the average reconstructed transverse momentum of anti- $k_t$  jets with distance parameter  $R = 0.6$  is shown as a function of the average number of collisions per bunch crossing for a truth jet  $p_T^{truth}$  between 20 and 25 GeV; both figures from [92].

distance parameter  $R = 0.6$  rises linearly by approximately 850 MeV per reconstructed primary vertex and by about 210 MeV per average interaction.

A correction is derived from these results to remove the pile-up dependence of the reconstructed jet  $p_T$ . The linear offset is parametrised as

$$\begin{aligned} \Omega(N_{PV}, \mu, \eta_{det}) &= p_T^{jet}(N_{PV}, \mu, \eta_{det}) - p_T^{truth} \\ &= \frac{\partial p_T}{\partial N_{PV}}(\eta_{det}) (N_{PV} - N_{PV}^{ref}) + \frac{\partial p_T}{\partial \mu}(\eta_{det}) (\mu - \mu^{ref}) \\ &= \alpha(\eta_{det}) \cdot (N_{PV} - N_{PV}^{ref}) + \beta(\eta_{det}) \cdot (\mu - \mu^{ref}), \end{aligned}$$

with  $p_T^{jet}(N_{PV}, \mu, \eta_{det})$  denoting the reconstructed jet transverse momentum under the pile-up conditions characterised by  $N_{PV}$  reconstructed primary vertices and  $\mu$  average interactions per bunch crossing. The offset depends on the jet pseudorapidity. It is used here without the jet origin correction which will be discussed in the next section and is denoted by  $\eta_{det}$ .  $p_T^{truth}$  indicates the truth jet transverse momentum, found by matching the reconstructed calorimeter jets to the particle jets. The scaling coefficients  $\alpha$  and  $\beta$  only depend on the calorimeter region  $\eta_{det}$ . The resulting offset-corrected transverse jet momentum is then given by

$$p_T^{corr} = p_T^{jet} - \Omega(N_{PV}, \mu, \eta_{det}). \quad (5.3)$$

For the calibration, the arbitrary reference values for the pile-up conditions were chosen as  $N_{PV}^{ref} = 4.9$  and  $\mu^{ref} = 5.4$ . The offset correction at the reference values is zero,  $\Omega(N_{PV} = N_{PV}^{ref}, \mu = \mu^{ref}) = 0$ .

The results from Monte Carlo simulations have been validated in data, using the transverse momentum balance between jets and reference objects that are not affected by pile-up. Two approaches have been used: the balance between a jet and a photon from prompt photon production  $p_T^{\text{jet}}/p_T^\gamma$  and between jets reconstructed from calorimeter energy depositions matched to jets reconstructed from charged particle tracks in the inner detector  $p_T^{\text{jet}}/p_T^{\text{trackjet}}$ . Systematic uncertainties have been introduced to cover the bias between both methods as will be discussed in section 5.4.5.

### 5.2.2. Jet origin correction

The direction of a topo-cluster is given by the vector from the nominal centre of the ATLAS detector to the energy-weighted barycentre of the constituent calorimeter cells within the cluster as described in section 5.1.1. The jet algorithm calculates the jet four momentum as the sum of the four momenta of the constituent topo-clusters. As part of the jet calibration [74, 101], the jet direction is corrected to take the actual position of the primary interaction vertex into account. The direction of each topo-cluster within a jet is re-calculated such that it originates from the primary hard-scattering vertex of the event. The direction of the jet is updated accordingly, following the same combination scheme as above. The jet pseudorapidity after the jet origin correction is denoted by  $\eta_{\text{origin}}$ .

### 5.2.3. Jet energy scale correction

Up to this point in the calibration chain, the jets are calibrated at the electromagnetic energy (EM) scale. The EM scale correctly measures energy depositions from particles in electromagnetic showers. For the electromagnetic calorimeter, the EM scale has been established with electrons from test beam measurements [103–105], and it has been refined *in situ* with events from  $Z \rightarrow e^+e^-$  decays in proton-proton collisions [106]. In the case of the hadronic calorimeter, the EM scale has been established with test-beam electrons [107], and it has been validated with muons from test beams [107] and cosmic rays [108].

Starting from the EM scale, a calibration is applied to correct for several effects that influence the jet energy measurement [101]: Due to the *non-compensating* nature of the calorimeter, the hadronic component of the jets has a lower response than the electromagnetic part. *Dead material*, e. g. cables and support structures, induces energy losses in inactive detector regions. Further energy loss can occur due to particles that are not stopped in the active part of the calorimeter (*leakage*). In addition, the jet energy can be reduced by particles which are not included in the reconstruction of the jet at the calorimeter level because they are too far away from the jet axis, a phenomenon called *out-of-cone* effect. Finally, energy loss may occur from reduced reconstruction efficiencies and from calorimeter energy depositions below the noise thresholds.

The energy calibration is implemented in the form of correction factors that depend on the jet energy and pseudorapidity. These factors have been derived from Monte Carlo simulations by relating the energy of reconstructed jets to that of matched jets on the particle level and measuring the average jet response

$$\mathcal{R}_{\text{EM}}^{\text{jet}} = E_{\text{EM}}^{\text{jet}}/E_{\text{truth}}^{\text{jet}}. \quad (5.4)$$

Following this step, the jets are said to be calibrated at the EM+JES scale.

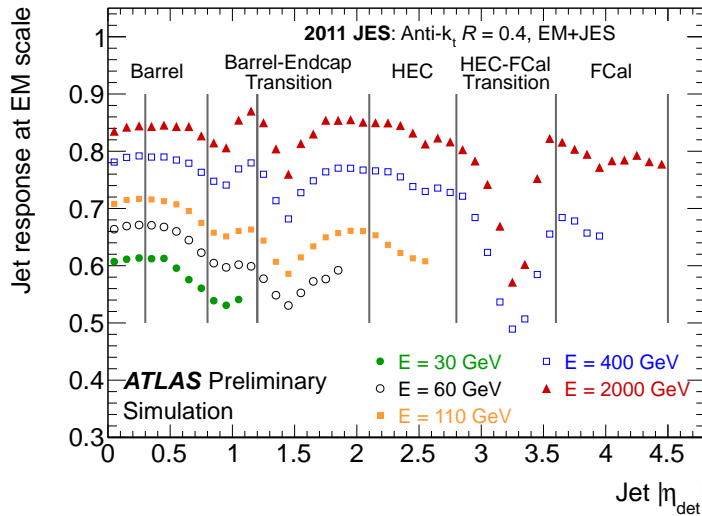


**Figure 5.3.** The jet energy response  $E_{\text{jet}}^{\text{EM}}/E_{\text{jet}}^{\text{truth}}$  as a function of the jet pseudorapidity for different jet energies, before the jet origin correction. The different calorimeter regions are indicated by vertical lines. The results have been obtained from PYTHIA Monte Carlo simulations of inclusive jet samples; from [74].

Figure 5.3 shows the average jet response  $\mathcal{R}_{\text{EM}}^{\text{jet}}$  for different bins in energy as a function of the jet pseudorapidity  $\eta_{\text{det}}$  before the jet origin correction.  $\eta_{\text{det}}$  is used in order to preserve the more direct relation between the detector pseudorapidity and the corresponding calorimeter region. The jet response is about 0.6 for central jets with an energy at the EM+JES scale of 30 GeV and increases to more than 0.8 for jets with energies of 2000 GeV, due to the increasing electromagnetic energy fraction of the hadronic showers [109]. Within the barrel part of the calorimeter, the response is relatively flat as a function of the jet pseudorapidity, while it shows stronger variations in the transition regions. Most pronounced is the reduction in the jet response in the transition region between the hadronic end-cap (HEC) and the forward calorimeter (FCal) where the response decreases from about 0.8 to less than 0.6 for jets with calibrated energies of 2000 GeV due to the lower density of active calorimeter material. The average jet energy scale correction in each bin is given by the inverse of the response value.

#### 5.2.4. Jet pseudorapidity correction

Since the ATLAS calorimeter is composed of several components, it is not instrumented in a fully uniform way. As a result, the pseudorapidity of the reconstructed jets carries a small bias towards the better instrumented regions of the calorimeter. This effect is explained by the higher energy response of topo-clusters in these better instrumented regions and can be studied in Monte Carlo simulations [74, 101]. The correction that is applied to compensate for the effect depends on the jet pseudorapidity before the origin correction  $\eta_{\text{det}}$  and the calibrated jet energy  $E_{\text{EM+JES}}$ . It is found to be very small, with  $\Delta\eta = \eta_{\text{truth}} - \eta_{\text{origin}} < 0.01$  for most calorimeter parts and with some larger deviations in the transition regions between different calorimeter components which do not exceed  $\Delta\eta = 0.05$ .

### 5.3. Residual calibration with *in situ* techniques

The jet energy calibration described above is based on results from Monte Carlo simulations. One exception is the origin correction that is based on the position of the primary collision vertex measured in data. This correction calibrates, however, the jet direction, not the energy. In this section, an additional calibration is described that accounts for residual differences between the data and the Monte Carlo simulation. This residual calibration makes use of techniques that rely on the transverse momentum balance between jets and suitable reference objects. The reference object can be a jet, a Z boson, a photon, or a system of low- $p_T$  jets. The average  $p_T$ -response is derived for each of the calibration techniques, and the results of the different methods are combined. The procedure is performed in data and in Monte Carlo simulations, and the residual *in situ* calibration is given by the response ratio:

$$\langle p_T^{\text{jet}}/p_T^{\text{ref}} \rangle_{\text{data}} / \langle p_T^{\text{jet}}/p_T^{\text{ref}} \rangle_{\text{MC}}. \quad (5.5)$$

The residual JES calibration is applied to jets in data.

As a first calibration step, the transverse momentum balance in events with exactly two high- $p_T$  jets [110] is used to adjust the response in the forward region,  $0.8 \leq |\eta| < 4.5$ , with that in a central reference region,  $|\eta| < 0.8$ . This correction is needed since the jet response still carries a residual dependence on the jet pseudorapidity after the Monte Carlo-based calibration described in the previous section. After the response is equalised over  $\eta$ , three further *in situ* techniques are used to derive the residual JES calibration for jets within  $|\eta| < 1.2$ .

The so-called *direct balance* technique [111] exploits the transverse momentum balance in events where a jet recoils against a Z boson which subsequently decays to an  $e^+e^-$  pair. The response  $p_T^{\text{jet}}/p_T^{\text{ref}}$  for Z boson transverse momenta between 15 and 200 GeV is determined in data and in Monte Carlo simulations. The *missing transverse momentum projection fraction* (MPF) [112] method uses events with a photon and a high- $p_T$  jet

to determine the transverse momentum balance between the photon and the so-called *hadronic recoil*. The MPF response is calculated from the missing transverse energy, projected on the direction of the photon. The method does not rely on a jet algorithm and is based on the assumption that the only missing transverse energy in  $\gamma$ +jet events arises from the jet and is due to dead material, calorimeter non-compensation and signal loss from noise suppression [101]. The technique uses photons with transverse momenta between 25 and 800 GeV. The *multijet balance* technique [113] exploits the transverse momentum balance in events in which a high- $p_T$  jet recoils against a system of low- $p_T$  jets. The method requires the low- $p_T$  jets to be within  $|\eta| < 2.8$  and the high- $p_T$  jet to be within  $|\eta| < 1.2$  and propagates the calibration and the uncertainties of the other two methods from lower to higher jet  $p_T$ . Via several iterations, high jet transverse momenta can be reached, until the number of events becomes too low in the TeV-range.

After the response ratios have been obtained with the different *in situ* techniques, they are combined in the residual JES calibration [74]. Since the results from the individual *in situ* methods have been derived with different binnings in  $p_T$ , a joint  $p_T$ -binning is defined as a first step of the combination. Next, the response ratio from each method is interpolated to the new binning. Finally, in every  $p_T$ -bin, the results of the different methods are combined as a weighted average, with weights inversely proportional to the squared uncertainties of each method. The resulting data-to-Monte Carlo response ratio is applied to jets in data as the residual JES calibration.

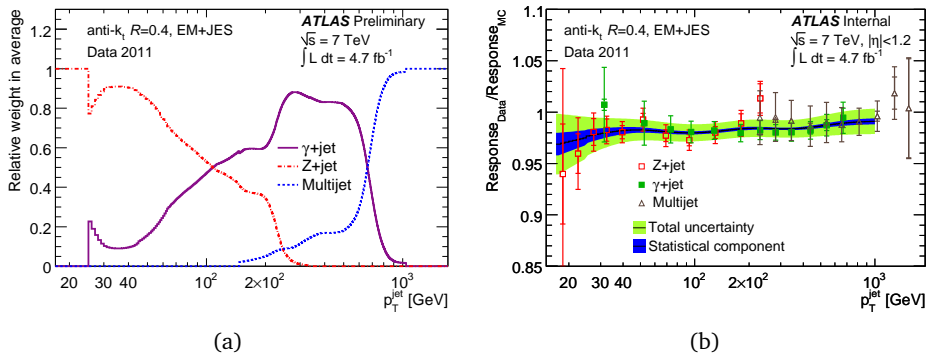


**Figure 5.4.** (a) Relative weights of each of the three *in situ* techniques used in the determination of the residual jet energy scale uncertainty as a function of the jet transverse momentum  $p_T^{\text{jet}}$ , for anti- $k_t$  jets with  $R = 0.4$ , calibrated at the EM+JES scale. (b) Jet response ratio as a function of the jet transverse momentum  $p_T^{\text{jet}}$  for jets with  $|\eta| < 1.2$ . The jets have been reconstructed with the anti- $k_t$  algorithm with  $R = 0.4$  and calibrated at the EM+JES scale. The response ratios obtained from the three *in situ* techniques are presented separately, with error bars indicating statistical and total uncertainties. The dark band represents the statistical and the light band represents the total uncertainty on the combination of the three methods; both figures from [74].

Figure 5.4(a) shows the relative contributions of the individual techniques in the statistical combination. At low  $p_T$ , the calibration is dominated by the Z+jet technique.

As this technique has uncertainties that are characteristic to the low- $p_T$  region, the residual calibration below  $p_T = 25$  GeV has been decoupled from the one at larger transverse momenta to prevent the low- $p_T$  uncertainties to influence the higher- $p_T$  ones through the combination. The contribution of the Z+jet events falls from about 90% at  $p_T^{\text{jet}} = 40$  GeV to about 50% at  $p_T^{\text{jet}} = 100$  GeV, where the  $\gamma$ +jet technique starts to dominate, until the multijet technique dominates from about  $p_T^{\text{jet}} = 600$  GeV on. From comparison with the jet transverse momenta in the  $\chi$ -distributions, it is observed that the dominant *in situ* methods in this analysis are the  $\gamma$ +jet and the multijet balance technique.

Figure 5.4(b) shows the combined residual JES calibration from the *in situ* methods, with statistical and systematic uncertainties. The systematic uncertainties on the jet energy scale from the *in situ* calibration will be discussed in more detail in the next section. Also shown are the individual response ratios for the Z+jet, the  $\gamma$ +jet and the multijet balance technique used in the combination. The results presented in figure 5.4(b) have been obtained for anti- $k_t$  jets with distance parameter  $R = 0.4$ , and they are compatible with those obtained for  $R = 0.6$  [74] as used in this thesis. Over the entire range in the jet transverse momentum, the response ratio in data is lower than in the Monte Carlo simulation. While this offset amounts to about 2% for jet  $p_T$  below 100 GeV, it is reduced to approximately 1% above jet transverse momenta above 200 GeV.

## 5.4. Jet energy scale uncertainty

The uncertainty on the jet energy scale is the dominant systematic uncertainty for the analysis presented in this thesis and is introduced in detail in this section.

### 5.4.1. Uncertainties from the *in situ* methods

The data-to-Monte Carlo response ratios measured with the *in situ* techniques are subject to statistical and systematic uncertainties. Examples are the systematic uncertainties arising from the Monte Carlo modelling in the Z+jet and in the  $\gamma$ +jet methods and the uncertainties due to the selection of the angle between the high- $p_T$  jet and the recoil system in the case of the multijet balance technique [74]. In total, 54 statistical and systematic uncertainty sources are taken into account for the Z+jet, the  $\gamma$ +jet and the multijet balance method. The components are considered as independent between each other and as fully correlated across the jet transverse momentum and pseudorapidity. For the final combination, the 54 uncertainty components arising from the different *in situ* methods are combined via pseudo-experiments in each  $p_T$ -bin. Uncertainty components associated with the pseudorapidity intercalibration technique depend on  $\eta$  and are therefore handled separately from the combination of the uncertainties from the Z+jet,  $\gamma$ +jet and multijet balance methods.

As can be inferred from figure 5.4(b), the JES uncertainty derived from the *in situ* methods is lowest for jets with  $p_T$  between about 55 and 500 GeV where it is smaller than 1%. The uncertainty for jets with  $p_T = 1$  TeV is approximately 1.5%. For larger jet transverse momenta, the JES uncertainty cannot be determined with the *in situ* methods since the number of events is too low. Instead, results from single-hadron response measurements are used in this high transverse momentum range.

#### 5.4.2. Combination with single hadron response measurements

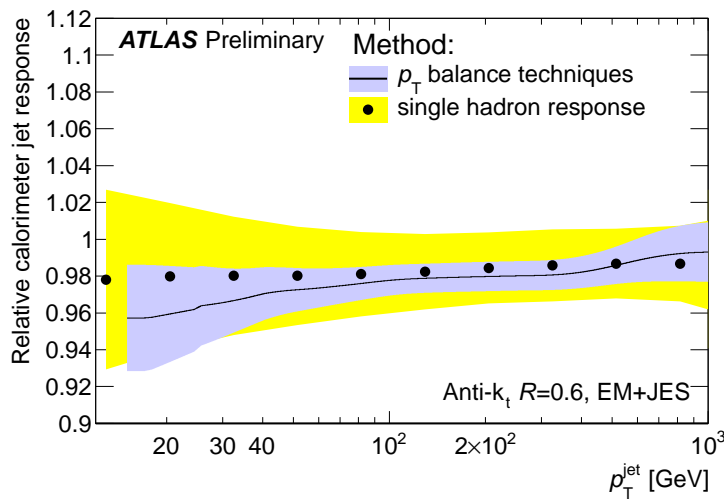


**Figure 5.5.** Jet response ratio obtained from single hadron response measurements (line) and from the *in situ* techniques (markers). The JES uncertainties are shown as a gray band for the former method and as yellow band for the latter; from [74].

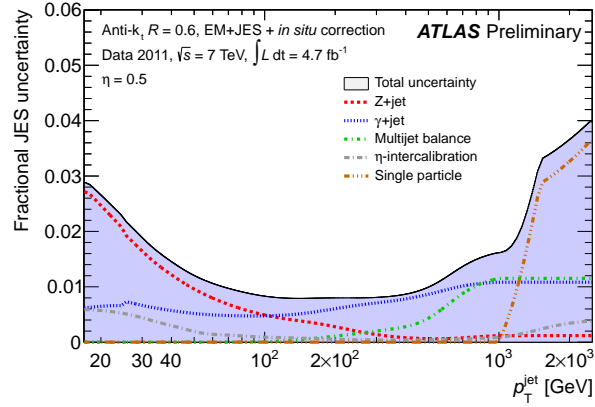
The residual JES calibration and the corresponding uncertainty obtained from the *in situ* methods has been compared to results from single hadron response measurements as discussed in [74] and the references therein. The idea of this technique is to describe a jet as the superposition of individual particles and derive the jet energy scale and its uncertainty from those of the constituents. Response measurements of pions in the momentum range between 20 and 350 GeV are available from the combined test-beam [73], and they are complemented in the lower momentum range,  $p < 20$  GeV, with measurements of single isolated hadrons in proton-proton collisions [114]. Figure 5.5 shows a comparison of the data-to-Monte Carlo response ratios and the corresponding uncertainties obtained from the *in situ* methods and from the single hadron response measurements. The results are consistent, and a negative offset of the response in data with respect to the one in the Monte Carlo simulation of approximately 2% is observed. Using the *in situ* calibration techniques, a significantly smaller JES uncertainty is achieved than with the single hadron response measurements.

For jets with  $p_T$  above 1 TeV, the number of events is too low for the *in situ* methods to be used, as was described above. Therefore, the JES uncertainty for these high transverse momenta is derived from the single hadron response measurements. More precisely, above 1 TeV, the total JES uncertainty is formally split into two components: The first component is given by the uncertainty from the *in situ* techniques fixed at their value at 1 TeV, and the second component, the *single particle* term, is defined by subtracting the first component in quadrature from the uncertainty from the single hadron response measurements. In this way, the magnitude of the total uncertainty above 1 TeV is equal to the uncertainty derived from the single hadron response measurements while the correlation between the uncertainties for jet transverse momenta below and above 1 TeV is partly retained. To allow for a continuous variation of the uncertainty, a linear interpolation between the results of the two methods is applied around 1 TeV. The treatment of the JES uncertainties for high jet transverse momenta has a major influence on the JES uncertainties in the analysis as will be discussed in chapter 8.

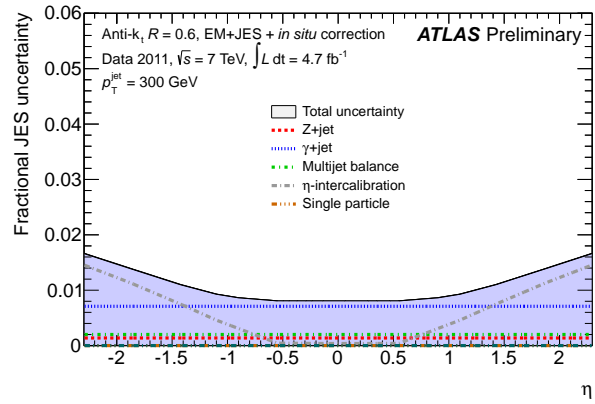
The relative JES uncertainty derived from the *in situ* methods and the single hadron response measurements is shown in figure 5.6(a) as a function of the jet transverse momentum for jets with  $\eta = 0.5$  and in figure 5.6(b) as a function of the jet pseudorapidity for jets with  $p_T = 300$  GeV. In addition to the total uncertainty, the individual contributions from the Z+jet, the  $\gamma$ +jet and the multijet balance methods are shown, as well as the ones from the pseudorapidity intercalibration and from the single hadron response measurements. For central jets, the uncertainty is lowest for transverse momenta between about 70 and 500 GeV where it amounts to approximately 1%. For lower  $p_T$  it rises to about 3% at  $p_T = 17$  GeV, and it rises to values of about 3.6% for jet transverse momenta of  $p_T = 2$  TeV. The strong rise of the uncertainties for jet transverse momenta above 1 TeV is due to the way the JES uncertainties are determined for these transverse momenta as described above. For jets with  $p_T = 300$  GeV, the uncertainty is smallest for central jets where it is lower than 1%. It rises to about 1.6% for jets with  $|\eta| = 2.3$ , due to the increasing uncertainty of the pseudorapidity intercalibration method with  $|\eta|$ . The  $\eta$ -dependence of the pseudorapidity intercalibration contribution to the JES uncertainty will be discussed in more detail in section 8.1.1 in the context of the evaluation of the JES uncertainties for this analysis.

### 5.4.3. Correlation of the uncertainties

Figure 5.7 shows the correlation between the JES uncertainties for anti- $k_t$  jets with  $R = 0.4$  across the range of jet transverse momenta, calculated from the full set of uncertainty components discussed in the above section. The JES uncertainty for jets with a transverse momentum of 100 GeV is almost 100% correlated with the uncertainty of jets with  $p_T = 70$  GeV. Any shift of the energy scale of jets at  $p_T = 100$  GeV would thus be accompanied by a relative shift of the same size for jets at 70 GeV. In contrast, the JES uncertainties for jets below  $p_T = 1$  TeV are only slightly correlated with those above  $p_T = 1$  TeV. This is due to the way the JES uncertainties are continued from the results obtained with the *in situ* techniques with the results from the single hadron



(a)



(b)

**Figure 5.6.** The relative JES uncertainty obtained from the *in situ* techniques and the single hadron response measurements for jets reconstructed with the anti- $k_t$  algorithm with  $R = 0.6$ : (a) presented as a function of the jet transverse momentum for jets with  $\eta = 0.5$  and (b) presented as a function of the jet pseudorapidity for jets with  $p_T = 300$  GeV; from [74].

response measurements towards the high- $p_T$  regime. It will become clear in the evaluation of the JES uncertainties for this analysis in section 8.1.1 that the correlations of the uncertainties are of great importance for the size of the final uncertainties in the analysis.

#### 5.4.4. Effective description of the uncertainty components from the *in situ* techniques

It is desirable to evaluate the JES uncertainty for the analysis in this thesis by the convolution of the individual uncertainty components with pseudo-experiments, as will be explained in detail in chapter 8. The *in situ* techniques alone already comprise 54 individual uncertainty components. Since the resulting total number of uncertainty

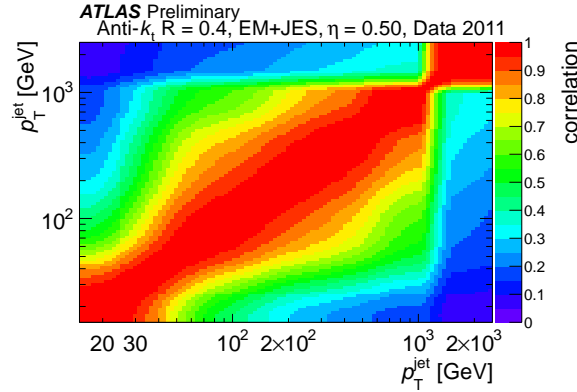


**Figure 5.7.** Bin-wise correlation between the jet energy scale (JES) uncertainties as a function of the transverse momentum of jets reconstructed with the anti- $k_t$  algorithm with distance parameter  $R = 0.4$  and calibrated with the EM+JES scheme; from [74].

components would be too large to be treated with pseudo-experiments, the number of components from the *in situ* methods is reduced in a way that preserves the total uncertainty and the correlation information [74].

A covariance matrix  $C^k$  is derived for every uncertainty source  $s^k$ . For each uncertainty component  $k$ , the entries  $C_{ij}^k = \rho_{ij}^k s_i^k s_j^k$  of the matrix denote the covariance between the uncertainties in the  $p_T$ -bins  $i$  and  $j$ . Since the uncertainty components are fully correlated across  $p_T$ ,  $\rho_{ij}^k$  is equal to one for all  $p_T$ -bins  $i$  and  $j$  and for all uncertainty sources  $s^k$ . Therefore, the entries of  $C^k$  can be written as  $C_{ij}^k = s_i^k s_j^k$ . The total covariance matrix  $C^{\text{tot}}$  is determined as the sum over the covariance matrices from the 54 uncertainty sources:

$$C^{\text{tot}} = \sum_{k=1}^{N_{\text{sources}}=54} C^k. \quad (5.6)$$

Since  $C^{\text{tot}}$  is symmetric, it may be diagonalised as

$$C^{\text{tot}} = S^T D S, \quad (5.7)$$

with a diagonal matrix  $D$  that contains the eigenvalues of  $C^{\text{tot}}$ , here denoted as  $\sigma_k^2$ , and an orthogonal matrix  $S$  that contains the eigenvectors  $V^k$ . Each vector  $\sigma_k^2 V^k$  represents a new effective uncertainty source. From equation 5.7, it follows that the entries of the total covariance matrix may be written as

$$C_{ij}^{\text{tot}} = \sum_{k=1}^{N_{\text{bins}}} \sigma_k^2 V_i^k V_j^k, \quad (5.8)$$

with  $N_{\text{bins}}$ , the number of  $p_T$ -bins.

It is possible to approximate the total covariance matrix with a smaller number  $N_{\text{eff}}$  of eigenvectors  $V^k$  corresponding to the largest eigenvalues  $\sigma_k^2$  by using

$$C_{ij}^{\text{tot}} \approx \sum_{k=1}^{N_{\text{eff}}} \sigma_k^2 V_i^k V_j^k + C', \quad (5.9)$$

with a residual uncertainty that is characterised by a covariance matrix  $C' \mathbb{1}$ . It is observed that for the current 54 uncertainty components from the *in situ* methods, a percent-level approximation of the total covariance matrix may be obtained by a selection of five effective components, plus the residual uncertainty component which is treated as uncorrelated in  $p_T$ . The strong reduction of the number of uncertainty components related to the *in situ* methods makes it possible to estimate the jet energy scale uncertainty with a feasible number of pseudo-experiments.

#### 5.4.5. Additional contributions to the jet energy scale uncertainty

Besides the JES uncertainty components described above, several other effects need to be taken into account. In the following, additional uncertainty components are introduced that are relevant for the analysis presented in this thesis.

The JES calibration and the corresponding uncertainty are derived with *in situ* methods that use Z+jet and  $\gamma$ +jet events. The jets in these events are mostly induced by high- $p_T$  quarks. It is therefore assumed that the JES for light quarks is determined correctly with the *in situ* techniques. An additional term, obtained by systematic Monte Carlo variations [74], is added to the JES uncertainties to account for the uncertainty on the response of gluon-initiated jets and on the fraction of gluon-initiated jets in the event sample. A more detailed discussion on the flavour composition uncertainty is presented in chapter 8 in the context of the JES uncertainties for this analysis.

The jets in the Monte Carlo-based calibration procedure are required to be isolated [74, 101]. An additional component is added to the JES uncertainty to take response differences between the data and the Monte Carlo simulation for non-isolated jets into account. The effect is studied with jets reconstructed from charged particle tracks that have been matched to jets from calorimeter energy depositions and compared between data and Monte Carlo simulations. The resulting uncertainty depends on the jet transverse momentum and on  $R_{\text{min}}$ , the minimal distance in  $(\eta \times \phi)$ -space to other calorimeter jets. It amounts to about 1-2% for jets with  $p_T$  below 100 GeV and with  $R_{\text{min}} = 0.7$  [113].

As described in section 5.2.1, the effect of pile-up is studied in Monte Carlo simulations, and an offset correction is applied to the jet transverse momenta as part of the calibration. The offset correction depends linearly on the number of primary vertices  $N_{pV}$  and the expected number of interactions per bunch crossing  $\mu$ . An uncertainty arises in the determination of the jet energy scale due to possible imperfections of the pile-up description in the Monte Carlo simulations. The effect is studied in data, by

comparing the jet  $p_T$  measured in the calorimeter with that of a jet reconstructed from charged particle tracks or with that of an isolated photon in prompt photon production. Both reference objects are expected to be insensitive to pile-up. For central jets with transverse momenta between 20 and 30 GeV, the uncertainties are smaller than 0.5% per reconstructed vertex for  $\mu = \mu^{\text{ref}}$ , and they are approximately 0.7% per interaction for jets in the same  $p_T$ -range and with  $N_{\text{PV}} = N_{\text{PV}}^{\text{ref}}$ . The uncertainty for central jets at higher transverse momentum is lower than 0.2% per reconstructed primary vertex and per additional interaction.

In total, the JES uncertainty components that were evaluated in the context of this analysis are the six effective components from the *in situ* methods and, in addition, one component that describes the uncertainties due to the pseudorapidity intercalibration, one component that corresponds to the uncertainty from single hadron measurements used at  $p_T > 1$  TeV, one component for the closure with respect to the *MC11b* Monte Carlo samples that were used to derive the calibration, one component for the uncertainty due to non-isolated jets, one component each for the jet flavour composition and the jet flavour response uncertainty, and two components for the in-time and out-of-time pile-up uncertainties. The Monte Carlo closure term is included by default but would only play a role for Monte Carlo samples that are, unlike the samples used in this analysis, from a different Monte Carlo production. The JES uncertainty for the analysis of the dijet angular distributions was evaluated by the convolution of these 14 uncertainty components, as will be described in chapter 8.



## 6. Event selection

Selection criteria are applied to the events in this analysis in order to ensure that only well-measured events comprising high-quality jets are used in the measurement of the dijet angular distributions. In addition, they serve to improve the sensitivity to phenomena beyond the Standard Model.

### 6.1. Overview of the event selection

The first part of this chapter summarises the event selection while selected topics will be explained further in section 6.2.

#### 6.1.1. Selection based on properties of the entire events

Here, the part of the event selection is presented that is based on general properties of the events, independent of the characteristics of individual jets.

##### **Good run list**

The data taking in ATLAS is organized in individual sessions called runs. Each run is further subdivided into so-called luminosity blocks, short time intervals of typically 1 to 2 minutes, characterized by stable beam and data taking conditions. After the data taking, quality criteria are assigned to each luminosity block in every run, in order to mark the detector components that were fully operational. For this analysis, the most important parts of the detector are the calorimeter and the inner detector. The time intervals of high-quality data are specified in the form of good run lists. For the analysis in this thesis, events are required to be in the `pro10-GoodRunList` [115].

##### **Trigger pre-selection**

Events passing different single inclusive jet triggers are used for the analysis of the angular distributions. The triggers differ in the required amount of the on-line calibrated transverse calorimeter jet energy. The thresholds of the triggers which are used in this

analysis are 75, 100, 180 and 240 GeV. The point of full efficiency may be different from these thresholds since a more refined calibration is applied off-line. In the event selection, the logical OR of all eligible triggers is applied already at an early stage to reduce the sample size. The trigger selection will be further discussed in section 6.2.4.

### Primary collision vertex

The events are required to contain a well-measured primary collision vertex [116]. In order to select the vertex from the hardest scatter against additional pile-up vertices, the primary collision vertex is defined as the one for which the sum of the squared transverse momenta of all associated charged particle tracks is the highest. In order for the event to be retained in the analysis, at least two tracks must be associated to the primary collision vertex.

### LAr data errors

A selection is applied to remove events in which the data from the liquid argon (LAr) calorimeter were corrupted by noise bursts or data integrity errors. The corresponding events were marked with an error flag. Only events where this error flag was set to zero are used in the analysis.

### 6.1.2. Selection based on jet properties

Jets are reconstructed from topological calorimeter clusters with the anti- $k_t$  algorithm with distance parameter  $R = 0.6$ . They are calibrated using Monte Carlo-based methods that are complemented with *in situ* techniques as discussed in chapter 5. The events are then selected based on the properties of these jets.

#### Two or more jets in the rapidity acceptance

All jets with rapidity  $|y_{\text{jet}}| < 4.4$  are accepted. Subsequently, events are required to contain at least two jets.

#### Jets from problematic calorimeter regions

To ensure that the dijet system is reconstructed from well-measured high- $p_T$  jets, further quality criteria are applied to the events. Events with jets that are reconstructed from energy deposits in calorimeter regions that impede a precise energy measurement are

rejected if the  $p_T$  of those jets is higher than 30% of the second highest jet  $p_T$  in the event. The identification of such jets will be discussed in section 6.2.1.

### Temporary LAr hardware problem

A part of the data taking was affected by a temporary defect of the liquid argon calorimeter readout, leading in particular to a pseudorapidity-dependent reduction of the jet response by 30% [117]. In order to retain as much of the data in the corresponding run range as possible while avoiding a bias in the  $\chi$ -distributions due to pseudorapidity-dependent selections, events are rejected based only on the  $\phi$  coordinates of the leading jets in  $p_T$ . The detector region defined by  $-0.88 < \phi_{\text{jet}} < -0.50$  covers the affected part of the calorimeter and is used to define the event selection. In the run range where the readout problem was present ( $180614 \leq \text{run} < 185353$ ), events are retained only if neither the azimuthal angle of the leading nor of the subleading jet is in this calorimeter region. Furthermore, events are also rejected if any other jet with a  $p_T$  of more than 30% of the subleading jet  $p_T$  points to this region in  $\phi$ . As this selection only depends on the azimuthal angle of the jets, it does not influence the final  $\chi$ -distributions, as will be discussed in section 6.2.2.

### Fake jets

Further quality criteria are applied to the individual jets. Fake jets can be reconstructed from calorimeter electronics noise, beam-induced backgrounds or cosmic rays. Events are only kept in the analysis if neither the leading nor the subleading jet is a fake jet. The exact definition and identification of fake jets will be specified in section 6.2.1.

### Kinematic selection

The leading jet in  $p_T$  must have a transverse momentum above 100 GeV, and the subleading jet must have a transverse momentum above 50 GeV. The events are required to have  $y^* \equiv 0.5 \cdot |y_1 - y_2| < 0.5 \cdot \ln 30$  and  $y_B \equiv 0.5 \cdot |y_1 + y_2| < 1.1$ , with  $y_1$  and  $y_2$  denoting the rapidities of the leading and subleading jet. Events must have a dijet mass  $m_{jj}$  above 800 GeV. The kinematic selection will be motivated and further discussed in section 6.2.3.

The  $\chi$ -distributions are measured in five dijet invariant mass bins. All events within one mass bin are required to have passed the same inclusive jet trigger. The correspondence between the dijet mass bins and the triggers is reported in table 6.3 and will be motivated in section 6.2.4.

The number of events after each step of the event selection is presented in table 6.1. In the last five rows, the number of events does not decrease monotonically with the dijet invariant mass due to the different prescaling conditions of the triggers.

### 6.1.3. Additional event selection in the simulation

An additional selection is applied to correct the pile-up simulation in the Monte Carlo samples. As discussed in chapter 4, the simulation of the QCD processes is performed in ranges of  $\hat{p}_T$ , the transverse momentum of the hard subprocess. To obtain the full prediction for any observable, the contributions have thus to be weighted according to the cross sections of the  $\hat{p}_T$ -ranges before they are combined. Pile-up is simulated by subsequently adding minimum bias events to the events that comprise the hard interaction. In extremely rare cases, the additional interactions result in jets with larger  $p_T$  than those from the nominal hard scattering, causing wrong event weights. For example, in a jet  $p_T$ -spectrum, these events would be assigned to the high- $p_T$  part of the distribution and nevertheless receive the large event weight corresponding to the low  $\hat{p}_T$ -value of their nominal hard interaction, resulting in a spike in the spectrum. To correct for the effect, the transverse momenta of the reconstructed jets are compared with those of the jets before the detector simulation (*truth jets*), and the events are required to fulfil  $\overline{p}_T < 2 \cdot p_{T,\text{truth}}^{\text{max}}$  and  $\overline{p}_T < 2.5 \cdot \hat{p}_T$ . Here,  $\overline{p}_T$  denotes the average  $p_T$  of the two jets in the reconstructed dijet system, and  $p_{T,\text{truth}}^{\text{max}}$  is the largest  $p_T$  of all truth jets from the nominal hard interaction. This selection only affects events with jet transverse momenta below approximately 200 GeV and at a rate of roughly 1 in 2 million events in this analysis.

**Table 6.1.** The number of events after each step of the event selection. The numbers are obtained from data and correspond to the full integrated luminosity of  $\mathcal{L} = 4.8 \text{ fb}^{-1}$ . The input volume of the experimental and simulated data has been greatly reduced by a preparatory step which required the dijet invariant mass to be larger than 700 GeV. The number of experimental data events is thereby reduced from about 485 million by a factor of roughly 16 to about 30 million. The number of events at this level defines the starting point for the event counts presented in this table. The last column specifies whether a selection is applied on data and/or on Monte Carlo events. In order to be accepted in one of the dijet invariant mass bins specified in the last five rows, the events in data are required to have passed the selected trigger for that bin as discussed in section 6.2.4.

Description	Number of data events	Applied on
Input data set	29255783	Data/MC
Good run list	26974246	Data
Trigger pre-selection	7620356	Data/MC
Primary collision vertex	7619752	Data
LAr data errors	7589729	Data
Jet multiplicity in the acceptance	7589729	Data/MC
Jets in problematic calorimeter regions	7589148	Data/MC
Temporary LAr hardware problem	7271126	Data/MC
Fake jets	7269162	Data/MC
$p_T$ requirements on the dijet system	7264933	Data/MC
$y^*$ requirement on the dijet system	6691880	Data/MC
$y_B$ requirement on the dijet system	5874309	Data/MC
$m_{jj}$ requirement on the dijet system	4225200	Data/MC
Hard pile-up subtraction		MC
$800 < m_{jj} < 1200 \text{ GeV}$	13642	Data/MC
$1200 < m_{jj} < 1600 \text{ GeV}$	4132	Data/MC
$1600 < m_{jj} < 2000 \text{ GeV}$	35250	Data/MC
$2000 < m_{jj} < 2600 \text{ GeV}$	28464	Data/MC
$2600 < m_{jj} < 7000 \text{ GeV}$	2706	Data/MC

## 6.2. Detailed description of the event selection

The most important aspects of the event selection are discussed in this section.

### 6.2.1. Selection of well-measured jets

As a jet measurement, this analysis is in principle sensitive to possible imperfections in the jet identification and reconstruction process. Care has thus been taken to perform the analysis with only well-measured jets. The selection follows a common ATLAS procedure [118] and is explained below.

A jet may be reconstructed in calorimeter areas where the energy measurement is imprecise. Two cases are considered [119]: First, jets are rejected if more than half of their energy originates from calorimeter cells that have been labelled as problematic and whose energy has been extrapolated from neighbouring cells. The selection is evaluated at the electromagnetic energy scale which has been introduced in chapter 5. Second, jets are rejected if more than half of their energy originates from the scintillators located in the gap between the barrel and the end-caps of the tile calorimeter. Both of these types of jets are labelled *ugly* in the ATLAS nomenclature.

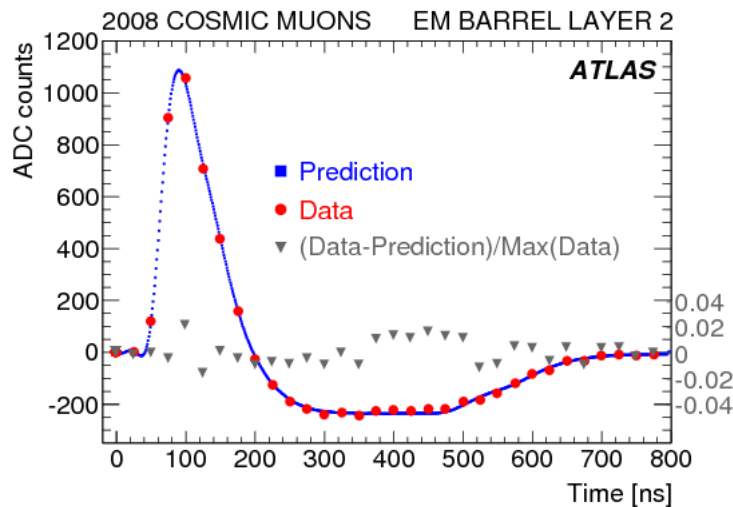


**Figure 6.1.** Pulse shape of a cell in the barrel part of the electromagnetic calorimeter. The data (red) have been obtained from cosmic muons, and they are compared with results from Monte Carlo simulations (blue). Also shown is the relative difference between the simulation and the measurement (grey); from [120].

Jets can also be accidentally reconstructed from calorimeter noise, beam-induced background and cosmic rays. These fake jets are called *bad* in the ATLAS nomenclature. Noise in the calorimeter electronics can resemble real energy deposits and may thus

trigger the reconstruction of fake jets. The two main sources of calorimeter noise are coherent noise in the electromagnetic calorimeter (EM) and sporadic noise bursts in the hadronic end-cap calorimeter (HEC). In the latter case, a small number of noisy cells contributes a significant fraction to the jet energy. A way to detect fake jets from calorimeter noise is to exploit the ionisation pulse shape in the calorimeter cells since showers from real particles lead to different pulse shapes than the ones induced by noise. The analogue calorimeter signals are amplified and shaped before they are sampled at the LHC bunch crossing frequency. Typically five samples are read out per cell. The amplitude of these samples is then digitised by analogue-to-digital converters (ADCs) such that the signal is characterised by a set of five ADC counts [67, 120].

On the cell level, a pulse quality  $Q_{\text{cell}}^{\text{LAr}}$  may be defined by the squared difference of the measured and predicted pulse shapes, summed over the five time samples of the signal,

$$Q_{\text{cell}}^{\text{LAr}} = \sum_{j=1}^5 (s_j - A g_j^{\text{phys}})^2. \quad (6.1)$$

Here,  $s_j$  denotes the amplitude of sample  $j$ , measured in ADC counts. It is compared with the normalised ionisation shape  $g_j^{\text{phys}}$ , taken from a simulation of the electronics response, and scaled with  $A$ , the amplitude of the signal. Figure 6.1 shows the comparison of a simulated pulse shape with one measured in cosmic muon events in a cell of the liquid argon electromagnetic calorimeter.

Jet contain the energy contribution from several calorimeter cells, and thus the pulse shape quality at the cell-level can be used to define a quality criterion for entire jets. A bad pulse shape on the cell-level is defined by  $Q_{\text{cell}}^{\text{LAr}} > 4000$ , the fraction of HEC cells with bad pulse shapes in a jet is denoted by  $f_Q^{\text{HEC}}$ , and the fraction of LAr calorimeter cells with bad pulse shapes in a jet is defined by  $f_Q^{\text{LAr}}$ . Furthermore, an average jet quality  $\langle Q \rangle$  can be defined from the weighted average of the pulse qualities of all constituent cells in a jet.  $\langle Q \rangle$  is normalised to be between 0 and 1. Since the quality as defined here is a measure of the discrepancy between predicted and observed pulse shapes, a small quality  $\langle Q \rangle$  corresponds to well-measured jets and vice-versa.

Fake jets from coherent noise have a large average jet quality  $\langle Q \rangle$ , high  $f_Q^{\text{LAr}}$  and a large fraction  $f^{\text{EM}}$  of their energy deposited in the electromagnetic calorimeter. In comparison, jets from sporadic noise bursts are characterised by a large  $\langle Q \rangle$ , high  $f_Q^{\text{HEC}}$  and a large fraction  $f_{\text{HEC}}$  of their energy deposited in the hadronic end-cap calorimeter. Furthermore, cells adjacent to cells with sporadic noise bursts measure negative energies  $E_{\text{neg}}$  induced by the capacitive coupling in the calorimeter.

Apart from calorimeter electronics noise, fake jets can arise from beam-induced background and cosmic rays. Since these types of background both stem from particles that do not originate from the main collision, the resulting fake jets may be detected by exploiting the spatial energy distribution in the detector. As presented in section 3.2.1, the inner detector provides tracking information in the region with  $|\eta| < 2$ . This information may be used to define the charged fraction  $f_{\text{ch}}$  of a jet in that region as the scalar

sum of the momenta of the tracks pointing to the jet, divided by the jet transverse momentum measured in the calorimeter. A small charged fraction is typical for a fake jet from cosmic rays or beam-induced background. Furthermore, a small electromagnetic fraction  $f_{EM}$  or a large maximum energy fraction  $f_{max}$  in a single layer of the calorimeter are characteristic for fake jets from these backgrounds.

Following the need for different performance goals, several sets of jet selection criteria have been defined by the ATLAS collaboration based on the quantities introduced above [118]. According to the strength of the applied selections, they have been categorised under the names *Tight*, *Medium*, *Loose* and *Looser*. The last one is the default recommendation for jet analyses in ATLAS, and it is used in this work. This selection has been designed to provide a significant reduction of the number of fake jets while keeping an efficiency of more than 99.8% for jets with transverse momenta above  $p_T^{\text{jet}} > 20$  GeV. The corresponding selection criteria are listed in table 6.2. In the ATLAS nomenclature, *good jets* are those jets that are neither bad nor ugly. In the analysis presented here, care is taken to only use events with a well-measured dijet system reconstructed from good constituent jets.

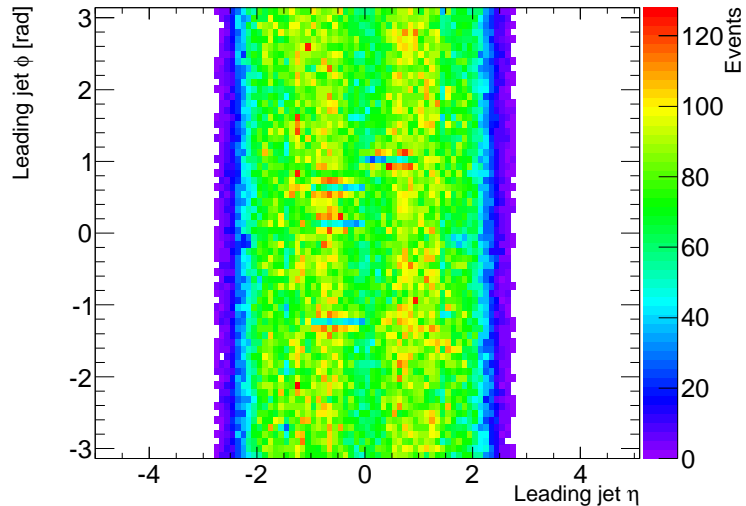
**Table 6.2.** The ATLAS criteria [118] for the removal of fake jets from cosmic rays and calorimeter noise used in this analysis.

Description	Criteria
HEC spikes	$(f_{\text{HEC}} > 0.5 \text{ and }  f_Q^{\text{HEC}}  > 0.5 \text{ and } \langle Q \rangle > 0.8)$ or $( E_{\text{neg}} > 60 \text{ GeV})$
Coherent noise	$(f_{EM} > 0.95 \text{ and } f_Q^{\text{LAr}} > 0.8 \text{ and } \langle Q \rangle > 0.8 \text{ and }  \eta  < 2.8)$
Non-collision background	$(f_{max} > 0.99 \text{ and }  \eta  < 2)$ or $(f_{EM} < 0.05 \text{ and } f_{ch} < 0.05 \text{ and }  \eta  < 2)$ or $(f_{EM} < 0.05 \text{ and }  \eta  \geq 2)$

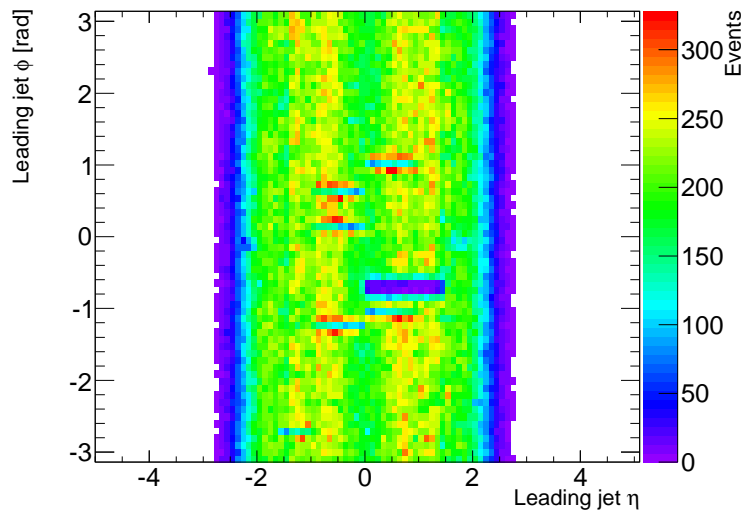
### 6.2.2. Temporary LAr hardware problem

Starting in April 2011, a temporary hardware failure in a subsystem of the liquid argon (LAr) calorimeter readout led to problems in the measurement and reconstruction of jets. The hardware problem occurred in the front-end boards in one front-end crate of the electromagnetic barrel calorimeter as described in section 3.2.2. The jet response was reduced by about 30% in the affected area, which covered approximately  $[0, 1.4] \times [-0.74, -0.64]$  in  $(\eta \times \phi)$  [117]. The problematic hardware could be recovered during a technical stop in July 2011, leaving the range of runs with  $180614 \leq \text{run} < 185353$  affected. These runs correspond to the data taking periods E to H and an integrated

luminosity of about  $1 \text{ fb}^{-1}$ . A list of all data taking periods and the corresponding run ranges has been given in section 3.3.



(a)



(b)

**Figure 6.2.** Distribution of the azimuthal angle  $\phi$  and pseudorapidity  $\eta$  of the leading jet in  $p_T$  in events after the analysis selection. Shown are events observed in data, in the data periods B and D (a) and in the data periods E to G (b); also appeared in [89].

The effect of the LAr hardware problem is seen drastically in the spatial distributions of jets. Figure 6.2(a) shows the distribution of the azimuthal angle and the pseudorapidity of the leading jet in events after the analysis selection for the data taking periods B and D, i. e. before the hardware problem occurred. For comparison, figure 6.2(b) shows

the same quantity, but for the data taking periods E to G, i.e. in the time where the hardware problem was present. The region affected by the hardware failure is clearly visible as a reduction of the jet count from about 200 to about 50 in the affected area. The minimum for jet pseudorapidities  $\eta \approx 0$  is due to the event selection. In addition, the effect of failed components of the tile calorimeter is visible as a slight alteration of the jet count in form of small stripes, as e.g. around 1 rad in  $\phi$  and between 0 and 1 in  $\eta$ . These small hardware effects are taken into account in the Monte Carlo simulation.

The hardware problem in the liquid argon calorimeter introduces an asymmetric feature in the jet spatial distributions. Since the  $\chi$ -analysis is by design sensitive to jet rapidities and pseudorapidities, it is of paramount importance to avoid the introduction of an  $\eta$ -dependent bias. A Monte Carlo study was conducted to assess the impact of the hardware failure on the analysis and to establish a fast and reliable solution. In the Monte Carlo study, the situation in data was mimicked by reducing the response of all jets within the affected area by 30%. Subsequently, three strategies were evaluated and compared: first, to refrain from any additional selection, second, to remove events with high- $p_T$  jets pointing to the affected area, or third, to remove events with high- $p_T$  jets that have the same  $\phi$  coordinate as the affected area. The second strategy was tested by requiring that neither the leading, nor the subleading jet, nor any other jet with  $p_T$  larger than 30% of the subleading jet  $p_T$  points to the affected area. The third strategy was studied by requiring that neither the leading, nor the subleading jet, nor any other jet with  $p_T$  larger than 30% of the subleading jet  $p_T$  coincides with the affected area in the azimuthal angle. This strategy is motivated by the aim to avoid an  $\eta$ -dependent bias in the  $\chi$ -distributions.

To assess the effect of the three different strategies, the  $\chi$ -distributions were calculated for each scenario, and the ratio with respect to the distributions in the default situation, without the hardware problem, was determined. The results are shown in figure 6.3. They are very similar for all dijet invariant mass bins. When no additional event selection is applied, the distributions with the hardware failure lie about 2.5% below the nominal distributions at low  $\chi$ -values and about 1% higher at high  $\chi$ -values. When events are rejected based on the  $(\eta \times \phi)$ -coordinates of the high- $p_T$  jets, the distributions with the hardware failure lie about 3.5% below the nominal distributions at low  $\chi$ -values and about 1.5% higher at high  $\chi$ -values. Finally, when events are rejected based on the  $\phi$ -coordinate of the high- $p_T$  jets, the distributions with the hardware failure lie about 1.5% above the nominal distributions at low  $\chi$ -values and about 0.5% lower at high  $\chi$ -values. Within the statistical uncertainties, the distributions agree with the nominal ones when this strategy is used.

While the third strategy leads to a larger reduction of the number of events as compared with the other two, it leads to the  $\chi$ -spectra with the smallest shape distortion. It was thus decided to adopt this strategy to address the hardware problem in the LAR calorimeter. At a later stage, the hardware failure was also included in the official Monte Carlo simulation. For the analysis, it was, however, decided to keep the above-

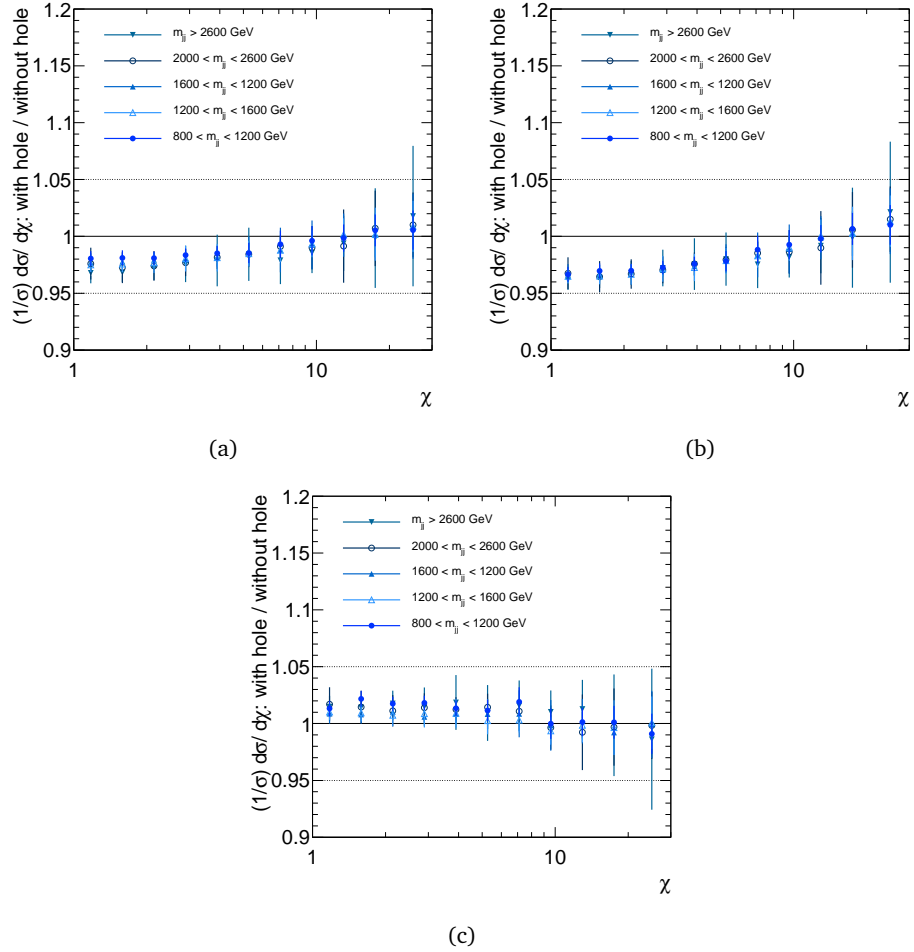


**Figure 6.3.** Evaluation of different strategies for the treatment of the hardware failure in the LAr calorimeter. Shown are the ratios in the Monte Carlo simulation, of the normalised, differential  $\chi$ -distributions after artificially reducing the jet response in the affected area by 30% with respect to the nominal distributions. The ratios are presented in the five dijet invariant mass bins of the analysis and with statistical uncertainties. (a) No additional selection is applied. (b) Events are rejected based on the  $(\eta \times \phi)$ -coordinates of the highest- $p_T$  jets. (c) Events are rejected based on the  $\phi$ -coordinates of the highest- $p_T$  jets.

mentioned strategy in order to retain the physically-motivated flat shapes of the  $\chi$ -distributions in QCD.

In conclusion, the selection as discussed above is applied to data and Monte Carlo events in the run range  $180614 \leq \text{run} < 185353$ , corresponding to the data taking periods E to H with an integrated luminosity of approximately  $1 \text{ fb}^{-1}$ .

### 6.2.3. Kinematic selection

In order to increase the sensitivity of the analysis to physics beyond the Standard Model, additional kinematic selections are applied to the events.

The events are required to contain two high- $p_T$  jets. The leading jet must have a transverse momentum above 100 GeV, and the subleading jet must have a transverse momentum above 50 GeV. These selections are asymmetric to facilitate the compensation of real and virtual contributions in the NLO correction, as motivated e. g. in [121]. The exact values of these cuts haven been chosen for consistency with the Standard Model dijet measurement [122]. The  $p_T$ -cuts only remove very few events in practice, since the requirement on the dijet invariant mass of 800 GeV leads to an intrinsic condition on the  $p_T$  of the leading jets: A basic estimation shows that for the dominating dijet topologies with  $m_{jj}^2 \approx 4p_T^2 \cosh^2 y^*$ , the minimal transverse momentum, reached for dijet events with  $\chi$ -values close to 30, is about  $p_T^{\min} \approx 0.18 \cdot m_{jj}^{\min}$ . For example, in the lowest dijet mass bin, the minimal mass is 800 GeV, resulting in minimal transverse momenta of about 140 GeV. This will also be seen in section 7.2 where the distributions of kinematic variables are discussed. For dijet masses above 2 TeV, the minimal  $p_T$  in the dijet case is about  $0.18 \cdot 2 \text{ TeV} \approx 353 \text{ GeV}$ . The few events that are removed by the  $p_T$ -cuts are events with non-dijet topologies, in which e. g. a hard jet with  $p_T$  above 100 GeV recoils against two jets with transverse momenta below 50 GeV.

The contribution of possible signals from new phenomena is primarily expected at low  $\chi$ -values as shown in chapter 2. Therefore, the analysis starts at the smallest possible value,  $\chi_{\min} = 1$ . The boundaries of the  $\chi$ -bins were optimised for efficiency and purity in previous analyses. They are defined as  $\chi_n = \exp(0.3 \cdot n)$ , with  $n \in 0, \dots, 10$ , and the upper boundary of the last  $\chi$ -bin is set to 30. The upper bound has been chosen to facilitate the comparison with earlier dijet publications [123]. It is implemented as a cut on  $y^* \equiv \frac{1}{2}(y_1 - y_2)$ , with  $|y^*|$  being required to be smaller than  $\frac{1}{2} \log 30 \approx 1.7$ .

An additional improvement of the sensitivity is provided by a selection on the boost of the dijet system, expressed in terms of  $y_B = \frac{1}{2}(y_1 + y_2)$ . It has been shown in section 1.2.2 that the differential dijet cross section for initial protons is given by a convolution of the partonic cross section and the PDFs. The contribution of signals from physics beyond the Standard Model is expected to modify the partonic cross section  $\hat{\sigma}$ , which is smeared out by the convolution with the PDFs. In order to optimise the sensitivity to new phenomena, it is thus desirable to restrict the longitudinal momentum ranges ( $x_{1,2}$ ) of the partons. Since  $m_{jj}^2 = x_1 x_2 s$  and  $y_B = \frac{1}{2} \ln(\frac{x_1}{x_2})$ , a cut on  $x_1$  and  $x_2$  may be achieved by restricting  $y_B$  in every dijet invariant mass bin. In the analysis,  $|y_B| < 1.1$  is chosen. This selection restricts the momentum ranges of the partons as desired while retaining enough statistics for the analysis. Together with the  $y^*$ -cut, the selection of the boost of the dijet system constrains the rapidities of the two leading jets to within  $|y_{1,2}| \lesssim 2.8$ , consistent with the rapidity acceptance in the dijet resonance analysis [2]. In this well-understood central detector region, the jet energy scale uncertainties are

in general smaller than in the forward region as discussed in chapter 5. The rapidity selection for the two leading jets is illustrated in figure 6.4.

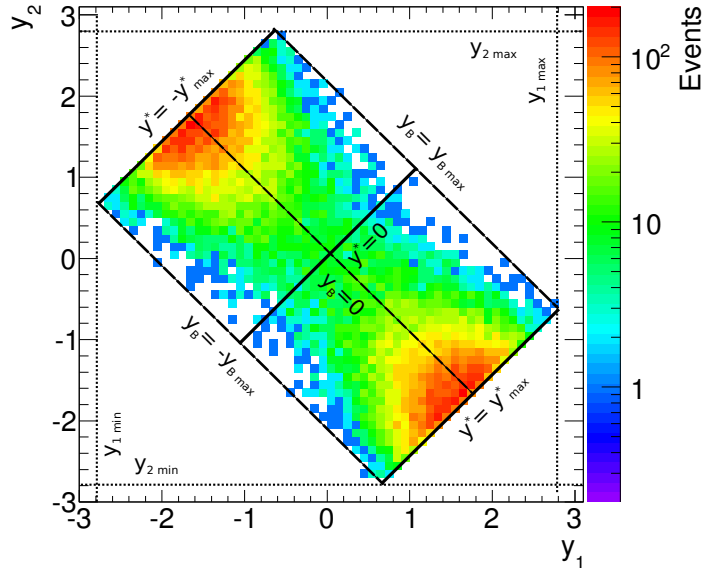


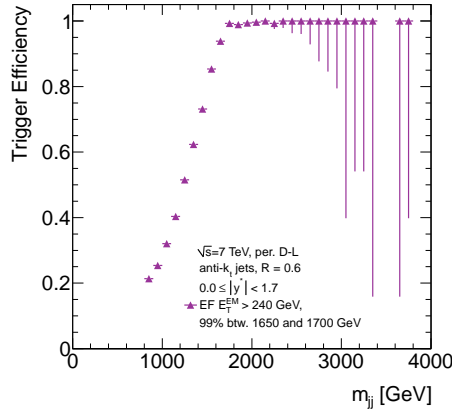
**Figure 6.4.** Illustration of the rapidity selection for the two leading jets. The events have been measured in data and have passed the analysis selection. Their dijet invariant mass is between 2000 and 7000 GeV.

#### 6.2.4. Trigger

The dijet angular analysis presented in this thesis investigates normalised, differential  $\chi$ -distributions in bins of the dijet invariant mass. Every data event in the final distributions is required to have passed a trigger, and it is important that the trigger is fully efficient in the respective dijet mass bin. The trigger efficiency is particularly important to avoid shape distortions in the  $\chi$ -distributions. Different  $\chi$ -values in the same dijet mass bin correspond to different jet  $p_T$ , as will be shown e. g. in figure 7.4. Therefore,  $p_T$ -dependent trigger inefficiencies would propagate into  $\chi$ -dependent inefficiencies. The triggers used in this analysis are inclusive single jet triggers, with the trigger chains specified in table 6.3. Details about the ATLAS trigger scheme may be found in section 3.2.5.

The trigger efficiencies have been established using a *bootstrapping method* that deduces the efficiency of a higher-threshold jet trigger from a fully efficient lower-threshold one. The efficiencies are defined as per-event efficiencies by the fraction of events that pass both the higher-threshold and the lower-threshold trigger, divided by the number of events that pass the lower-threshold trigger. To facilitate the definition of the dijet invariant mass bins for the analysis, the trigger efficiencies are evaluated as a function

of the dijet invariant mass. All but the highest-threshold trigger were prescaled during the data taking, with varying prescale values over time. This leads to a reduced effective luminosity in the corresponding dijet mass bins. In order to obtain sufficient statistics for the evaluation of the trigger efficiencies, the trigger decision before the application of prescales was recalculated offline.



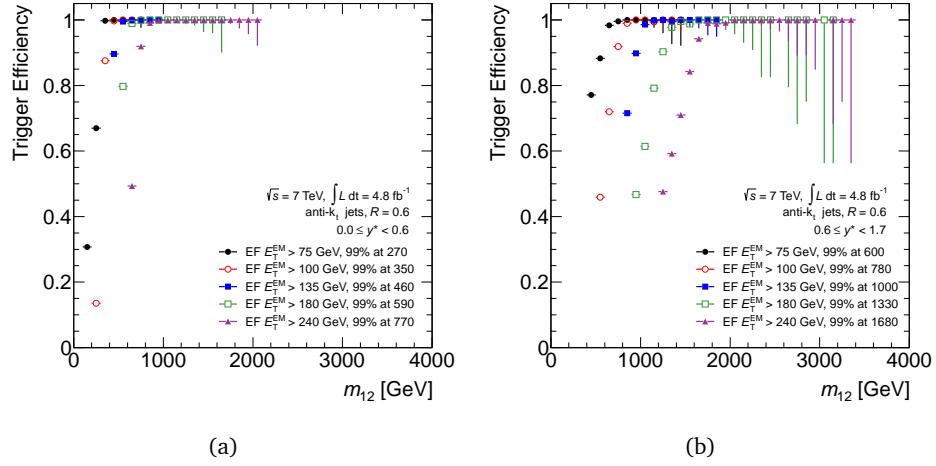
**Figure 6.5.** The efficiency of the EF-j240-a4tc-EFFS trigger. The efficiency is shown as a function of the dijet invariant mass and with statistical uncertainties; also appeared in [89].

Figure 6.5 shows the efficiency of the EF-j240-a4tc-EFFS trigger for events with  $|y^*|$  between 0 and 1.7. The efficiency has been obtained after the analysis selection and is reported with statistical uncertainties as a function of the dijet invariant mass. Also reported is the dijet invariant mass at which the efficiency reaches 99%. Likewise, the efficiencies of all high-level triggers used in the  $\chi$ -analysis are reported in figure 6.6, separately for events with  $|y^*| < 0.6$  in figure 6.6(a) and for events with  $0.6 \leq |y^*| < 1.7$  in figure 6.6(b). The triggers demonstrate the expected turn-on behaviour. The 99% efficiency points are higher in the case of the events with larger  $y^*$ -values as compared to the events with smaller  $y^*$ -values since for every dijet invariant mass, events with higher  $y^*$ -values comprise jets with lower  $p_T$  and are thus less likely to pass a trigger

**Table 6.3.** The dijet invariant mass bins in the  $\chi$ -analysis and the corresponding trigger chains.

$m_{jj}$ [GeV]	Event filter	Level-2	Level-1
800 - 1200	EF-j75-a4tc-EFFS	L2-j70	L1-J50
1200 - 1600	EF-j100-a4tc-EFFS	L2-j95	L1-J75
1600 - 2000	EF-j180-a4tc-EFFS	L2-j95	L1-J75
2000 - 2600	EF-j240-a4tc-EFFS	L2-j95	L1-J75
2600 - 7000	EF-j240-a4tc-EFFS	L2-j95	L1-J75

with a given  $p_T$ -threshold. The trigger efficiency points are therefore determined from the former events.



**Figure 6.6.** Trigger efficiencies as a function of the dijet invariant mass. Shown are the efficiencies for events after the analysis selection, with statistical uncertainties. The triggers with thresholds of 75, 100, 180 and 240 GeV for the on-line calibrated transverse energy are used in the analysis. (a) The efficiencies for events with  $|y^*| < 0.6$ . (b) The efficiencies for events with  $0.6 \leq |y^*| < 1.7$ ; both figures from [89].

Following the determination of the trigger efficiencies, the dijet invariant mass bins of the analysis are defined by the following boundaries: 800, 1200, 1600, 2000, 2600 and 7000 GeV. The lower boundaries are chosen close to the efficiency points of the triggers to profit from the higher statistics in the steeply falling dijet invariant mass spectrum. The definitions include a safety margin to ensure that the events are in the trigger plateau region. Taking the expected number of data events into account, an additional high-mass search bin is defined for dijet masses above  $m_{jj} = 2600$  GeV to increase the sensitivity to new phenomena [124]. The resulting dijet invariant mass bins are exclusive (i. e. non-overlapping), and the events in each bin are required to have passed one trigger as summarised in table 6.3.



## 7. Data verification

This chapter presents a selection of verification and validation studies that have been performed to spot potential problems and to improve the understanding of the data and Monte Carlo events which pass the event selection.

### 7.1. Event yields

The event yield, defined as the number of events per run after the analysis selection divided by the luminosity of the run, provides valuable information about the stability of the data taking conditions. Any unexpected deviation from a flat behaviour would indicate potential problems in the data taking and would need to be addressed to avoid a bias in the final distributions.

Figure 7.1 shows the event yields for the five dijet invariant mass bins used in the analysis. In the mass bin  $1600 < m_{jj} < 2000$  GeV, the larger error bars in the second half of the data taking period are due to the prescaling of the trigger that has been used for this mass bin. The mass bins  $2000 < m_{jj} < 2600$  GeV and  $2600 < m_{jj} < 7000$  GeV each contain one entry with large uncertainty. The corresponding runs are 182013 for the second-highest mass bin and 180212 for the highest. In both cases, the runs had relatively low luminosities of the order of  $100 \text{ nb}^{-1}$ .

The event yield is about 12% lower in the range  $180614 \leq \text{run} < 185353$  in every dijet invariant mass bin. This is the run range affected by the LAr calorimeter failure discussed in section 6.2.2. The yield reduction is consistent with the reduced acceptance: The events are rejected if either the leading or the subleading jet in  $p_T$  or any jet with  $p_T > 0.3 \cdot p_T^2$  points to the region  $-0.88 < \phi_{\text{jet}} < -0.50$ , which amounts to about 6% of  $2\pi$ . Here,  $p_T^2$  denotes the transverse momentum of the subleading jet. Due to the dominating back-to-back topology of the events, about 12% of the events are rejected in the corresponding run range. Overall, the yield is approximately constant in all mass bins. It was thus concluded that the data taking conditions have been stable over time.

## 7. Data verification

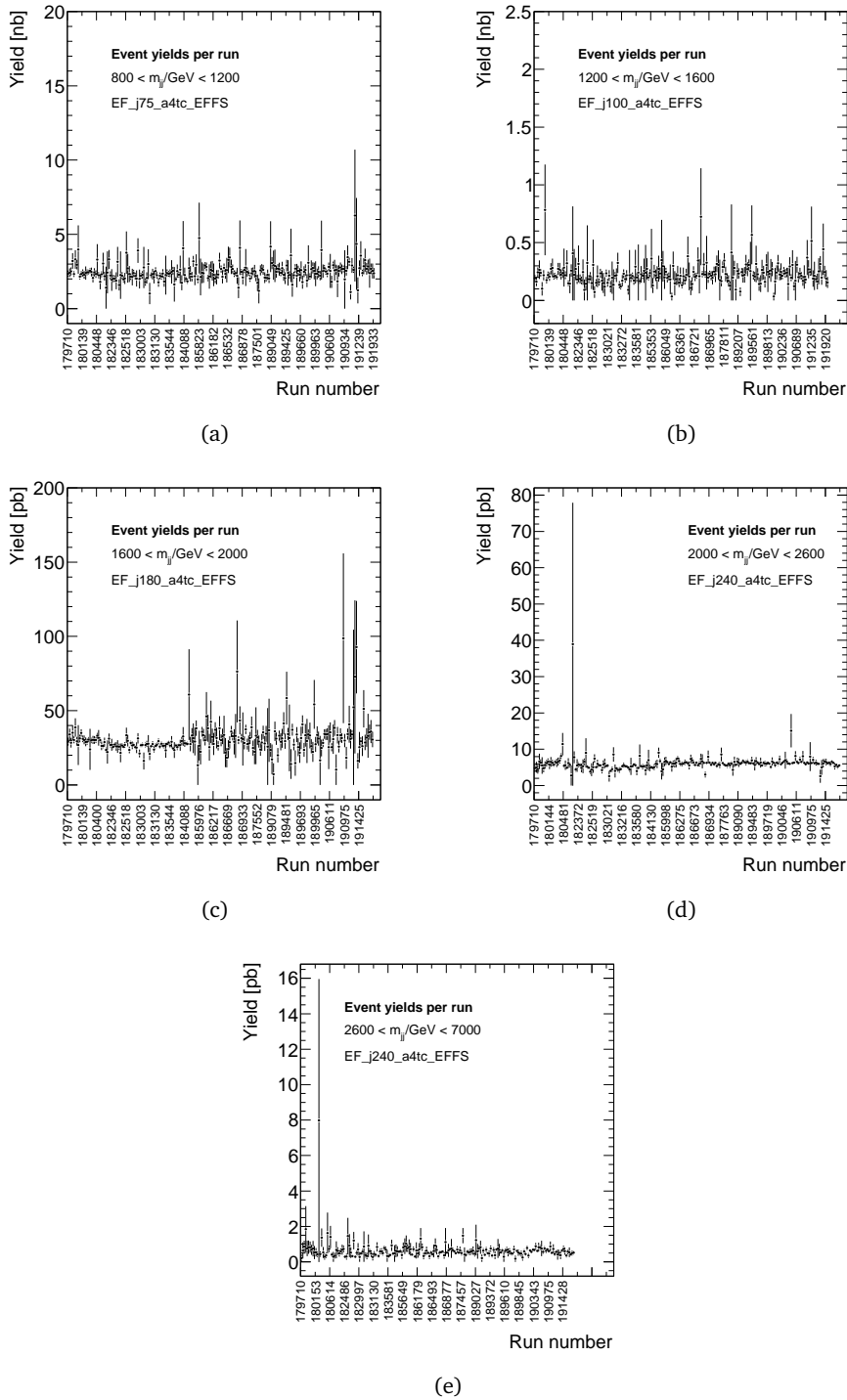


**Figure 7.1.** The event yields after the analysis selection for events measured in data, reported with statistical uncertainties. Shown are the distributions for events with dijet masses (a) between 800 and 1200 GeV, (b) between 1200 and 1600 GeV, (c) between 1600 and 2000 GeV, (d) between 2000 and 2600 GeV and (e) between 2600 and 7000 GeV; updated version of the figures which appeared in [89].

## 7.2. Kinematic distributions

Figures 7.2 to 7.5 present the distributions of several kinematic quantities after the event selection. Shown are the transverse momentum, the rapidity and the azimuthal angle of the leading and the subleading jets for events with dijet invariant masses above 2000 GeV, corresponding to the union of events in the two highest dijet mass bins of the analysis. Both the data and the Monte Carlo QCD prediction are shown with statistical uncertainties. Also reported are the ratios of the data with respect to the Monte Carlo QCD prediction.

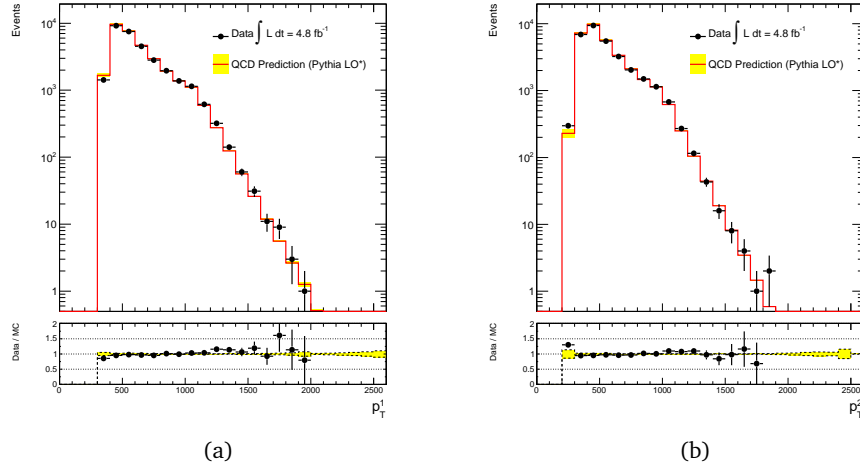


**Figure 7.2.** The transverse momentum distributions of the leading (a) and the subleading jet (b) after the event selection for the analysis. Shown are the distributions for events with dijet invariant masses above 2000 GeV. The Monte Carlo QCD predictions are weighted to the integrated luminosity of the data. In the upper panels, the QCD predictions (solid, red lines) and the data (circles) are shown with statistical uncertainties. The lower panels show the ratio of the data with respect to the Monte Carlo predictions with statistical uncertainties; both figures also appeared in [89].

The distributions of the leading and the subleading jet  $p_T$  shown in figure 7.2 have the expected steeply falling shape. In particular, the minimum transverse momentum values are in agreement with the basic estimation described in section 6.2.3: For dijet invariant masses above 2000 GeV, the smallest expected jet  $p_T$  in events with ideal dijet topologies is expected to be approximately equal for the leading and the subleading jet and lie in the vicinity of  $0.18 \times 2000 \text{ GeV} \approx 353 \text{ GeV}$ .

The distributions of the leading and the subleading jet rapidities presented in figure 7.3 show the double-peak structure expected at high dijet invariant masses: Using again the leading-order approximation  $m_{jj}^2 \approx 4p_T^2 \cosh^2 y^*$  and estimating the dijet invariant mass of the events with  $m_{jj} \approx 2000 \text{ GeV}$  and the transverse momenta with  $p_T^1 \approx p_T^2 \approx 500 \text{ GeV}$  as justified by figure 7.2, it follows that  $y^* \approx \pm 1.32$  for the dijet system. Assuming mostly low boosts  $y_B \approx 0$ ,  $y_{1,2} \approx \pm 1.32$  can be deduced also for the individual jets,

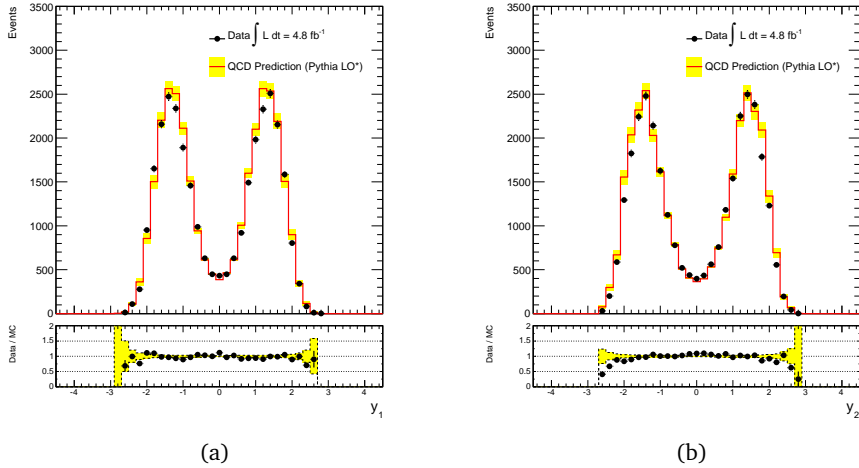


**Figure 7.3.** The rapidity distributions of the leading (a) and the subleading jet (b) after the event selection for the analysis. Shown are the distributions for events with dijet invariant masses above 2000 GeV. The Monte Carlo QCD predictions are weighted to the integrated luminosity of the data. In the upper panels, the QCD predictions (solid, red lines) and the data (circles) are shown with statistical uncertainties. The lower panels show the ratio of the data with respect to the Monte Carlo predictions with statistical uncertainties; both figures also appeared in [89].

consistent with the distributions shown in figure 7.3. The rapidities of both leading jets are restricted to  $|y_{1,2}| < 2.8$  by the selections applied to  $y^*$  and  $y_B$  as discussed in section 6.2.3.

Figure 7.4 shows the two-dimensional distributions of transverse momenta versus rapidities of the two leading jets in events in the Monte Carlo simulation for the lowest and the highest dijet invariant mass bins used in the analysis. Results for the intermediate mass bins are collected in appendix A.1. For each mass bin, the distributions are presented separately for events with  $\chi$  below and above 3.32. It is observed that events with small  $\chi$  correspond to events with a dijet system of two jets with high  $p_T$  and small rapidity and vice versa.

The azimuthal distributions of the leading jets shown in figure 7.5 are flat as expected from the symmetric detector acceptance. The event selection introduced to mitigate the effect of the temporary LAr hardware error described in section 6.2.2, is visible as small dips in the  $\phi$  distributions around  $-0.74 < \phi_{\text{jet}} < -0.64$  and shifted by  $\pi$  to about  $2.4 < \phi_{\text{jet}} < 2.5$ , due to the dominating dijet topologies.

In conclusion, the study shows that the distributions of the kinematic variables are qualitatively and quantitatively well understood in the data and in the Monte Carlo simulation. In addition, it confirms that the Monte Carlo QCD prediction provides a satisfying description of the data.

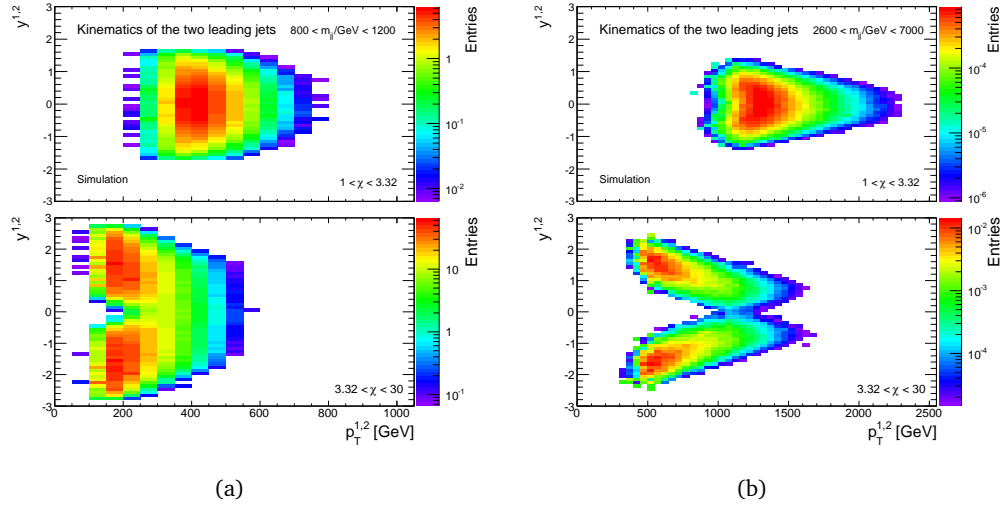


**Figure 7.4.** Distribution of the leading and the subleading jet transverse momentum  $p_T^{1,2}$  versus rapidity  $y^{1,2}$  for events in the lowest (a) and the highest (b) dijet invariant mass bins of the analysis, obtained from Monte Carlo simulation. The upper figures show events with  $\chi < 3.32$  whereas the lower plots show events with  $3.32 < \chi < 30$ ; both figures also appeared in [89].

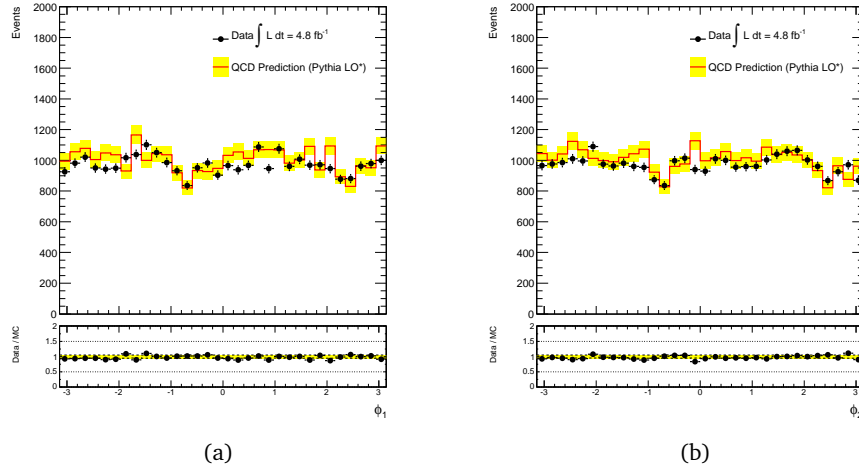


**Figure 7.5.** The distributions of the azimuthal angle of the leading (a) and the subleading jet (b) after the event selection for the analysis. Shown are the distributions for events with dijet invariant masses above 2000 GeV. The Monte Carlo QCD predictions are weighted to the integrated luminosity of the data. In the upper panels, the QCD predictions (solid, red lines) and the data (circles) are shown with statistical uncertainties. The lower panels show the ratio of the data with respect to the Monte Carlo predictions with statistical uncertainties; both figures also appeared in [89].

### 7.3. Pile-up reweighting

Due to the high luminosity of the LHC, the energy measurement in the ATLAS calorimeter is affected by additional interactions that overlay the primary hard scatter in the same bunch crossing as well as by energy depositions in other bunch crossings occurring during the integration time of the liquid argon calorimeter. The magnitude of both effects correlates with  $\mu$ , the mean number of interaction per bunch crossing.  $\mu$  may be determined as [92]

$$\mu = \frac{L \times \sigma_{\text{inel}}}{N_{\text{bunch}} \times f_{\text{LHC}}}, \quad (7.1)$$

from the average instantaneous luminosity  $L$  over a time interval  $\Delta t$ , the total inelastic  $pp$  cross section  $\sigma_{\text{inel}} = 71.5 \text{ mb}$ , the number of colliding bunches  $N_{\text{bunch}}$  in the LHC and the revolution frequency  $f_{\text{LHC}}$  in the LHC.  $f_{\text{LHC}}$  is approximately 11 kHz. As a result of the changing luminosity conditions and the different bunch filling patterns of the LHC over the year, the distribution of  $\mu$  is in general different from one data period to another.

Figure 7.6(a) shows the evolution of the maximum of  $\mu$  as a function of the day in 2011. For example, run 180664, recorded on May 11th, 2011, in period E, had an instantaneous luminosity range from 761 to  $788 \times 10^{30} \text{ cm}^{-2}\text{s}^{-1}$  and 700 colliding bunches, corresponding to  $\mu \approx 7$ . In comparison, run 189610, recorded on September 11th, 2011, in period I, had an instantaneous luminosity range from 2163 to  $2603 \times 10^{30} \text{ cm}^{-2}\text{s}^{-1}$  and 1317 colliding bunches, corresponding to  $\mu \approx 11.5$ . After a technical stop in September 2011, the beam size at the interaction point was reduced, and the mean value of  $\mu$  consequently increased from roughly 6.3 in the first half to about 11.6 in the second half of the 2011 dataset. This is shown in figure 7.6(b). A measure for the size of the beam at the interaction point is  $\beta^*$ , the distance from the interaction point at which the beam has twice the width of that at the interaction point.  $\beta^*$  was reduced from 1.5 to 1.0 m after the technical stop.

At the time when the Monte Carlo samples used in the analysis were generated, the distributions of  $\mu$  in the various data periods could not be foreseen in detail, and Monte Carlo samples with educated estimates of the later data conditions were produced. Furthermore, in the final data set, the relative contribution of any given data period to the total integrated luminosity, i. e. the percentage of the total number of events that was recorded in that period, depends on the evolution of the trigger prescales. More precisely, since a given trigger records more data in times where its prescale is low than in times where it has a high prescale, the relative contribution of the different pile-up conditions depends on the corresponding trigger prescale settings. In the Monte Carlo samples, a certain a-priori estimate of the relative contribution of the different data periods is made.

In order to obtain a good matching between the  $\mu$ -distributions in data and the Monte Carlo simulation, the Monte Carlo events are reweighted for the analysis. Following ATLAS recommendations [126], the relative luminosity contributions of the Monte

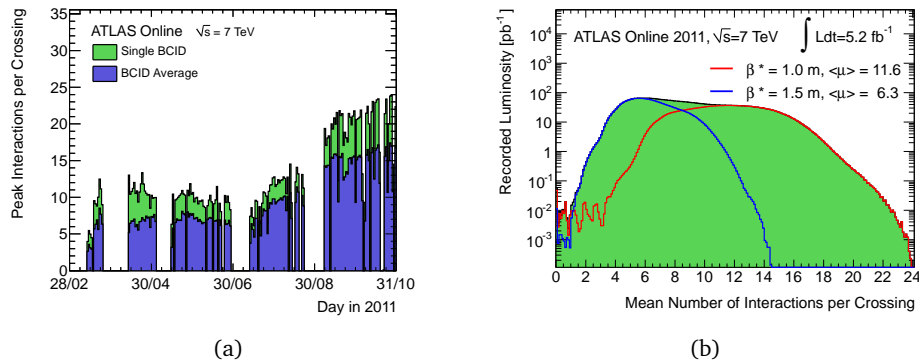


**Figure 7.6.** The evolution of the mean number of interactions per bunch crossing over the year. (a) The maximum average number of interactions per bunch crossing  $\mu_{\text{max}}$  as a function of the day in 2011. The maximum among all bunch crossings is shown in green, and the maximum averaged over all bunch crossings is shown in blue. (b) The average number of interactions per bunch crossing, weighted by the luminosity. Shown are the distributions for  $\beta^* = 1.5 \text{ m}$  (blue line, before the technical stop in September 2011), for  $\beta^* = 1.0 \text{ m}$  (red line, after the technical stop) and the sum (green area); both figures from [125].

Carlo samples with different pile-up conditions are first matched to the ones in data. Second, the relative weight of the  $\mu$ -values in the Monte Carlo simulation are matched to those in data for every period.

Figure 7.7 shows the distributions of  $\mu$  in the five dijet invariant mass bins that are used in the analysis after the event selection. The distributions in the Monte Carlo simulation before and after the reweighting are compared to the distribution in data. The events have passed different triggers depending on the dijet mass bin. The triggers were prescaled differently during the year. For example, the trigger that is used for the mass bin  $1600 < m_{jj} < 2000 \text{ GeV}$  was strongly prescaled in the second half of the year, and thus the data in this mass bin were mostly recorded in conditions with a mean  $\langle \mu \rangle$  around 6. On the other hand, the trigger that is used for the two highest mass bins,  $2000 < m_{jj} < 2600 \text{ GeV}$  and  $2600 < m_{jj} < 7000 \text{ GeV}$ , was not prescaled. Therefore, the  $\mu$ -distributions in the data of these two dijet mass bins contain both the early component with mean  $\mu$ -values around six and the later component with higher mean  $\mu$ -values of twelve and more. The study confirms that, following the pile-up reweighting, the  $\mu$ -distribution in the Monte Carlo simulation provides a good description of the  $\mu$ -distribution in the data.

## 7. Data verification

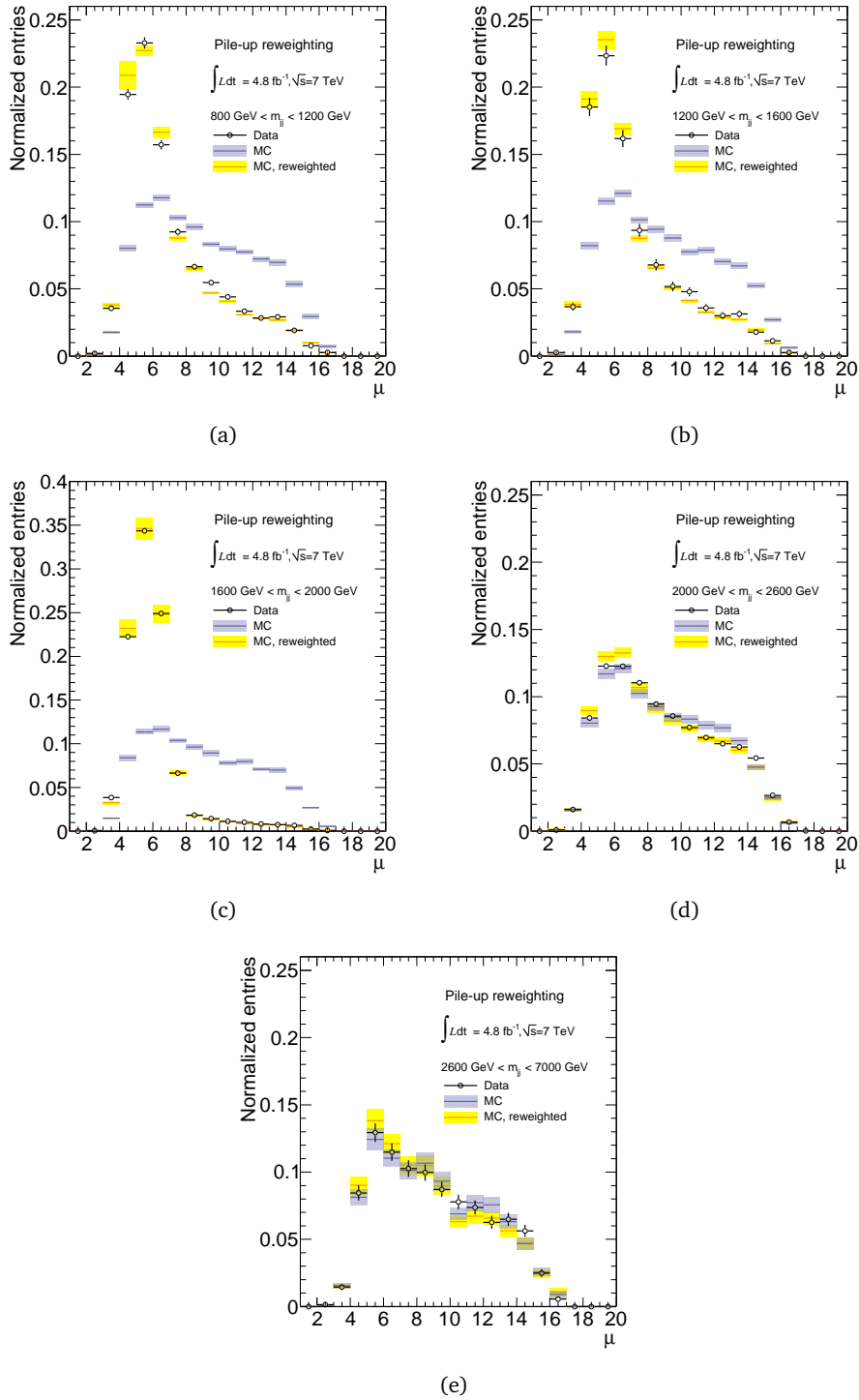


**Figure 7.7.** The distribution of the average number of interactions per bunch crossing  $\mu$ , shown for the QCD prediction before (solid, blue line) and after (solid, orange line) the pile-up reweighting, with bands denoting the statistical uncertainties. The data points (open circles) are shown with statistical uncertainties. The distributions are presented for events with dijet invariant masses (a) between 800 and 1200 GeV, (b) between 1200 and 1600 GeV, (c) between 1600 and 2000 GeV, (d) between 2000 and 2600 GeV and (e) between 2600 and 7000 GeV; also appeared in [89].

## 7.4. Residual pile-up effects

As described in section 5.2.1, pile-up effects are already taken into account during the jet calibration procedure. Furthermore, the average number of interactions per bunch crossing  $\mu$  is well described in the Monte Carlo simulation after the reweighting as shown in the previous section. The analysis presented in this thesis uses high- $p_T$  jets and is thus expected to be relatively robust against pile-up effects. The following two sections present studies that have been performed in order to establish the validity of this assumption.

### 7.4.1. In-time pile-up

Due to the high luminosity at the LHC, several proton collisions may occur in the same bunch crossing. These *in-time pile-up* interactions affect the energy measurement of jets from the primary hard scatter. As mentioned in section 3.2.1, the timing resolution of the inner detector allows to assign the correct bunch crossing ID to tracks and vertices. The number of reconstructed primary vertices may thus be used to quantify the amount of in-time pile-up interactions in an event. As discussed in [92], the transverse momentum of anti- $k_t$  jets with distance parameter  $R = 0.6$  in the central calorimeter region is increased on average by 850 MeV for every additional reconstructed primary vertex. A correction to the jet  $p_T$  for in-time pile-up effects is applied during the jet calibration procedure as described in section 5.2.1.

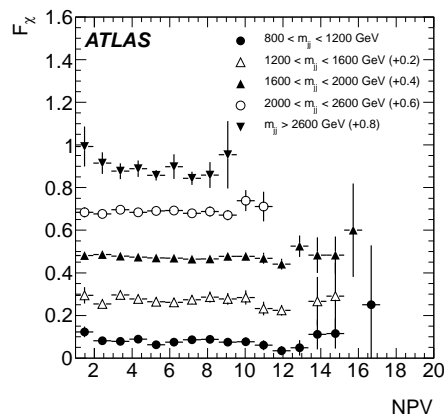


**Figure 7.8.**  $F_\chi$  as a function of the number of reconstructed primary vertices NPV. Shown are the distributions from data in the five dijet invariant mass bins of the analysis, with statistical uncertainties. Different offsets have been applied for the visualisation; from [2].

A study has been conducted to ensure that no residual in-time pile-up effects influence the measurement of the  $\chi$ -distributions in the analysis. To this end, the shape quantity  $F_\chi$  has been investigated in the dijet invariant mass bins of the  $\chi$ -analysis.  $F_\chi$  is defined

as the fraction of the number of events  $N_{\text{central}}$  with  $|y^*| < 0.6$ , corresponding to  $\chi < 3.32$ , with respect to the total number of events  $N_{\text{total}}$  with  $\chi < 30$  as a function of the dijet invariant mass,

$$F_\chi(m_{jj}) = dN_{\text{central}}(m_{jj})/dN_{\text{total}}(m_{jj}). \quad (7.2)$$

The single-number quantity  $F_\chi$  describes the shape of the  $\chi$ -spectra and can be studied conveniently as a function of the number of primary vertices.  $F_\chi$  may also be used as an observable to search for new phenomena as done e. g. in [2]. Figure 7.8 shows  $F_\chi$  in the five dijet invariant mass bins of the analysis, with statistical uncertainties. No significant dependence on the number of primary vertices is observed. It has thus been concluded that the analysis is not affected by in-time pile-up.

#### 7.4.2. Out-of-time pile-up

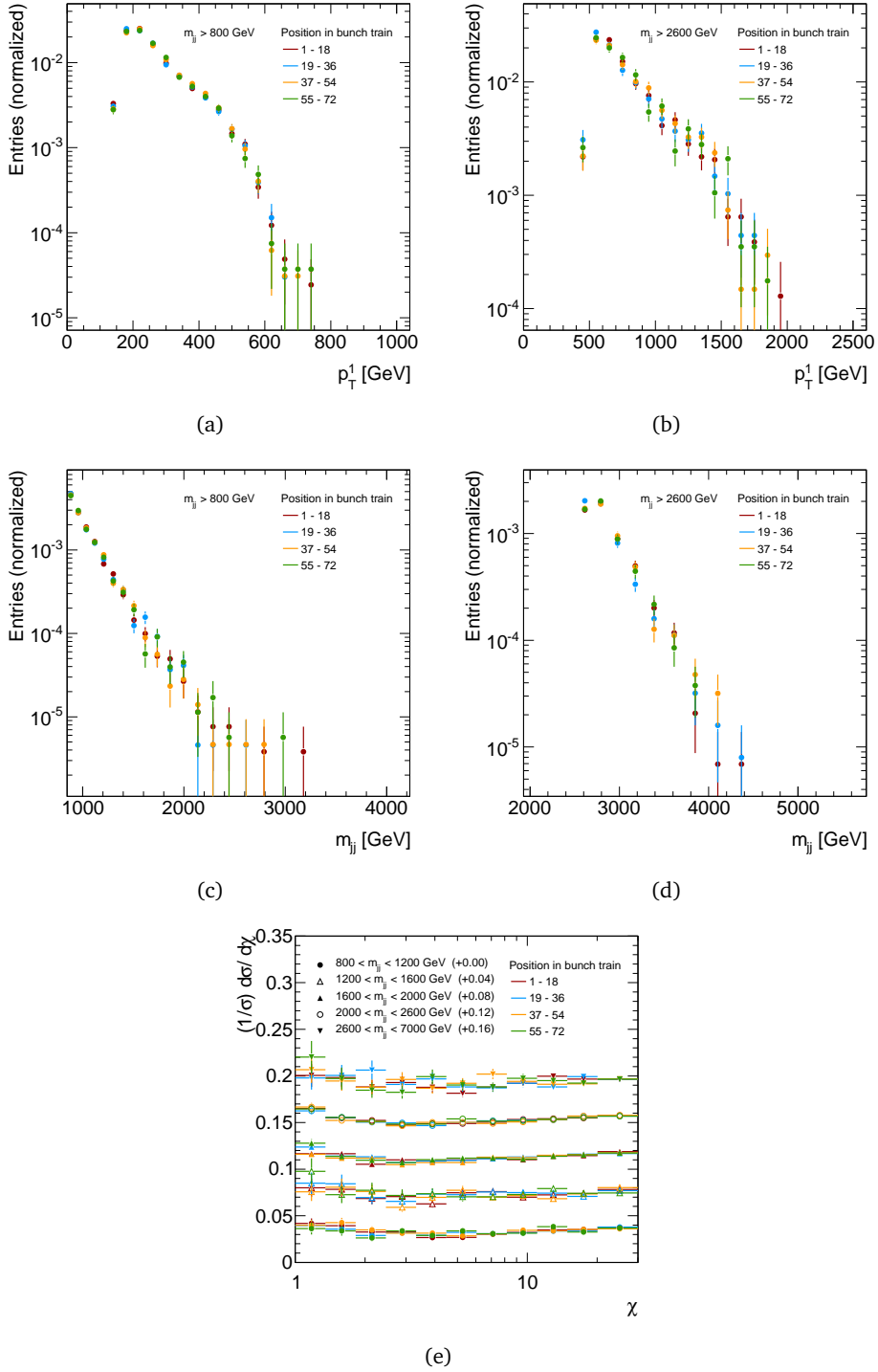
In addition to the effect of in-time pile-up, the energy deposits from collisions in other bunch crossings can affect the jet measurement. This process, called *out-of-time pile-up*, leads to an average increase in the jet transverse momentum of about 210 MeV for every additional interaction for anti- $k_t$  jets with  $R = 0.6$  in the central calorimeter region as shown in [92]. Based on the results of these studies and in parallel to the procedure undertaken for in-time pile-up, a correction for out-of-time pile-up effects is applied in the jet calibration. A study of the dependence of the event properties on the event position in the LHC bunch trains has been performed to ensure that there is no residual influence of out-of-time pile-up effects on the analysis. The results for different observables in the  $\chi$ -analysis are summarized below.

Figure 7.9 shows the distributions of the transverse momentum  $p_T^1$  of the leading jet and the dijet invariant mass for events in the data with dijet masses above 800 GeV and above 2600 GeV. Distributions with lower dijet mass thresholds may be found in appendix A.2. The spectra are shown in four broad bins of the bunch train position and are presented with statistical uncertainties. To allow for a shape comparison between the samples that correspond to different bunch positions and contain in general very different numbers of events, all spectra have been normalised to unit area. The  $p_T^1$  and  $m_{jj}$  distributions for the different bunch group positions are compatible among each other within the uncertainties for all dijet invariant mass bins. Figure 7.9(e) presents the normalised, differential spectra of  $\chi$  in the five dijet mass bins used in the analysis for different positions in the bunch trains. The distributions have been measured in data and are presented with statistical uncertainties. The  $\chi$ -spectra for the different bunch train positions are compatible within the uncertainties for all five dijet invariant mass bins.

Additional information may be gained by studying the mean values of distributions of quantities of interest for the analysis as a function of the exact position in the bunch trains. Figure 7.10 shows the mean values of  $p_T^1$  and  $\chi$  in data as a function of the position in the bunch trains for the five dijet invariant mass bins of the analysis. Also

shown are constant fits to the data points. Both  $\hat{p}_T^1$  and  $\hat{\chi}$  show no dependence on the position in the bunch trains.

$F_\chi$  is used here again to establish the robustness of the shape of the  $\chi$ -distributions against out-of-time pile-up effects. Figure 7.11 shows  $F_\chi$  in the five dijet invariant mass bins of the analysis as a function of the position in the bunch trains. As in the case of the other spectra, the distributions have been measured in data and are presented with statistical uncertainties. Also shown are constant fits to the data.  $F_\chi$ , and therefore the shape of the  $\chi$ -spectra, is independent of the position in the bunch trains. In conclusion, the study confirms the expectation that the angular distributions are not affected by out-of-time pile-up.



**Figure 7.9.** The distribution of several kinematic observables for different positions in the bunch trains. Shown are events after the analysis selection, measured in data and presented with statistical uncertainties: the transverse momentum of the leading jet for events with dijet invariant mass above 800 GeV (a) and above 2600 GeV (b), the dijet invariant mass above 800 GeV (c) and above 2600 GeV (d) and the normalised, differential  $\chi$ -distributions (e), to which different offsets have been applied for the visualisation. All distributions have been normalised to unit area; figure (e) also appeared in [89].

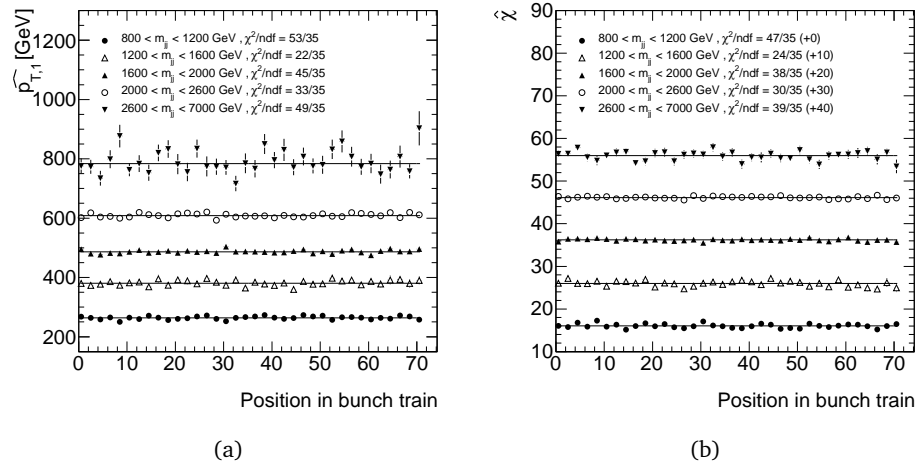


**Figure 7.10.** Distribution mean values of the transverse momentum of the leading jet  $p_{T,1}^1$  (a) and  $\chi$  (b) in the five dijet invariant mass bins of the analysis. Offsets have been applied to the  $\chi$  distributions for the visualisation. The distributions have been measured in data (markers) and are shown with statistical uncertainties, as a function of the position in the bunch trains. Also shown are constant fits to the distributions (solid lines), together with the reduced  $\chi^2$ .

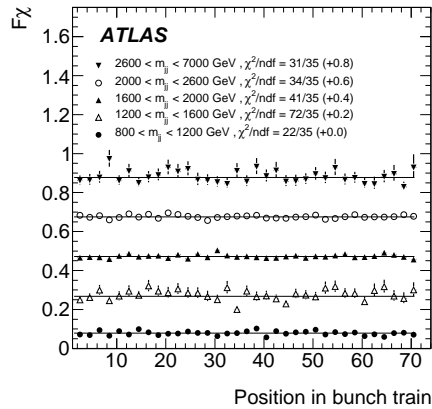


**Figure 7.11.**  $F_\chi$  as a function of the position in the bunch trains for the five dijet invariant mass bins of the  $\chi$ -analysis. The distributions have been measured in data (markers) and are shown with statistical uncertainties. Also shown are constant fits to the distributions (solid lines), together with the reduced  $\chi^2$ ; also appeared in [2].

## 7.5. Events with high- $p_T$ jets

In this section, the events that contained the jets with the largest transverse momenta in the analysis are discussed. The jet with the highest  $p_T$  was recorded on April 22nd, 2011, in event 41086080 in run 180144. The event is depicted in figure 7.12. The leading jet in the event had a transverse momentum of  $p_T^1 = 1994$  GeV, while the sub-leading jet had a transverse momentum of  $p_T^2 = 1815$  GeV. The invariant mass of the dijet system was  $m_{jj} = 3827$  GeV. The dijet topology of the event is reflected in the similarity of the  $p_T$  of the two leading jets and also by the azimuthal opening angle between them,  $\Delta\phi = 3.12$  rad, corresponding to an almost-perfect back-to-back topology. Both jets were very central, with  $y_1 = -0.02$  and  $y_2 = 0.16$ . The corresponding value of  $y^*$  was  $-0.09$ , and  $\chi$  was  $1.2$ , close to the minimum of  $\chi_{\min} = 1$ .

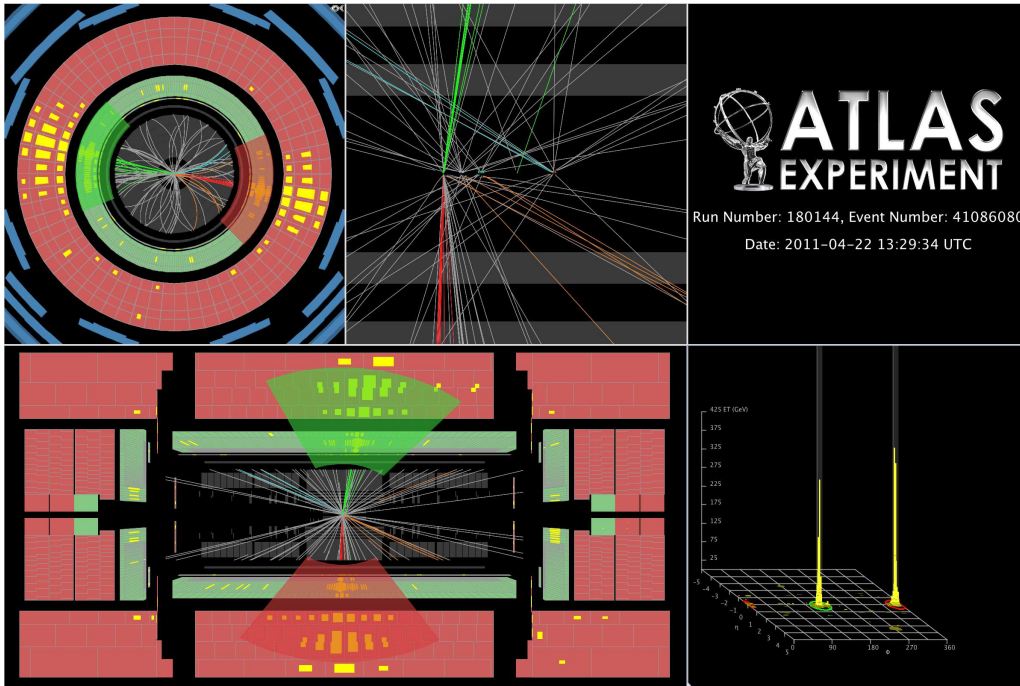


**Figure 7.12.** The event that contained the jet with the highest  $p_T$  in the analysis. In this event, the leading jet had a transverse momentum of  $p_T^1 = 1994$  GeV, and the sub-leading jet had a transverse momentum of  $p_T^2 = 1815$  GeV. The invariant mass of the dijet system was  $m_{jj} = 3827$  GeV. Only tracks with  $p_T^{\text{track}} > 500$  MeV are displayed. The event was recorded on April 22nd, 2011.

The dijet system was also characterised by a very low boost,  $y_B = 0.07$ , reflected in the almost back-to-back topology visible in the  $\rho z$ -view, at the bottom-left of figure 7.12. Applying a LO approximation [9], the longitudinal momentum fractions of the two colliding partons may be estimated as  $x_1 = x_T \exp(y_B) \cosh y^*$  and  $x_2 = x_T \exp(-y_B) \cosh y^*$ . With  $x_T = 2p_T / \sqrt{s}$  and  $p_T \approx (p_T^1 + p_T^2) / 2$ , it follows that  $x_1 \approx 0.29$  and  $x_2 \approx 0.27$ .

**Table 7.1.** The events that contained the jets with the highest  $p_T$  in the analysis.

$p_T^1$ [GeV]	$p_T^2$ [GeV]	$m_{jj}$ [GeV]	$\chi$	Run	Event
1994	1815	3827	1.2	180144	41086080
1892	1763	3728	1.5	183081	29591437
1861	1836	4049	2.3	179938	12054480
1817	1602	3431	1.1	186877	32207511

Table 7.1 provides an overview of the kinematic characteristics of the four events in the analysis in which the leading jet had the largest transverse momenta. All four events are characterised by a dijet system with approximately similar transverse momenta in the leading and the subleading jet and a small  $\chi$ -value. In addition, the dijet invariant mass was larger than 3400 GeV for all four events. Event displays of the remaining events mentioned in table 7.1, together with information about the events with the highest dijet invariant masses, is provided in appendix A.3.



## 8. Systematic uncertainties

In this chapter, studies of systematic effects on the analysis are presented. The experimental uncertainties are discussed in section 8.1, followed by the presentation of the theoretical uncertainties in section 8.2.

### 8.1. Experimental uncertainties

#### 8.1.1. Jet energy scale

The jet energy scale (JES) uncertainty is often among the dominant uncertainties in jet measurements. One of the major strengths of the presented analysis is its robustness with respect to the JES uncertainty. This has been discussed in chapter 2 in the context of the theories for new phenomena that can be probed with this analysis. The JES uncertainty does however have residual effects, and the study of these effects is of vital importance for the measurement.

The first residual effect of the JES uncertainty is the modification of the dijet invariant mass of the events. Since the dijet mass is calculated from the four vectors of the two jets with the highest  $p_T$  as  $m_{jj}^2 = (p_1 + p_2)^2$ , it is directly sensitive to a scaling of the jet four vectors by the JES uncertainty. Since the analysis measures normalised spectra in bins of the dijet invariant mass, the change in  $m_{jj}$  can lead to migrations between these mass bins and thus to modifications of the resulting  $\chi$ -distributions.

The statement made in chapter 2 that the  $\chi$ -value of a given event is not changed by a re-scaling of the jet four vectors is only true as long as  $\chi$  is calculated from the same pair of jets. The JES uncertainty can have the effect of modifying the transverse momenta of the jets in such a way that their order in  $p_T$  is altered. If the dijet system is reconstructed from a different pair of jets, the values of  $m_{jj}$  and  $\chi$  of the event are changed in a discontinuous way. This second effect of the JES uncertainty poses a challenge to the determination of the total JES uncertainty on the  $\chi$ -distributions, since it requires to vary all uncertainty components simultaneously.

The jets have been calibrated using techniques based on Monte Carlo simulations and on residual *in situ* corrections [74] as described in chapter 5. The systematic uncertainty on the resulting JES is determined from the uncertainties of the various methods that contribute to the calibration. The JES uncertainties are described in the form of

separate components, also called *nuisance parameters*, which are fully correlated across  $p_T$  and  $\eta$  and independent among each other. The initial number of nuisance parameters corresponding to the *in situ* JES calibration is reduced from 54 to 6. Further contributions, such as from pile-up, the jet flavour composition and the event topology are taken into account as additional nuisance parameters. In total, the JES uncertainties for the  $\chi$ -analysis are described by 14 uncertainty components.

Since the individual JES uncertainty components are independent among each other, it may be considered to perform separate up- and downward shifts of each component by  $1\sigma$  and add the results in quadrature, according to standard uncertainty propagation. In general, the total uncertainty on any function of the individual sources of uncertainty can be obtained in this way only under two assumptions: First, the function under consideration must be differentiable with respect to the variables that are varied in order to allow for its Taylor expansion. Second, the variation of the function must be small under small variations of the variables, in order to obtain a meaningful result when cutting the series off after the linear term.

As already mentioned above, the assumptions for quadratic error propagation are not generally fulfilled in this analysis. Each event in the final  $\chi$ -distributions is characterised by its dijet invariant mass  $m_{jj}$  and its  $\chi$ -value. The operation of ordering all jets in an event by their transverse momenta and calculating the invariant mass and  $\chi$  from the two jets with the highest  $p_T$  is not differentiable with respect to  $p_T$ , since the first step is not. As a result, the premise of the quadratic error propagation is not fulfilled and in particular, no generally true statement can be made about the size of the uncertainty on  $m_{jj}$  and  $\chi$  given the size of the uncertainties on the jet transverse momenta.

As an example, the effect of two uncertainty components  $c_1$  and  $c_2$  on an event with a three-jet topology may be considered. Assume that the leading jet ( $j_1$ ) has a high transverse momentum, and that the second ( $j_2$ ) and the third jet ( $j_3$ ) have mutually similar  $p_T$ . Assume also that neither  $c_1$  nor  $c_2$  change the transverse momenta of  $j_1$  and  $j_2$ , but that both increase the transverse momentum of  $j_3$  to a value close to the  $p_T$  of  $j_2$ . In this scenario,  $m_{jj}$  and  $\chi$  are invariant under individual variations of  $c_1$  and  $c_2$ . Consequently, a quadratic sum of the uncertainties will leave the dijet kinematics approximately unchanged, too. In contrast, if both components are varied simultaneously, the  $p_T$  of  $j_3$  may become higher than the  $p_T$  of  $j_2$ , such that  $m_{jj}$  and  $\chi$  are now calculated from  $j_1$  and  $j_3$ , with in general different results with respect to the original values. Thus, the effect of simultaneous variations of the uncertainty components is not captured when performing a quadratic error propagation on non-differentiable uncertainty distributions. In this analysis, the JES uncertainty is therefore evaluated with pseudo-experiments.

To evaluate the JES uncertainty for the  $\chi$ -analysis with pseudo-experiments, all 14 JES components are varied simultaneously, assuming a Gaussian distribution for the uncertainties. More specifically, in every pseudo-experiment, each jet four vector in a

given event is multiplied by a factor  $f_{\text{JES}}$ , defined by

$$f_{\text{JES}} = \prod_{i=1}^{N_{\text{NP}}} (1 + r_i \cdot u_i(\text{jet})). \quad (8.1)$$

$N_{\text{NP}}$  denotes the number of nuisance parameters and amounts to 14 in the case of this analysis. Each  $r_i$  is a random number drawn from a Gaussian distribution centered at zero and with standard deviation set to one.  $u_i$  is the  $1\sigma$  value of the uncertainty  $i$ .  $u_i$  depends in general on properties of the jet, e. g. its energy, transverse momentum or distance to other jets. A pseudo-experiment is characterised by the set of 14 random numbers. Within each pseudo-experiment, the same set of random numbers is used for all jets. In this way, the correlation of each uncertainty component across pseudorapidity and transverse momentum is taken into account.

For each pseudo-experiment, the  $\chi$ -spectra are determined as in the nominal analysis. The result of the full set of  $N_{\text{PE}}$  pseudo-experiments is a set of  $N_{\text{PE}}$  normalised  $\chi$ -spectra for each dijet invariant mass bin. In every such dijet invariant mass bin and in every  $\chi$ -bin, the total  $+1\sigma$  JES uncertainty is determined by the interval that contains 68% of the upward fluctuations in that bin, and the  $-1\sigma$  uncertainty is obtained in the same way from the set of all downward fluctuations in that  $\chi$ -bin. Furthermore, the full set of  $\chi$ -spectra from the JES variations is used later in the determination of  $p$ -values and limits described in chapters 9 and 10.

In the following, the relative contribution of the individual uncertainty components is investigated. Then, the convergence of the JES uncertainty estimate from pseudo-experiments is studied. Finally, the resulting JES uncertainties for the  $\chi$ -analysis are presented.

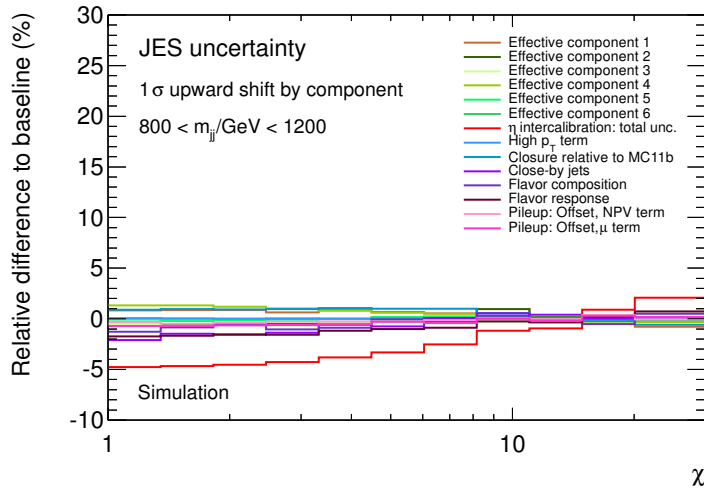
### Individual JES components

Insight into the relative importance of the individual components of the JES uncertainty can be gained by performing independent variations of these components and determining the influence on the  $\chi$ -distributions. More precisely, the  $\chi$ -distributions are calculated after shifting one of the 14 uncertainty components by  $+1\sigma$  and  $-1\sigma$  of the uncertainty, while keeping the other 13 components fixed. Then, the relative difference with respect to the nominal  $\chi$ -distributions is obtained. The procedure is repeated for all 14 uncertainty components.

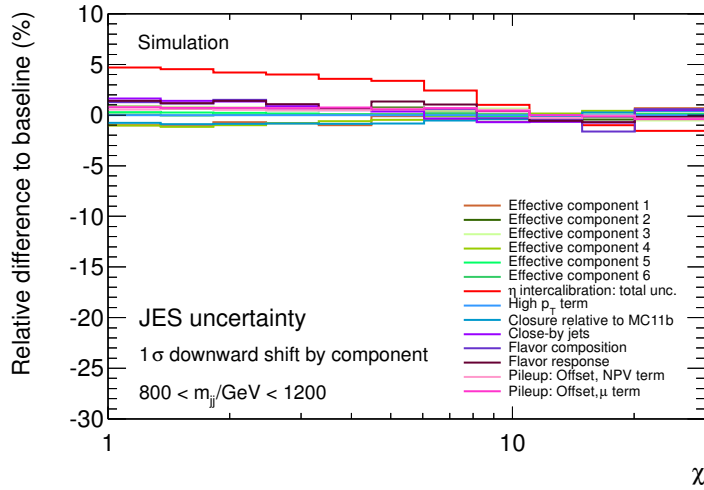
The influence of separate  $1\sigma$  upward and downward shifts of the individual JES components is shown in figure 8.1 for Monte Carlo events in the lowest dijet invariant mass bin of the analysis. The effect on the highest invariant mass bin will be shown later in this chapter, and the distributions for the intermediate dijet invariant mass bins are shown in appendix A.4. In the lowest dijet mass bin, the uncertainty due to the pseudorapidity intercalibration method is clearly dominant over all other components. It is largest at low values of  $\chi$  and reaches a value of about  $-(+)5\%$  for  $1\sigma$  upward

(downward) shifts. The effect of the other components is less than 2% over the entire  $\chi$ -range.

The reason for the large contribution of the pseudorapidity intercalibration lies in the uncertainty of the Monte Carlo modelling used in the intercalibration method [110]. Figure 8.2(a) shows the total uncertainty and the contributions of the individual uncertainties on the pseudorapidity intercalibration as a function of the jet pseudorapidity  $\eta_{\text{det}}$  without the jet origin correction discussed in chapter 5 for anti- $k_t$  jets with a dis-

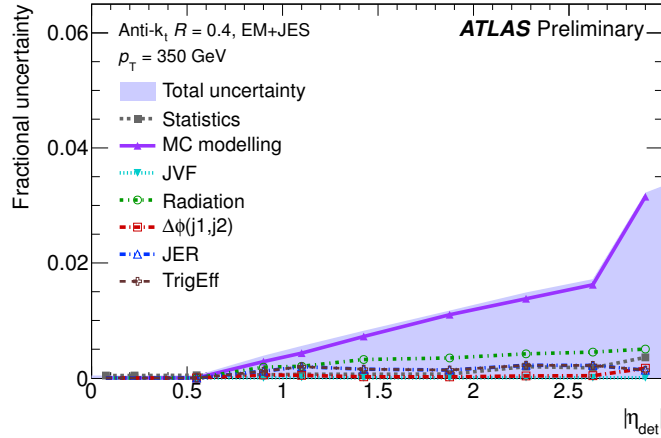


(a)

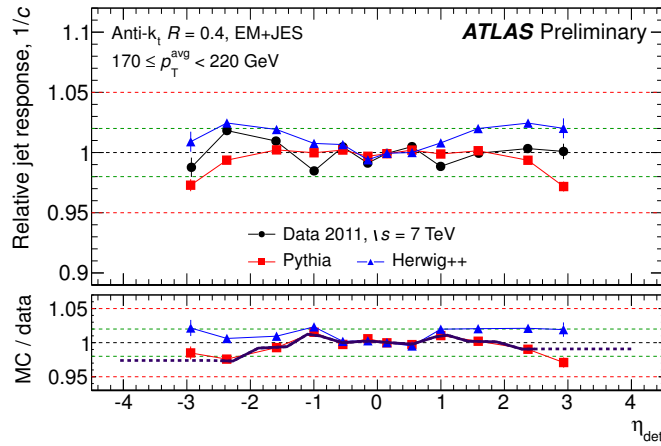


(b)

**Figure 8.1.** The individual components of the JES uncertainty for events with dijet invariant masses between 800 and 1200 GeV. Shown is the effect of  $1\sigma$  upward shifts (a) and downward shifts (b) on the normalised  $\chi$ -distribution; both figures also appeared in [89].



(a)



(b)

**Figure 8.2.** (a) The uncertainties on the pseudorapidity intercalibration method as a function of the jet  $\eta_{\text{det}}$  for anti- $k_t$  jets with a distance parameter of  $R = 0.4$  and a transverse momentum of  $p_T = 350$  GeV. (b)  $1/c$  as a function of the jet pseudorapidity for jets reconstructed with the anti- $k_t$  algorithm with distance parameter  $R = 0.4$  and  $170 < p_T^{\text{avg}} < 220$  GeV, where  $p_T^{\text{avg}} = (p_T^{\text{probe}} + p_T^{\text{ref}})/2$  (see text). The ratios between the response from data and the two Monte Carlo generators are given in the lower panel; both figures from [110].

tance parameter of  $R = 0.4$  and transverse momenta above 350 GeV. Clearly, the uncertainty due to the Monte Carlo modelling is dominant. The modelling uncertainty originates from the response difference predicted by the PYTHIA and HERWIG++ Monte Carlo generators, as can be seen in figure 8.2(b). The plot shows the dependence of the relative jet response  $1/c$  on the jet pseudorapidity for anti- $k_t$  jets with distance parameter  $R = 0.4$  for the case where the average transverse momentum  $p_T^{\text{avg}}$  of the dijet system is between 170 and 220 GeV. As discussed in section 5.2.4, the jet response is defined as the ratio of the transverse momentum  $p_T^{\text{probe}}$  of a jet in the probed region

of the detector and the transverse momentum  $p_T^{\text{ref}}$  of a jet in a reference region by  $1/c = p_T^{\text{probe}}/p_T^{\text{ref}}$ . According to [110], the response difference between the two Monte Carlo generators is likely due to the difference between the  $p_T$ -ordered parton showers in PYTHIA compared with the angular-ordered parton showers in HERWIG++.

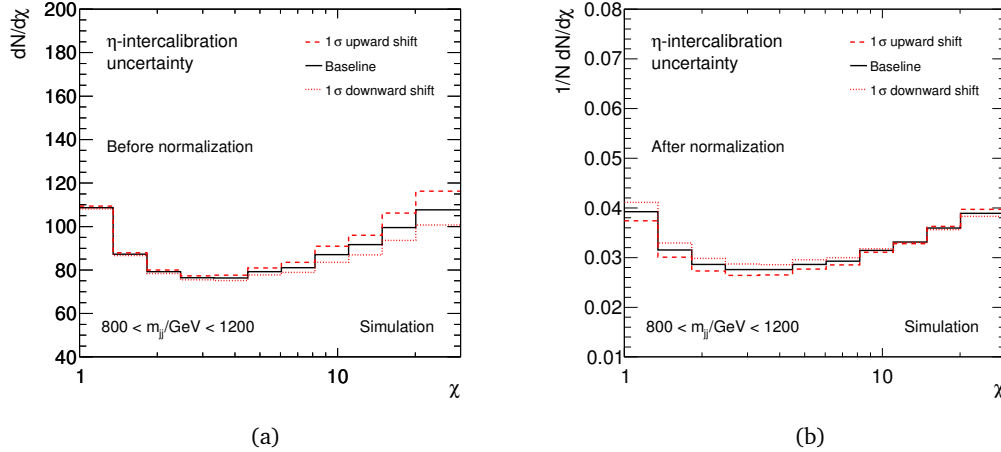


**Figure 8.3.** The influence of the normalisation of the  $\chi$ -distributions on the pseudorapidity intercalibration component of the JES uncertainty. Shown are distributions obtained from the Monte Carlo simulation for events in the lowest dijet invariant mass bin. The solid black lines show the nominal distributions, while dashed, red lines denote the  $+1\sigma$  shift and dotted, red lines denote the  $-1\sigma$  shift of the uncertainty component. (a) Distributions before the normalisation. (b) Distributions after the normalisation.

As can be seen from figure 8.2(a), the intercalibration uncertainty increases with the jet pseudorapidity. Furthermore, as shown in figure 7.4, large values of  $y$  and thus  $\eta$  correspond in general to large  $\chi$ -values. The seemingly counter-intuitive dependence of the intercalibration uncertainty on the  $\chi$ -distributions in figure 8.1 is due to the way the events are distributed among the  $\chi$ -range. The broad bins at large values of  $\chi$  are populated by more events than the bins at low values of  $\chi$ . As can be seen in figure 8.3, shape differences at high  $\chi$ -values are therefore approximately cancelled by the normalisation and arise as shape differences at low  $\chi$ -values.

To assess the importance of the shape of the individual uncertainties, the strongly pseudorapidity-dependent uncertainty from the  $\eta$ -intercalibration is compared to an uncertainty that is assumed to be large but almost flat in pseudorapidity in the default ATLAS procedure. The flavour composition uncertainty is among the largest uncertainties on the  $\chi$ -spectra in all dijet invariant mass bins before they are normalized. Jets initiated by quarks (*quark jets*) have a different response compared to jets initiated by gluons (*gluon jets*) mainly because of their different particle content [101]. For any jet transverse momentum, gluon jets contain more particles on average, and these are also softer than in light quark jets. In addition, gluon jets are wider, i. e. the energy density in the central part of the jet is lower. Gluon jets at low jet  $p_T$  calibrated with the

EM+JES scheme introduced in chapter 5 have a calorimeter response that is between 6% and about 8% lower than light quark jets, with the difference decreasing to about 2% at high jet  $p_T$  [74].

If a data sample consists only of light quark and gluon jets, the detector response to the sample can be expressed as  $\mathfrak{R}_s = f_g \mathfrak{R}_g + (1 - f_g) \mathfrak{R}_q$  where  $f_g$  denotes the fraction of gluon jets in the sample, and  $\mathfrak{R}_q$  and  $\mathfrak{R}_g$  are the responses to light quark and gluon jets respectively [74]. A decrease in the gluon fraction by the flavor composition uncertainty  $\Delta f_g$  increases the sample response by  $\Delta \mathfrak{R}_s^+ = \Delta f_g / f_g \times (\mathfrak{R}_q - \mathfrak{R}_s)$ , and an increase in the gluon fraction by  $\Delta f_g$  decreases the sample response by  $\Delta \mathfrak{R}_s^- = \Delta f_g / (1 - f_g) \times (\mathfrak{R}_s - \mathfrak{R}_g)$ . These asymmetric upwards and downwards shifts depend on the difference between the response of the sample and the response of light quark or gluon jets. In addition, they also depend on the gluon fraction and the uncertainty on the gluon fraction. In the analysis presented here, an ATLAS recommendation was used that conservatively assumes a gluon fraction of  $f_g = 50\%$  and an uncertainty on the gluon fraction of  $\Delta f_g = 50\%$ , independent of the jet transverse momentum and pseudorapidity. With this assumption, the flavour composition uncertainty is governed by the response difference between quark and gluon jets and has the maximal size, due to the cancellation of the pre-factors  $\Delta f_g / f_g$ . Furthermore, the relative uncertainty for up- and downward shifts of the gluon fraction is symmetric in this case.

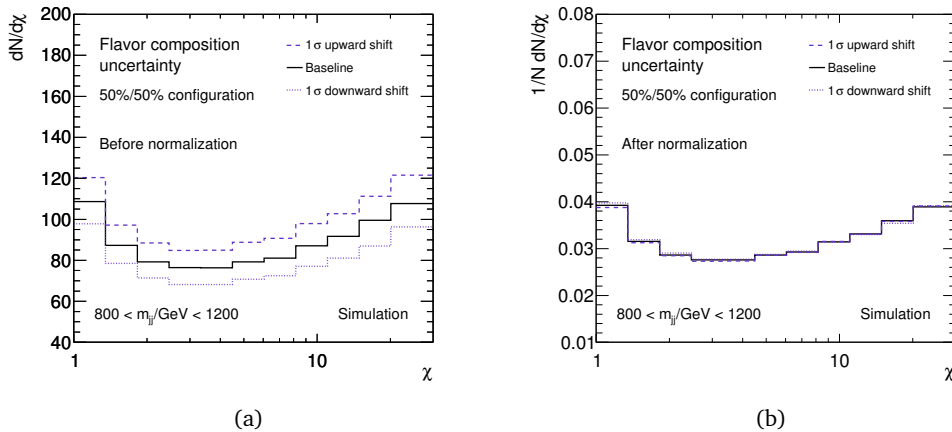


**Figure 8.4.** The influence of the normalisation of the  $\chi$ -distributions on the flavour composition uncertainty component of the JES uncertainty. A gluon fraction of 50% with an uncertainty of 50% is assumed. The distributions have been obtained from the Monte Carlo simulation for events in the lowest dijet invariant mass bin. The solid black lines show the nominal distributions, while the dashed, magenta lines denote the  $+1\sigma$  and the dotted, magenta lines denote the  $-1\sigma$  shift of the uncertainty component. (a) Distributions before the normalisation. (b) Distributions after the normalisation.

Figure 8.4 shows the result of  $1\sigma$  up- and downward shifts of the flavour composition uncertainty on the  $\chi$ -distributions. Consistent with the conservative assumption on the size of the gluon fraction and its uncertainty, the resulting shifts are large in magnitude,

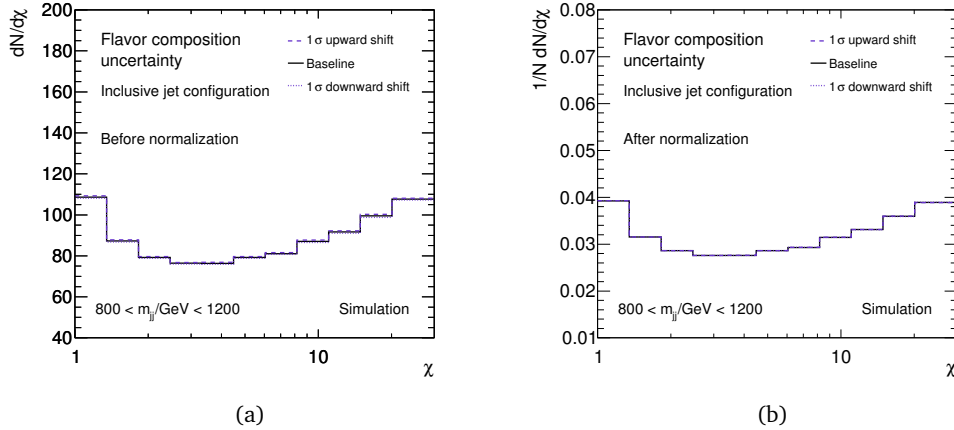


**Figure 8.5.** The influence of the normalisation of the  $\chi$ -distributions on the flavour composition uncertainty component of the JES uncertainty. The flavour composition and its uncertainty correspond to a sample of QCD inclusive jets. The distributions have been obtained from the Monte Carlo simulation for events in the lowest dijet invariant mass bin. The solid black lines show the nominal distributions, while the dashed, magenta lines denote the  $+1\sigma$  and the dotted, magenta lines denote the  $-1\sigma$  shift of the uncertainty component. (a) Distributions before the normalisation. (b) Distributions after the normalisation.

but they result in a global shift of the distributions since the uncertainty is roughly constant as a function of the jet pseudorapidity. Therefore, after the normalisation, the contribution of the flavour composition uncertainty is very small compared to the other uncertainty components like the pseudorapidity intercalibration component. This behaviour under the normalization of the  $\chi$ -distributions raises the question whether a more realistic assumption for the flavour composition uncertainty which may be less flat in the pseudorapidity would yield equally small uncertainties in the normalised  $\chi$ -spectra. Therefore, the results for a more realistic model corresponding to a sample of inclusive QCD jets [113] are shown in 8.5. The response of the sample and the gluon fraction are obtained from PYTHIA predictions, and the uncertainty on the gluon fraction is evaluated from the mean difference between the gluon fraction predicted by PYTHIA and two different Monte Carlo generators, POWHEG and HERWIG++. The resulting uncertainty on the gluon fraction decreases fast from about 7% at low jet  $p_T$  to below 2% for higher  $p_T$ . The resulting uncertainties and the induced shifts of the  $\chi$ -spectra are thus very small, even before the normalisation of the distributions. In conclusion, the influence of the flavour composition uncertainty on the normalised  $\chi$ -distributions is negligible when compared to other components, such as the pseudorapidity intercalibration.

Figure 8.6 shows the effect of individual shifts of all JES uncertainty components on the  $\chi$ -distributions in the highest dijet invariant mass bin of the analysis. Here, the effective component 1 is dominant for intermediate and large  $\chi$ -values, where it induces shifts of about  $+(-)7\%$  for  $1\sigma$  upward (downward) variations at intermediate  $\chi$ -values and of about  $-(+ )5\%$  for  $1\sigma$  upward (downward) variations at large  $\chi$ -values. The most

important contribution to the effective component 1 are the uncertainties of the multijet balance technique [113]. At low  $\chi$ -values, the uncertainties are dominated by the high- $p_T$  term. The resulting changes are as high as 14% (-15%) for  $1\sigma$  upward (downward) shifts.

The high- $p_T$  term predominantly affects events in the first four  $\chi$ -bins, corresponding to  $\chi \lesssim 3.32$ . Figure 8.7 shows that, in contrast to the pseudorapidity intercalibration, the shape uncertainty introduced by the high- $p_T$  term is dominant at low  $\chi$ -values already

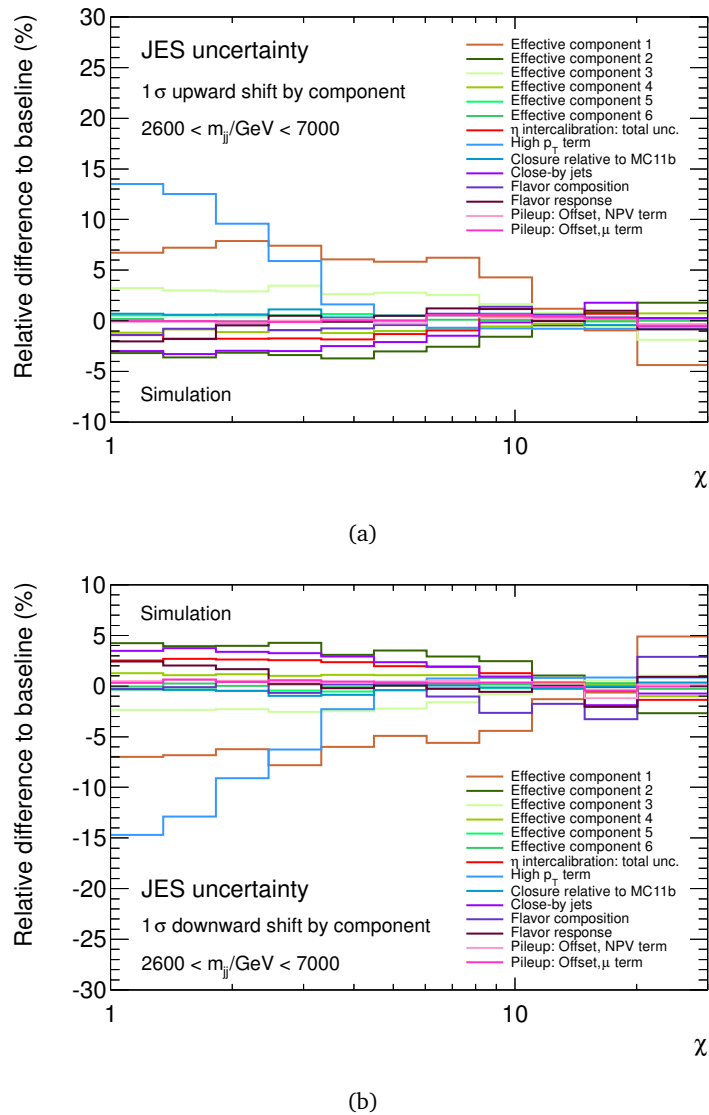


**Figure 8.6.** The individual components of the JES uncertainty for events with dijet invariant masses between 800 and 1200 GeV. Shown is the effect of  $1\sigma$  upward shifts (a) and downward shifts (b) on the  $\chi$ -distribution; both figures also appeared in [89].

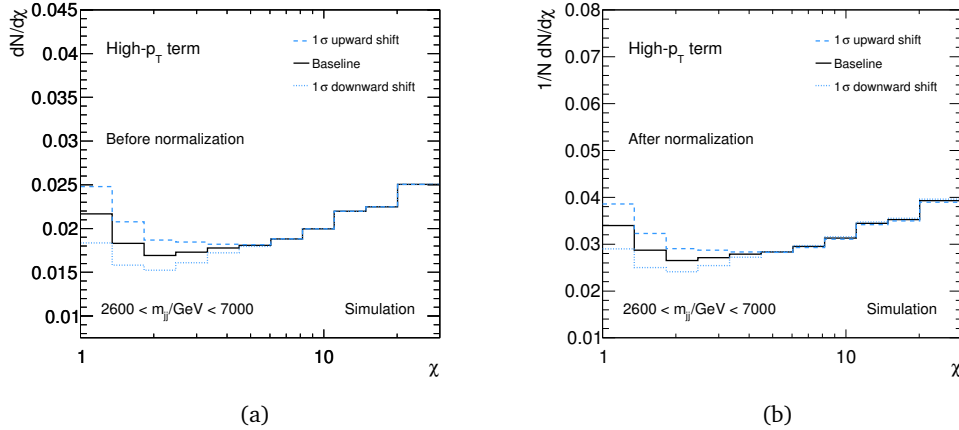


**Figure 8.7.** The influence of the normalisation of the  $\chi$ -distributions on the high- $p_T$  component of the JES uncertainty. The distributions have been obtained from the Monte Carlo simulation for events in the highest dijet invariant mass bin of the analysis. The solid black lines show the nominal distributions, while the dashed, blue lines denote the  $+1\sigma$  and the dotted, blue lines denote the  $-1\sigma$  shift of the uncertainty component. (a) Distributions before the normalisation. (b) Distributions after the normalisation.

before the normalisation. The events in this  $\chi$ -region contain jets with transverse momenta above 1 TeV, as may be seen in figure 7.4(b). The uncertainties obtained from the *in situ* methods are complemented with results from single hadron response measurements for these jets as discussed in section 5.4.2. In this technique, it is assumed that a jet can be described as a superposition of individual particles such that the jet response and the JES uncertainty can be extrapolated from the properties of the constituent particles. At large jet transverse momenta, the dominant uncertainty components within the single hadron measurement itself are the response difference between the data and the Monte Carlo simulation observed in the ATLAS Combined Test Beam [73] analysis and the uncertainty for hadrons with  $p > 400$  GeV, i. e. beyond the kinematic reach of the CERN SPS. The high- $p_T$  component of the JES uncertainty is zero below  $p_T = 1$  TeV. From there on, it increases approximately linearly with a decrease in slope at  $p_T = 1.5$  TeV, reaching an uncertainty of about 3% for a jet  $p_T$  of 2 TeV. Figure 5.6(a) shows the fractional JES uncertainty obtained from the *in situ* methods as a function of the jet  $p_T$ , including the high- $p_T$  term which is denoted as *single particle* in that plot. No dependence on the jet pseudorapidity is assumed in this uncertainty component.

### Convergence of the JES uncertainty estimate

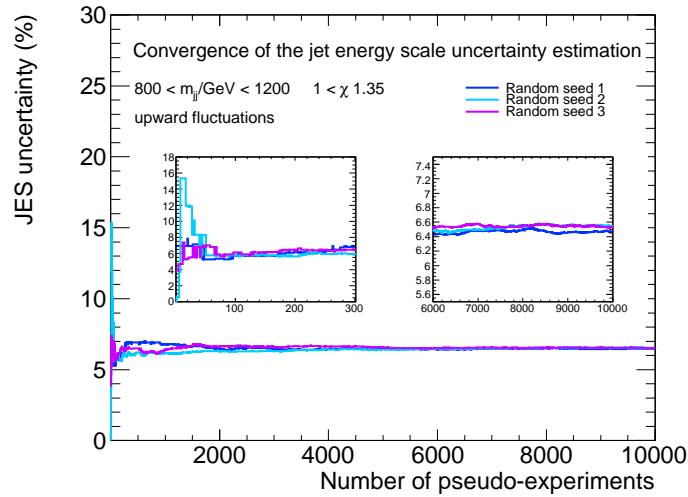
In order to propagate the uncertainty on the JES to the final results, different methods can be considered. A basic approach would be to perform two variations of the analysis, in which all jet energies are shifted up and down by one standard deviation to obtain an uncertainty band from the two resulting variations of the final distributions.

The  $\chi$ -analysis presented in this thesis aimed to use the available information in a more conclusive way. As explained above, the pseudo-experiment approach correctly accounts for situations in which the ordering of the jets by their transverse momenta is changed. It allows to incorporate independent variations of the individual JES uncertainty components while taking the correlations of the individual components across transverse momentum and pseudorapidity into account.

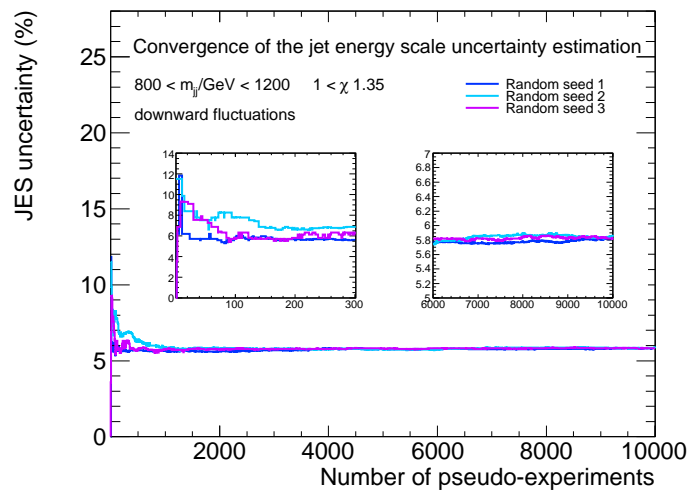
Since the JES uncertainty is sampled from a 14-parameter space, it was not clear a-priori whether the estimate converges with a feasible number of pseudo-experiments. A poor convergence would lead to inconclusive results if the evaluation is performed with a small number of pseudo-experiments. In the worst case, the intended improvement of the estimate would be treated for a less precise result. It has therefore been of great importance for the analysis to investigate the convergence of the pseudo-experiment approach.

Figure 8.8 shows the evolution of the JES uncertainty estimate as a function of the number of pseudo-experiments for the first  $\chi$ -bin in the lowest dijet invariant mass bin of the analysis, obtained from three statistically independent samples. All three samples have been obtained using the exactly same procedure as described at the beginning of this chapter but starting with three different random seeds. They all show the same global evolution with large initial fluctuations. In the third sample, where the largest fluctuations are observed, the uncertainty estimate varies between 6% and almost 16% within the first 60 pseudo-experiments. The amplitude of the fluctuations decreases with the incorporation of several thousands of pseudo-experiments, until the uncertainty estimate converges in all three samples to approximately 6.6% with very small remaining fluctuations of less than 0.1% when 10000 iterations are used.

Since for any individual sample, the uncertainty estimate for a given number of pseudo-experiments intrinsically contains the results from all previous pseudo-experiments, the evolution proceeds in a highly correlated way. Moreover, it can be seen from the figure that the convergence to the same value is a non-trivial result, as the estimates from the three statistically independent samples start from completely different values and exhibit very different initial fluctuations. It is thus a powerful statement that, within the statistical uncertainties, the same results are obtained from the three statistically independent samples. The same is observed for the estimation of the  $-1\sigma$  band from the negative fluctuations of the JES uncertainty shown in figure 8.8(b) and the JES uncertainty estimates in the other dijet invariant mass bins, as presented in figure 8.9 and in appendix A.4. The largest difference in the estimates from any of the statistically independent samples for the same dijet invariant mass bin is observed in figure 8.9(a) and is smaller than 0.5% after 10000 iterations and thus within the expected uncertainties of the method. The pseudo-experiment approach may therefore be safely used for the determination of the JES uncertainty in the analysis.

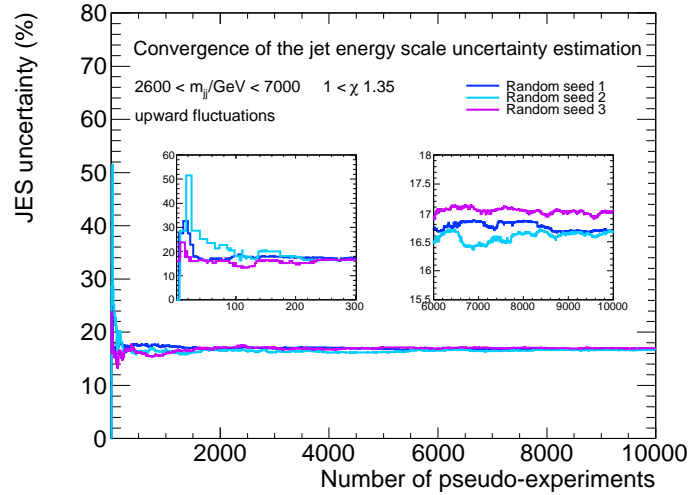


(a)

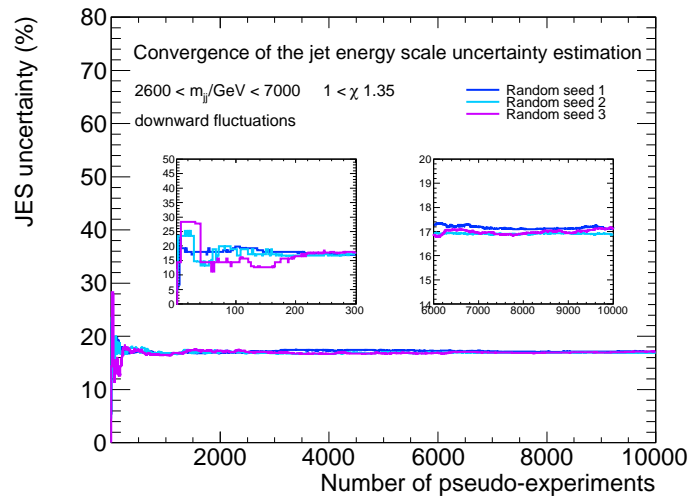


(b)

**Figure 8.8.** The evolution of the JES uncertainty estimate as a function of the number of pseudo-experiments used. Shown is the uncertainty estimate in the first  $\chi$ -bin for events with dijet invariant masses between 800 and 1200 TeV. The inlays show a zoomed view of the left part (left inlay) and of the right part (right inlay) of the  $x$ -axis. The uncertainties have been determined from three statistically different sets of pseudo-experiments (3 coloured lines). Figure (a) shows the uncertainty determined from upward fluctuations and figure (b) the one from downward fluctuations; both figures also appeared in [89].



(a)



(b)

**Figure 8.9.** The evolution of the JES uncertainty estimate as a function of the number of pseudo-experiments used. Shown is the uncertainty estimate in the first  $\chi$ -bin for events with dijet invariant masses between 2600 and 7000 TeV. The inlays show a zoomed view of the left part (left inlay) and of the right part (right inlay) of the  $x$ -axis. The uncertainties have been determined from three statistically different sets of pseudo-experiments (3 coloured lines). Figure (a) shows the uncertainty determined from upward fluctuations and figure (b) the one from downward fluctuations; both figures also appeared in [89].

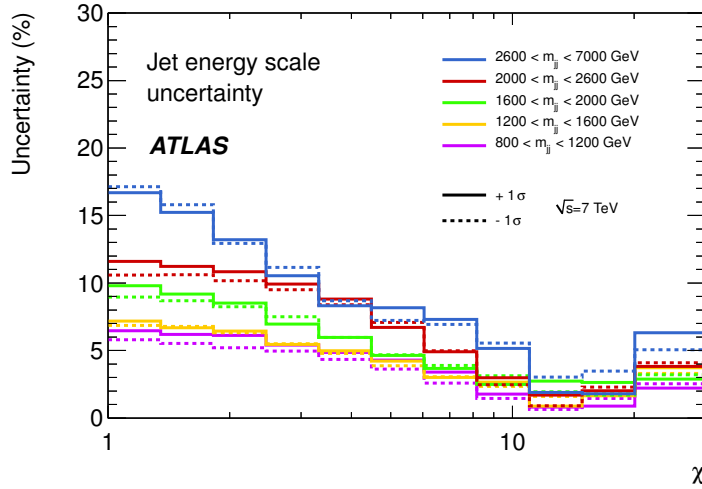


**Figure 8.10.** The JES uncertainties on the  $\chi$ -distributions. Shown are the  $+1\sigma$  (solid lines) and  $-1\sigma$  (dashed lines) uncertainties for the five dijet invariant mass bins of the analysis; also appeared in [2].

### Resulting JES uncertainties

Figure 8.10 shows the resulting JES uncertainties for the five dijet invariant mass bins of the analysis. The smallest uncertainties are observed in the lowest dijet invariant mass bin. For dijet invariant masses between 800 and 1200 GeV, they reach 7% at maximum for low  $\chi$ -values, while they can be as high as 17% for dijet invariant masses between 2600 and 7000 GeV.

#### 8.1.2. Jet energy and angular resolution

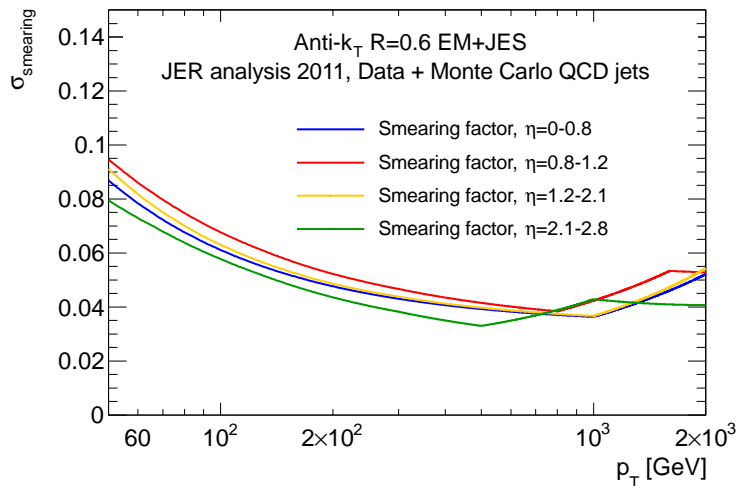
This section discusses the uncertainties on the  $\chi$ -distributions that are related to the jet energy and angular resolution.

In ATLAS, the jet energy resolution (JER) and the corresponding uncertainty have been studied in data and compared to Monte Carlo predictions [127]. In the 2011 dataset, the JER in data was found to be in agreement with the one in the Monte Carlo simulation within the uncertainties [128], such that no additional smearing of the jet energy in the Monte Carlo simulation was necessary. The results have been obtained with *in situ* methods which use the transverse momentum balance in events with high- $p_T$  jets.

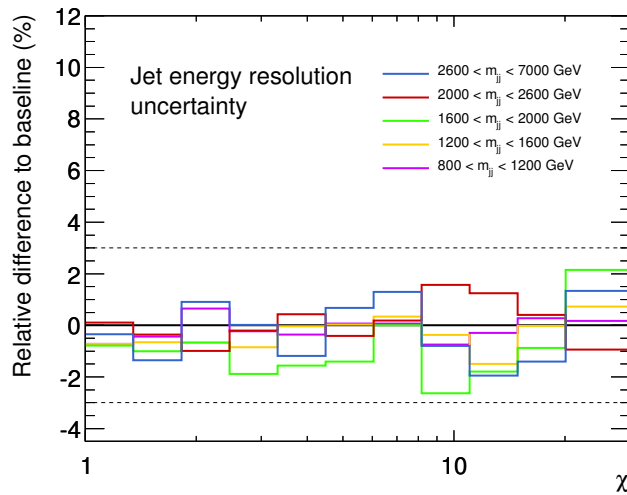
Following ATLAS recommendations [128], the residual effect of the JER uncertainty on the  $\chi$ -analysis is evaluated as follows. For each jet, a smearing factor  $s$  is obtained, based on the jet pseudorapidity and transverse momentum, as

$$s = \sqrt{(\text{JER}_{\text{MonteCarlo}} + U_{\text{JER}})^2 - \text{JER}_{\text{MonteCarlo}}^2} \quad (8.2)$$

Here,  $JER_{\text{MonteCarlo}}$  denotes the JER in the Monte Carlo simulation, and  $U_{\text{JER}}$  is the uncertainty on the JER. Figure 8.11(a) shows the smearing factors as a function of the jet transverse momentum, for different values of the jet pseudorapidity. They can be as high as 10% for jet  $p_T$  below 60 GeV and lie between 4% and 6% for jets with transverse momenta above 1 TeV. The four vectors of all jets in an event are re-scaled by random numbers drawn from a Gaussian distribution centred at zero and with the standard deviation set to the smearing factor. Then, the  $\chi$ -distributions are calculated, and their



(a)



(b)

**Figure 8.11.** (a) The jet energy resolution (JER) smearing factors as a function of the jet transverse momentum  $p_T$  in different bins of jet pseudorapidity  $\eta$ ; from [89]. (b) The jet energy resolution uncertainties on the  $\chi$ -distributions. The uncertainties are shown in the five dijet invariant mass bins of the analysis; also appeared in [89].

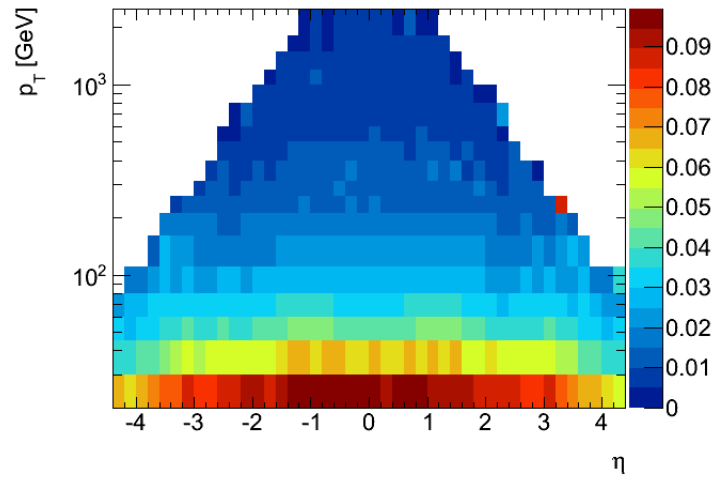
relative deviations from the nominal  $\chi$ -distributions are determined. Figure 8.11(b) shows the relative difference of the  $\chi$ -distributions after the JER smearing with respect to the nominal distributions for the five dijet invariant mass bins of the analysis. The relative shifts in the  $\chi$ -distributions due to the JER uncertainty lie below 3% in all five dijet invariant mass bins.

The second effect considered in this section is the influence of the finite jet angular resolution (JAR) on the  $\chi$ -distributions. Since the events in the analysis are characterised by the values of  $m_{jj}$  and  $\chi$  calculated from the two leading jets in  $p_T$ , uncertainties in the angular measurement of the individual jets can propagate into the final observables.

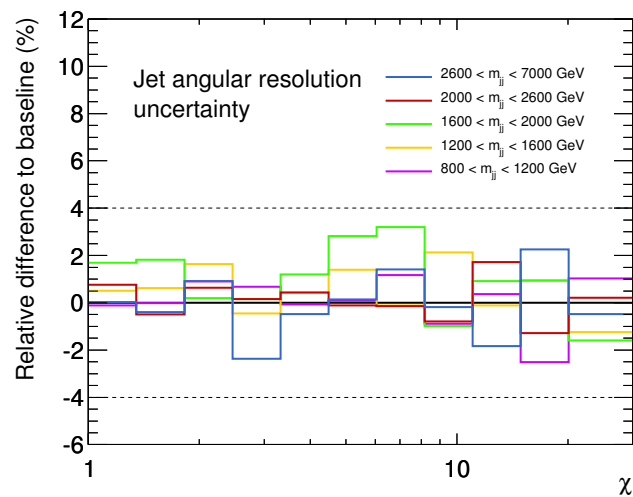
In [89], the JAR has been studied in bins of jet pseudorapidity and transverse momentum by matching jets in the Monte Carlo simulation before (*truth jets*) and after the calorimeter simulation (*calorimeter jets*) within a cone of  $\Delta R = 0.3$  and evaluating their absolute difference in pseudorapidity. The JAR has been approximated by the RMS of the resulting distribution. Figure 8.12(a) shows the resulting JAR as a function of the jet transverse momentum and pseudorapidity. For jets with  $p_T > 100$  GeV and  $|\eta| < 3.0$ , the resolution is not larger than 3%.

The effect of the JAR on the  $\chi$ -distributions is evaluated by shifting the pseudorapidity of each jet by a random number drawn from a Gaussian distribution with a standard deviation of 0.04 and centred at zero, keeping the mass and the energy of the jets fixed. Then, the relative differences of the modified  $\chi$ -distributions with respect to the nominal ones are determined. The results are shown in figure 8.12(b). In all five dijet invariant mass bins of the analysis, the effect of the finite JAR does not exceed 4%.

Due to their small size when compared to the systematic effects arising from the jet energy scale and from the factorisation and renormalisation scales discussed in the next section, it has been decided in ATLAS not to assign JER and JAR systematic uncertainties for the calculation of  $p$ -values and limits.



(a)



(b)

**Figure 8.12.** (a) The jet angular resolution uncertainty as a function of the jet transverse momentum and pseudorapidity; from [89]. (b) The angular energy resolution uncertainties for the  $\chi$ -distributions. The distributions are shown in the five dijet invariant mass bins of the analysis; also appeared in [89].

## 8.2. Theoretical uncertainties

This section describes the influence of the theoretical uncertainties on the  $\chi$ -analysis.

### 8.2.1. Parton distribution functions

The differential cross sections in  $\chi$  for processes with protons in the initial state are obtained by convolving the partonic cross sections with the proton PDFs as described in section 1.2.2. The PDFs are obtained by fits to data from e. g. deep inelastic scattering experiments as discussed in [21] and the references therein. The fit procedure includes a number of free parameters. The allowed variations of these parameters translate into uncertainties on the PDFs which in turn lead to uncertainties on cross section predictions. In the so-called Hessian method, a matrix that has the dimension  $N$  of the number of free fit parameters is diagonalised. The resulting  $N$  eigenvector directions are used to determine the PDF uncertainty on an observable via the *Master Equation* suggested in [21]:

$$\Delta X_{\max}^+ = \sqrt{\sum_{i=1}^N \left( \max(X_i^+ - X_0, X_i^- - X_0, 0) \right)^2} \quad (8.3)$$

$$\Delta X_{\max}^- = \sqrt{\sum_{i=1}^N \left( \max(X_0 - X_i^+, X_0 - X_i^-, 0) \right)^2}. \quad (8.4)$$

Here,  $\Delta X_{\max}^+$  is the positive and  $\Delta X_{\max}^-$  is the negative PDF uncertainty. The sum runs over the  $N$  free fit parameters.  $X_i^+$  and  $X_i^-$  denote the predictions from the two directions corresponding to the eigenvector  $i$ , and  $X_0$  denotes the prediction from the central PDF value. Consequently, to obtain the PDF uncertainties for an observable, the calculation of  $2N$  cross section predictions is required, corresponding to the  $2N$  error PDFs. The APPLgrid software [129] allows the fast a-posteriori convolution of PDFs with pre-calculated partonic cross sections. To evaluate the effect of PDF uncertainties on the  $\chi$ -analysis presented in this thesis, APPLgrid was used in connection with NLOJET++ [30–33] and the 52 error members of the CT10 NLO PDF set [94].

Figure 8.13 shows the PDF uncertainties on the normalised, differential  $\chi$ -distributions. The uncertainties do not exceed 1.1% in any of the five dijet invariant mass bins.

### 8.2.2. Factorisation and renormalisation scales

For the calculation of the cross sections in the framework of the QCD improved parton model discussed in section 1.2.2, choices for the renormalisation scale  $\mu_R$  and the factorisation scale  $\mu_F$  have to be made. When calculated to all orders, the cross sections

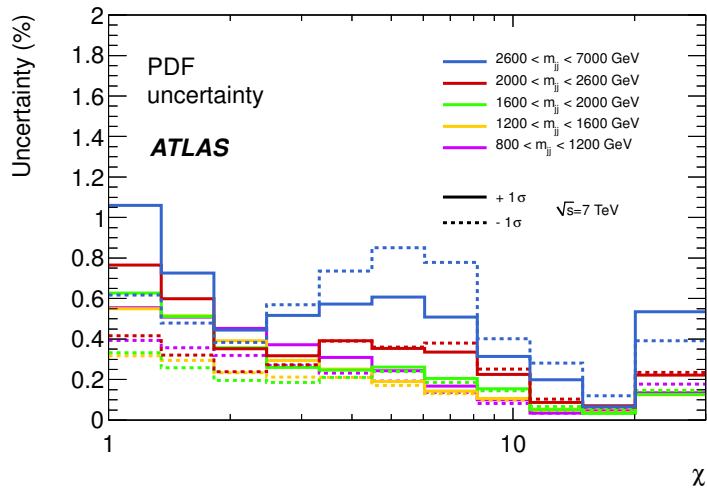


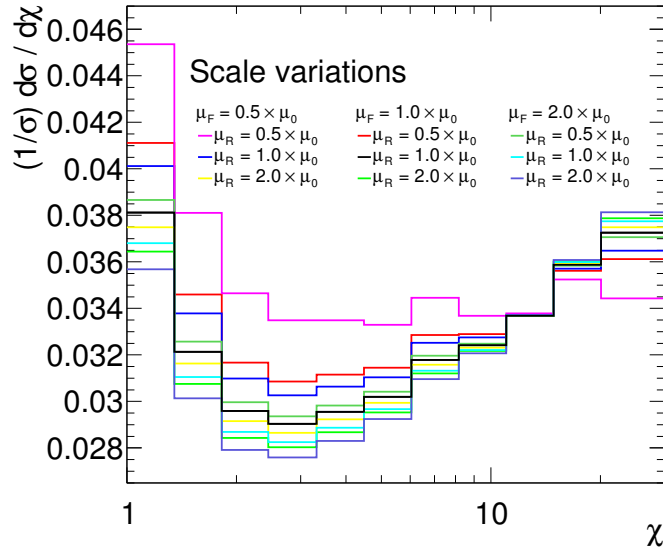
**Figure 8.13.** The PDF uncertainties on the  $\chi$ -distributions. Shown are the  $+1\sigma$  (solid lines) and  $-1\sigma$  (dashed lines) uncertainties in the five dijet invariant mass bins of the analysis; also appeared in [2].

do not depend on the scales [9]. In practice, all cross sections are calculated to finite order, such that the results carry an intrinsic scale dependence.

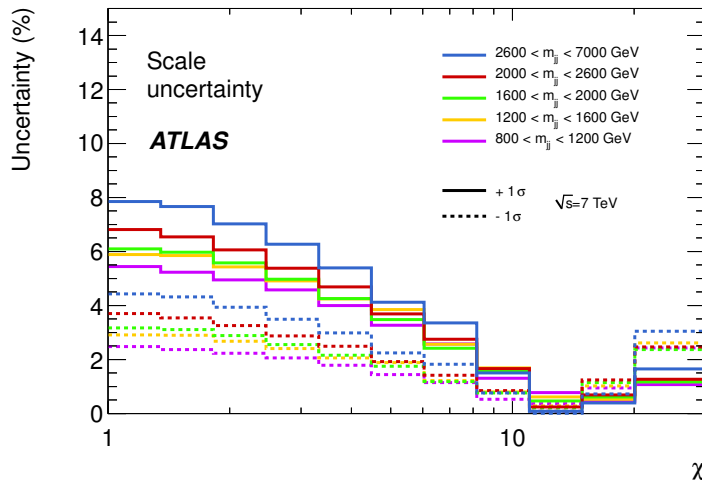
In this section, the effect of the residual scale dependence on the  $\chi$ -distributions is studied. To this end, the  $\chi$ -distributions are calculated in the five dijet invariant mass bins with  $\mu_F$  and  $\mu_R$  independently varied by factors of 0.5, 1.0 and 2.0 around the nominal choice of  $\mu_0 = (p_T^1 + p_T^2)/2$ , the average transverse momentum of the dijet system. As in the case of the PDF uncertainties, APPLgrid [129] was used in connection with NLOJET++ [30–33] and the CT10 NLO PDF set to perform the scale variations. In each  $m_{jj}$ -bin of the analysis, the resulting eight variations of the  $\chi$ -distributions are compared with the nominal one.

Figure 8.14(a) shows the scale variations in the highest dijet invariant mass bin of the analysis,  $2600 < m_{jj} < 7000$  GeV, for the normalised  $\chi$ -distributions. At low  $\chi$ -values, the variation  $\mu_R = \mu_F = 0.5 \times \mu_0$  leads to the largest upward shift, whereas the variation  $\mu_R = \mu_F = 2.0 \times \mu_0$  leads to the largest downward shift. Due to the normalisation of the  $\chi$ -spectra, the situation is opposite for high  $\chi$ -values. Consistent with earlier publications [57] and after discussions with the Standard Model group in ATLAS, the scale uncertainty on the  $\chi$ -distributions is taken from the second largest deviation in every  $\chi$ -bin, in positive and negative direction, effectively removing the two cases discussed above. Figure 8.14(b) shows the resulting uncertainty bands. As illustrated in figure 8.14(a) for the case of the highest dijet mass bin, the positive scale uncertainty is larger than the negative uncertainty. Both uncertainties increase with the dijet mass and are largest for low  $\chi$ -values. For example, for dijet masses between 800 and 1200 GeV, the uncertainties are largest for events with  $\chi < 2$ , where the positive uncertainty amounts

to about 5.5%. In comparison, the highest overall values are reached for dijet masses above 2600 GeV with values of about 8% for upward shifts and  $\chi < 2$ .



(a)



(b)

**Figure 8.14.** (a) Scale variations in the highest dijet invariant mass bin. Shown are the normalised  $\chi$ -distributions obtained by independent variations of the renormalisation scale  $\mu_R$  and the factorisation scale  $\mu_F$  by factors of two compared with the baseline values. (b) The scale uncertainties on the  $\chi$ -distributions. Shown are the  $+1\sigma$  (solid lines) and  $-1\sigma$  (dashed lines) uncertainties in the five dijet invariant mass bins of the analysis; also appeared in [2].

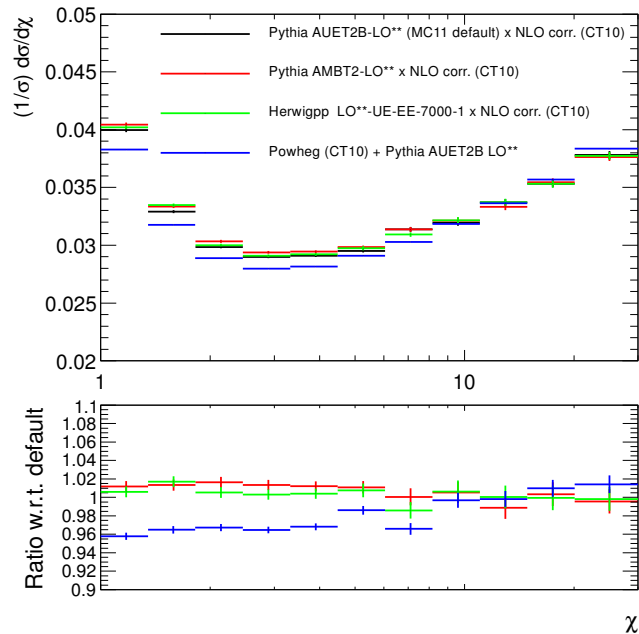
### 8.2.3. Monte Carlo generators and configurations

In this section, a comparison of background predictions obtained with different Monte Carlo generators and different configurations of the simulation is presented. The Monte Carlo generators used in this work can in general be configured by parameters that are not fully constrained a-priori and that may be adjusted to better describe the observed data. The simulation of the underlying event is among the configurable parts of the simulation. The  $\chi$ -distributions have been generated with PYTHIA [22] in two different configurations, and with one configuration each for HERWIG++ [85] and POWHEG [130]. More specifically, PYTHIA has been used with the default AUET2B-LO\*\* and with the AMBT2-LO\*\* configuration [87]. The former is an updated version of the AUET2 configuration [131] and uses underlying event data for the simulation of multiple parton interactions whereas the latter configuration uses minimum bias events for this purpose.

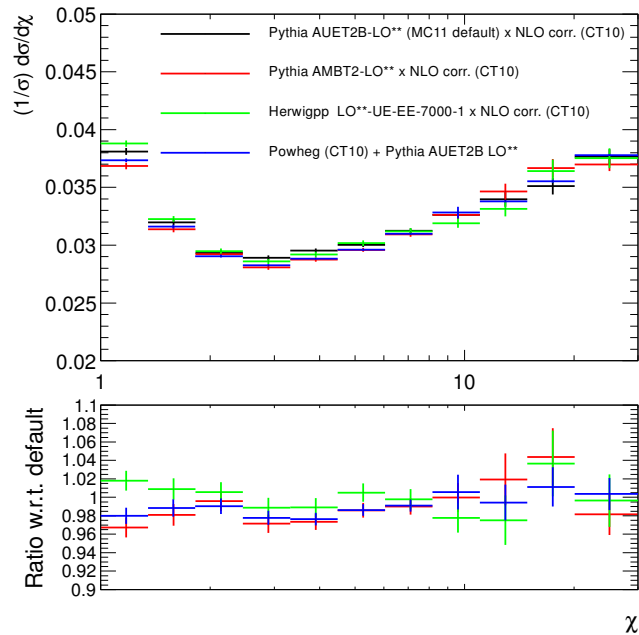
The HERWIG++ generator [85] has been used with the LO\*\*-UE-EE-7000-1 configuration [132]. HERWIG++ is the successor of HERWIG [133] (*Hadron Emission Reactions With Interfering Gluons*). It uses angular-ordered parton showers and a cluster hadronisation model [134]. To take NLO effects for the two PYTHIA samples and the HERWIG++ simulation into account, NLOJET++ [30–33] has been used with the CT10 NLO PDF set [94] to derive K-factors for the three samples as described in section 4.3.

POWHEG (*Positive Weight Hardest Emission Generator*) [130] is used to simulate QCD dijet events by calculating the so-called *underlying Born configuration* at NLO accuracy followed by the hardest parton branching. POWHEG uses the CT10 PDFs and is interfaced with PYTHIA 6 in the AUET2B-LO\*\* configuration for the subsequent event generation.

Figure 8.15 shows the normalised, differential  $\chi$ -distributions for the different generators and configurations described above. The distributions are shown for events with dijet invariant masses between 800 and 1200 GeV in figure 8.15(a) and with masses between 2000 and 2600 GeV in figure 8.15(b), with statistical uncertainties. The lower panels show the ratios with respect to the nominal simulation from PYTHIA with the AUET2B-LO\*\* configuration, also with statistical uncertainties. In the lowest dijet mass bin, the predictions from the AMBT2-LO\*\* PYTHIA configuration and from HERWIG++ agree with the default simulation within 2%. The prediction from POWHEG is about 4% lower at low and intermediate values of  $\chi$  and about 2% higher at high values of  $\chi$ . For the higher dijet masses, the HERWIG++ prediction agrees with the prediction obtained with the nominal settings within 3%. The predictions with the AMBT2-LO\*\* PYTHIA configuration agrees within 3.5%. The POWHEG prediction agrees with the nominal settings within 2%. The differences between the nominal background prediction from PYTHIA with the AUET2B-LO\*\* parameters and the one obtained with PYTHIA and the AMBT2-LO\*\* parameters and the one obtained with HERWIG++ are considered negligible for the analysis. The POWHEG prediction is used to provide a cross-check of the  $p$ -values for the agreement of the data with the Standard Model QCD expectation in chapter 9.



(a)



(b)

**Figure 8.15.** Comparison of Monte Carlo predictions from different generators and with different configurations. Shown are the normalised, differential  $\chi$ -distributions obtained from the PYTHIA 6 generator with two different configurations (black and red line), and the same distributions obtained with HERWIG++ (green line) and POWHEG (blue line), with statistical uncertainties. (a) Events with dijet invariant masses between 800 and 1200 GeV. (b) Events with dijet invariant masses between 2000 and 2600 GeV. The lower panels show the ratios of the three variations with respect to the default setting (PYTHIA with the AUET2B-LO\*\* configuration), with statistical uncertainties; both figures from [89].

## 9. Experimental results

This chapter presents the results of the analysis of the dijet angular distributions in  $4.8 \text{ fb}^{-1}$  of proton-proton collisions collected with the ATLAS detector. The agreement of the data with the QCD prediction is subsequently quantified with two statistical tests.

Figure 9.1 shows the observed dijet angular distributions as normalised, differential spectra of  $\chi$  in five bins of the dijet invariant mass. Also shown is the QCD prediction, together with the corresponding theoretical and the total theoretical and experimental uncertainties. The expected  $\chi$ -distributions were obtained from the PYTHIA Monte Carlo generator [22] and have been multiplied with bin-wise K-factors to incorporate NLO effects as discussed in section 4.3. The angular distribution of a hypothetical quantum black hole signal with  $M_D = 4 \text{ TeV}$  and  $n = 6$  extra dimensions is shown in the highest dijet invariant mass bin. The  $\chi$ -distributions in the five dijet mass bins are also presented separately in figure 9.2.

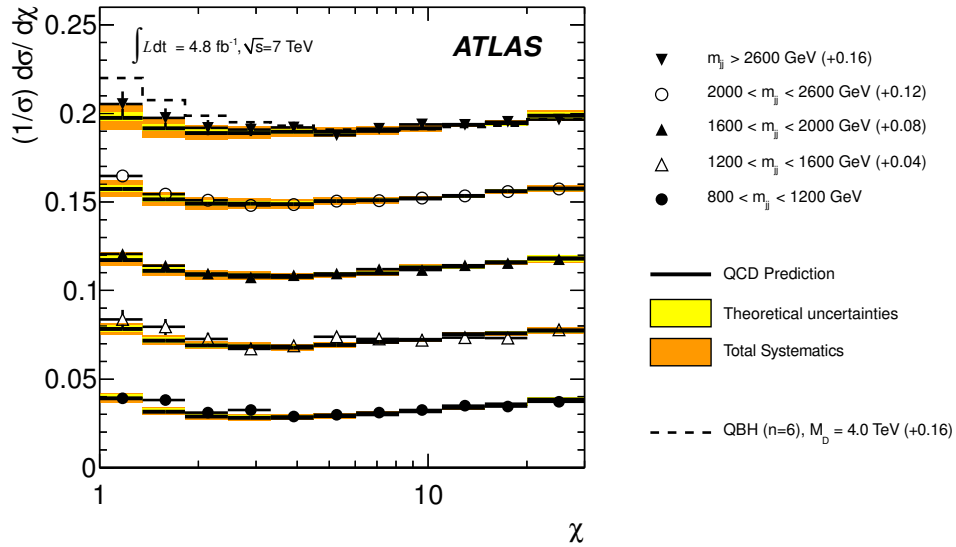


**Figure 9.1.** The  $\chi$ -distributions in the five dijet invariant mass bins. For the visualisation, different offsets have been applied to the five distributions. The QCD predictions (solid lines) are shown with theoretical uncertainties (yellow bands) and total systematic uncertainties (orange bands). The data points are shown with statistical error bars. The  $\chi$ -distribution of a hypothetical quantum black hole signal is shown in the highest dijet invariant mass bin (dashed line) for  $M_D = 4 \text{ TeV}$  and  $n = 6$  extra dimensions; also appeared in [2].

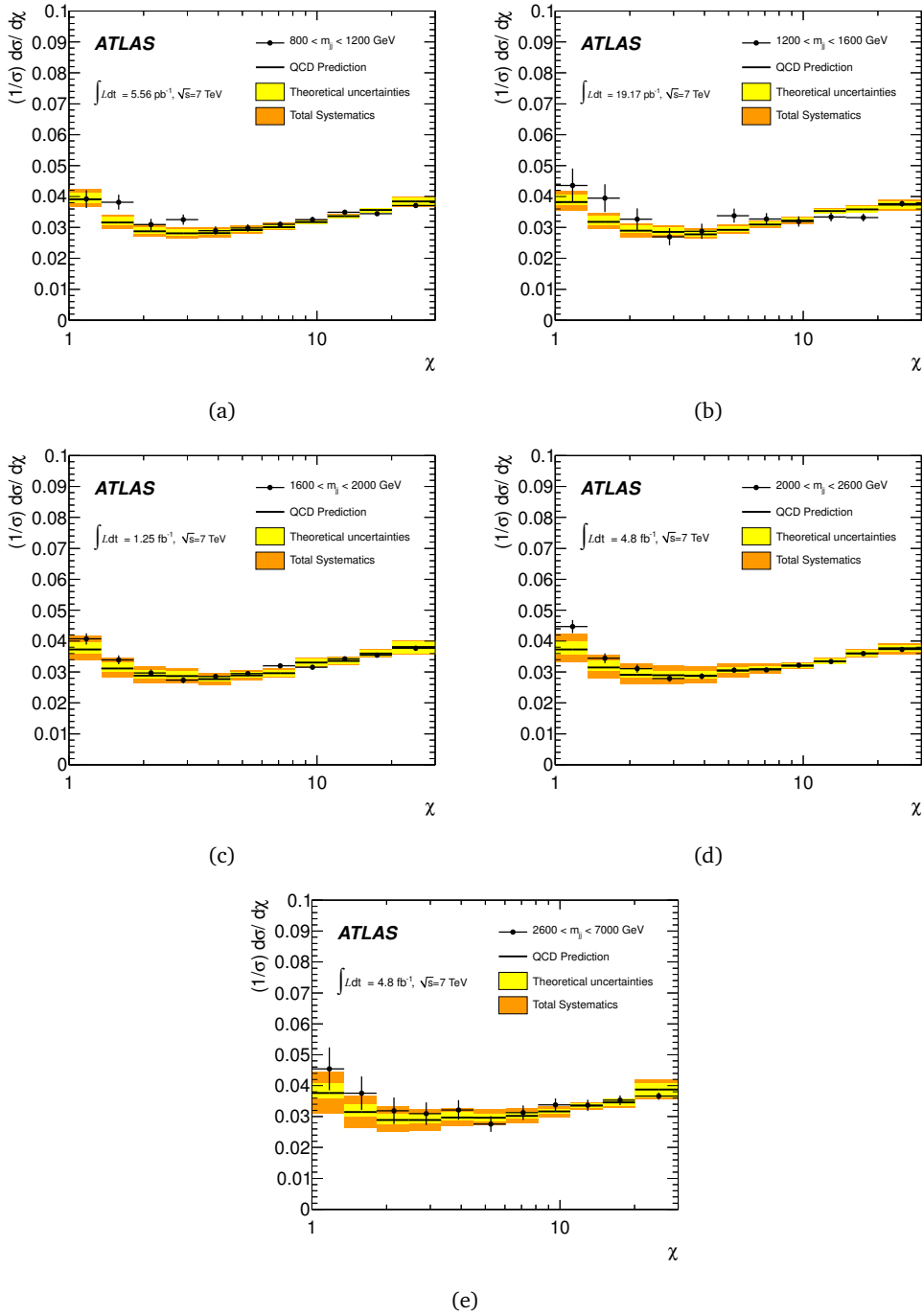


**Figure 9.2.** The  $\chi$ -distributions in the dijet invariant mass bins (a) from 800 to 1200 GeV, (b) from 1200 to 1600 GeV, (c) from 1600 to 2000 GeV, (d) from 2000 to 2600 GeV and (e) from 2600 to 7000 GeV. The QCD predictions (solid lines) are shown with theoretical uncertainties (yellow bands) and total systematic uncertainties (orange bands). The data points are shown with statistical error bars; also appeared in [2].

## 9.1. Statistical analysis of the agreement between the data and the background prediction

Only small differences between the data and the expectation from Standard Model QCD are observed in figures 9.1 and 9.2. The agreement is quantified with two different statistical tests. The first test uses a binned Poissonian likelihood and is sensitive to any deviation from the background hypothesis.

For each dijet invariant mass bin, a likelihood function is defined as the total probability for the observed  $\chi$ -distribution under the QCD hypothesis. Since the analysis is a shape analysis, the number of events in the QCD prediction is scaled to the number of events observed in the data in every dijet invariant mass bin. If  $\mu_i$  is the number of events in  $\chi$ -bin  $i$  predicted by the QCD simulation, the Poissonian probability  $p_i$  to observe  $n_i$  events in the data is given by

$$p_i = \frac{\mu_i^{n_i}}{n_i!} e^{-\mu_i}. \quad (9.1)$$

The likelihood  $\mathcal{L}$  is then obtained by the product of the probabilities over all  $\chi$ -bins

$$\mathcal{L} = \prod_{i=1}^{n_{\text{bins}}=11} p_i, \quad (9.2)$$

and the test statistic  $TS$  of the likelihood test is defined as

$$TS = -2 \log \mathcal{L}. \quad (9.3)$$

Pseudo-experiments are performed to obtain the distribution of the test statistic from an ensemble of background predictions that agree with the nominal simulation within the statistical and the systematic uncertainties. The latter have been discussed in chapter 8. Each pseudo-experiment results in a different  $\chi$ -spectrum and thus in a different value of the test statistic when compared with the  $\chi$ -distribution predicted by the nominal QCD hypothesis. Figure 9.3 shows the resulting distribution of the test statistic for the Standard Model QCD hypothesis for events with dijet invariant masses between 1600 and 2000 GeV. The distribution falls steeply with a long tail towards high values of  $-2 \log \mathcal{L}$ . Also shown is the value of the test statistic observed in the data.

The statistical significance of the measurement is quantified by the  $p$ -value which is calculated by integrating the normalised distribution of the test statistic above the value found in the data. By definition, the  $p$ -value is the probability that a fluctuation of the background within the statistical and systematic uncertainties results in a  $\chi$ -spectrum that deviates at least as much from the nominal spectrum as the one observed in the data. A small  $p$ -value corresponds to a  $\chi$ -spectrum that is in tension with the Standard Model QCD prediction. The test makes no statement about the compatibility of the observed data with any other model. In particular, a small  $p$ -value does not imply the presence of a signal contribution in the data but only quantifies the agreement of the observed data with the background assumption. Table 9.1 shows the  $p$ -values for the

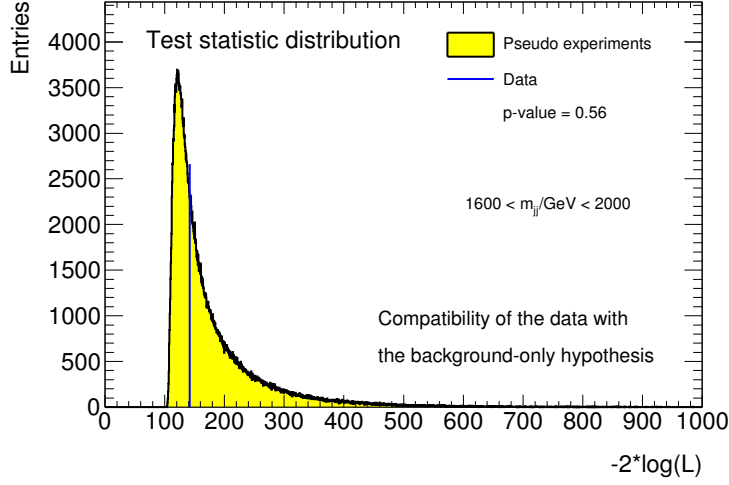


**Figure 9.3.** The log-likelihood test statistic for events with dijet invariant masses between 1600 and 2000 GeV. Shown is the distribution obtained by variations of the Standard Model QCD hypothesis within the statistical and systematic uncertainties (yellow area) and the value observed in the data (blue line).

log-likelihood test (LL) in the five dijet invariant mass bins. All  $p$ -values are large, confirming the compatibility of the observed data with the QCD hypothesis.

The second statistical test is an alteration of the BUMP HUNTER test [135, 136]. While the original BUMP HUNTER test is designed to search for resonant signals, the test applied here is adapted to search for a rise in the  $\chi$ -spectra towards low  $\chi$ -values. It is thus particularly sensitive to new phenomena which are expected to appear predominantly in this part of the  $\chi$ -distribution. The test is performed as follows: The number of events in the QCD prediction is first scaled to the observed number of events in the respective dijet invariant mass bin. The QCD prediction is used to obtain the probability  $\pi(n)$  for any event to be in one of the first  $n$   $\chi$ -bins. Then, the binomial probability  $p(n, N(n), N_{\text{tot}})$  to observe exactly  $N(n)$  out of  $N_{\text{tot}}$  total events in the first  $n$  bins, given the probability  $\pi(n)$ , is calculated by

$$p(n, N(n), N_{\text{tot}}) = \binom{N_{\text{tot}}}{N(n)} \pi(n)^{N(n)} (1 - \pi(n))^{N_{\text{tot}} - N(n)}. \quad (9.4)$$

The probability  $p_{\text{sum}}(n, N(n), N_{\text{tot}})$  to observe at least  $N(n)$  out of  $N_{\text{tot}}$  total events in the first  $n$  bins is

$$p_{\text{sum}}(n, N(n), N_{\text{tot}}) = \sum_{k=N(n)}^{N_{\text{tot}}} p(n, k, N_{\text{tot}}). \quad (9.5)$$

$p_{\text{sum}}(n, N(n), N_{\text{tot}})$  is evaluated for  $n$  between 3 and 11. The result is a set of nine probabilities, and the test statistic is defined as the minimum,

$$TS = \min(p_{\text{sum}}(3, N(3), N_{\text{tot}}), \dots, p_{\text{sum}}(11, N(11), N_{\text{tot}})). \quad (9.6)$$

**Table 9.1.** The statistical agreement of the observed  $\chi$ -distributions with the QCD prediction. Shown are the  $p$ -values for each of the five dijet invariant mass bins obtained with the log-likelihood (LL) and the BUMP HUNTER test. The  $\chi$ -interval with the largest deviation from the background prediction in the BUMP HUNTER test is also reported. The search interval of the BUMP HUNTER test was defined to start from the first  $\chi$ -bin and had to be at least three bins wide.

$m_{jj}$ [GeV]	LL	BUMP HUNTER	
	$p$ -value	$p$ -value	$\chi$ -interval
800 - 1200	0.23	0.17	bins 1 - 9
1200 - 1600	0.31	0.20	bins 1 - 7
1600 - 2000	0.56	0.37	bins 1 - 7
2000 - 2600	0.74	0.38	bins 1 - 3
2600 - 7000	0.83	0.37	bins 1 - 10

The  $p$ -value is calculated by the integration over the normalised test statistic distribution obtained from pseudo-experiments in which the background prediction is varied within the statistical and systematic uncertainties and compared to the nominal background prediction with the BUMP HUNTER test.

Table 9.1 shows the  $p$ -values obtained with the BUMP HUNTER test for the five dijet invariant mass bins of the analysis. Also shown are the  $\chi$ -intervals with the largest deviation from the background prediction. All  $p$ -values are large, indicating a good agreement between the data and the QCD hypothesis. The largest deviation from the QCD prediction is observed over the first nine  $\chi$ -bins in the lowest dijet mass bin with a corresponding  $p$ -value of 17%. The probability to observe a  $p$ -value of 17% or less in any of the five mass bins has been determined in pseudo-experiments and was found to be 43%. The observation that all  $p$ -values obtained in this test are smaller than 50% is consistent with the small excess of the data with respect to the QCD prediction at low and intermediate values of  $\chi$  in all dijet invariant mass bins observed in figure 9.1. The results of the BUMP HUNTER test confirm that this deviation is not significant.

## 9.2. Comparison with an alternative Monte Carlo prediction

The nominal description of the QCD background in this analysis is obtained with the PYTHIA Monte Carlo generator. As a further test of the agreement of the data with the Standard Model, the statistical analysis is repeated with a QCD prediction obtained with the POWHEG Monte Carlo generator [130]. More information about the comparison of the QCD prediction between PYTHIA and POWHEG has been given in section 8.2.3.

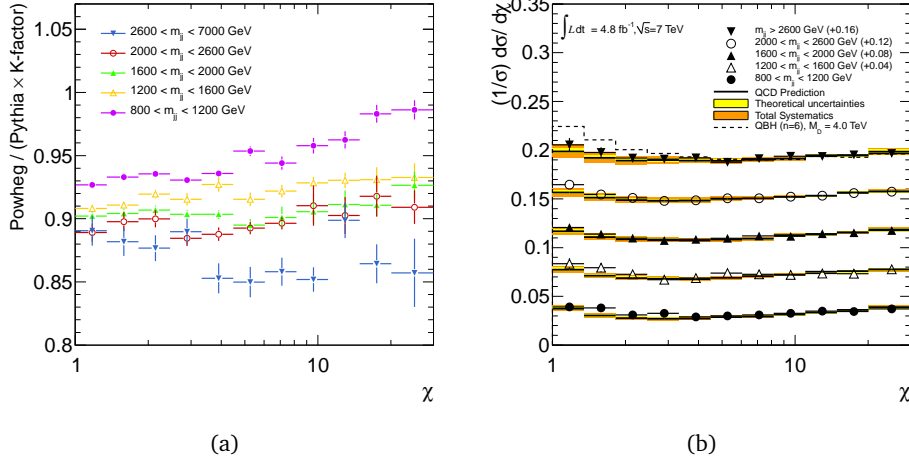


**Figure 9.4.** (a) Comparison of background predictions for the  $\chi$ -distributions obtained with the combination of POWHEG and PYTHIA to PYTHIA corrected with K-factors. Shown are the ratios of the distributions in the five dijet invariant mass bins of the analysis. (b) The  $\chi$ -distributions in the five dijet invariant mass bins. Different offsets have been applied to the distributions for the visualisation. The QCD predictions (solid lines) were obtained with the POWHEG generator and are shown with theoretical uncertainties (yellow bands) and total systematic uncertainties (orange bands). The data points are shown with statistical error bars. The  $\chi$ -distribution of a hypothetical quantum black hole signal is shown in the highest dijet invariant mass bin (dashed line) for  $M_D = 4$  TeV and  $n = 6$  extra dimensions.

Figure 9.4(a) shows a comparison of the background predictions obtained with the two Monte Carlo generators. Shown are the ratios of the predictions obtained with POWHEG with respect to the ones obtained with PYTHIA in the five dijet invariant mass bins. The average of the ratios over all  $\chi$ -bins decreases with the dijet invariant mass, from values of about 0.95 for high masses to about 0.87 for low masses. The ratios are relatively flat as a function of  $\chi$  with the largest variation between any two  $\chi$ -bins in the same dijet invariant mass bin being 6%, observed in the lowest mass bin. The comparison implies that the background predictions for the normalised  $\chi$ -distributions remain largely unchanged.

This is confirmed by figure 9.4(b) that shows the normalised, differential  $\chi$ -distributions in the five dijet mass bins with theoretical and total systematic uncertainties together with the observed data. The same offsets as in figure 9 have been applied to the distributions. As in the case of the nominal background prediction, only very small deviations of the data from the QCD prediction are observed.

To quantify the statistical agreement between the alternative QCD simulation and the data, the same statistical tests as in the case of the background prediction with PYTHIA have been performed. The results are given in table 9.2. Shown are the  $p$ -values in the five dijet invariant mass bins with the background predictions obtained from POWHEG for the log-likelihood test (LL) and the BUMPHUNTER test. In the case of the BUMPHUNTER

**Table 9.2.** The statistical agreement of the observed  $\chi$ -distributions with the QCD prediction from POWHEG. Shown are the  $p$ -values for each of the five dijet invariant mass bins obtained with the log-likelihood (LL) and the BUMPHUNTER test. The  $\chi$ -interval with the largest deviation from the background prediction in the BUMPHUNTER test is also reported. The search interval of the BUMPHUNTER test was defined to start from the first  $\chi$ -bin and had to be at least three bins wide.

$m_{jj}$ [GeV]	LL	BUMPHUNTER	
	$p$ -value	$p$ -value	$\chi$ -interval
800 - 1200	0.09	0.06	bins 1 - 4
1200 - 1600	0.27	0.15	bins 1 - 7
1600 - 2000	0.44	0.27	bins 1 - 7
2000 - 2600	0.70	0.41	bins 1 - 3
2600 - 7000	0.90	0.38	bins 1 - 8

test, the  $\chi$ -intervals with the largest deviation from the background hypothesis are also reported. The smallest  $p$ -values are observed in the lowest dijet invariant mass bin with both tests. With values of 9% and 6% for the log-likelihood and the BUMPHUNTER tests, respectively, these  $p$ -values are smaller than the ones observed when the PYTHIA prediction is used for the background simulation. This observation is in agreement with the slight inclination towards higher  $\chi$ -values of the ratio of the POWHEG prediction with respect to the PYTHIA prediction observed in the lowest dijet invariant mass bin in figure 9.4(a). From the size of all  $p$ -values, it has been concluded that the data are also in agreement with the background prediction from this alternative Monte Carlo generator.

In conclusion, two tests have been performed: a log-likelihood test that is sensitive to any differences between the predicted and observed  $\chi$ -distributions and the BUMPHUNTER test that is particularly sensitive to signal-like features in the  $\chi$ -distributions which are characterised by an excess of events at low  $\chi$ -values. Both tests indicate a good agreement of the observed data with the QCD hypothesis. The consistency has been confirmed by a test with an alternative Monte Carlo generator for the QCD prediction. The interpretation is thus that the measurement is in agreement with Standard Model predictions.



# 10. Constraints on physics beyond the Standard Model

The analysis presented in the previous chapter showed that the observed data are in agreement with the Standard Model QCD prediction. The measurement can thus be used to constrain the characteristic parameters of the two theories for new phenomena which were introduced in chapter 2. Bayesian limits at 95% C.L. are reported on the compositeness scale  $\Lambda$  in a quark contact interaction model with destructive interference and on the reduced Planck scale  $M_D$  in a model for quantum black hole production with six extra dimensions.

## 10.1. Bayesian framework

As discussed in [10] and the references therein, Bayes' theorem for conditional probabilities can be interpreted as an expression for the *degree of belief* in a hypothesis,

$$p(\text{theory}(\xi)|\text{data}) = \frac{p(\text{data}|\text{theory}(\xi)) \times p(\text{theory}(\xi))}{p(\text{data})}. \quad (10.1)$$

Here, the hypothesis, symbolically written as *theory*, corresponds to a prediction for the  $\chi$ -distributions. It is specified by a theory parameter  $\xi$  such as the compositeness scale  $\Lambda$  or the reduced Planck scale  $M_D$ . Before the experiment is carried out, the subjective degree of belief in a certain value of the theory parameter is characterised by the *prior* probability density function (pdf)  $p(\text{theory}(\xi))$ . In this thesis, prior pdfs which are constant in  $1/\Lambda^4$ ,  $1/\Lambda^2$  and  $1/M_D^4$  have been used as discussed below. The *data* denote the result of the measurement and correspond to the observed  $\chi$ -distributions.  $p(\text{theory}(\xi)|\text{data})$ , the *posterior* pdf, expresses the updated degree of belief in the hypothesis with parameter  $\xi$  after the experiment has been carried out and the data are known.

Bayes' theorem relates the posterior pdf to the prior pdf via  $p(\text{data}|\text{theory}(\xi))$  and  $p(\text{data})$ .  $p(\text{data}|\text{theory}(\xi))$  is the *likelihood* to observe the measured data under the signal hypothesis specified by the theory parameter  $\xi$ .  $p(\text{data})$  is the probability to observe the data. In this context, it plays the role of a normalisation constant which is chosen such that the right-hand-side of equation 10.1 is a properly normalised pdf when evaluated as a function of  $\xi$ .

The first step in the Bayesian analysis is the determination of the posterior pdf for all values of  $\xi$  in the studied parameter range. Then, the 95% credibility level (C.L.) lower limit  $\xi_{95\%}^-$  on  $\xi$  is defined by

$$\int_{\xi_{95\%}^-}^{\infty} d\xi p(\text{theory}(\xi)|\text{data}) = 0.95 \cdot \int_0^{\infty} d\xi p(\text{theory}(\xi)|\text{data}), \quad (10.2)$$

and the upper limit  $\xi_{95\%}^+$  is

$$\int_0^{\xi_{95\%}^+} d\xi p(\text{theory}(\xi)|\text{data}) = 0.95 \cdot \int_0^{\infty} d\xi p(\text{theory}(\xi)|\text{data}), \quad (10.3)$$

where  $\xi = \infty$  represents the largest possible value of  $\xi$ , and  $\xi = 0$  is the lowest possible value. In this analysis, upper limits are set on inverse powers of  $\Lambda$  and  $M_D$  which translate into lower limits on these scales.

The sensitivity of an experiment to a certain model of new phenomena can be characterised by the expected limit  $\bar{\xi}_{95\%}^{+/-}$ . It is obtained by evaluating equation 10.2 or 10.3 after replacing the experimental data with simulations of the background prediction, sampled within the corresponding statistical and systematic uncertainties. Each of these pseudo-experiments results in a different posterior pdf and thus in a different value of  $\xi_{95\%}^{+/-}$ . The expected limit is defined as the median of the resulting distribution.

## 10.2. Determination of the posterior probability density function

The calculation of the posterior pdf is performed by the evaluation of the right-hand-side of equation 10.1 as described above. Since the contribution from possible signals is primarily expected at high dijet masses, the  $\chi$ -distributions in the highest dijet invariant mass bin of the analysis are used for the limit setting. Various assumptions can be made for the prior pdf. Often, a *non-informative prior pdf* is used to express the lack of knowledge about the value of the theory parameter as discussed in [10] and the references therein. Here, the prior pdfs are chosen to be constant in  $1/\Lambda^4$  and  $1/M_D^4$ . In order to be normalisable, they are set to zero below  $1/\Lambda^4 = 0$  and  $1/M_D^4 = 0$  and above cut-off values that are arbitrarily chosen outside the physically interesting parameter range.

In the case of the quark contact interaction model, a comparison is made with a prior pdf constant in  $1/\Lambda^2$ . Depending on the partonic subprocesses, the quark contact interaction model gives in general rise to three terms in the differential cross section as was discussed in chapter 2: a pure contact interaction term, a pure Standard Model QCD term and an interference term. While the first prior pdf is motivated by the dependence of the cross section of the pure contact interaction term on  $\Lambda$ , the second

one is motivated by the dependence of the cross section of the interference term on  $\Lambda$ . All choices for the prior pdfs are consistent with earlier analyses [123]. With the prior pdfs defined in this way and  $p(\text{data})$  being a constant of integration, the evaluation of the right-hand-side of equation 10.1 reduces to the evaluation of the likelihood  $p(\text{data}|\text{theory}(\xi))$  for the observed data and varying theory predictions, characterised by  $\Lambda$  and  $M_D$ .

For binned data with a fixed number of total entries, i. e. for the analysis of normalised spectra, the Poissonian likelihood [10] which was also used for the determination of  $p$ -values in chapter 9 can be applied,

$$p(\text{data}|\text{theory}(\xi)) = \mathcal{L}(\xi) = \prod_{i=1}^{n_{\text{bins}}=11} p_i(\xi), \quad \text{with} \quad p_i(\xi) = \frac{\mu_i^{n_i}(\xi)}{n_i!} e^{-\mu_i(\xi)}. \quad (10.4)$$

The product is evaluated over all eleven  $\chi$ -bins in the highest dijet mass bin, after scaling the predicted total number of events to the one in data.  $p_i$  denotes the Poissonian probability to observe  $n_i$  events in  $\chi$ -bin  $i$  when  $\mu_i$  events are predicted by the hypothesis. The result of this calculation is the value of the likelihood, and thus the posterior probability density, for one value of the theory parameter  $\xi$ .

The expected number of events  $\mu_i(\xi)$  is derived from Monte Carlo simulations of the two signal hypotheses. Predictions for the quark compositeness scenario at leading order and with destructive interference were obtained with the PYTHIA generator. The fraction of the cross section corresponding to pure QCD processes was corrected for NLO effects with the K-factors described in section 4.3. Monte Carlo samples for  $\Lambda$  set to 4, 6, 8 and 10 TeV were generated. For the quantum black hole model in which no interference with the Standard Model QCD interactions is assumed, the signal simulation was performed by adding events generated with BLACKMAX and PYTHIA to the Standard Model QCD prediction. The QCD contribution has been multiplied with the bin-wise K-factors before the quantum black hole signal was added. Samples with  $M_D$  set to 0.75, 1.00, 1.50, 2.00, 2.25, 2.50, 2.75, 3.00, 3.50, 4.00, 4.50, 5.00, 5.50 and 6.00 TeV were produced.

### 10.3. Parametrisation of the signal hypotheses

To allow the integration that is needed for the limit calculation described in equation 10.3, the full form of the posterior pdf must be known for all values of  $\xi$  in the studied parameter range. Due to limited computing resources, Monte Carlo samples were, however, only available for the set of theory parameters mentioned above.

To circumvent this problem, interpolating fits were used to derive theory predictions for arbitrary values of the model parameters, as has been done in earlier analyses [123]. In every  $\chi$ -bin, the normalised differential cross section  $(1/\sigma)d\sigma/d\chi$ , containing both the contributions from the signal and QCD as described above, was fitted as a function of  $1/\Lambda^4$ ,  $1/\Lambda^2$  or  $1/M_D^4$ , depending on the hypothesis and the choice of the prior pdf and

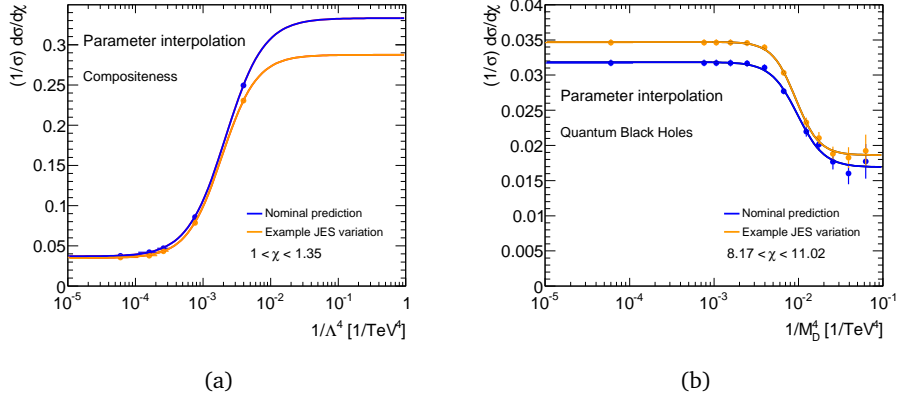


**Figure 10.1.** Interpolation of the signal prediction as a function of the theory parameters in the highest dijet invariant mass bin,  $2600 < m_{jj} < 7000$  GeV. Both the interpolation for the nominal signal prediction (blue curves) and for one variation of the prediction within the jet energy scale uncertainties (orange curves) are shown. The markers correspond to the predictions from the available Monte Carlo samples with statistical uncertainties. (a) Fit for the contact interaction model in the range  $1 < \chi < 1.35$ . (b) Fit for the quantum black hole scenario in the range  $8.17 < \chi < 11.02$ .

using the available Monte Carlo predictions as sampling points for the fits. In agreement with the previous analyses, the fit function was chosen to be

$$f(x) = a_1 + a_2 \cdot (1 / \exp(a_3 \cdot (a_4 - \log x) + 1)), \quad (10.5)$$

with the fit parameters  $a_1$ ,  $a_2$ ,  $a_3$  and  $a_4$ . The fit function is motivated by the dependence of the normalised differential angular distributions on the parameters in the models for new phenomena: For every value of  $\chi$ , they are expected to be approximately constant for small  $x$ , i. e. large characteristic scales, until the value of the model parameter is within the reach of the experiment. Beyond this point, they change fast as the characteristic scale decreases and  $x$  increases. Finally, for very small values of the model parameter, i. e. large values of  $x$ , the differential  $\chi$ -spectrum asymptotically approaches the isotropic shape predicted by the signal models, such that the normalised dijet angular distributions no longer depend on the value of the theory parameter. The interpolation was performed for the nominal signal simulation as well as for variations of the model prediction within the experimental uncertainties. The latter will be discussed in the next section.

Figure 10.1 shows the result of the interpolation and the available Monte Carlo data points for the nominal signal prediction in one  $\chi$ -bin for each of the two models. Figure 10.1(a) presents the results for  $\chi$  between 1 and 1.35, i. e. for central events, in the contact interaction model. As expected, the normalised differential cross section rises as the value of the compositeness scale decreases. Small values of  $1/\Lambda^4$  correspond to the QCD-dominated regime. Figure 10.1(b) shows the results for the quantum black hole model in the 8th  $\chi$ -bin which contains  $\chi$ -values between 8.17 and 11.02. Since the signal predominantly appears at low  $\chi$ -values, the normalised differential cross section

at high values of  $\chi$  decreases as  $M_D$  decreases.  $M_D \rightarrow \infty$  describes the case where no contribution from quantum black hole production is added to the distributions expected from QCD. The interpolation provides a satisfying description of the signal prediction as a continuous function of the model parameters. As a result of this interpolation, the posterior pdf can be determined for all values of the characteristic scales of the two models.

## 10.4. Inclusion of systematic uncertainties

The dependence of the theory prediction on systematic uncertainties needs to be taken into account when calculating the likelihood  $p(\text{data}|\text{theory}(\xi))$ . Formally, the uncertainties can be included via nuisance parameters  $\nu$  in the Bayesian framework as described in [10] and the references therein. Examples for nuisance parameters in this analysis are the components of the residual jet energy scale calibration such as the flavour composition of the sample or the correction for the pseudorapidity intercalibration discussed in chapter 8. The likelihood is marginalised as

$$p(\text{data}|\text{theory}(\xi)) = \int d\nu \pi(\nu) \cdot p(\text{data}|\text{theory}(\xi, \nu)). \quad (10.6)$$

Here,  $\nu$  denotes the set of  $k$  nuisance parameters  $\nu = \{\nu_1, \nu_2, \dots, \nu_k\}$ . Since the values of the nuisance parameters are not known exactly, the likelihood has to be integrated over all possible values of  $\nu$ , weighted with a pdf  $\pi(\nu)$  that describes the degree of believe in a possible set of the values.  $\pi(\nu)$  has the form of a  $k$ -dimensional pdf  $\pi(\nu) = \pi_1(\nu_1) \cdot \pi_2(\nu_2) \cdot \dots \cdot \pi_k(\nu_k)$ . In practise, the integral is approximated by a sum over an ensemble of pseudo-experiments in which the nuisance parameters  $\nu$  are varied within their uncertainties according to  $\pi(\nu)$ .

The nuisance parameters considered here were the fourteen components of the jet energy scale and the two scales  $\mu_R$  and  $\mu_F$ . Together, these represent the sources of the largest experimental and the largest theoretical uncertainty in the analysis as discussed in chapter 8. Each of the fourteen components of the jet energy scale was sampled from a Gaussian distribution with the mean set to the most probable value of the parameter and whose standard deviation corresponds to the uncertainty on the parameter. The interpolation procedure which was introduced in the previous section was used to obtain the theory prediction for each variation of the jet energy scale as a function of the theory parameters. Two examples are shown in figure 10.1. They confirm that the interpolation provides a satisfying description of the signal prediction as a function of the theory parameters also if the jet energy scale is changed with respect to its nominal value.

The impact of the renormalisation and factorisation scale uncertainties on the normalised  $\chi$ -distributions were assumed to be the same as for the distributions predicted by Standard Model QCD. The baseline values and the eight variations of these scales discussed in chapter 8 have been used on top of the jet energy scale variations to take the theoretical uncertainties into account.

## 10.5. Limits for quark contact interactions

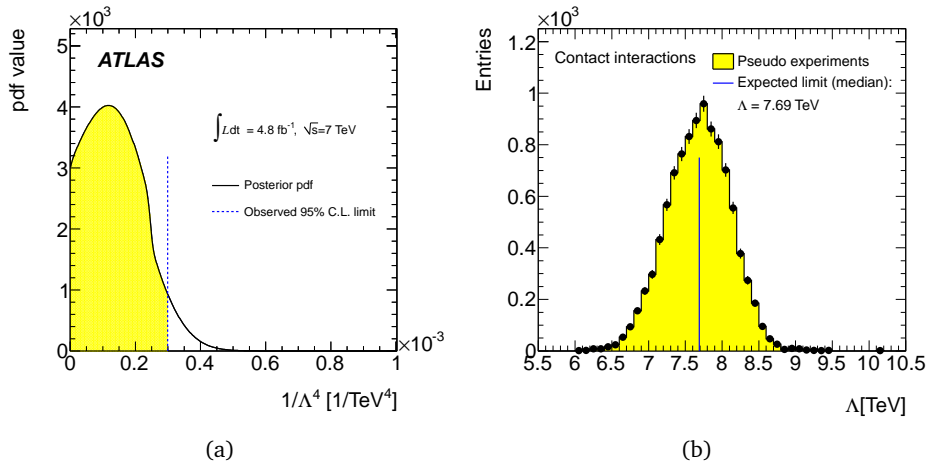


**Figure 10.2.** (a) The posterior pdf (black, solid line) and the observed 95% C.L. limit (blue, dashed line) for the contact interaction model and a prior pdf constant in  $1/\Lambda^4$ , with  $\Lambda$  denoting the compositeness scale; also appeared in [2]. (b) The limit distribution from QCD pseudo-experiments (black markers and yellow area) and the expected limit (blue line) for the contact interaction model and a prior pdf constant in  $1/\Lambda^4$ ; also appeared in [89].

Figure 10.2(a) shows the resulting posterior pdf for the contact interaction scenario with destructive interference and a prior pdf constant in  $1/\Lambda^4$ . The yellow area contains 95% of the area under the curve, such that the observed limit is 7.6 TeV. Figure 10.2(b) shows the limit distribution from QCD pseudo-experiments. The median of the distribution, i.e. the expected limit, is 7.7 TeV. A prior flat in  $1/\Lambda^2$  was used for comparison. Figure 10.3(a) shows the corresponding posterior pdf. The observed limit is 8.0 TeV in this case. The expected limit is 8.1 TeV, and figure 10.3(b) shows the distribution from which this number has been obtained. The fact that the observed limits are slightly below the expected ones is consistent with the observation that the data show a slight signal-like behaviour as seen in figure 9.1.

Before the LHC era, the most stringent lower limits on the compositeness scale in quark contact interactions were obtained in dijet angular analyses at the Tevatron. An analysis by the  $D\bar{0}$  experiment constrained  $\Lambda$  to be above 3.06 TeV at 95% C.L. [55]. Contrary to other studies [40], the  $D\bar{0}$  results yield the same limits for destructive and constructive interference. Initial calculations for the expected performance of the LHC experiments predicted a limit on  $\Lambda$  between 20 and 40 TeV with a centre-of-mass energy of  $\sqrt{s} = 14$  TeV at the design luminosity [40, 137]. In models that assume also the leptons to be composite, the compositeness scale may be constrained even further. However, as they are less general, these models are not discussed here. An analysis of the ATLAS data from 2010 with an integrated luminosity of  $36 \text{ pb}^{-1}$  of  $pp$  collisions at  $\sqrt{s} = 7$  TeV obtained a lower limit of 6.6 TeV on  $\Lambda$  from the analysis of the  $\chi$ -distributions [123]. The same publication also reported lower limits of 9.5 TeV from the analysis of the

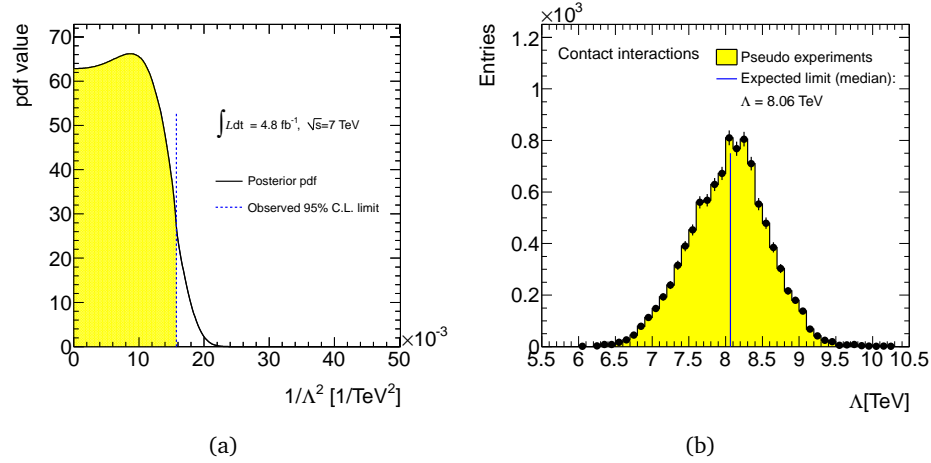


**Figure 10.3.** (a) The posterior pdf (black, solid line) and the observed 95% C.L. limit (blue, dashed line) for the contact interaction model and a prior pdf constant in  $1/\Lambda^2$ , with  $\Lambda$  denoting the compositeness scale. (b) The limit distribution from QCD pseudo-experiments (black markers and yellow area) and the expected limit (blue line) for the contact interaction model and a prior pdf constant in  $1/\Lambda^2$ ; both figures also appeared in [89].

variable  $F_\chi(m_{jj})$ . These limits, calculated with a modified frequentist approach [138], were much stronger than the expected limit of 5.7 TeV since fewer central events with masses above 2.2 TeV than predicted were observed. A Bayesian approach yielded a similar expected limit as the frequentist method and an observed limit that was only 1 TeV higher. An analysis of the dijet angular distributions by the CMS experiment with a comparable integrated luminosity and at the same centre-of-mass energy set a lower limit of  $\Lambda = 5.6 \text{ TeV}$  [61].

The analysis in this thesis improved the expected lower limits published in [61, 123] by 2 TeV or more, depending on the statistical method and the observable. Compared to the Bayesian observed limit from [123], the observed limit has been improved by 900 GeV, consistent with the fact that a downward fluctuation was observed in the earlier analysis, whereas the data appear slightly signal-like here. The observed lower limit in this analysis is also 2 TeV higher than the observed limit in [61] which was obtained with a frequentist approach.

Very recently, CMS published an updated limit on the quark compositeness scale at  $\Lambda = 9.9 \text{ TeV}$  from the study of inclusive jet  $p_T$  spectra [139] with an integrated luminosity of  $5 \text{ fb}^{-1}$  at  $\sqrt{s} = 7 \text{ TeV}$ . The difference in performance with respect to the analysis presented here is explained by the lower jet energy scale uncertainty at high  $p_T$  used by the CMS collaboration [140, 141]. In the future, ATLAS will be able to improve the current limits by the analysis of the data collected at  $\sqrt{s} = 8 \text{ TeV}$  and by reducing the jet energy scale uncertainty at high  $p_T$ , which is a limiting factor of the analysis, as shown in chapter 8.

## 10.6. Limits for quantum black holes

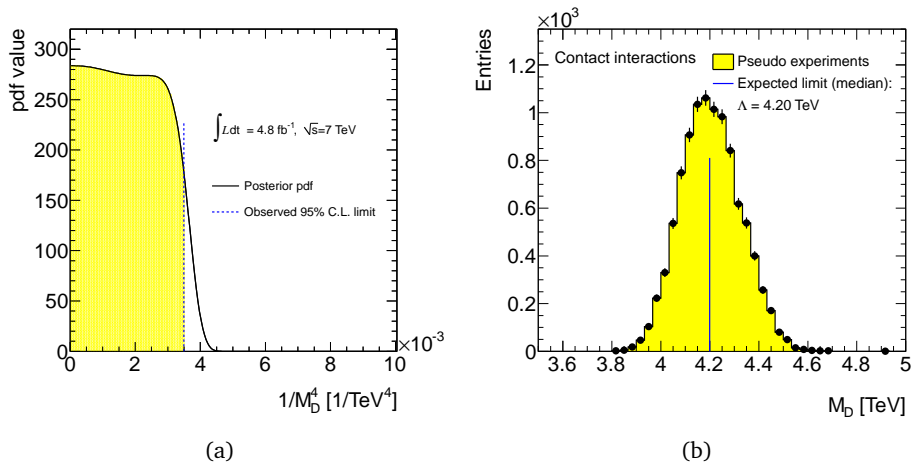


**Figure 10.4.** (a) The posterior pdf (black, solid line) and the observed 95% C.L. limit (blue, dashed line) for the quantum black hole model and a prior pdf constant in  $1/M_D^4$ , with  $M_D$  denoting the reduced Planck scale. (b) The limit distribution from QCD pseudo-experiments (black markers and yellow area) and the expected limit (blue line) for the quantum black hole model and a prior pdf constant in  $1/M_D^4$ ; both figures also appeared in [89].

Figure 10.4(a) shows the posterior pdf for the quantum black hole model with  $n = 6$  extra dimensions and a prior pdf constant in  $1/M_D^4$ . The observed limit on  $M_D$  is 4.11 TeV. Figure 10.4(b) shows the distribution of limits obtained using simulated data without signal contribution. The expected limit on  $M_D$  is 4.20 TeV. As in the case of the contact interaction scenario, the observed limit is slightly below the expected one, consistent with the observed data.

The ATLAS collaboration previously published limits on the reduced Planck scale obtained in the analysis of dijet events in  $36 \text{ pb}^{-1}$  of  $pp$  collisions at  $\sqrt{s} = 7 \text{ TeV}$  [123]. The 95% C.L. lower limits were 3.49 TeV from the analysis of the  $\chi$ -distribution and 3.69 TeV from the analysis of the shape parameter  $F_\chi$  for a quantum black hole model with  $n = 6$  extra dimensions. Values between 0.75 TeV and 3.64 TeV were excluded at 95% C.L. by the analysis of the dijet mass spectrum. These limits have been superseded by the work presented in this thesis: The observed limit was improved by 420 GeV with respect to the best lower limit reported in [123], while the expected lower limit was improved by 830 GeV.

The reduced Planck scale can also be constrained by analysing complementary signatures at the LHC albeit with smaller sensitivity. One signature of ADD extra dimensions are monojet events. In this model, the introduction of extra dimensions into which only gravity can propagate leads to an enlarged production of gravitons which can escape into the additional dimensions. These gravitons can be co-produced with hadronic jets, and the experimental signature are monojet events with missing trans-

verse energy. The reduced Planck scale has been constrained to be above 2.51 TeV for  $n = 6$  ADD extra dimensions by the analysis of monojet events in  $4.7\text{fb}^{-1}$  of  $pp$  collision data at  $\sqrt{s} = 7\text{TeV}$  collected with ATLAS [142]. The corresponding analysis of monojet events at  $\sqrt{s} = 7\text{TeV}$  by the CMS collaboration with an integrated luminosity of  $5.0\text{fb}^{-1}$  set a lower limit of 2.38 TeV on the reduced Planck scale in a model with six ADD extra dimensions [143]. CMS has also searched for quantum black holes in dijet and multiparticle final state events. The analyses, however, used a different model of quantum black holes, and no direct limits on the reduced Planck scale have been derived [144, 145].

In conclusion, the presented analysis has found the data to be in agreement with the Standard Model prediction. Consequently, the data in the highest dijet invariant mass bin have been used to improve the lower limits on the characteristic scales of two models for phenomena beyond the Standard Model with respect to earlier analyses. The compositeness scale  $\Lambda$  has been constrained to be above 7.6 TeV, and the reduced Planck scale  $M_D$  has been confined to values above 4.11 TeV for a quantum black hole model with  $n = 6$  extra dimensions. The observed limits were close to the expected limits for both models. In the future, ATLAS will be able to further improve the sensitivity to new phenomena beyond the Standard Model by the analysis of the  $\sqrt{s} = 8\text{TeV}$  data and by reducing the jet energy scale uncertainty at high transverse momenta.



# 11. Conclusions

The high-energy proton-proton collisions at the LHC can be used to probe QCD interactions at the highest momentum transfers and to search for physics beyond the Standard Model. Dijet angular distributions, normalised to the cross section, are well-suited for such searches due to their reduced sensitivity to systematic uncertainties. In this thesis, the full 2011 dataset of proton-proton collisions at a centre-of-mass energy of  $\sqrt{s} = 7$  TeV, corresponding to an integrated luminosity of  $4.8 \text{ fb}^{-1}$  and recorded with the ATLAS detector, has been used to measure the dijet angular distributions in five bins of the dijet invariant mass.

Various studies have been performed to analyse the stability of the data taking conditions, the contributions from pile-up and the distributions of kinematic observables. A strategy to retain the physically-motivated flat shape of the dijet angular distributions under the influence of a pseudorapidity-dependent change of the detector response to jets was developed and implemented. The highest dijet mass was observed at 4.36 TeV, while the highest jet transverse momentum was found at 1.99 TeV.

The dominant experimental uncertainty is due to the jet energy scale and has been evaluated using pseudo-experiments. The approach includes the full available correlation information. The uncertainty on the normalised angular distributions increases with the dijet mass and reaches 17% for the highest dijet masses. The uncertainties due to the jet energy and jet angular resolution have been observed to be negligible. The dominant theoretical uncertainty originates from the uncertainty on the renormalisation and factorisation scales. It increases with the dijet mass and reaches 8% for the highest dijet masses. The uncertainty due to the parton distribution functions is below 1.2% for all dijet masses.

The data have been compared to a QCD prediction obtained from Monte Carlo simulations and corrected for NLO effects. No statistically significant deviation has been observed, and 95% C.L. Bayesian exclusion limits have been set on the characteristic parameters of two models for physics beyond the Standard Model. In a quark contact interaction scenario with destructive interference, the compositeness scale  $\Lambda$  is excluded below 7.6 TeV, while the expected limit was 7.7 TeV. A quantum black hole model with six extra dimensions is excluded for values of the reduced Planck scale  $M_D$  below 4.1 TeV, while the expected exclusion was below 4.2 TeV.

In the future, the analysis of the dijet angular distributions will profit from the increased centre-of-mass energy and an improved knowledge of the jet energy scale at the largest transverse momenta.



# A. Supplementary material

## A.1. Kinematic distributions

Figure A.1 shows the distribution of the leading and the subleading jet transverse momenta versus rapidities for the intermediate dijet invariant mass bins, obtained from Monte Carlo simulations. The kinematic selection is discussed in chapter 6.

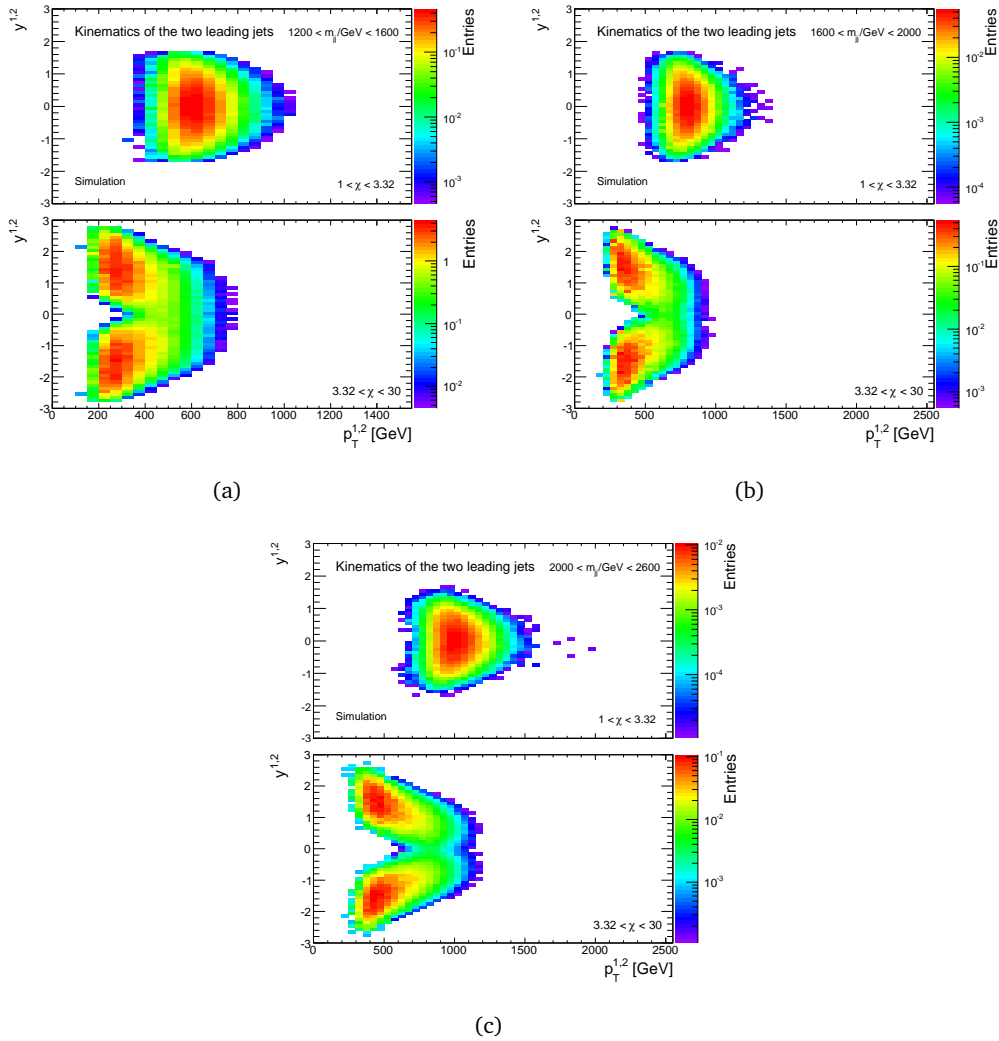


**Figure A.1.** Distribution of the leading and the subleading jet transverse momentum  $p_T^{1,2}$  versus rapidity  $y^{1,2}$  for events in (a) the second-lowest, (b) the third-lowest and (c) the second-highest dijet invariant mass bins of the analysis obtained from Monte Carlo simulations. The upper figures show events with  $\chi < 3.32$ , whereas the lower plots show events with  $3.32 < \chi < 30$ ; also appeared in [89].

## A.2. Out-of-time pile-up

This section contains kinematic distributions for the intermediate dijet invariant mass bins, used in the analysis of out-of-time pile-up effects. Figure A.2 shows the distribution of the transverse momentum of the leading jet measured in data for different positions in the bunch trains. Figure A.3 shows the corresponding distributions for the dijet invariant mass. The study of out-of-time pile-up effects is discussed in chapter 7.

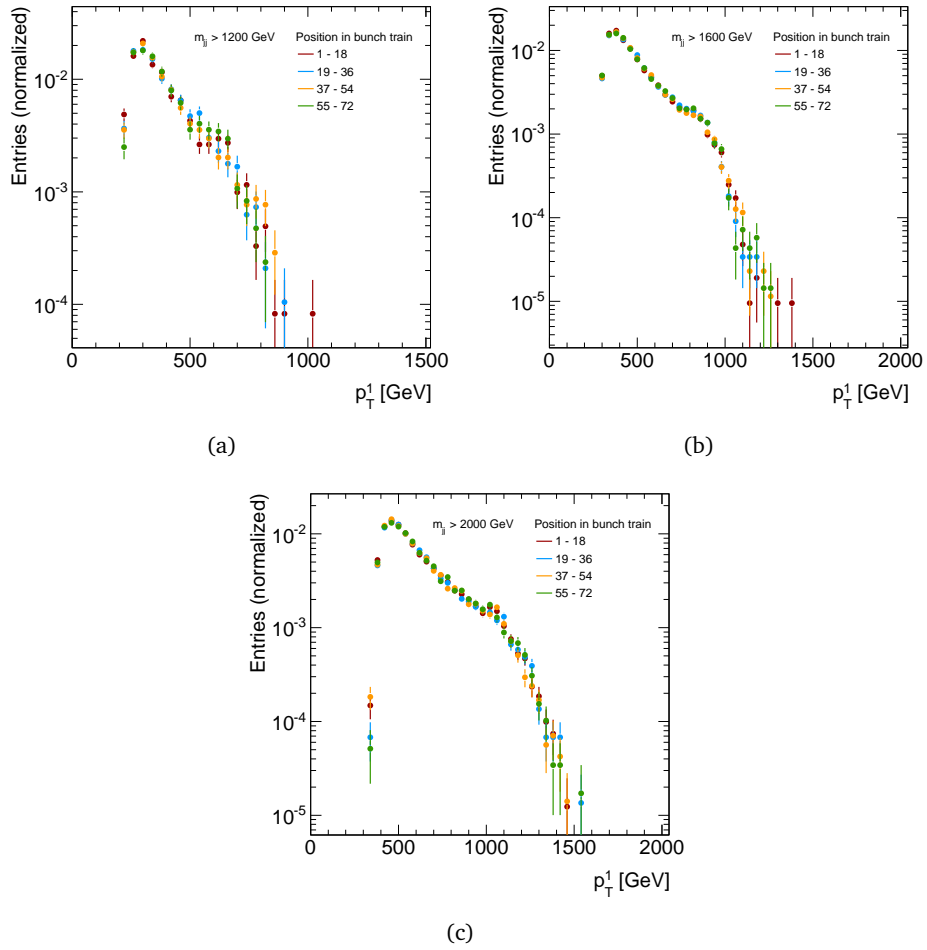


**Figure A.2.** The transverse momentum of the leading jet for events with dijet invariant masses (a) above 1200 GeV (b) above 1600 GeV and (c) above 2000 GeV after the analysis selection and for different positions in a bunch train. The distributions have been measured in data and are shown with statistical uncertainties. All distributions have been normalised to unit area.

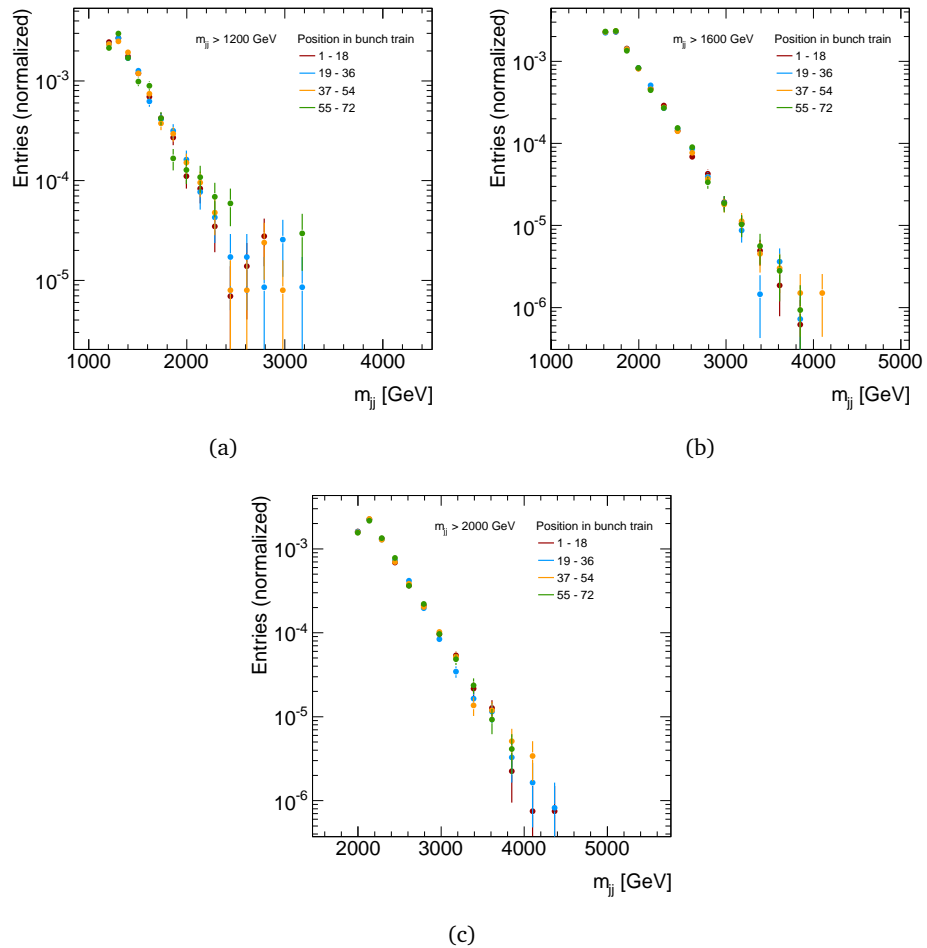


**Figure A.3.** The dijet invariant mass (a) above 1200 GeV, (b) above 1600 GeV and (c) above 2000 GeV after the analysis selection and for different positions in a bunch train. The distributions have been measured in data and are shown with statistical uncertainties. All distributions have been normalised to unit area.

### A.3. Events with high- $p_T$ jets and high dijet invariant masses

This section provides additional information about the events with high- $p_T$  jets and high dijet invariant masses discussed in section 7.5. First, the events that contained the leading jets with the second-, third- and fourth-largest  $p_T$  are shown in figures A.4 to A.6. Second, information about the events with the highest and second-highest dijet invariant mass is provided in in table A.1 and complemented with the event displays in figures A.7 and A.8.

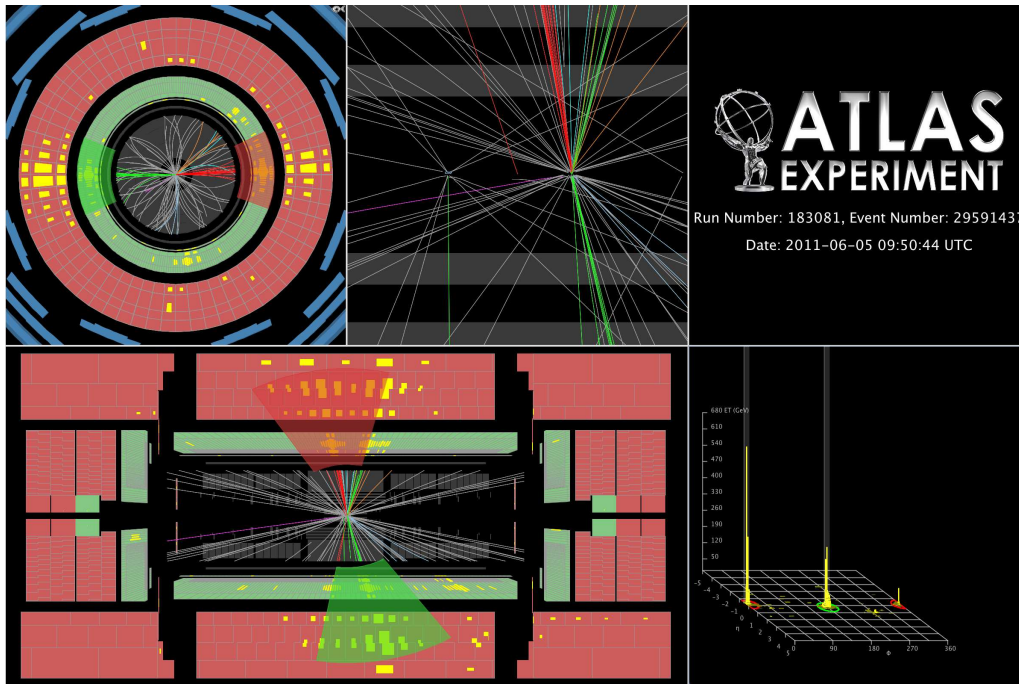


**Figure A.4.** The event with the second-highest leading jet- $p_T$  in the analysis. In this event, the leading jet had a transverse momentum of  $p_T^1 = 1892$  GeV, and the subleading jet had a transverse momentum of  $p_T^2 = 1763$  GeV. The invariant mass of the dijet system was  $m_{jj} = 3728$  GeV. Only tracks with  $p_T^{\text{track}} > 500$  MeV are displayed. The event was recorded on June 5th, 2011.

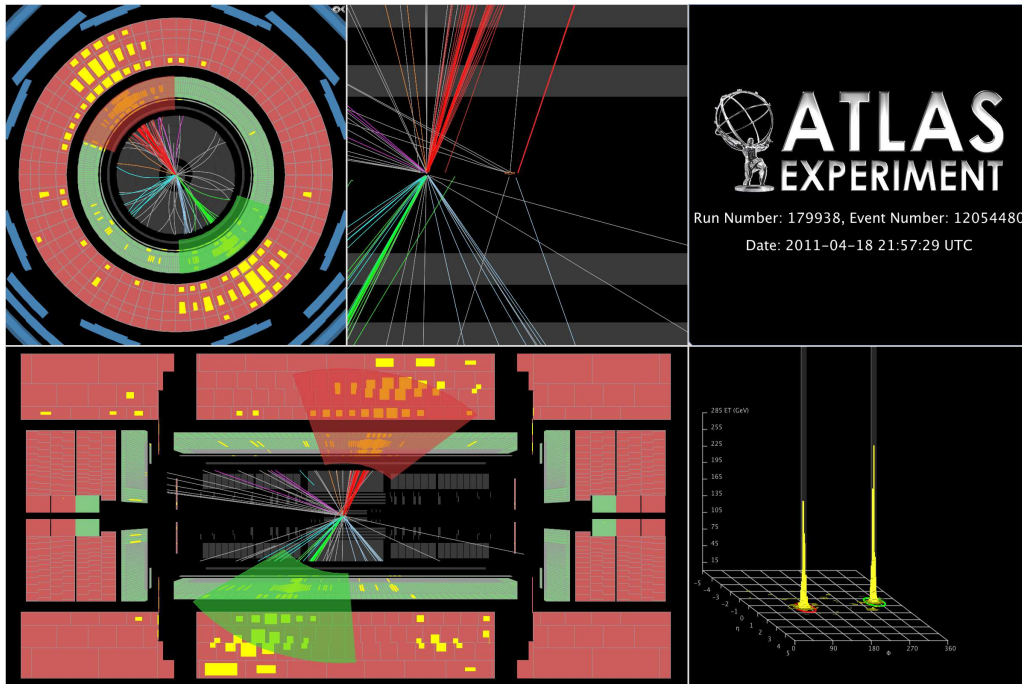


**Figure A.5.** The event with the third-highest leading jet- $p_T$  in the analysis. In this event, the leading jet had a transverse momentum of  $p_T^1 = 1861$  GeV, and the subleading jet had a transverse momentum of  $p_T^2 = 1836$  GeV. The invariant mass of the dijet system was  $m_{jj} = 4049$  GeV. Only tracks with  $p_T^{\text{track}} > 500$  MeV are displayed. The event was recorded on April 18th, 2011.

**Table A.1.** The events with the highest dijet invariant mass in the analysis.

$p_T^1$ [GeV]	$p_T^2$ [GeV]	$m_{jj}$ [GeV]	$\chi$	Run	Event
907	789	4358	24.4	186965	202038333
941	679	4346	27.0	189049	65749467

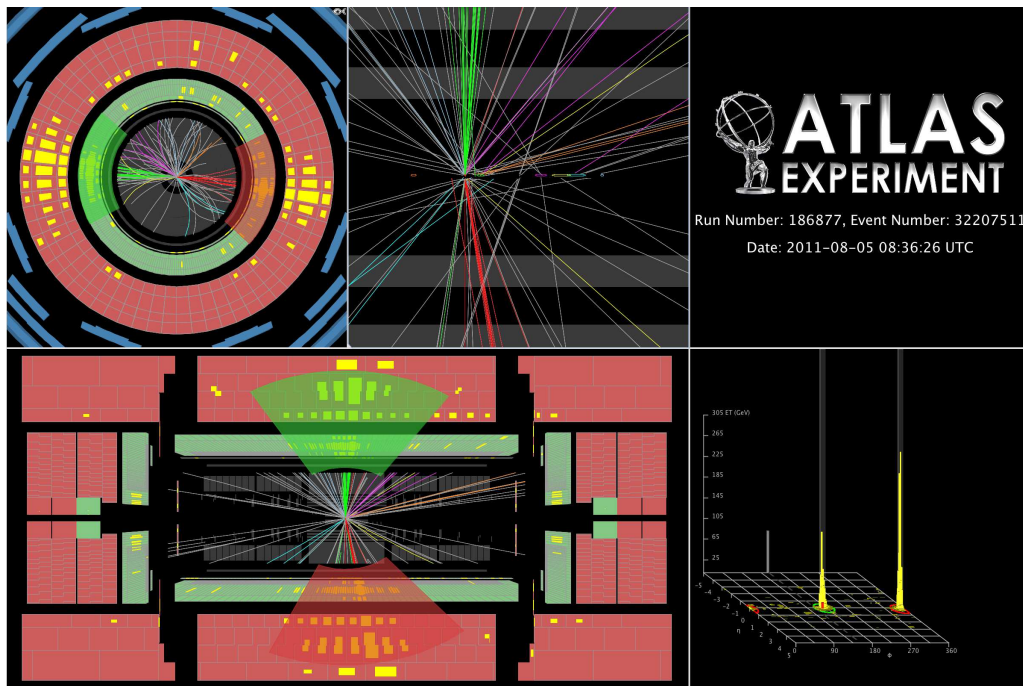


**Figure A.6.** The event with the fourth-highest leading jet- $p_T$  in the analysis. In this event, the leading jet had a transverse momentum of  $p_T^1 = 1817 \text{ GeV}$ , and the subleading jet had a transverse momentum of  $p_T^2 = 1602 \text{ GeV}$ . The invariant mass of the dijet system was  $m_{jj} = 3431 \text{ GeV}$ . Only tracks with  $p_T^{\text{track}} > 500 \text{ MeV}$  are displayed. The event was recorded on August 5th, 2011.

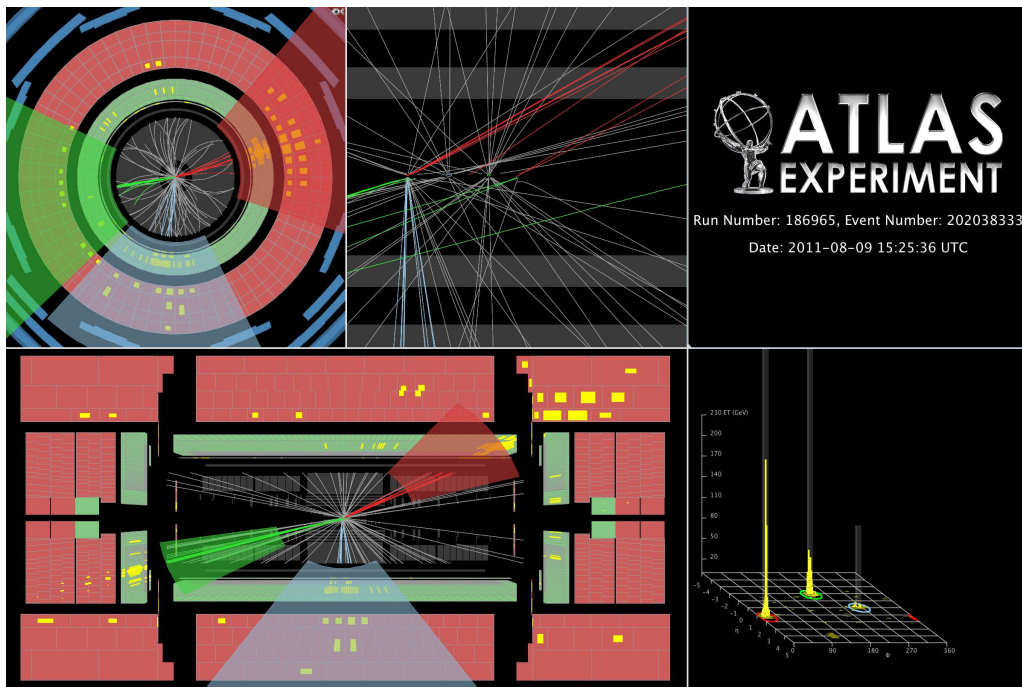


**Figure A.7.** The event with the highest dijet invariant mass in the analysis. In this event, the leading jet had a transverse momentum of  $p_T^1 = 907$  GeV, and the subleading jet had a transverse momentum of  $p_T^2 = 789$  GeV. The invariant mass of the dijet system was  $m_{jj} = 4358$  GeV. Only tracks with  $p_T^{\text{track}} > 500$  MeV are displayed. The event was recorded on August 9th, 2011.

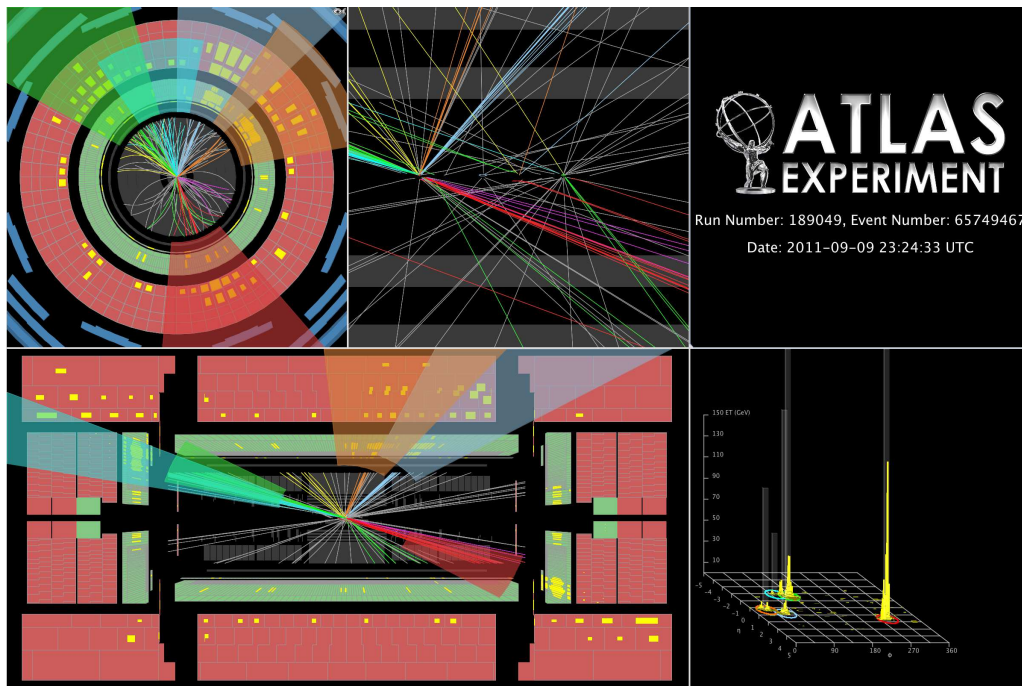
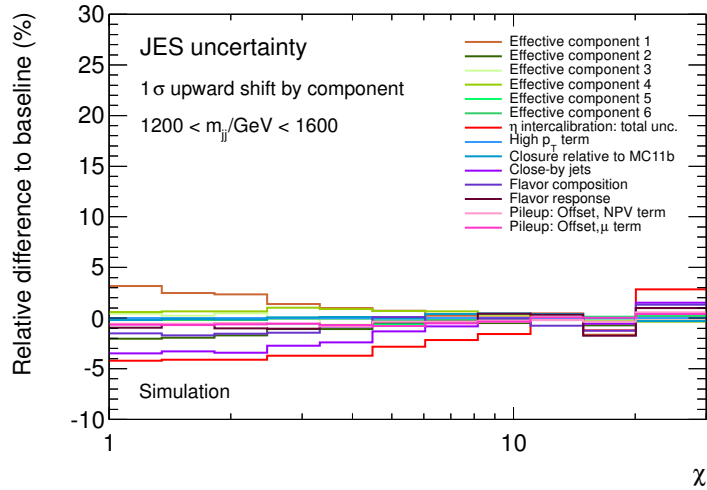


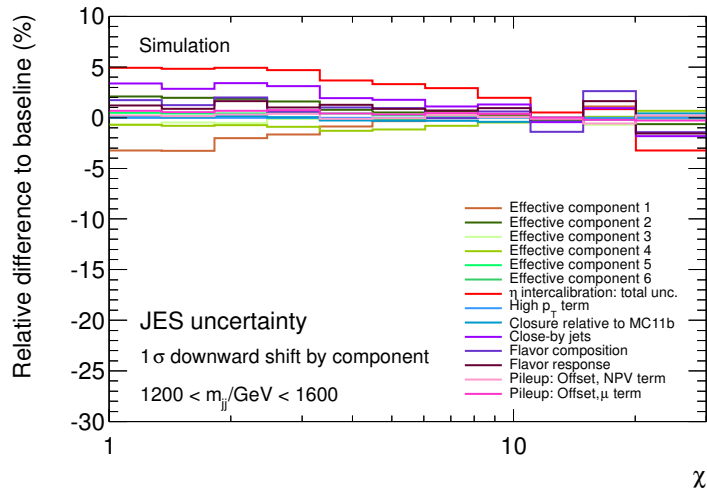
**Figure A.8.** The event with the second-highest dijet invariant mass in the analysis. In this event, the leading jet had a transverse momentum of  $p_{\text{T}}^1 = 941$  GeV, and the subleading jet had a transverse momentum of  $p_{\text{T}}^2 = 679$  GeV. The invariant mass of the dijet system was  $m_{jj} = 4346$  GeV. Only tracks with  $p_{\text{T}}^{\text{track}} > 500$  MeV are displayed. The event was recorded on September 9th, 2011.

## A.4. Jet energy scale uncertainty

Figures A.9 to A.11 show the contributions of the individual JES components on the analysis. Reported are the effects of separate  $+1\sigma$  and  $-1\sigma$  shifts on the dijet angular distributions obtained from Monte Carlo simulations. Figures A.12 to A.14 show the evolution of the JES uncertainty estimate as a function of the number of pseudo-experiments for statistically independent estimates. The distributions complement the studies discussed in chapter 8.

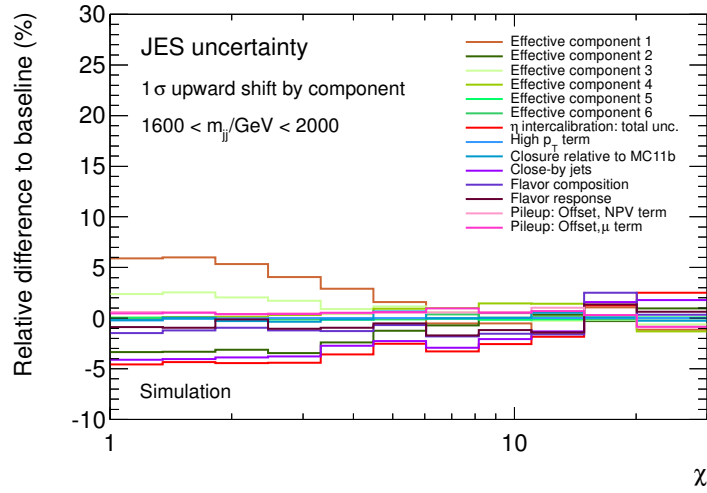


(a)

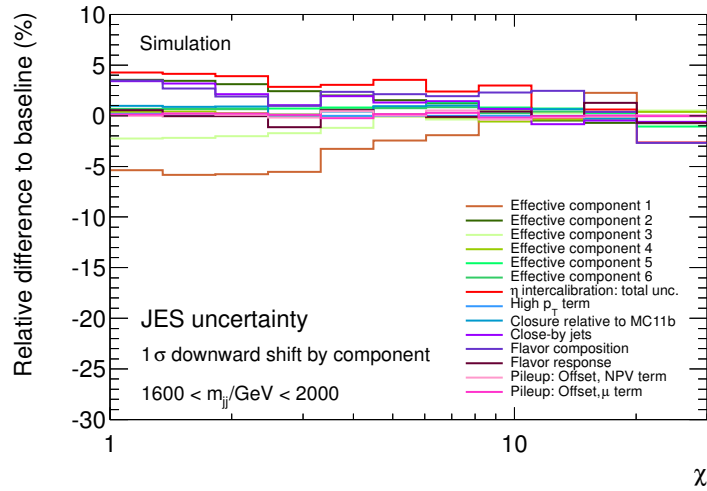


(b)

**Figure A.9.** The individual components of the jet energy scale (JES) uncertainty for events with dijet invariant masses between 1200 and 1600 GeV. Shown is the effect of  $1\sigma$  upward shifts (a) and downward shifts (b) on the  $\chi$ -distribution; also appeared in [89]

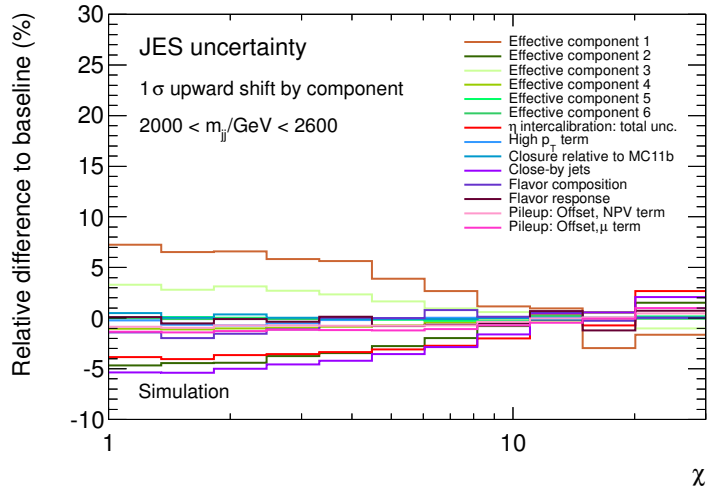


(a)

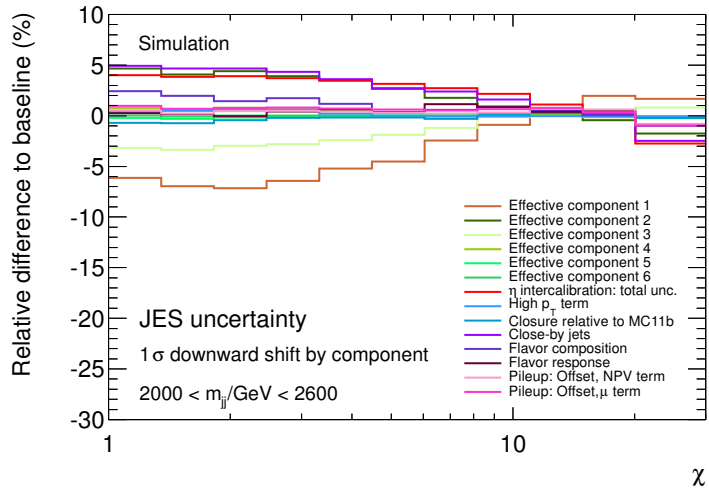


(b)

**Figure A.10.** The individual components of the jet energy scale (JES) uncertainty for events with dijet invariant masses between 1600 and 2000 GeV. Shown is the effect of  $1\sigma$  upward shifts (a) and downward shifts (b) on the  $\chi$ -distribution; also appeared in [89]

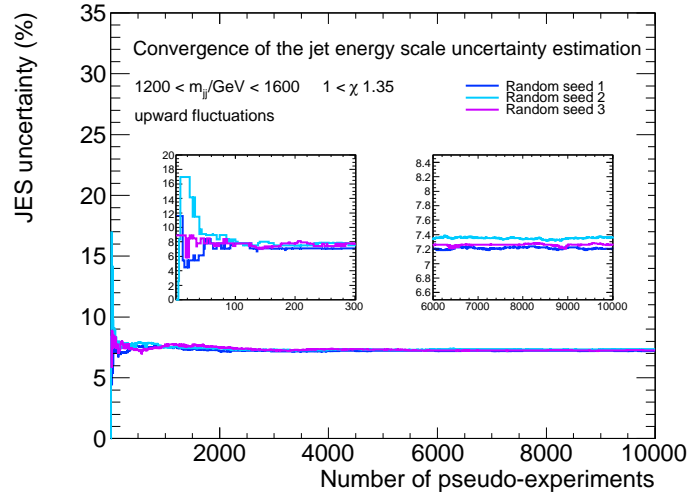


(a)

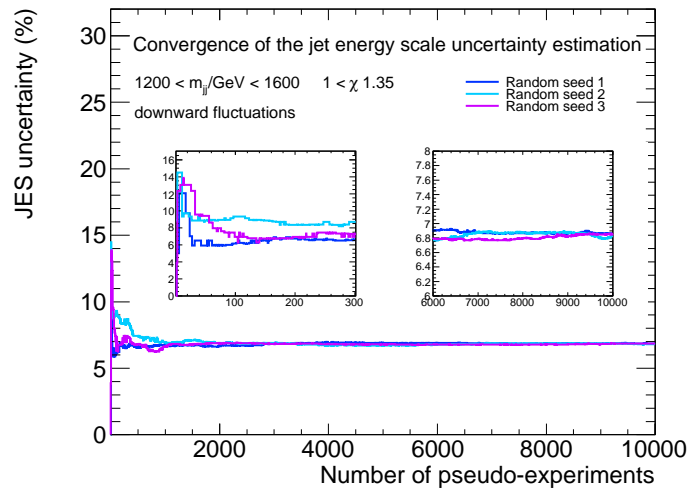


(b)

**Figure A.11.** The individual components of the jet energy scale (JES) uncertainty for events with dijet invariant masses between 2000 and 2600 GeV. Shown is the effect of  $1\sigma$  upward shifts (a) and downward shifts (b) on the  $\chi$ -distribution; also appeared in [89]

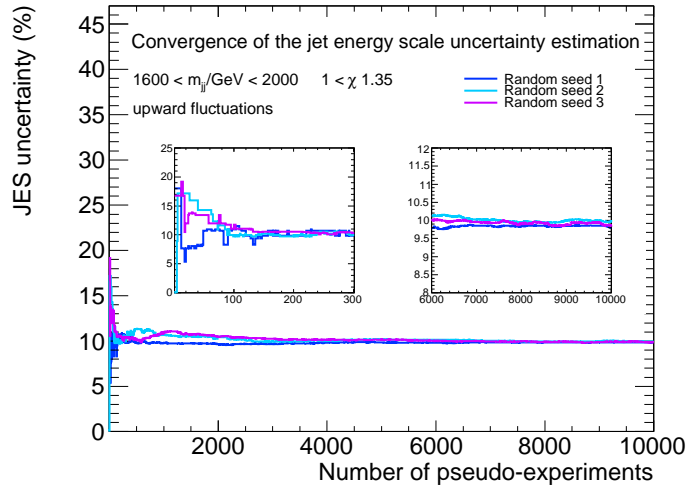


(a)

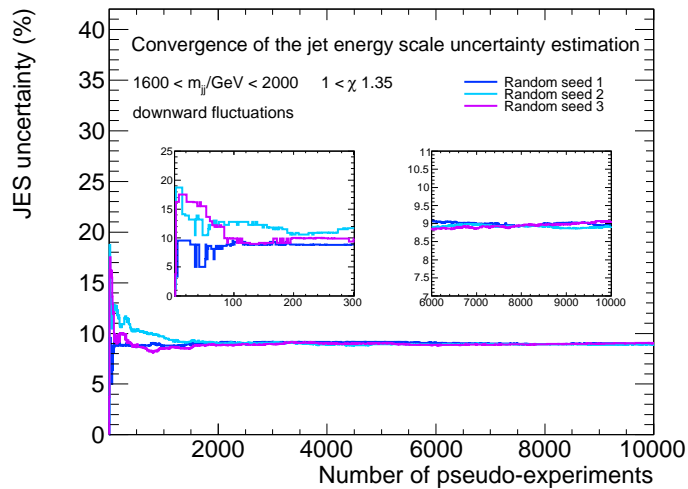


(b)

**Figure A.12.** The evolution of the JES uncertainty estimate as a function of the number of pseudo-experiments. Shown is the uncertainty estimate in the first  $\chi$ -bin for events with dijet invariant masses between 1200 and 1600 TeV. The inlays show a zoomed view of the left part (left inlay) and of the right part (right inlay) of the  $x$ -axis. The uncertainties have been determined from three statistically different sets of pseudo-experiments (3 coloured lines). Figure (a) shows the uncertainty determined from upward fluctuations and figure (b) the one from downward fluctuations.

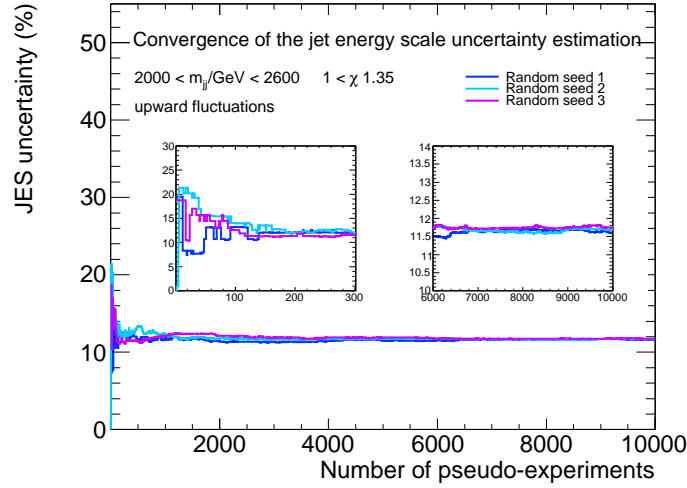


(a)

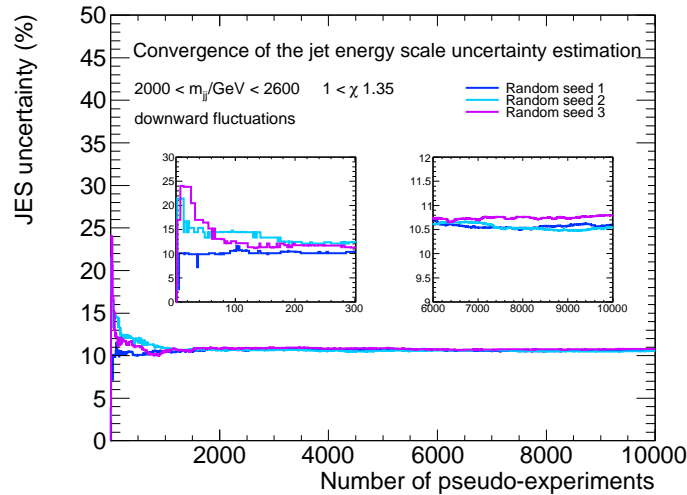


(b)

**Figure A.13.** The evolution of the JES uncertainty estimate as a function of the number of pseudo-experiments. Shown is the uncertainty estimate in the first  $\chi$ -bin for events with dijet invariant masses between 1600 and 1000 TeV. The inlays show a zoomed view of the left part (left inlay) and of the right part (right inlay) of the  $x$ -axis. The uncertainties have been determined from three statistically different sets of pseudo-experiments (3 coloured lines). Figure (a) shows the uncertainty determined from upward fluctuations and figure (b) the one from downward fluctuations.



(a)



(b)

**Figure A.14.** The evolution of the JES uncertainty estimate as a function of the number of pseudo-experiments. Shown is the uncertainty estimate in the first  $\chi$ -bin for events with dijet invariant masses between 2000 and 2600 TeV. The inlays show a zoomed view of the left part (left inlay) and of the right part (right inlay) of the  $x$ -axis. The uncertainties have been determined from three statistically different sets of pseudo-experiments (3 coloured lines). Figure (a) shows the uncertainty determined from upward fluctuations and figure (b) the one from downward fluctuations.

# Bibliography

- [1] ATLAS Collaboration, *Search for new physics in dijet mass and angular distributions using  $4.8 \text{ fb}^{-1}$  of  $pp$  collisions at  $\sqrt{s} = 7 \text{ TeV}$  collected by the ATLAS detector*, Tech. Rep. ATLAS-CONF-2012-038, CERN, Geneva, 2012.
- [2] ATLAS Collaboration, G. Aad et al., *ATLAS search for new phenomena in dijet mass and angular distributions using  $pp$  collisions at  $\sqrt{s} = 7 \text{ TeV}$* , Journal of High Energy Physics **1301** (2013) 029. Supplementary information at [atlas.web.cern.ch/Atlas/GROUPS/PHYSICS/PAPERS/EXOT-2011-21](http://atlas.web.cern.ch/Atlas/GROUPS/PHYSICS/PAPERS/EXOT-2011-21).
- [3] G. Kane, *Modern elementary particle physics*. Perseus Publishing, 1993.
- [4] “Standard Model.” [en.wikipedia.org/wiki/Standard\\_Model](http://en.wikipedia.org/wiki/Standard_Model). Retrieved 01-04-2013.
- [5] ATLAS Collaboration, G. Aad et al., *Observation of a new particle in the search for the Standard Model Higgs boson with the ATLAS detector at the LHC*, Physics Letters B (2012).
- [6] CMS Collaboration, S. Chatrchyan et al., *Observation of a new boson at a mass of  $125 \text{ GeV}$  with the CMS experiment at the LHC*, Physics Letters B (2012).
- [7] ATLAS Collaboration, *Study of the spin of the Higgs-like boson in the two photon decay channel using  $20.7 \text{ fb}^{-1}$  of  $pp$  collisions collected at  $\sqrt{s} = 8 \text{ TeV}$  with the ATLAS detector*, Tech. Rep. ATLAS-CONF-2013-029, CERN, Geneva, 2013.
- [8] CMS Collaboration, *Properties of the Higgs-like boson in the decay  $H$  to  $ZZ$  to  $4l$  in  $pp$  collisions at  $\sqrt{s} = 7$  and  $8 \text{ TeV}$* , Tech. Rep. CMS-PAS-HIG-13-002, CERN, Geneva, 2013.
- [9] R. K. Ellis, W. J. Stirling, and B. R. Webber, *QCD and collider physics*, vol. 8. Cambridge University Press, 2003.
- [10] J. Beringer et al., *Review of particle physics*, Physical Review D **86** no. 1, (2012) 010001.
- [11] G. t Hooft and M. Veltman, *Regularization and renormalization of gauge fields*, Nuclear Physics B **44** no. 1, (1972) 189–213.
- [12] C. Bollini and J. Giambiagi, *Dimensional renormalization: The number of dimensions as a regularizing parameter*, Il Nuovo Cimento **12** no. 1, (1972).

- [13] G. 't Hooft, *Dimensional regularization and the renormalization group*, Nuclear Physics B **61** (1973) 455–468.
- [14] W. A. Bardeen et al., *Deep-inelastic scattering beyond the leading order in asymptotically free gauge theories*, Physical Review D **18** no. 11, (1978) 3998.
- [15] J. Collins and D. Soper, *The theorems of perturbative QCD*, Annual Review of Nuclear and Particle Science **37** (1987) 383–409.
- [16] R. Feynman, *Photon-hadron interactions*. Frontiers in physics. W.A. Benjamin, Incorporated, Advanced Book Program, 1972.
- [17] H1 and ZEUS Collaborations, F. Aaron, et al., *Combined measurement and QCD analysis of the inclusive  $e^\pm p$  scattering cross sections at HERA*, Journal of High Energy Physics **2010** no. 1, (2010) 1–63.
- [18] V. N. Gribov and L. N. Lipatov, *Deep inelastic ep scattering in perturbation theory*, Soviet Journal of Nuclear Physics **15** (1972) 438–450.
- [19] G. Altarelli and G. Parisi, *Asymptotic freedom in parton language*, Nuclear Physics B **126** no. 2, (1977) 298–318.
- [20] Y. L. Dokshitzer, *Calculation of structure functions of deep-inelastic scattering and  $e^+e^-$  annihilation by perturbation theory in quantum chromodynamics*, Soviet Journal of Experimental and Theoretical Physics **46** (1977) 641.
- [21] J. M. Campbell, J. Huston, and W. Stirling, *Hard interactions of quarks and gluons: a primer for LHC physics*, Reports on Progress in Physics **70** no. 1, (2006) 89.
- [22] T. Sjöstrand, S. Mrenna, and P. Skands, *PYTHIA 6.4 – Physics and manual*, Journal of High Energy Physics **2006** no. 05, (2006) 026.
- [23] B. Andersson et al., *Parton fragmentation and string dynamics*, Physics Reports **97** (1983) 31–145.
- [24] B. Andersson, *The Lund model*. Cambridge Monographs on Particle Physics, Nuclear Physics and Cosmology. Cambridge University Press, 1998.
- [25] G. P. Salam, *Towards jetography*, The European Physical Journal C-Particles and Fields **67** no. 3, (2010) 637–686.
- [26] M. Cacciari, G. P. Salam, and G. Soyez, *The anti- $k_t$  jet clustering algorithm*, Journal of High Energy Physics **2008** no. 04, (2008) 063.
- [27] R. Devenish and A. Cooper-Sarkar, *Deep inelastic scattering*. Oxford University Press, 2004.

- 
- [28] S. Mandelstam, *Determination of the pion-nucleon scattering amplitude from dispersion relations and unitarity. General theory*, Physical Review **112** no. 4, (1958) 1344.
- [29] B. Combridge, J. Kripfganz, and J. Ranft, *Hadron production at large transverse momentum and QCD*, Physics Letters B **70** no. 2, (1977) 234–238.
- [30] Z. Nagy, *Three-jet cross sections in hadron-hadron collisions at next-to-leading order*, Physical Review Letters **88** no. 12, (2002) 122003.
- [31] Z. Nagy, *Next-to-leading order calculation of three-jet observables in hadron-hadron collisions*, Physical Review D **68** no. 9, (2003) 094002.
- [32] S. Catani and M. H. Seymour, *A general algorithm for calculating jet cross sections in NLO QCD*, Nuclear Physics B **485** no. 1, (1997) 291–419.
- [33] S. Catani and M. Seymour, *Erratum to “A general algorithm for calculating jet cross sections in NLO QCD” [Nucl. Phys. B 485 (1997) 291-419]*, Nuclear physics B **510** (1998) 503–504.
- [34] ATLAS Collaboration, G. Aad et al., *Measurement of inclusive jet and dijet production in pp collisions at  $\sqrt{s} = 7$  TeV using the ATLAS detector*, Physical Review **D86** (2012) 014022.
- [35] E. Rutherford, *The scattering of  $\alpha$  and  $\beta$  particles by matter and the structure of the atom*, The London, Edinburgh, and Dublin Philosophical Magazine and Journal of Science **21** no. 125, (1911) 669–688.
- [36] E. Bloom et al., *High-energy inelastic ep scattering at  $6^\circ$  and  $10^\circ$* , Physical Review Letters **23** (1969) 930–934.
- [37] M. Breidenbach et al., *Observed behavior of highly inelastic electron-proton scattering*, Physical Review Letters **23** no. 16, (1969) 935–939.
- [38] E. Eichten, I. Hinchliffe, K. Lane, and C. Quigg, *Supercollider physics*, Reviews of Modern Physics **56** no. 4, (1984) 579.
- [39] E. Eichten, I. Hinchliffe, K. Lane, and C. Quigg, *Erratum: Supercollider physics*, Reviews of Modern Physics **58** no. 4, (1986) 1065.
- [40] P. Chiappetta and M. Perrottet, *Possible bounds on compositeness from inclusive one jet production in large hadron colliders*, Physics Letters B **253** no. 3, (1991) 489–493.
- [41] N. Arkani-Hamed, S. Dimopoulos, and G. Dvali, *The hierarchy problem and new dimensions at a millimeter*, Physics Letters B **429** no. 3, (1998) 263–272.

- [42] N. Arkani-Hamed, S. Dimopoulos, and G. Dvali, *Phenomenology, astrophysics, and cosmology of theories with submillimeter dimensions and TeV scale quantum gravity*, Physical Review D **59** no. 8, (1999) 086004.
- [43] L. Randall and R. Sundrum, *Large mass hierarchy from a small extra dimension*, Physical Review Letters **83** no. 17, (1999) 3370–3373.
- [44] L. Randall and R. Sundrum, *An alternative to compactification*, Physical Review Letters **83** no. 23, (1999) 4690–4693.
- [45] S. Dimopoulos and G. Landsberg, *Black holes at the Large Hadron Collider*, Physical Review Letters **87** no. 16, (2001) 161602.
- [46] S. B. Giddings and S. Thomas, *High energy colliders as black hole factories: The end of short distance physics*, Physical Review D **65** no. 5, (2002) 056010.
- [47] K. Thorne, *Nonspherical gravitational collapse – A short review*, in *Magic without magic: John Archibald Wheeler. A collection of essays in honor of his sixtieth birthday*. W.H. Freeman, 1972.
- [48] P. Meade and L. Randall, *Black holes and quantum gravity at the LHC*, Journal of High Energy Physics **2008** no. 05, (2008) 003.
- [49] D.-C. Dai et al., *BlackMax: A black-hole event generator with rotation, recoil, split branes, and brane tension*, Physical Review D **77** no. 7, (2008) 076007.
- [50] CDF Collaboration, F. Abe et al., *Dijet angular distribution in  $p\bar{p}$  collisions at  $\sqrt{s}=1.8$  TeV*, Physical Review Letters **69** no. 20, (1992) 2896–2900.
- [51] CDF Collaboration, F. Abe et al., *Measurement of dijet angular distributions by the Collider Detector at Fermilab*, Physical Review Letters **77** no. 27, (1996) 5336–5341.
- [52] DØ Collaboration, B. Abbott et al., *Measurement of dijet angular distributions and search for quark compositeness*, Physical Review Letters **80** no. 4, (1998) 666–671.
- [53] DØ Collaboration, B. Abbott et al., *Dijet mass spectrum and a search for quark compositeness in  $p\bar{p}$  collisions at  $\sqrt{s}=1.8$  TeV*, Physical Review Letters **82** no. 12, (1999) 2457–2462.
- [54] DØ Collaboration, B. Abbott et al., *Limits on quark compositeness from high energy jets in  $p\bar{p}$  collisions at 1.8 TeV*, Physical Review D **62** no. 3, (2000) 031101.
- [55] DØ Collaboration, V. Abazov et al., *Measurement of dijet angular distributions at  $\sqrt{s}=1.96$  TeV and searches for quark compositeness and extra spatial dimensions*, Physical Review Letters **103** no. 19, (2009) 191803.

- 
- [56] ATLAS Collaboration, G. Aad et al., *Search for quark contact interactions in dijet angular distributions in pp collisions at  $\sqrt{s} = 7$  TeV measured with the ATLAS detector*, Physics Letters B **694** no. 4-5, (2011) 327–345.
- [57] ATLAS Collaboration, G. Aad et al., *A search for new physics in dijet mass and angular distributions in pp collisions at TeV measured with the ATLAS detector*, New Journal of Physics **13** no. 5, (2011) 053044.
- [58] ATLAS Collaboration, G. Aad et al., *Search for new particles in two-jet final states in 7 TeV proton-proton collisions with the ATLAS detector at the LHC*, Physical Review Letters **105** no. 16, (2010) 161801.
- [59] CMS Collaboration, V. Khachatryan et al., *Search for quark compositeness with the dijet centrality ratio in pp collisions at  $\sqrt{s} = 7$  TeV*, Physical Review Letters **105** no. 26, (2010) 262001.
- [60] CMS Collaboration, V. Khachatryan et al., *Search for dijet resonances in 7 TeV pp collisions at CMS*, Physical Review Letters **105** no. 21, (2010) 211801.
- [61] CMS Collaboration, V. Khachatryan et al., *Measurement of dijet angular distributions and search for quark compositeness in pp collisions at  $\sqrt{s} = 7$  TeV*, Physical Review Letters **106** no. 20, (2011) 201804.
- [62] CMS Collaboration, S. Chatrchyan et al., *Search for resonances in the dijet mass spectrum from 7 TeV pp collisions at CMS*, Physics Letters B **704** no. 3, (2011) 123–142.
- [63] ATLAS Collaboration, G. Aad et al., *Search for new physics in the dijet mass distribution using  $1 \text{ fb}^{-1}$  of pp collision data at  $\sqrt{s} = 7$  TeV collected by the ATLAS detector*, Physics Letters B **708** (2012) 37–54.
- [64] CDF Collaboration, F. Abe et al., *Inclusive jet cross section in pp collisions at  $\sqrt{s} = 1.8$  TeV*, Physical Review Letters **77** no. 3, (1996).
- [65] CDF Collaboration, T. Affolder et al., *Measurement of the differential dijet mass cross section in  $p\bar{p}$  collisions at  $\sqrt{s} = 1.8$  TeV*, Physical Review D **61** no. 9, (2000) 91101.
- [66] D. Stump et al., *Inclusive jet production, parton distributions, and the search for new physics*, Journal of High Energy Physics **2003** no. 10, (2003) 046.
- [67] ATLAS Collaboration, G. Aad et al., *The ATLAS experiment at the CERN Large Hadron Collider*, Journal of Instrumentation **3** no. 08, (2008) S08003.
- [68] M. Benedikt, P. Collier, V. Mertens, J. Poole, and K. Schindl, *LHC design report*. CERN, Geneva, 2004.
- [69] “The detector site.” [www.atlas.ch/photos/detector-site-surface.html](http://www.atlas.ch/photos/detector-site-surface.html).

- [70] CMS Collaboration, S. Chatrchyan et al., *The CMS experiment at the CERN LHC*, Journal of Instrumentation **3** no. 08, (2008) S08004.
- [71] ALICE Collaboration, K. Aamodt et al., *The ALICE experiment at the CERN LHC*, Journal of Instrumentation **3** no. 08, (2008) S08002.
- [72] LHCb Collaboration, A. A. Alves Jr et al., *The LHCb detector at the LHC*, Journal of Instrumentation **3** no. 08, (2008) S08005.
- [73] E. Abat et al., *Study of energy response and resolution of the ATLAS barrel calorimeter to hadrons of energies from 20 to 350 GeV*, Nuclear Instruments and Methods in Physics Research Section A: Accelerators, Spectrometers, Detectors and Associated Equipment **621** no. 1, (2010) 134–150.
- [74] ATLAS Collaboration, *Jet energy scale and its systematic uncertainty in proton-proton collisions at  $\sqrt{s} = 7$  TeV with ATLAS 2011 data*, Tech. Rep. ATLAS-CONF-2013-004, CERN, Geneva, 2013.
- [75] ATLAS Collaboration, G. Aad et al., *Improved luminosity determination in pp collisions at  $\sqrt{s} = 7$  TeV using the ATLAS detector at the LHC*, To be published in The European Physics Journal C (2013). arXiv:1302.4393.
- [76] ATLAS Collaboration, “ATLAS run query.” [atlas-runquery.cern.ch](http://atlas-runquery.cern.ch).
- [77] S. Haywood et al., *ATLAS Inner Detector: Technical Design Report, 1*. Technical Design Report ATLAS. CERN, Geneva, 1997.
- [78] S. Haywood et al., *ATLAS Inner Detector: Technical Design Report, 2*. Technical Design Report ATLAS. CERN, Geneva, 1997.
- [79] W. Lampl et al., *Calorimeter clustering algorithms: Description and performance*, Tech. Rep. ATL-LARG-PUB-2008-002. ATL-COM-LARG-2008-003, CERN, Geneva, 2008.
- [80] L. Ancu et al., *The design and performance of the ATLAS jet trigger for the Event Filter*, Tech. Rep. ATL-COM-DAQ-2011-048, CERN, Geneva, 2011.
- [81] ATLAS Collaboration, “Evolution of trigger prescales.” [atlas-trigconf.cern.ch/psevo/](http://atlas-trigconf.cern.ch/psevo/).
- [82] ATLAS Collaboration, “COMA Period description report.” [atlas-tagservices.cern.ch/tagservices/RunBrowser/runBrowserReport/rBR\\_Period\\_Report.php?fnt=data11\\_7TeV&pn=AllYear](http://atlas-tagservices.cern.ch/tagservices/RunBrowser/runBrowserReport/rBR_Period_Report.php?fnt=data11_7TeV&pn=AllYear).
- [83] T. Sjöstrand, S. Mrenna, and P. Skands, *A brief introduction to PYTHIA 8.1*, Computer Physics Communications **178** no. 11, (2008) 852–867.

- 
- [84] A. Sherstnev and R. Thorne, *Parton distributions for LO generators*, The European Physical Journal C – Particles and Fields **55** no. 4, (2008) 553–575.
- [85] M. Bähr et al., *HERWIG++ – Physics and manual*, The European Physical Journal C **58** no. 4, (2008) 639–707.
- [86] A. Buckley et al., *General-purpose event generators for LHC physics*, Physics Reports **504** no. 5, (2011) 145–233.
- [87] ATLAS Collaboration, *ATLAS tunes of PYTHIA 6 and PYTHIA 8 for MC11*, Tech. Rep. ATL-PHYS-PUB-2011-009, CERN, Geneva, 2011.
- [88] E. Richter-Was, D. Froidevaux, and L. Poggioli, *ATLFAST 2.0 – A fast simulation package for ATLAS*, Tech. Rep. ATL-PHYS-98-131, CERN, Geneva, 1998.
- [89] D. Adams et al., *Search for new phenomena in dijet mass and angular distributions using  $4.8 \text{ fb}^{-1}$  of  $pp$  collisions at  $\sqrt{s} = 7 \text{ TeV}$  collected by the ATLAS detector: supporting documentation*, Tech. Rep. ATL-COM-PHYS-2012-801, CERN, Geneva, 2012.
- [90] ATLAS Collaboration, G. Aad et al., *The ATLAS simulation infrastructure*, The European Physical Journal C – Particles and Fields **70** no. 3, (2010) 823–874.
- [91] S. Agostinelli et al., *GEANT4 – A simulation toolkit*, Nuclear Instruments and Methods in Physics Research Section A: Accelerators, Spectrometers, Detectors and Associated Equipment **506** no. 3, (2003) 250–303.
- [92] ATLAS Collaboration, G. Aad et al., *Pile-up corrections for jets from proton-proton collisions at  $\sqrt{s} = 7 \text{ TeV}$  in ATLAS in 2011*, Tech. Rep. ATLAS-CONF-2012-064, CERN, Geneva, 2012.
- [93] R. Corke and T. Sjöstrand, *Interleaved parton showers and tuning prospects*, Journal of High Energy Physics **2011** no. 3, (2011) 1–52.
- [94] H.-L. Lai et al., *New parton distributions for collider physics*, Physical Review **D82** (2010) 074024.
- [95] N. Boelaert, *Dijet angular distributions in proton-proton collisions at  $\sqrt{s} = 7 \text{ TeV}$  and  $\sqrt{s} = 14 \text{ TeV}$* . PhD thesis, Lund University, 2010.
- [96] F. Bloch and A. Nordsieck, *Note on the radiation field of the electron*, Physical Review **52** no. 2, (1937) 54.
- [97] T. Kinoshita, *Mass singularities of Feynman amplitudes*, Journal of Mathematical Physics **3** (1962) 650.
- [98] T. Lee and M. Nauenberg, *Degenerate systems and mass singularities*, Physical Review **133** no. 6B, (1964) B1549.

- [99] W. Giele and E. N. Glover, *Higher-order corrections to jet cross sections in  $e^+e^-$  annihilation*, Physical Review D **46** no. 5, (1992) 1980.
- [100] W. T. Giele, E. N. Glover, and D. A. Kosower, *Higher-order corrections to jet cross sections in hadron colliders*, Nuclear Physics B **403** no. 3, (1993) 633–667.
- [101] ATLAS Collaboration, G. Aad et al., *Jet energy measurement with the ATLAS detector in proton-proton collisions at  $\sqrt{s} = 7$  TeV*, The European Physics Journal **C73** (2013) 2304.
- [102] G. S. M. Cacciari, G.P. Salam, “FastJet.” fastjet.fr.
- [103] E. Abat et al., *Combined performance studies for electrons at the 2004 ATLAS combined test-beam*, Journal of Instrumentation **5** no. 11, (2010) P11006.
- [104] M. Aharrouche et al., *Measurement of the response of the ATLAS liquid argon barrel calorimeter to electrons at the 2004 combined test-beam*, Nuclear Instruments and Methods in Physics Research Section A: Accelerators, Spectrometers, Detectors and Associated Equipment **614** no. 3, (2010) 400–432.
- [105] M. Aharrouche et al., *Response uniformity of the ATLAS liquid argon electromagnetic calorimeter*, Nuclear Instruments and Methods in Physics Research Section A: Accelerators, Spectrometers, Detectors and Associated Equipment **582** no. 2, (2007) 429–455.
- [106] ATLAS Collaboration, G. Aad et al., *Electron performance measurements with the ATLAS detector using the 2010 LHC proton-proton collision data*, The European Physical Journal C – Particles and Fields **72** no. 3, (2012) 1–46.
- [107] P. Adragna et al., *Testbeam studies of production modules of the ATLAS Tile Calorimeter*, Nuclear Instruments and Methods in Physics Research Section A: Accelerators, Spectrometers, Detectors and Associated Equipment **606** no. 3, (2009) 362–394.
- [108] G. Aad et al., *Readiness of the ATLAS tile calorimeter for LHC collisions*, The European Physical Journal C – Particles and Fields **70** no. 4, (2010) 1193–1236.
- [109] R. Wigmans, *Calorimetry: Energy measurements in particle physics*. Oxford Science Publications. Clarendon Press, 2000.
- [110] ATLAS Collaboration, *In situ jet pseudorapidity intercalibration of the ATLAS detector using dijet events in  $\sqrt{s} = 7$  TeV proton-proton 2011 data*, Tech. Rep. ATLAS-CONF-2012-124, CERN, Geneva, 2012.
- [111] ATLAS Collaboration, *Probing the measurement of jet energies with the ATLAS detector using Z+jet events from proton-proton collisions at  $\sqrt{s} = 7$  TeV*, Tech. Rep. ATLAS-CONF-2012-053, CERN, Geneva, 2012.

- 
- [112] ATLAS Collaboration, *Probing the measurement of jet energies with the ATLAS detector using photon+jet events in proton-proton collisions at  $\sqrt{s} = 7$  TeV*, Tech. Rep. ATLAS-CONF-2012-063, CERN, Geneva, 2012.
- [113] ATLAS Collaboration, *TeV-scale jet energy calibration using multijet events including close-by jet effects at the ATLAS experiment*, Tech. Rep. ATLAS-CONF-2013-003, CERN, Geneva, 2013.
- [114] ATLAS Collaboration, G. Aad et al., *Single hadron response measurement and calorimeter jet energy scale uncertainty with the ATLAS detector at the LHC*, European Physical Journal **C73** (2013) 2305.
- [115] ATLAS Collaboration, “ATLAS pro-10 Good Run List.” [atlasdqm.web.cern.ch/atlasdqm/grlgen/Archive/CombinedPerf/JetEtMiss/JetEtMiss\\_v01/data11\\_7TeVperiodAllYear\\_DetStatus-v36-pro10\\_CoolRunQuery-00-04-08\\_JetEtMiss.xml](http://atlasdqm.web.cern.ch/atlasdqm/grlgen/Archive/CombinedPerf/JetEtMiss/JetEtMiss_v01/data11_7TeVperiodAllYear_DetStatus-v36-pro10_CoolRunQuery-00-04-08_JetEtMiss.xml).
- [116] ATLAS Collaboration, *Performance of primary vertex reconstruction in proton-proton collisions at  $\sqrt{s} = 7$  TeV in the ATLAS experiment*, Tech. Rep. ATLAS-CONF-2010-069, CERN, Geneva, 2010.
- [117] S. Asai et al., *Further search for squarks and gluinos using final states with jets and missing transverse momentum with the ATLAS experiment in  $\sqrt{s} = 7$  TeV proton-proton collisions: supporting documentation*, Tech. Rep. ATL-PHYS-INT-2011-085, CERN, Geneva, 2011.
- [118] ATLAS Collaboration, *Selection of jets produced in proton-proton collisions with the ATLAS detector using 2011 data*, Tech. Rep. ATLAS-CONF-2012-020, CERN, Geneva, 2012.
- [119] ATLAS Collaboration, *Data-quality requirements and event cleaning for jets and missing transverse energy reconstruction with the ATLAS detector in proton-proton collisions at a center-of-mass energy of  $\sqrt{s} = 7$  TeV*, Tech. Rep. ATLAS-CONF-2010-038, CERN, Geneva, 2010.
- [120] G. Aad et al., *Readiness of the ATLAS liquid argon calorimeter for LHC collisions*, The European Physical Journal C – Particles and Fields **70** no. 3, (2010) 723–753.
- [121] S. Frixione and G. Ridolfi, *Jet photoproduction at HERA*, Nuclear Physics B **507** no. 1, (1997) 315–333.
- [122] N. Boelaert et al., *Measurement of high mass dijet production in pp collisions at  $\sqrt{s} = 7$  TeV using the ATLAS detector*, Tech. Rep. ATL-COM-PHYS-2012-1250, CERN, Geneva, 2012. To be published. The reference to the current version of the supporting documentation is reported.

- [123] ATLAS Collaboration, G. Aad et al., *Search for new physics in dijet mass and angular distributions in pp collisions at  $\sqrt{s} = 7$  TeV measured with the ATLAS detector*, New Journal of Physics **13** (2011) 053044.
- [124] N. Boelaert, “Updates in dijet  $\chi$  analysis.” [indico.cern.ch/getFile.py/access?contribId=2&resId=0&materialId=slides&confId=136361](http://indico.cern.ch/getFile.py/access?contribId=2&resId=0&materialId=slides&confId=136361).
- [125] ATLAS Collaboration, “ATLAS Luminosity Public Results.” [twiki.cern.ch/twiki/bin/view/AtlasPublic/LuminosityPublicResults](http://twiki.cern.ch/twiki/bin/view/AtlasPublic/LuminosityPublicResults).
- [126] ATLAS Collaboration, “ATLAS Pile-up reweighting.” [twiki.cern.ch/twiki/bin/viewauth/AtlasProtected/ExtendedPileupReweighting](http://twiki.cern.ch/twiki/bin/viewauth/AtlasProtected/ExtendedPileupReweighting).
- [127] ATLAS Collaboration, G. Aad et al., *Jet energy resolution in proton-proton collisions at  $\sqrt{s} = 7$  TeV recorded in 2010 with the ATLAS detector*, European Physical Journal **C73** (2013) 2306.
- [128] ATLAS Collaboration, “ATLAS Jet Calibration Tools.” [twiki.cern.ch/twiki/bin/viewauth/AtlasProtected/JetCalibrationToolsWinter2011?rev=31](http://twiki.cern.ch/twiki/bin/viewauth/AtlasProtected/JetCalibrationToolsWinter2011?rev=31).
- [129] T. Carli et al., *A posteriori inclusion of parton density functions in NLO QCD final-state calculations at hadron colliders: the APPLGRID project*, The European Physical Journal C – Particles and Fields **66** no. 3, (2010) 503–524.
- [130] S. Frixione, P. Nason, and C. Oleari, *Matching NLO QCD computations with Parton Shower simulations: the POWHEG method*, Journal of High Energy Physics **2007** no. 11, (2007) 070.
- [131] *New ATLAS event generator tunes to 2010 data*, Tech. Rep. ATL-PHYS-PUB-2011-008, CERN, Geneva, 2011.
- [132] S. Gieseke, C. Röhr, and A. Siódmok, *Colour reconnections in HERWIG++*, The European Physical Journal C **72** no. 11, (2012) 1–18.
- [133] G. Marchesini and B. Webber, *Monte Carlo simulation of general hard processes with coherent QCD radiation*, Nuclear Physics B **310** no. 3, (1988) 461–526.
- [134] B. R. Webber, *A QCD model for jet fragmentation including soft gluon interference*, Nuclear Physics B **238** no. 3, (1984) 492–528.
- [135] CDF Collaboration, T. Aaltonen et al., *Global search for new physics with 2.0 fb<sup>-1</sup> at CDF*, Physical Review D **79** no. 1, (2009) 011101.
- [136] G. Choudalakis, *On hypothesis testing, trials factor, hypertests and the BumpHunter*, arXiv:1101.0390 (2011).
- [137] ATLAS Collaboration, *ATLAS detector and physics performance. Technical design report. Vol. 2 (1999)*, tech. rep., CERN-LHCC-99-15.

- 
- [138] A. L. Read, *Presentation of search results: the  $CL_s$  technique*, Journal of Physics G: Nuclear and Particle Physics **28** no. 10, (2002) 2693.
- [139] CMS Collaboration, S. Chatrchyan et al., *Search for contact interactions using the inclusive jet  $p_T$  spectrum in  $pp$  collisions at  $\sqrt{s} = 7$  TeV*, Physical Review D **87** (2013) 052017.
- [140] CMS Collaboration, S. Chatrchyan et al., *Determination of jet energy calibration and transverse momentum resolution in CMS*, Journal of Instrumentation **6** (2011).
- [141] R. Eusebi on behalf of the CMS collaboration, “Jet energy corrections and uncertainties: reducing their impact on physics measurements.” [indico.cern.ch/getFile.py/access?contribId=22&sessionId=0&resId=0&materialId=slides&confId=176585](http://indico.cern.ch/getFile.py/access?contribId=22&sessionId=0&resId=0&materialId=slides&confId=176585).
- [142] ATLAS Collaboration, G. Aad et al., *Search for dark matter candidates and large extra dimensions in events with a jet and missing transverse momentum with the ATLAS detector*, Journal of High Energy Physics **1304** (2013) 075.
- [143] CMS Collaboration, S. Chatrchyan et al., *Search for dark matter and large extra dimensions in monojet events in  $pp$  collisions at  $\sqrt{s} = 7$  TeV*, Journal of High Energy Physics **2012** no. 9, (2012) 1–37.
- [144] CMS Collaboration, S. Chatrchyan et al., *Search for narrow resonances and quantum black holes in inclusive and  $b$ -tagged dijet mass spectra from  $pp$  collisions at  $\sqrt{s} = 7$  TeV*, Journal of High Energy Physics **2013** no. 1, (2013) 1–40.
- [145] CMS Collaboration, S. Chatrchyan et al., *Search for microscopic black holes in  $pp$  collisions at  $\sqrt{s} = 8$  TeV*, arXiv:1303.5338 (2013). Submitted to the Journal of High Energy Physics.



# Acknowledgements

This project could only be accomplished with the help and guidance of many people.

Most importantly, I would like to thank Prof. Hans-Christian Schultz-Coulon for the freedom he gave me to develop and follow my own scientific interest by pursuing this analysis, and for the guidance and the encouragement he has provided whenever it was needed. I would also like to thank him for the opportunity to travel to CERN whenever necessary and for supporting me in various ways, the attendance of two conferences being only one example.

PD Klaus Reyers has kindly agreed to be the second referee for this thesis, and I would like to thank him very much for the time invested.

Many members of the ATLAS and ILC groups at the Kirchhoff-Institute in Heidelberg have provided insight or help at some point during this work. I would like to thank Victor for supervising me throughout the first half of my PhD; Rainer for all the time he spent reading and discussing my thesis; Monica for discussions about physics and about all the small and big things that come with working in a large collaboration; and Martin, because without him, I would not have been in this group. I would like to thank Felix, Veit, Sahill and Micha for sharing this time and for their friendship. I am also very thankful to Valerie, Julia, Alessandra, Heiko and Yuriy who all helped proofreading my thesis in the last weeks and who contribute to the enjoyable atmosphere in the group.

This thesis would not have been the same without my colleagues at CERN. In particular, Nele is the one who helped me immensely in getting started in the dijet group, put trust in my work and spent endless hours explaining to me what she had learned before. I would like to thank Caterina for many discussions on the jet uncertainties, for saving me from starving more than once and for the pictures of BobTheCat that have accompanied me in the last weeks. I would like to thank Frederik and his family for all the nice evenings and the good food whenever I was at CERN and Eugen and Ryan for the productive and successful collaboration on the dijet analyses.

I am grateful to my family for the never-ending support and encouragement.

Finally, my biggest thanks goes to Sirin for constantly reminding me that there is a life without jets, calibrations and corrections and that, even if they might not be enough to explain some scale differences, four dimensions are plenty to enjoy a life together.